Development of Fe-50Co Alloy and its Composites by Spark Plasma Sintering

Mahesh Kumar Mani

A thesis submitted to the Cardiff University in candidature for the degree of

Doctor of Philosophy

Wolfson Centre for Magnetics
Cardiff School of Engineering
Cardiff University
Wales, United Kingdom

January 2014

Declaration

This work has not previously been accepted in substance for any degree and is not concurrently submitted in candidature for any degree.

Signed …… (Candidate) Date ……...

Statement 1

This thesis is being submitted in partial fulfilment of the requirements for the degree of PhD.

Signed …… . (Candidate) Date ……...

Statement 2

This thesis is the result of my own independent work/investigation, except where otherwise stated. Other sources are acknowledged by explicit references.

Signed ……. (Candidate) Date ……...

Statement 3

I hereby give consent for my thesis, if accepted, to be available for photocopying and for inter-library loan, and for the title and summary to be made available to outside organisations.

Signed ……. (Candidate) Date ……...

Acknowledgement

This research was supported by Cardiff University's flagship award named "The President's Research Scholarship". I would like to offer my special thanks to Cardiff University and Cogent power Ltd., part of Tata steel U.K for selecting me to offer this prestigious scholarship.

I am deeply grateful to my academic supervisors, Dr. J. P Hall and Prof. S.L Evans for their wide-ranging discussions and constructive suggestions from the inception to the end of my doctoral study. It would have been very difficult to reach to this stage without their constant support and guidance. I am greatly indebted to Prof. M.J. Reece and Dr. G. Viola in Queen Mary University, London for their support in preparing the samples using the spark plasma sintering facility at Nanoforce Technology Ltd., London. They also offered valuable feedback and constructive advices throughout my PhD.

I wish to thank Dr. P. Davies, Dr. T. Davies in Cardiff School of Chemistry for helping me to use the characterisation facilities for my research work. I appreciate the help offered by Miss R. Ramdas to use the DSC and XRD facilities in Cardiff School of Chemistry. I would like to express my sincere thanks to Mr. Clive Clark in the mechanical workshop for his invaluable support in cutting all the sintered samples on time. I have been greatly benefitted from a magnetic property measurement system, which is a brainchild of Dr. P.I Anderson in Wolfson centre for Magnetics. I thank Dr. M. Harbottle in Cardiff School of Engineering for offering me the permission to use the optical microscope. I appreciate the help offered by Dr. A.A. Antonysamy in GKN aerospace, U.K in measuring the density of few sintered materials using a gas pycnometer. I extend my thanks also to Dr. Nik Reeves-McLaren in the University of Sheffield, Dr. Michael Faulkner in the University of Manchester and Mr. Georgi Lalev in Cardiff School of Optometry for helping me in the advanced materials characterisation such as XRD with Co source, high resolution SEM and TEM.

I would particularly like to thank my friends and colleagues in Wolfson centre, Dr. S. Ramanathan, Mr. L. Mierczak, Mr. V. Goel, Dr. Y. Melikhov and Mr X. Xu, for their support and encouragement in the course of my research study. My gratitude goes to all the students and staff members in Wolfson centre for Magnetics for maintaining an amicable ambiance all the way through my PhD.

Last but not least, I owe my deepest gratitude to my parents, Mr. K. Mani and Mrs. M. Subbulakshmi, my brother Mr. M. Nagaraj, my friends and relatives for their support and continuous encouragements during the whole of my life.

Abstract

Composite strengthening was attempted to improve the mechanical strength and toughness of the brittle near equiatomic Fe-Co alloy. The matrix alloy chosen for this research falls in the Fe-(30-50) Co group, which are known for their highest saturation induction (B-sat) and Curie temperature among the commercial soft magnetic alloys. The reinforcements, which exhibited a wide range of aspect ratios, included SiC particulates, SiC whiskers and carbon nanotubes (CNTs). In order to minimize the interfacial reaction between the reinforcements and the Fe-50Co alloy (matrix) and to realise higher compact density, spark plasma sintering (SPS) was selected for rapid compaction of materials. Reinforcements were coated using electroless deposition with Ni-P, copper and cobalt to modify the interfacial chemistry and thickness, and hence the final properties of the composites.

A comprehensive study on the sintering variables found, within the range of examination and under constant heating and cooling rates, the optimum maximum temperature, soaking time and mechanical pressure of 900^{o}C, 2-5 minutes and 80 MPa to rapidly consolidate the Fe- 50Co alloy to near-theoretical density. The volume fraction and size of the ordered regions in the monolithic alloy and hence the magnetic properties, were sensitive to the heating rate, cooling rate, temperature at which the mechanical pressure was applied and removed and post heat treatments.

The influence of reinforcement coatings on the wetting characteristics, and in turn the properties, was compared using SiC particulate Fe-50Co composites. The introduction of bare and coarse (20 μm) SiC particulates negatively affected both magnetic and mechanical properties. Electroless Co coating of particulates improved both the flexural properties and magnetic characteristics such as permeability and coercivity by promoting the formation of narrower interfaces and better bonding.

The addition of bare and coated whiskers in Fe-Co alloys enhanced densification and grain growth of the matrix. Copper coating over whiskers was found to be not helpful in realising uniform dispersion, whereas Co and Ni-P coating aided to achieve uniform dispersion of whiskers in the matrix. The amorphous Ni-P coating on whiskers was nanocrystallised during the rapid sintering process and resulted in a material with highly improved mechanical strength and ductility in comparison to the monolithic and other whisker reinforced composite materials.

A novel attempt to prepare bulk Fe based alloy composites reinforced with CNTs was also undertaken. Both soft magnetic and mechanical property enhancements were observed in composites with lower vol% of CNTs (i.e. < 1.5%, in the range of examination up to 10%) due to the improvement of compact density by CNTs. An increase in the CNT vol% produced a negative effect on saturation induction and mechanical properties due to the agglomeration of CNTs and reduction in compact density. SPS helped to retain the structural integrity of CNTs during processing. Electroless Ni-P coating over the CNTs helped to reduce the structural damage of CNTs during processing and to improve the mechanical strength and ductility at a marginal cost of saturation induction, in comparison to the monolithic compacts and bare CNT reinforced composites.

To date accurate temperature assessment of the compact in the SPS die has been difficult due to the remote position of the pyrometer within the body of the die. It has been found that the ferromagnetic Curie transition can be successfully employed to calibrate SPS pyrometer during processing.

Table of Contents

List of Figures

List of Tables

Chapter 1

General Introduction

Modern power generation systems, actuators, magnetic bearings used in transport systems and energy storage systems such as flywheels demand soft magnetic materials with good mechanical properties [1-4]. The materials selected for these applications should exhibit good mechanical properties because they could be subjected to one or many of the following conditions during service: high stress, cyclic stress and high temperatures. Additionally, the material should possess high saturation induction to minimize the amount of material used and high Curie temperature to retain the magnetic characteristics at higher operating temperature. The frequency of operation determines the requirements of other magnetic properties, which are structure-sensitive such as coercivity, remanence and permeability [5].

Fe-(30-50)Co alloys are a class of soft magnetic alloys (SMA) that possess highest saturation induction (2.3–2.45 T) and Curie temperature (920-985^{o}C) among the commercial SMA [3]. In Fe-Co alloys, Fe-50Co alloy possess the highest permeability and zero magnetocrystalline anisotropy. Fe-50Co is very brittle due to the thermodynamically favourable long range ordering at temperatures lower than 720^{o}C. Many efforts, including solid solution strengthening, precipitate hardening, metal deformation and heat treatment following ductility improvements with ternary additions were made in the past to improve the strength and ductility of Fe-Co alloys [6]. However, composite strengthening, which possess unique advantages over the aforementioned strengthening methods such as enhancement of creep resistance and ability to tune the final properties by controlling the volume fraction of reinforcements was not attempted in Fe-Co alloys.

The soundness of a composite is determined by the characteristics of the interface between the matrix and reinforcements. The interfacial reactions can be optimised by adopting one or more of the following approaches: coating of the reinforcement, modification of the matrix composition, specific treatments to the reinforcement and control of the process parameters [7]. In this study, the first and last methods have been adopted to control the interfacial chemistry and thickness, which respectively include, coating of the selected reinforcement and selection of a low temperature and rapid fabrication process.

Reinforcements can be decorated with metallic, ceramic, bilayer and multilayer coatings containing metals and/or ceramics layers by chemical vapour deposition (CVD), physical vapour deposition (PVD), thermal spraying, sol-gel process, electrolytic, electroless

and cementation methods. Electroless plating offers many advantages over other methods including deposit uniformity, economic advantages, magnetic property selectivity and fast plating rate [8].

Spark plasma sintering is a relatively new rapid-compaction technique that is used to process a wide variety of materials including metals, alloys, ceramics, composites, nanocrystalline and amorphous materials. The compaction is achieved by the simultaneous application of mechanical pressure and very high pulsed DC current through a graphite die containing the powders. The unique characteristics of SPS routes includes low sintering temperatures, very fast heating rates up to 600 ^{o}C/min, rapid cooling rates, short holding time, high pressure applied during sintering, high throughput due to high current (>1000A) and low voltage (<10 V), clean grain boundaries because of plasma activation and flexible sintering environment [9]. The engineering benefits of spark plasma sintering are short processing time, no need for additives, prior cold compaction and controlled atmospheres [10].

The aim of the research was to find an optimum amount of reinforcements, which differed in their aspect ratios, and a suitable reinforcement coating for improving the mechanical properties of the brittle Fe-50Co matrix. The reinforcements chosen for this investigation included SiC particulates, SiC whiskers and multi-walled carbon nanotubes. In order to minimize the thickness of the interfacial reaction zone and to preserve the structural quality of the reinforcements (in the case of carbon nanotube (CNT) composites), spark plasma sintering was chosen to fabricate the materials. In addition, to understand the influence of the SPS variables on the sintering behaviour of this technologically important ferromagnetic matrix alloy, extensive experiments were performed on the unreinforced material. The reasons for the increase and decrease in magnetic and mechanical properties of the monolithic Fe-Co and its composites were explained by correlating the property values with the microstructural, crystallographic structural and fractographic features. The materials prepared for this study included:

- Monolithic Fe-50Co by varying the sintering temperature, pressure, time, rate of pressure application, temperature at which the pressure was applied and released, heating and cooling rate
- Monolithic Fe-50Co alloy and pure Fe above and below the Curie temperature to study the influence of magnetic nature of the ferromagnetic materials on sintering
- Fe-Co composites containing 5 and 10 vol% of as-received and Ni-P, Co, copper and duplex (Cu and Ni-P) plated SiC particulates

- Composites containing up to 5.5 vol% of SiC whiskers in the as-received and Ni-P, Cu and Co plated conditions
- Carbon nanotube reinforced composites containing up to 10 vol% of CNTs in the plasma treated and electroless Ni-P plated conditions

References

1. R.E. Quigley, Proc. of IEEE Applied Power Electronics Conf., More electric aircraft, 906-911 (1993).
2. R.T. Fingers, J.E. Coate, R.E. Dowling, Mechanical properties of iron-cobalt alloys for power applications, Proc. of Intersociety Energy Conversion Engineering Conf. **1**, 563-568 (1997).
3. R.S. Sundar and S.C. Deevi, Soft magnetic FeCo alloys: alloy development, processing, and properties, *International Materials Reviews* **50**, 157-192 (2005)
4. D. Howe, Magnetic actuators, *Sensors and Actuators* **81**, 268–274 (2000).
5. Z. Turgut, M. Huang, J.C. Horwath and R. T. Fingers, High strength bulk Fe–Co alloys produced by powder metallurgy, *J. Appl. Phys.* **103**, 07E724 (2008)
6. T. Sourmail, Near equiatomic FeCo alloys: Constitution, mechanical and magnetic properties, *Progress in Materials Science* **50**, 816–880 (2005)
7. T.P.D. Rajan, R.M. Pillai and B.C. Pai, Reinforcement coatings and interfaces in aluminium metal matrix composites, *J. Mater. Sci.* **33**, 3491-503 (1998).
8. P. Sahoo and S.K. Das, Tribology of electroless nickel coatings – A review, *Mater. and Design* **32**, 1760–75 (2011).
9. V. Mamedov, Spark plasma sintering as advanced PM sintering method, *Powder Metallurgy* **45**, 322-328 (2002).
10. J.R. Groza, A. Zavaliangos, Sintering activation by external electrical field, *Mater. Sci. Eng. A* **287 (2),** 171–177 (2000).

Chapter 2
Literature Review

2.1 Introduction

In the last century, applications involving power production and distribution, actuators, magnetic shielding, data storage and microwave communication have increased the motivation to research materials that can easily be magnetised and demagnetised under a small external field. The materials used in such applications are termed soft magnetic materials and are characterised by high initial permeability in the range of 1.1 to 100 000 and low coercivity in the range of 0.4–1000 A/m [1]. Those materials are broadly classified into three groups: metallic alloys, intermetallics and ceramics.

The recent strong push for the inclusion of electric technologies in new civil and military transport platforms has fuelled the quest for materials with stringent mechanical properties in addition to good soft magnetic properties. The reasons behind the thrust include improvements in environmental impact, increased reliability, maintainability and supportability, in comparison to the currently used hydraulic, pneumatic and mechanical power transfer systems [2,3,4]. As the transport industry is concerned with the weight and some rotating parts in the machines may be subjected to higher temperatures during service, the magnetic material selected should possess high saturation magnetisation to minimize the weight of the material used and high Curie temperature to retain the magnetic properties at high operating temperatures. From Table 2.1, it is clearly evident that Fe-Co alloys are the most suitable materials which can satisfy the magnetic requirements for these more electric transport applications (META). In the past three decades, many efforts have been directed at improving the physical, magnetic and mechanical properties of Fe-Co alloys through various alloy design principles.

Currently, Fe-Co alloys are widely used

- To maximize savings in weight and space in high performance transformers, rotors for active magnetic bearings, racing car generators, fuel pump motors, torpedo motors, magnetostrictive transducers for underwater detection
- To maximize flux concentration in mass spectrometers, NMR medical equipment, pole tips for high field magnets, magnetically driven actuators in impact printers, high performance loudspeakers, solenoids and valves for aircraft and missiles, diaphragms in telephone handsets, solenoid valves, flux guiding parts in inductive speed counters, electromagnetically controlled intake and exhaust nozzles [1].

Table 2.1 *Saturation induction and Curie T of commercial soft magnetic alloys [1]*

Material	Saturation magnetiz. (T)	Curie point (^{o}C)
Iron	2.15	770
Low carbon steels	2.0–2.15	~770
Ferritic steels (Fe–Cr–Ni)	1.2–1.7	–
Fe–(1–3%)Si alloys	1.9–2.0	730–750
Ni–Fe alloys	0.8–1.6	250–500
Fe3Al alloys	1.14	540
Fe–(30–50)Co	2.3–2.45	920–985
Amorphous Fe–Co–B	1.9	370–420

2.2 Fe-Co alloys

2.2.1 Phase transitions in Fe-Co alloys

Fe atoms added in the Co system arrange orderly in a thermodynamically favourable B2 structure ($\alpha^{'}$) with CsCl configuration, in the composition range of 30-75 at % of Fe as shown in Fig. 2.1(a). In the aforementioned composition range, the degree of order of any alloy decreases with the increase in temperature below the order-disorder temperature (Fig. 2.1(b)) [5]. On heating, the disordered alloy (α) undergoes a polymorphous transformation into an fcc phase (γ). The Curie temperature of FeCo overlaps with the α-γ transformation temperature. Similar to the critical ordering temperature, the Curie temperature also depends on the alloy composition. The alloy with 46 at.% Co shows a maximum Curie temperature of 985^{o}C.

2.2.2 Magnetic properties of near equiatomic Fe-Co alloys

In the Fe-Co system, Fe–(30–50)Co possesses the highest saturation magnetisation (Fig. 2.2(a)) and Fe-50Co exhibits the highest permeability (Fig. 2.2(b)). MacLaren et al. [6] studied the influence of cobalt addition in the iron system with first-principles electronic-structure calculations and showed that the exhibition of high saturation magnetisation at near equiatomic compositions is due to combined effects of constant cobalt moment and varying iron moment from 2.2 μB in pure Fe to over 3.0 μB in alloys of 50 at. % or more Co. The increase in atomic moments of Fe is attributed to a change in the nearest neighbour coordination of Fe atoms as ordering brings Co atoms into the environment of each Fe atom at the maximum number.

In addition, the ordered Fe-Co alloy with equiatomic composition displays zero magnetocrystalline anisotropy in the fully ordered condition as shown in Fig. 2.3. Some of the important magnetic properties of stoichiometric FeCo alloy is summarised in Table 2.2.

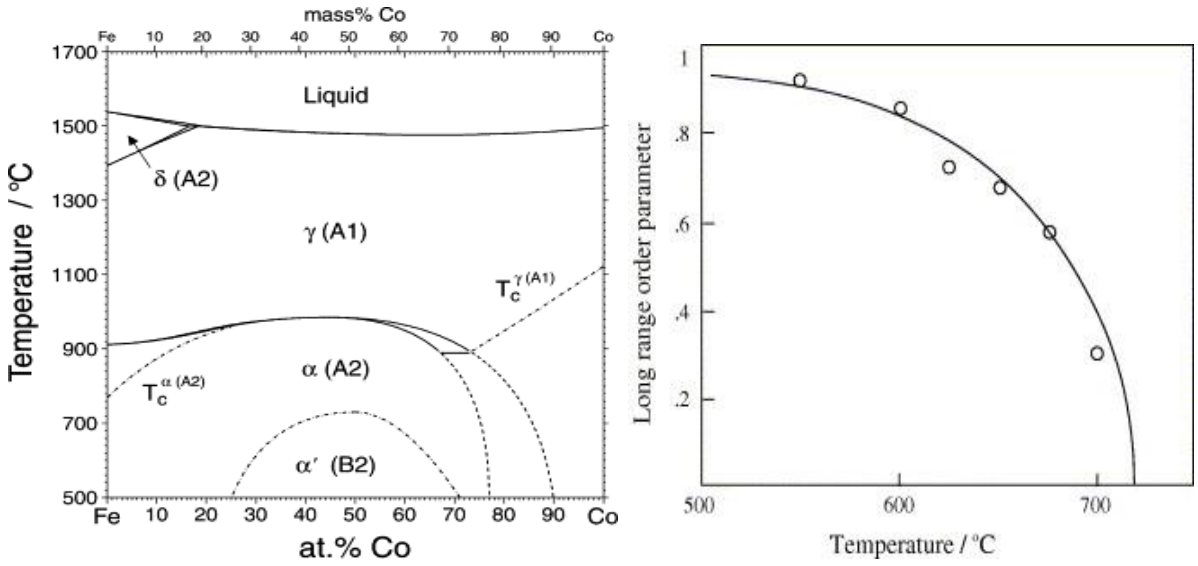

Fig. 2.1 (a) Phase diagram of binary Fe-Co system showing ordered bcc(α′), disordered bcc (α), delta bcc(δ) and fcc (γ) phases and Curie temperature (T_c) after [7] (b) Variation of long range parameter as a function of temperature in Fe-49Co-2V after [5].

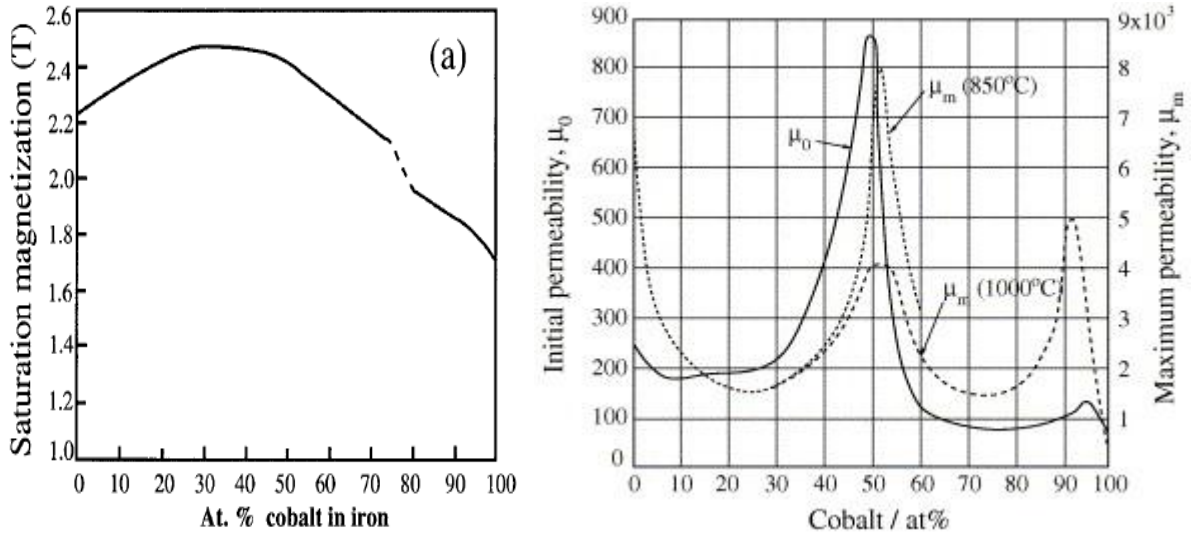

Fig. 2.2 Variation of: (a) saturation magnetisation [1]; (b) permeability [8] with Co content in Fe-Co alloys; heat treatment temperature is shown in parentheses in (b).

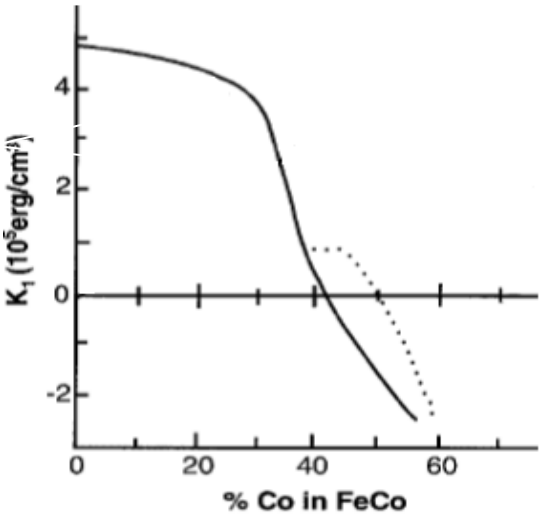

Fig. 2.3 Variation of magnetic anisotropic constant (K_1) with Co content; dotted line shows variation in ordered condition after [1]

Table 2.2 *Magnetic properties of Fe-50Co alloy in the ordered condition [1]*

Property	Value
Curie temperature (^oC)	980
Saturation magnetisation (T)	2.4
Coercivity (A m^{-1})	150
Initial permeability	800
Maximum permeability	5000–8000
Saturation magnetostriction (ordered condition)	
λ_{100}	$150x10^{-6}$
λ_{111}	$25x10^{-6}$
$\lambda_{polycrystal}$	$60x10^{-6}$
Magnetocrystalline anisotropy constant (Jm^{-3})	0

2.2.3 Processing of binary FeCo alloys

Conventionally, binary Fe-Co alloys are cast and hot worked at temperatures greater than 900^{o}C to break down the cast microstructure [9, 10]. During hot working, the material undergoes dynamic recrystallization (DRX) or recovery depending on Fe/Co ratio. DRX occurs readily when the Co/Fe ratio is greater than or equal to 1, whereas recovery is common in Fe rich alloys. Fe-Co alloys (with 0.6% V) are difficult to cold roll in the ordered state because the hardness of the ordered alloy increases rapidly with the amount of cold working and cracks formed even at a reduction as low as 5% owing to rapid work hardening [11]. On the contrary, disordered alloy exhibits sufficient room temperature ductility and

relatively moderate work hardening rates and hence, could be cold worked up to 40% at room temperature.

2.2.4 Effect of long range ordering on magnetic properties

The near equiatomic FeCo alloys are subjected to annealing treatments to tune the long range order parameter (S) and in turn the magnetic properties. Up on ordering, the magnetic saturation moment increases by 4 % (Fig. 2.4(a)) [12]. At ambient temperature, the coercivity of the disordered alloy is lower than that of the ordered alloy (Fig. 2.4(b)) [13]. The coercivity of the ordered alloys decrease with increase in test temperature, whereas the coercivity of the disordered alloys increase with temperature up to 500^{o}C. The increase in coercivity in disordered alloy can be attributed to the building up of internal stresses with the ordering fraction. Ordering occurs rapidly at temperatures greater than 500^{o}C and hence, the coercivity of the disordered alloy matches with that of ordered ones.

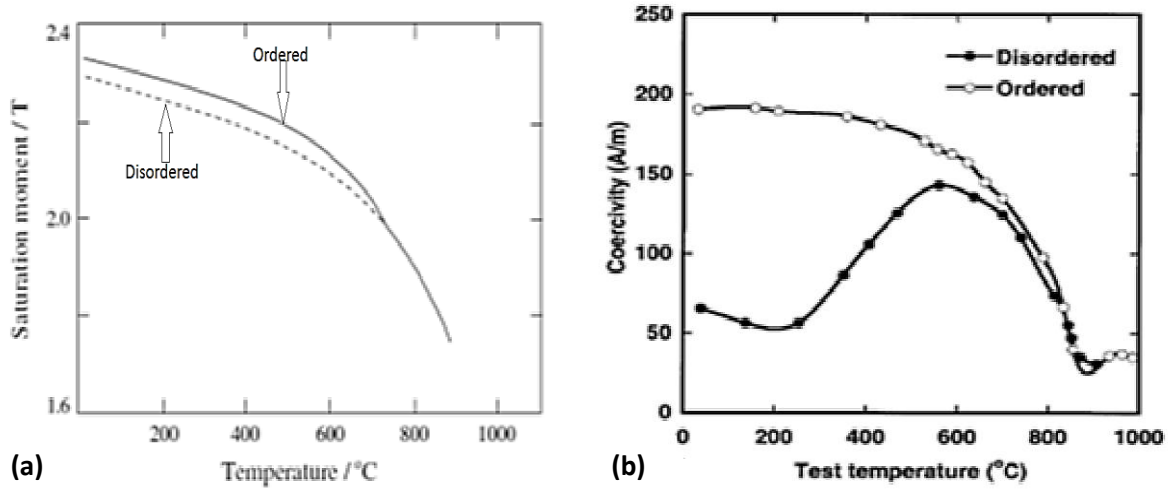

Fig. 2.4 Variation of (a) saturation moment [12]; and (b) coercivity [13] with test temperature in stoichiometric FeCo alloy

2.2.5 Effect of magnetocrystalline anisotropy and grain size on coercivity

The magnetic properties of soft magnetic alloys can be tailored by controlling the magnetic anisotropy through the thermo-mechanical treatments. The magnetocrystalline anisotropy energy is the energy that directs the magnetisation of the ferromagnetic crystal along certain crystallographic axes called the easy axes of magnetisation. This arises mainly because of the interaction of the magnetisation with the crystal lattice, which occurs via the orbital overlap of electrons: spin-orbit coupling. The magnitude of anisotropy is denoted using anisotropy constant K_1, which depends on state of order and Co content [14]. FeCo

alloys possess an attractive magnetic property, namely low magnetocrystalline anisotropy. Yu et al. [15] showed that in FeCo alloys the coercivity depends on K_1 and grain size as follows,

$$H_c \sim 3\sqrt{\frac{kT_cK_1}{aM_S}}\frac{1}{D}$$

Where H_c is the coercivity, D the grain size, M_s the saturation magnetisation, K_1 the magnetocrysatlline anisotropy, T_c the Curie temperature and a the lattice constant.

2.2.6 Fe-Co-V alloys

The near equiatomic FeCo alloy is brittle at room temperature due to the ordered B2 structure [16,17,18] and exhibited a brittle fracture mode in both the ordered and disordered states. Fracture was predominantly intergranular with a small amount of transgranular cleavage, see Fig. 2.5 [19]. This mechanical behaviour poses serious problems during fabrication and operational purposes. Also, Fe-50Co shows lower resistivity values. This will increase the eddy current loss under ac operating conditions.

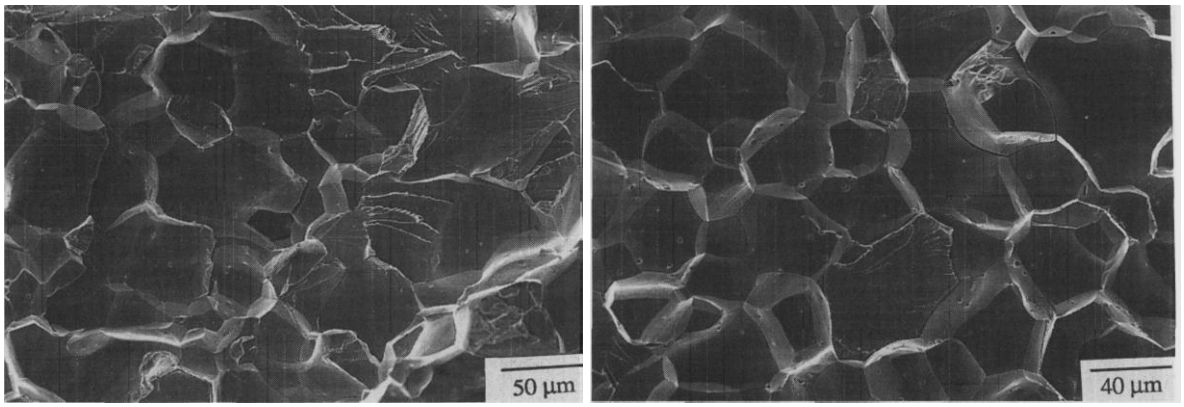

Fig. 2.5 SEM micrographs of fractured surface of: (a) disordered; and (b) ordered Fe-50Co [19]

In 1932, White and Wahl [20] overcame the brittleness problem by adding 2% V to the stoichiometric alloy and reported cold workability of about 90 % at the marginal cost of magnetic performance. The Fe-50%Co and Fe-49%Co-2%V were commercially named as Permendur and Supermendur or 2V-Permendur, respectively. In 1961, Chen stated that the beneficial effect of V on ductility resides in its ability to scavenge the detrimental impurity elements in Fe-Co alloys [8]. Kawahara [18,21] refuted this and reported that cold-workability of Fe-Co alloys can also be improved by addition of ternary elements namely chromium, carbon, nickel, molybdenum, tungsten, tantalum and niobium. These elements, by forming compounds with Co_3X formulation, hinder ordering in zones adjacent to the precipitates and promote ductility [21]. Kawahara's statement on ductility impartment by a few dispersed ductile regions in a bulk material is difficult to conceive [17] and the

mechanism behind the ductility improvement by V is still not clear. The phase transitions and structures of commercially important FeCo and FeCoV alloys were studied extensively to employ these materials in power generation applications. The binary Fe-50Co alloy shows entirely ferritic (α) structure below 1000 ^{o}C, whereas, in the presence of V a non-magnetic phase (γ) co-exists with α below 700^{o}C [22].

2.2.7 Attempts to improve mechanical properties of Fe-Co based alloys

Mechanical properties of the Fe-Co system are influenced by a number of factors such as grain size, alloying elements, precipitates, the final heat treatment that determines the degree of order/disorder and degree of recrystallization [1]. Fe-Co alloys exhibit higher strength in the ordered state than in the disordered state. Stoichiometric FeCo is highly brittle and fails in an intergranular manner in both ordered and disordered states. The most commonly added alloying elements in the Fe-Co system to promote precipitation hardening are V and Nb [17,23]. In addition to strengthening by forming precipitates and by promoting grain refinement, they also suppress ordering, increase ductility and electrical resistivity and aid in grain refinement.

Sundar et al. [24] reviewed the works of Kawahara et al. [25] on the improvement of the mechanical properties of Fe-Co alloys by ternary additions and summarised the consequences on saturation magnetisation and coercivity (Table 2.3). FeCoV alloys are precisely heat treated at temperatures around 700^{o}C to tune the extent of recrystallization, ordering and size and volume fraction of γ phase, as all these microstructure features have major effects on final magnetic and mechanical properties. Increasing the annealing temperature beyond 700 ^{o}C imparts no significant effect on coercivity and strength values, both in the ordered and disordered state [26,27,28].

Sourmail [17] has summarised the efforts made to improve the mechanical properties of Fe-Co alloys with and without V by alloy additions and thermo-mechanical treatments. Interstitial boron and carbon additions, showing no effects on the fracture behaviour of equiatomic Fe-Co, help in the ductility enhancement of ordered FeCo-2V by forming fine boride and carbide precipitates [29]. Grain boundary strengthening, by reducing the grain size to nanometer levels (100 nm), has also been attempted to improve the yield strength and elongation values of ordered FeCo-2V up to 2.3 GPa and 22 % [30]. Yu et al. prepared tungsten and alumina reinforced FeCo composites by an electroless plating method and achieved higher yield strength and hardness values and lower creep rate in the as-deposited

state compared to the monolithic material [31]. Sundar et al [32] formulated a new generation FeCo based alloy by adding V, Nb, Mo, C, and B and achieved hardness values of 600 HV after age hardening heat treatment at 600 ^{o}C. They also reported high yield strength (1516 MPa), good creep resistance, high room temperature electrical resistivity (70–75 μΩ cm,) and higher magnetic hysteresis loss in the age hardened material compared to commercial FeCo-V alloys. It has been reported that improvements in mechanical properties could be realised only at the expense of magnetic properties because the imperfections playing a positive role in strengthening exert negative consequences on magnetic properties [24].

Table.2.3 *Mechanical and magnetic properties of FeCo–X alloys [24]*

Composition (at%)	YS (MPa)	% Elong.	Saturation induction (T)	Coercive force (kA/m)
FeCo–0.5C	458	15.0	2.36	1.0
FeCo-2V	380	17.7	2.3	3.9
FeCo–2C	1050	9.0	2.37	2.5
	838	15.5	2.34	1.0
FeCo–0.5Cr	1295	6.0	2.35	2.8
FeCo–2Cr	1117	1.7	2.29	2.4
FeCo–0.5Mo	1491	8.7	2.33	2.0
FeCo–0.5W	1538	7.0	2.33	2.3
FeCo–2W	1909	1.7	2.21	2.0
FeCo–2W	2092	8.9	2.24	2.2
FeCo–0.5Ta	1547	1.0	2.33	2.1
FeCo–2Ta	1961	0.6	2.24	2.8
FeCo–0.5Nb	1393	5.8	2.33	2.2
FeCo–2Nb	1765	–	2.16	3.3
FeCo–2Ni	1578	3.3	2.34	2.4

Bulk amorphous structures with diameters of about 5 mm, exhibiting fracture strength as high as 5545 MPa, Young's modulus of up to 282 GPa and higher glass transition temperature (650 ^{o}C) have been produced by a casting route in the FeCo systems by adding early transition metals like Zr, Hf, Nb, Ta, Mo and metalloid elements such as B, P, Si. The above mentioned elements aid in forming glassy structures by producing deep eutectics in all ferromagnetic transition metal systems [33]. However, these amorphous materials are thermally less stable and are always associated with size limitations to suppress crystallisation.

2.2.8 Powder metallurgy of Fe-Co alloys

The magnetic materials used in electrical machines, which operate under changing flux, are in thin laminate form to minimize eddy current loss. The mechanical properties of

these thin sheets can be improved during fabrication by varying the deformation and post heat treatment parameters. However, modern power generation systems which utilise Fe-Co alloys demands rotors, as large as 0.5 m in diameter, because the power output in electrical machines is directly proportional to the size and rotational speed of the rotor. As discussed above, the ordered intermetallic Fe-50% Co alloys are brittle and are difficult to deform without any ternary addition. Such bulk geometries can be realised from the brittle raw materials by adopting a powder metallurgy (PM) route.

In addition, PM also offers a number of advantages for the mass production of soft magnetic components: materials and energy savings in the manufacture of complex shaped parts; dimensional accuracy; excellent surface finish; and an environmental friendly process capable of achieving tailor-made alloy compositions, purity, homogeneity, and especially, isotropic magnetic properties.

In magnetic materials engineering, powder metallurgy is the preferred method to compact soft magnetic precursors with organic or inorganic encapsulation [34,35,36] and about 80 % of permanent (hard) magnets [37]. The PM route is also followed to fabricate components from soft magnetic powders without any coating. The effects of sintering variables such as sintering temperature, pressure and atmosphere on magnetic performance were studied in iron based alloy systems [38]. It has been published that permeability and coercivity are strongly affected by changes in material processing and alloying schemes whereas, saturation induction is less sensitive to processing variables and is primarily influenced by the amount and type of alloy and the density of the finished part. Bas et al.[39] compared and presented the sintering characteristics of pure iron, phosphorous–iron, silicon–iron, nickel–iron and cobalt–iron together with new coated materials based on encapsulated iron powders.

Attempts were also made to fabricate dense compacts by various PM processes by understanding the sinterability of ductile FeCoV and brittle FeCo powders. Dense FeCo compacts prepared by metal injection moulding (MIM) at 1330^{o}C showed higher permeability, coercivity and mechanical hardness and lower saturation magnetisation than that of less dense FeCoV prepared from pre-alloyed powder by the same route at 1330^{o}C [40]. This contradicts the report of sintered Fe-Co alloy exhibiting saturation magnetisation of 1.7 T compared with 2.0T for FeCoV sintered alloy [41]. Yamagishi et al. studied the sintering behaviour of Fe-Co pre-alloyed powder with pure Co powders and reported compacts exhibiting relative density of 95% and magnetization of 2.15 T in a magnetic field of 4 kA/m and a coercive force of 160 A/m [42]. Gas atomised FeCoV powders sintered after

vacuum ball milling by HIP at 750^{o}C under a pressure of 193 MPa for 6 hrs and heat treated at 730 °C followed by a rapid quench to room temperature resulted in compacts with yield strengths of 870 MPa, average coercivity values of 509 A/m and maximum permeability values of 1100 [43].

In general, the magnetic performance of components fabricated by PM route can be improved by reducing three dimensional imperfections such as impurities and pores introduced during powder densification. Advancements in sintering technologies to minimize defect levels have led to the investigation of means to activate the sintering process. This resulted in the development of spark plasma sintering, which uses electric current to activate the consolidation. The method has been employed extensively over the past decade with results showing clear benefits over conventional methods including pressureless sintering, hot-pressing and others.

2.3 Spark Plasma Sintering

Spark plasma sintering (SPS) is a relatively new compaction technique which utilises the heat generated in the sintering system when a pulsed DC current passes through both electrically conducting graphite dies and the conducting powders to be compacted. For non-conducting powders, only the graphite die and punches heated due to resistance act as the heat source. A schematic diagram depicting the main parts of SPS system is shown in Fig. 2.4. The powder to be compacted is loaded into a die usually made of graphite. The employment of graphite as the material for punches and dies limits the external sintering pressure to a value of 100 MPa. The pressure applied during compaction is uniaxial, which can be maintained at a constant value or changed in the subsequent stages. The sintering temperature is measured using a thermocouple inserted through a horizontal die-hole about 1-2 mm away from the loaded powders. Sintering is carried out under any one of the commonly used environments including vacuum, air, nitrogen and argon. The heat generated in the system by ON-OFF DC pulse voltage and a current from a pulse generator and high applied mechanical stress activates diffusion-oriented processes and the electric field present in the system enhances the diffusion rate. Therefore, very dense components can be produced at comparatively low temperature in short duration.

Minier et al. [44] showed that under identical sintering conditions, the electric power delivered to the SPS system and the resultant microstructure depends on the geometry of the die and the sample and the heating volume, irrespective of the electrical characteristics of the sample. The heating volume for conductive samples includes the punches, the sample and to

some extent the dies, whereas for the non-conductive samples it relates to the punches/die setup only. An increase in die dimension reduces the grain size for conductive samples. Conversely, it promotes grain growth for non-conductive materials.

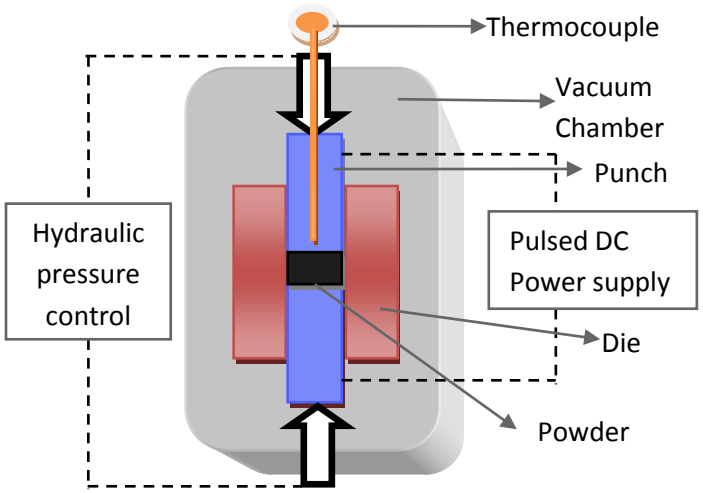

Fig. 2.6 Schematic representation of SPS system

In SPS, the consolidation takes place in two stages: (1) an initial activation through the application of a pulsed current; (2) the subsequent heating and densification by using DC current [45]. Certain characteristics of SPS such as low sintering temperatures, very fast heating rates up to 600 ^{o}C/min, rapid cooling rates because of their low thermal inertia and forced cooling, short holding time, high pressure applied during sintering, high throughput due to high current (>1000A) and low voltage (<10 V), clean grain boundaries because of plasma activation and flexible sintering environment differentiate it from conventional sintering. This technique is being employed to process a wide variety of materials such as metals and alloys [46,47], functionally graded materials [48], structural and functional ceramics [49,50] and composites [51], nanocrystalline materials [52], non-equilibrium composites [53], porous materials [54], textured materials [55], amorphous materials [56] and nanocrystalline and amorphous coatings [57]. In addition to the above mentioned characteristic advantages, certain benefits such as higher density, smaller grain size, no need for additives or prior cold compaction paved the way for its success in the fabrication of various engineering materials such as ferroelectrics, magnetics, piezoelectrics, pyroelectrics, superconductors, transparent ceramics, biomaterials, armour materials etc., as summarised by Munir et al. [58]. Due to the enhanced sintering ability of this technique over other sintering technologies, many attempts have been made to understand the exact consolidation mechanism of SPS. Joule heating and a mechanism suggesting plasma formation between particles have been proposed to explain the sintering behaviour. Although Joule heating

remains widely accepted [59,60,61], Hulbert et al. [62] in their recent investigation using in situ atomic emission spectroscopy, direct visual observations and ultrafast in situ voltage measurements indicated that there is no plasma or sparking during the SPS process. The exact mechanism governing the densification still remains unclear.

2.3.1 SPS in magnetic materials technology

Spark plasma sintering has been widely employed in the field of magnetics to fabricate soft magnetic materials starting from Fe based amorphous precursors such as melt spun ribbons [56,63], powders [64,65] and FeCo based metallic glassy powders [66] because it helps to retain the amorphous structure and in turn its characteristics such as high saturation induction, high permeability (μ), and low coercivity (H_c) in sintered compacts. It has also been demonstrated that dual-phase bulk metallic glass composites exhibiting good soft magnetic properties and ultra-high strength can be fabricated from a mixture of Ni-based and Fe-based glassy alloy powders by SPS [67]. As most of the magnetic materials are Fe based, spark plasma consolidation of such powders in graphite dies is always associated with carbonation (100-200 μm) at the surface of the sample [46]. The carbonation problem can be overcome either by embedding the green body in an inert powder such as alumina or TiN and SPS the whole volume [38] or by grinding off the carbide layer on the surface [68].

Herzer reported that nanocrystalline materials with grain size less than 100 nm (i.e) below ferromagnetic exchange length, exhibit D^6 dependence of coercivity unlike conventional polycrystalline materials, which show 1/D dependence [69]. This anomalous behaviour, analogous to the effect of grain size on strength in nanocrystalline materials [70], has promoted the development of nanocrystalline magnetic materials [71,72]. Such beneficial microstructures exhibiting very low coercivity values can be maintained in bulk form by processing the nanocrystalline Co [73], Fe-36Ni [74] powders by SPS because plasma sintering can be performed at relatively low temperatures for short duration, which suppresses grain growth and promotes densification kinetics [46]. Nicula et al. [75] prepared nanocrystalline Fe-Co-V-Cr alloys powders (10 nm) by mechanosynthesis route and compacted the powders using SPS. They reported that the electric field/pulsed current applied during sintering favours strong interparticle bonding and rapid densification of the nanocrystalline powders without coarsening of the microstructure below 900^{o}C. Kim et al. [76] attained 95% of the theoretical density and magnetisation of 230 emu/g in nanocrystalline Fe-30% Co alloys prepared by SPS at 900°C for 5 min under a pressure of 60 MPa. The advantageous nanocrystalline microstructure can also be achieved by annealing the

spark plasma sintered amorphous soft magnetic materials [77]. SPS has been employed to consolidate ferromagnetic shape memory alloy particulate composites after mixing microsized NiTi with micro and nanosized Fe powders. It has been showed that nanosized Fe powders tend to fill in the gaps between microsized TiNi powders much better than microsized Fe powders, resulting in strong bonding and better mechanical and magnetic properties [78].

Cha et al. [79] prepared a composite using ferro magnetic powder particles surrounded by an electrical insulating layer (Somaloy 500 and 550) and a lubricant (Kenolube) by SPS at 200^{o}C and by conventional sintering at 500^{o}C and reported improved fracture strength of about 1.5 times in the SPS composite. However, both materials showed nearly equal iron-loss of about 11.3 W/kg when tested at 100Hz and 1000 mT.

It has also been reported that a new class of hard magnetic material with two kinds of magnetic phases: one a hard magnetic phase used to achieve a high coercive field and the other a soft ferromagnetic phase to provide a high saturation polarization, can be fabricated from Fe-based [80], Sm based [81], Nd based amorphous precursors [82] or Nd-Fe-B amorphous powders coated with α-Fe, Co or FeCo nanoparticles [83,84] by spark plasma sintering and subsequent heat treatment. The hard amorphous precursors were consolidated at the lowest sintering temperatures possible to minimize the degradation of the hard magnetic phase, the formation of soft magnetic phase and grain growth. Lupu et al. [85] obtained two phase composite magnets by plasma sintering a mixture of ball milled powders prepared from nonstoichiometric Nd based nanocrystalline melt spun ribbons with FeSiB or CoFeSiB amorphous wires. They showed that the addition of FeSiB and CoFeSiB soft magnetic powders increases the remanent magnetization of the SPS magnets from 4.8–5 to 6.2–6.5 kG, while the estimated maximum energy product is also increased from 24–25 to 27–29 MGOe. SPS has also been attempted in the fabrication of nanostructured ferrites from soft chemistry powders exhibiting superparamagnetism at room temperature [86,87]. It has been observed that the short processing time does not help to realise the systematically desired spinel cobalt ferrite from whatever starting powders compared to conventional sintering [86]. In the SPS Gd compacts prepared using the powders obtained by inert gas condensation, a reduced ferromagnetic response has been observed in nanocrystalline Gd than in microcrystalline Gd [88].

2.4 Composites

2.4.1 Introduction

Composites are a class of engineered or naturally occurring materials made from at least two constituent materials with inherently different physical and chemical properties which remains separate and distinct in the finished structures. The constituent materials are grouped into reinforcements and matrix depending on the role played by them. The reinforcements are usually much stronger and stiffer than the matrix and give the composite its improved mechanical properties. The matrix holds the reinforcements in an orderly pattern. Because the reinforcements are usually discontinuous, the matrix also helps to transfer load among the reinforcements. Based on the matrix material, composites are broadly classified into four types: polymer matrix, ceramic matrix, metal matrix and carbon matrix composites. Reinforcements are usually available in various forms like fibers, whiskers, laminates, flakes, particulates, microspheres.

In the following sections, attempts made to reinforce with short fibres namely carbon nanotubes in metal, ceramic and polymer matrices and SiC whiskers in metallic and ceramic matrices and particulates like SiC particles in metallic matrices have been reviewed.

2.4.2 CNT composites

In 1991, Iijima [89] discovered a new form of carbon named Carbon nanotubes (CNTs) with outstanding mechanical, thermal and electrical properties in soot produced by the carbon arc method. Since his discovery, active research to understand their structure and the structure-property correlation has gained momentum. Based on the number of layers of carbon forming the structure, CNTs are broadly classified into two groups, namely single walled nanotubes (SWNTs) and multi-walled nanotubes (MWNTs). Depending on the orientation of the six membered ring relative to the arbitrarily denoted axis of the tube, SWNTs are classified into three different classes namely: arm-chair, zig-zag and chiral. The armchair and zigzag nanotubes are symmetric with respect to the axial planes whereas, chiral nanotubes are non-symmorphic i.e their mirror image is not identical to the original, as shown in Fig. 2.5 [90]. The electrical conductivity of CNTs is strongly dependant on their diameter and the helicity of the arrangement of graphitic rings in their walls [91]. About one-third of the zigzag and chiral nanotubes and all armchair nanotubes behave similar to a metal in conducting electricity, whereas two-thirds of zigzag and chiral nanotubes (with different diameters) behave like a semiconductor [92]. In terms of mechanical properties, CNTs

possess exceptionally high tensile strength, Young's modulus of elasticity and resilience. The mechanical properties predicted theoretically are higher than those obtained by experiments [93,94]. This deviation may be attributed to the defects introduced in the structure during synthesis and processing. The Young's modulus of CNTs prepared by electric arc or laser ablation with minimum disorder or defects is close to that of graphite (approximately 1 TPa) whereas that of CNTs synthesised by a catalytic method with high defect densities exhibit strong diameter dependence in the range of 10-200 GPa [94,95]. Similarly, the tensile strength of CNTs shows a strong dependence on crystallinity and defect concentration and varies between 13-52 GPa for SWNTs and 11-150 GPa for MWNTs [94,95,96,97]. The characteristics of CNTs that exert a dominant role on their properties include length, diameter, chirality, crystallinity, purity and concentration of defects such as structural defects, defects due to bond rotation, doping induced defects and non-sp^2 carbon defects. Lehman et al. [98] showed that the above-mentioned characteristics of interest can be studied only by combining three or more of the following characterisation techniques: scanning electron microscopy, transmission electron microscopy (TEM), fast Fourier transform of high-resolution TEM, Raman spectroscopy, thermogravimetric analysis, Fourier transform infrared spectroscopy, X-ray fluorescence spectroscopy and Brunauer–Emmett–Teller (BET) analysis.

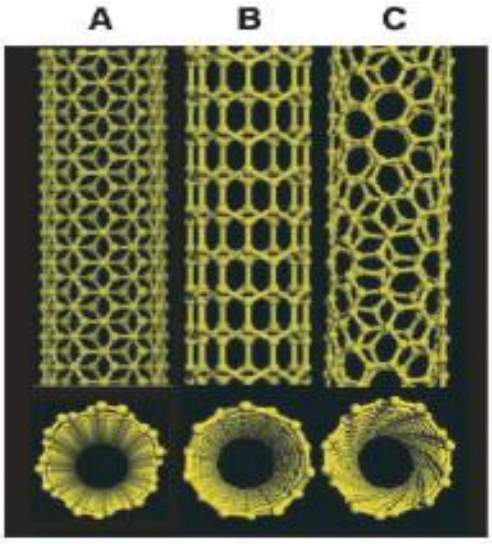

Fig. 2.7 Schematic illustrations of structure of: (A) armchair; (B) zig-zag; (C) chiral SWNTs [99]

Because of their extremely small size, high surface area, porous morphology, structure-sensitive electronic behaviour, high aspect ratio, small tip radius of curvature, high stiffness,

extraordinary strength and high on-axial thermal conductivity, CNTs are considered to have a great potential for the fabrication of the following devices [92,99,100]

a) Electrochemical devices like 'super capacitors' exhibiting giant capacitance, electromechanical actuators, electrodes in lithium batteries;
b) Field emission electron sources for flat panel displays, lamps, x-ray and microwave generators, gas discharge tubes, scanning electron microscope;
c) Next generation nanometer sized electronic devices such as miniaturised diodes and transistors; and
d) Sensors and probes like tips for atomic probe microscopes, nanoscopic tweezers, nanobalances for weight measurements in the femtogram to pictogram range.

In addition to the developments in using individual CNTs, several advancements have also been made in CNT-based continuous fibres and clusters in terms of their fabrication methods, characterization and modeling of mechanical and physical properties, and applications [101]. Furthermore, the efficiency of these nanostructures as reinforcements has been tested in matrices based on polymers, ceramics and metals.

2.4.2.1 Polymer matrix CNT composites

Since the discovery of CNTs, research on the incorporation of CNTs into a wide variety of polymer matrices has gained momentum because of lower temperature and fewer complications associated with polymer matrix composite fabrication than ceramic or metallic counterparts [102, 103, 104, 105]. The CNTs are more effective in polymer matrices, which possess lower modulus than metals and ceramics, because they carry large share of the load. Most of the work on polymer matrix CNT composites has been aimed at exploiting the mechanical characteristics of CNTs rather than their electronic or optical properties, although interest in those fields is growing [103]. Despite the fact that the mechanical and electrical performance of a polymer based composite is strongly dependent on the quality of the nanotubes (arc grown or catalytically produced), characteristics such as good bonding between tubes and polymer matrix, interfacial chemistry, homogenisation and alignment of tubes also play equally important roles [102]. The fabrication technology selected should help to realise the attributes of a sound composite. Polymer matrix composites can be produced by any one of the following routes depending on the polymer used [105],

a) The nanotube dispersion is mixed with a solution of the polymer and the solvent dissolving the polymer is evaporated in a controlled way. This technique can be

employed for polymers that freely dissolve in common solvents such as polyvinyl alcohol and polystyrene

b) The CNTs are vigorously mixed in a molten polymer and extruded to achieve nanotube alignment. This method can be used for thermoplastic polymers like acrylonitrile butadiene styrene, polypropylene and polycarbonate

c) The CNTs are mixed with the monomer rather than the polymer and subjected to in situ polymerisation. This route can be exploited for polyemers like polyaniline, polystyrene and polyimide

d) The polymer and CNTs are deposited in layers alternatively onto a substrate and cured to promote crosslinking. This technology can be attempted for polyethyleneimine, polydiallyldimethylammonium chloride.

2.4.2.2 Ceramic matrix CNT composites

CNTs are added as reinforcements in hard, stiff and thermally stable structural and functional ceramics to improve mainly toughness and to some extent hardness, electrical conductivity, thermal shock resistance and wear resistance [105, 106, 107, 108, 109]. Many mechanisms have been proposed to explain the toughness enhancement by CNTs like CNT pull-out, crack deflection, crack bridging and CNT rupture [108, 110, 111, 112]. Because of the high melting temperature of the matrix, these composites are often prepared by a powder metallurgy route. Despite much advancement in processing technologies, fabrication of a dense CNT reinforced composite with homogenous dispersion of nanotubes in hard ceramics and strong bonding between tubes and matrix remains as a huge challenge. Several approaches such as sol-gel processing [113], in situ synthesis of CNTs on fine transition metal particles, such as Fe, Co or Ni mixed with ceramic particles [114], attrition milling [115], colloidal processing under ultrasonic agitation and/or ball milling with surfactants followed by solvent evaporation [116] or freeze drying [117] have been attempted to promote homogenisation. The powder mixtures have been consolidated by one of the following powder compaction techniques: hot isostatic pressing (HIP) [114, 116, 118], spark plasma sintering (SPS) [105, 107,119] or pressureless sintering [117]. Although improvements in mechanical characteristics such as toughness [110, 115, 120], hardness [121], bending strength [110], Young's modulus [118] and functional properties such as electrical conductivity [122] and thermal conductivity [119] have been realised due to the introduction of CNTs compared to the monolithic material, some researchers reported decreased properties due to the difficulties associated in achieving a homogeneous, pore free

microstructure with well-aligned nanotubes [123, 124]. Zhu et al. [122] observed anisotropic mechanical and electrical behaviour in ceramic composites modified by electric field-induced alignment of carbon nanotubes. It has also been accounted that composites with higher volume percentage of CNTs show reduced mechanical properties due to the poor cohesion between fibres and matrix or due to the presence of porosity and clustering of CNTs [117, 118]. CNTs, by enhancing the mass transport during sintering, have also been reported to improve the sinterability of ceramic nanocomposites [125].

2.4.2.3 Metal matrix CNT composites

Nanosized carbon based fillers are added to a metal matrix to achieve one or more of the following characteristics of the primary metal matrix as reviewed by Neubauer et al. [126] and Bakshi et al. [127] :

- To improve the mechanical properties
- To reduce the coefficient of thermal expansion
- To improve the thermal conductivity
- To enhance corrosion resistance
- To reduce the coefficient of friction
- To improve the electrical conductivity

Unlike polymer matrix composites, incorporation of CNTs homogenously in a reactive metal matrix with minimal deleterious interfacial reactions is a huge challenge. Researchers tried to use CNTs to reinforce light weight aerospace metals and their alloys like Al [128, 129, 130, 131, 132, 133, 134], Mg [135, 136] and Ti [137, 138] to improve their mechanical properties and conductive metals like Ag [139] and Cu [140, 141] to enhance their mechanical and electrical characteristics. Some attempts were made in Ni based systems through electrochemical [142], laser [143] and electroless [144] deposition methods. In addition, the efficiency of CNTs in property improvements has also been tested in metals like Zn [145], alloys like Sn based solder alloys [146] and stainless steels [147], intermetallics [148] and bulk metallic glasses [149].

The main problems associated with the production of a CNT- metal matrix composite includes:

1. CNTs tend to cluster due to strong van der Waals forces of attraction between them [150].
2. Mechanical mixing to blend CNTs with metal powders will cause CNTs to sacrifice their structural integrity [151]. The large difference between CNTs and metal powders

in their density values (density of CNTs ranges from 1 to 2 g/cm^3 and that of metals, for eg. Al=2.7 g/cm^3 Cu= 8.94 g/cm^3) and their responses to polar solvents and surfactants due to dissimilar bond characters result in segregation of CNTs from metal powders during drying after slurry based processes like mechanical mixing in a liquid medium or ultrasonication [134]. Furthermore, incompatibility in adsorption of CNTs due to unfavourable geometries of metal powders, introduces obstacles in colloidal processing [152].

3. Due to poor wettability of carbon by materials such as Cu it would be very difficult to attain strong bonding between reinforcement and matrix [153, 154].
4. Materials based on Al, Ti and Fe react readily with carbon atoms and form carbides at the interface, which is detrimental in many cases [134-136] and advantageous in some cases [147].

Carbon nanotube reinforced metal matrix composites can be prepared by a variety of processing methods as summarised by Bakshi et al. [127] (Fig. 2.6).

Despite the availability of many fabrication technologies, most of the CNT-metal composites have been fabricated by powder metallurgy methods. Powder metallurgy remains the most popular technique that involves mixing CNTs with metal powder by grinding or mechanical alloying, followed by consolidation by compaction and sintering, cold isostatic pressing, hot isostatic pressing, or spark plasma sintering. In most cases, the composite compacts were subjected to post-sintering deformation processes such as rolling [141], equi-channel angular processing (ECAP) [155], extrusion [156], etc. In some cases, severe plastic deformation process like ECAP have been used to consolidate the powders mixture contained in a metal sheath [155, 157].

The electrochemical route, which embodies electroless plating and electrochemical deposition, has been employed to prepare one-dimensional composites of Ni-CNT, Cu-CNT, Co-CNT, Ni, Co based alloy-CNT on a substrate and bulk composites by compacting the metal plated CNTs. Ultrasonication and magnetic stirring have been used to keep the CNTs in suspension during plating. A comprehensive discussion of these methods is given in section 2.5.3.

Techniques involving melting and solidification were employed to make composites with low melting point matrices like Al [158], Mg [135, 158], and BMGs [149].

Only, Hwang et al. [143] prepared Ni-CNT composites by a laser deposition technique after roller mixing the constituent powders. The main limitation of these methods is clustering of suspended CNTs due to surface tension forces.

Thermal spraying involves deposition of molten and semi-molten particles onto a substrate to form a coating or free-standing structures. This technique has been extensively applied by Agarwal at al. [132, 133] to fabricate Al based CNT composites.

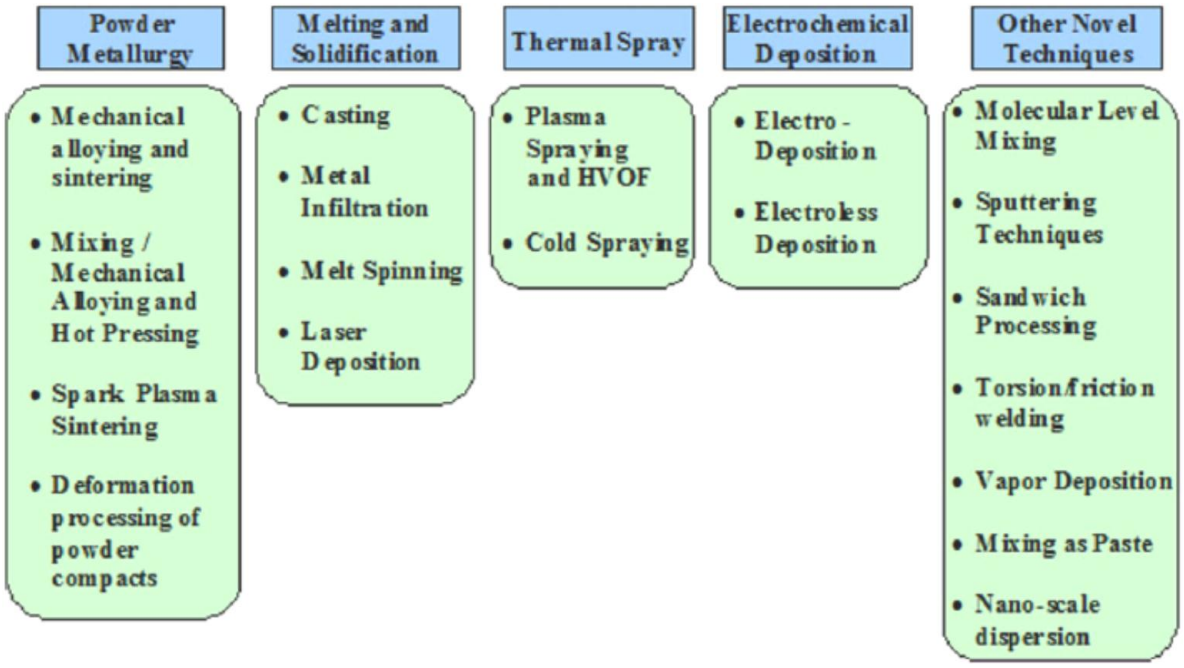

Fig. 2.8 Possible processing routes for metal matrix-CNT composites [127]

The pre-stated challenges can be conquered by taking appropriate precautionary steps and by selecting a suitable fabrication technique.

Most of the early studies utilised high-energy [128, 141] and low energy [128] ball milling to blend CNTs with metal powders. Colloidal processing, with some modifications is most widely used nowadays to mix powders. The van der Waals force between nanotubes can be overcome by dispersing CNTs in solvents, which are amides, particularly *N, N*-dimethylformamide (DMF) and *N* methylpyrrolidone (NMP) [159]. Inam et al. [125] reported that DMF possessing high values of dispersion component (δd) of the Hildebrand solubility parameter (δt) [160] is the best solvent for making homogeneous and agglomerate-free dispersions of CNTs. Another possibility to achieve CNT dispersion is to adopt methods that can alter the surface chemistry of tubes either covalently or non-covalently. Non-covalent surface modification involves treating the CNTs with surfactants like dodecyl-benzene sodium sulfonate (NaDDBS), Dowfax, sodium dodecyl sulphate (SDS) and Triton X-100 (TX) followed by ultrasonication [161]. The surfactants, by adsorbing on CNT's surface, act as a coupling agent and may introduce repulsive forces larger than van der Waals attractive forces. In covalent surface modification, functional groups like –COOH, =O, =C=O etc., are introduced on the surface of CNTs by several methods like plasma treatment [162],

fluorination [163], chemical treatments [164]. Additionally, while decorating the CNTs with organic/inorganic species, the chemical surface roughness created by the functional groups attached on the outer walls help to realise better coating by trapping more ions, atoms or molecules to be plated and by enhancing the adhesion of the coating [165, 166]. Guiderdoni et al. [167] overcame the segregation problem in colloidal processing by freeze drying the slurry containing CNTs and copper powders at 40 ^{o}C for 48 h in a vacuum and prepared the composites by SPS.

The problems due to density and bond character differences can be surmounted by coating the nanotubes with a suitable material having a density nearly equal to that of the matrix metal. Coating the reinforcements has added benefits such as improvement in interfacial bonding and reduction in Van der Waal's forces between the tubes. Kim et al. [168] prepared copper matrix composites with electroless Ni coated CNTs and reported significantly improved mechanical and tribological properties due to uniform dispersion of CNTs and dissolution bonding of Cu in nickel at the interface. In addition to electroless plating, the surface of CNTs can be decorated with a material layer by electrodeposition [142], sol-gel method [169], physical vapour deposition [170,171], chemical vapour deposition [172, 173] or a solvothermal method [174, 175]. Nie et al. [176] coated Mo on CNTs by a metal organic chemical vapour deposition [MOCVD] route and prepared (Mo-CNT) reinforced Al composites with enhanced mechanical properties by SPS. The Mo layer served as barrier in checking Al carbide formation at the interface. Junhui et al improved the interfacial bonding between carbon and Cu matrix by coating CNTs with W by MOCVD and reported improved wear characteristics [177].

In an effort to homogenously distribute CNTs in metallic matrix, some researchers synthesised CNTs in situ by a CVD route on homogenously dispersed Ni nano particles scattered evenly on the surface of Al powder. It has been observed that Al matrix composites prepared by pressing and sintering the Al(Ni) powders containing CNTs exhibit better mechanical performance than that obtained after ball milling CNTs and Ni-Al powders for 42 h [131].

Noguchi et al. [129] achieved uniform dispersion by compression moulding alternate stacks of CNTs in natural rubber and CNTs and metal mixture in natural rubber followed by heating the slab above the melting point of the metal in N_2 atmosphere to burn off the rubber. After the treatment, the resultant structure contained CNTs uniformly distributed in the metallic matrix and exhibited improved mechanical properties. In another study, dense CNT

reinforced Al composites were produced by spark plasma sintering followed by hot extrusion of moulded precursor devoid of natural rubber [130].

A technique named "molecular level mixing" has also been used to prepare Cu [140, 178], Co [179], Sn and SnSb [180] based CNT composites with uniformly dispersed reinforcements. This process involves acid treatment and functionalisation of CNTs to promote suspension, introduction of CNTs in salt bath under ultrasonication to deposit metal ions, drying and calcination to evaporate off the volatile matter and reduction to reduce the oxide on the surface. The nanocomposite powder produced can be processed by a powder metallurgy route to realise bulk composites [178].

2.4.3 SiC whisker composites

Silicon carbide whiskers possess excellent mechanical properties, with an average strength of 8.4 GPa and an average elastic modulus of 580 GPa, as well as excellent elevated temperature stability [181]. Several attempts have been made to incorporate SiC whiskers in brittle ceramic materials, light-weight aerospace and automobile metallic materials for property enhancements.

2.4.3.1 Ceramic matrix SiC whisker reinforced composites

It has been observed that discontinuous fibers like SiC whiskers, when incorporated in ceramic materials, will improve flexural strength, thermal shock resistance, hardness, creep resistance, wear resistance and in particular fracture toughness [182, 183,184]. The reinforced whiskers help to avert catastrophic failures in brittle ceramic matrices by crack bridging, whisker pullout and whisker bridging [185, 186, 187, 188, 189, 190] SiC whisker reinforced ceramic composite materials find applications in structural components used at elevated temperatures eg. in high efficiency heat engines and heat recovery systems, and for making cutting tools to machine special materials [182,183]. As ceramics melt at very high temperatures, these materials are processed by powder metallurgy route which involves mixing of SiC whiskers with ceramic powders, compaction and sintering. Slurry processing could be employed to orient whiskers in non-workable ceramic matrix composites [191].

2.4.3.2 Metal matrix SiC whisker reinforced composites

In the case of composites with metallic matrices, addition of whiskers improves strength, stiffness, wear, fatigue life and creep resistance [192, 193, 194]. Therefore, efforts were made to embed SiC short fibers in light weight metal and alloys such as Al [194, 195, 196, 197, 198, 199], Mg [200, 201] and heavy metals like Cu [202] and TiB whiskers in Ti and its alloys [203].Conventionally whisker reinforced metallic composites can be fabricated

by one of the following techniques: pressure-less infiltration [197], squeeze casting [194, 195, 200, 201] and powder metallurgy [193, 196, 198, 202]. The bulk composites are then subjected to secondary metal working operations to realise the required shape and size [196, 199], align the fibers in the forming direction [198] and to close the pores resulting from primary processing. In some cases, the formed composites are heat treated to relieve the stresses introduced during working and to obtain the desired microstructure in the matrix [195, 199].

In general, superior mechanical properties could be obtained in whisker composites by optimising the volume fraction of whiskers, orientation of whiskers, surface roughness, surface chemistry of the whiskers and matrix-whisker interfacial bonding [204].

2.4.4 SiC particle reinforced composites

SiC particulate metal-matrix composites with the reinforcements bonded incoherently and discontinuously with the matrix can be prepared by either ex-situ [205,206] or in-situ [207] methods. In the ex-situ route, SiC particles are prepared separately and introduced into the matrix mainly by infiltration and powder metallurgy, whereas in the in-situ method the hard particles are synthesised during composite fabrication by processes like reactive gas injection, reactive sintering, internal oxidation, reactive milling, cryomilling etc. [207]. SiC particles are widely employed as reinforcements in light metals and alloy composites based on Al [206, 208], Mg [209] and Ti [205, 210] to improve their mechanical performance and wear resistance. The elastic and plastic properties of these composites are influenced by variables like shape, size, orientation, distribution and volume fraction of reinforcements, matrix alloy, secondary treatments like forming and/or heat treatment, chemistry and thickness of interfacial reaction zone [210, 211, 212, 213] .

2.4.5 Interfaces and reinforcement coatings in composites

As discussed in previous sections, the soundness of a SiC particle, SiC whisker or CNT reinforced metal matrix composite (MMCs) is mainly dictated by the interfacial bonding between the composite constituents such as the reinforcements and the matrix metal. The load transfer efficiency between the two constituents and the amount of energy absorbed during crack propagation is greatly influenced by the nature of the interfacial bonding. For tough matrices, a high interfacial strength is desirable to favour matrix deformation. Conversely, for brittle matrices a low interfacial strength is desirable so that interfacial debonding, crack deflection, fibre fracture and fibre pull-out can occur [214, 215]. The interfacial bonding in MMCs with tough metal matrices should be sufficiently strong to

promote matrix plasticity on loading and to resist any debonding of the interface [216]. This can be realised by promoting the dissolution of matrix constituents in reinforcements or vice-versa at the interface [217]. Instead, most metal-based composites form intermetallic compounds at matrix-reinforcement junctions during fabrication [218, 219, 220, 221, 222]. In some cases, the second phase compounds formed at the interface improve the interfacial interaction and enhance mechanical properties of composites [223, 224]. In most cases, the brittle interfacial compounds formed at the interface exhibit deleterious effects on functional and mechanical properties [225]. Some systems, due to the absence of solubility between matrix and reinforcements, show poor bonding [153, 154]. Therefore, the full potential of reinforcements in MMCs can be realised by tailoring the interfacial reactions favourably to improve stiffness, creep resistance, and wear resistance without degrading the toughness.

The interfacial reactions can be optimised by adopting one or more of the following methods: modification of the matrix composition, coating of the reinforcement, specific treatments to the reinforcement and control of process parameters [226]. Among these, the most efficient technique to improve interfacial properties is coating of reinforcements. Reinforcements can be decorated with metallic, ceramic, bilayer or multilayer coatings containing metal and/or ceramic layers by chemical vapour deposition (CVD), physical vapour deposition (PVD), thermal spraying, sol-gel process, electrolytic, electroless and cementation methods. The electroless deposition technique has been employed in this work to coat micron and nano sized reinforcements such as SiC particulates, whiskers and CNTs with Ni-P, cobalt and copper.

2.5 Electroless plating

The electroless coating technology introduced by Brenner & Riddell in 1946 [227, 228] has been widely employed in surface engineering and metal finishing industries in recent years as it offers the following advantages,

1) Deposit uniformity (±2.5μm)
2) Excellent corrosion resistance
3) Good wear and abrasion resistance
4) Fast plating rate
5) High brightness
6) Good solderability/weldability/brazeability
7) Magnetic property selectivity

The electroless coatings are produced by controlled chemical reduction of metallic ions on a catalytic surface without the use of electricity. The radicals that initiate the plating process may be inherently present or can be introduced on the surface by treating them with a salt solution of a catalyst. For example, the electroless Ni plating reaction begins spontaneously on almost all Group VIII metals (Fe, Ni, Co, Pd, Pt, Rh) present on the surface in active form. Once initiated, the deposit/coating will act as a catalyst to the reduction reaction and the reaction continues as long as the surface remains in contact with the bath solution or until the solution is depleted of solute metallic ions. Hence, it is also known as "auto-catalytic plating". Electroless deposition yields a very uniform coating on any surface provided the catalyst radicals present or introduced are uniformly distributed on the surface and there is sufficient agitation to ensure a uniform concentration of metal ions and reducing agents. Employing this technique, one can achieve alloy and composite plating in addition to elemental plating by varying the bath composition and by introducing second phase filler materials in the bath respectively. Electroless plating can be performed under acidic or alkaline conditions. The main components of the electroless plating bath and their functions are summarised in Table 2.4 [229].

Table 2.4 *Electroless bath composition and their functions*

Component	Function
Metal ions	Source of metal
Reducing agent	Source of electrons
Complexants/Chelators	Stabilizes the solution
Accelerators	Activates reducing agent
Buffers	Controlling pH (long term)
pH regulators	Regulates pH of solution (short term)
Stabilizer	Prevents solution breakdown
Wetting agents	Increases wettability of the surfaces

2.5.1 Components of electroless plating bath

2.5.1.1 Reducing agents

Reducing agents aid in the reduction of metal ions on catalytic surfaces by releasing one of the following species: electrons, atomic hydrogen or hydroxyl ions. The most commonly used reducing agents are sodium hypophosphite, formaldehyde (especially for Cu), hydrazine, borohydrides, amine boranes and some of their derivatives. In electroless Ni

plating, the choice of reducing agents is governed by the final composition of the coating and the pH of the plating bath.

2.5.1.2 Complexing agents

Complexing agents are generally made of organic acids or their salts like acetate, succinate, propionate, citrate, malonate, malate etc or inorganic ions like pyrophosphate anion, ammonium ion. The main functions of complexing agents are [230],

1. They exert a buffering action and help to prevent the pH of the plating solution from falling too fast during plating.
2. They prevent the precipitation of metal salts e.g., basic salts or phosphites
3. They promote the formation of meta-stable complexes and help to reduce the concentration of free metal ions.

Complexing agents, by influencing the reaction mechanism play a dominant role in controlling the reaction rate and hence the nature of the deposit.

2.5.1.3 Stabilizer

These agents render stability to the electroless plating bath by preventing homogeneous reactions that initiate the random decomposition of the entire plating bath. In addition, some of the stabilizers accelerate the plating reactions. The stabilizers are broadly classified into four types,

1. Compounds of group IV elements (Se, Te, S)
2. Unsaturated organic acids (Maleic, itaconic)
3. Heavy metal cations (Sn^{+2}, Pb^{+2}, Sb^{+3}, Hg^{+})
4. Compounds containing oxygen (AsO_2^-, MoO_4^{2-}, IO_3^-)

The concentration of stabilizer added in the plating bath is a crucial parameter and is varied depending on its structural class. Excessive use of stabilization material(s) can result in the reduction of plating rate and bath life including poor metallurgical deposit properties. The complexing agent(s) and stabilizer(s) determine the composition and brightness of the deposit.

2.5.1.4 Surfactants

Surfactants are wetting agents that lower the surface tension of a liquid, allowing easier spreading, and lower the interfacial tension between two liquids or a liquid and solid surface. The most widely used surfactants are sodium dodecylsulfate (SDS), cetyl trimethyl

ammonium bromide (CTAB), sodium dodecyl benzene sulphonate, sodium lauryl sulphate and triethanolamine.

2.5.1.5 Buffers

Buffers are class of additives that are capable of neutralizing both acids and bases without appreciably changing the original pH of the solution. Buffer capacity is measured by the quantity of buffer required to change the pH by a given amount. The most commonly used acid buffers in electroless plating baths are acetic, propionic, glutaric, succinic and adipic acids.

The main factors affecting the electroless deposition rate include temperature, pH of the solution, concentration of metal ions in the solution, type of reducing agents, concentration of reducing agents, bath load and agitation [231].Henry [232] has summarised typical bath components and operating parameters for electroless plating of acid nickel, alkaline nickel, copper, gold, palladium and cobalt.

2.5.2 Pre-treatments for parts/particles with non-catalytic surfaces

As mentioned above, electroless plating cannot be triggered in materials with non-catalytic surfaces like ceramics, polymers and some metals, unless initiated by a pre-treatment step. In the case of ceramics, prior to the introduction of catalytic centres on surfaces, they are roughened by techniques like acid etching, functionalisation etc. to improve the coating adhesion and to increase the number of active sites. Non-catalytic surfaces corrugated on the atomic level can be decorated with catalyst seeds either by a single step activation process or by two step process involving surface sensitisation and activation. Single step catalyzation can be realised by treating the parts/particles in a solution containing Pd and Sn ions [233, 234, 235, 236] or in a polymer-stabilized Pd catalyst solution containing palladium acetate trimer, ammonium hydroxide, methanol and polyvinyl butyral [237]. In a conventional two-step process [238, 239], the ceramic particles are surface sensitised and activated by treating them with $SnCl_2$+HCl and $PdCl_2$+HCl solutions respectively. During activation, Pd^{2+} ions will be reduced to Pd atoms on the surface by Sn^{2+} ions deposited during sensitisation as shown by the following equation.

$$Sn^{2+}+Pd^{2+}\rightarrow Pd^{o}+Sn^{4+}$$

The palladium metal clusters deposited on the surface will act as nucleation sites for the subsequent electroless deposition. Sensitisation and activation can be represented schematically as shown below (Fig. 2.7).

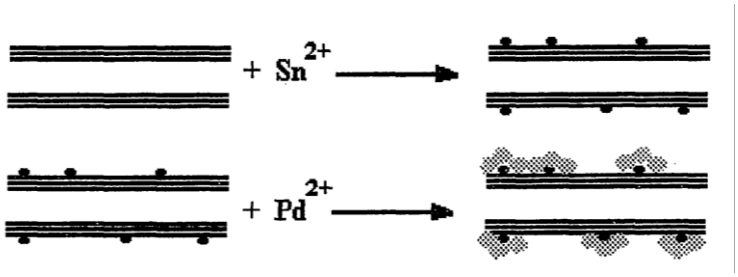

Fig. 2.9 Schematic showing the deposition of Sn and Pd on a ceramic surface during sensitisation and activation, respectively

2.5.3 Electroless plating of CNTs and SiC whiskers

CNTs have been decorated with metallic layers by the electroless plating method to realise one dimensional nanocomposites, which may be of interest to nanoscale material research and to improve the interfacial adhesion between CNTs and matrix materials in CNT reinforced composites. Certain characteristics of CNTs like low chemical reactivity, large surface curvature, small diameter and large aspect ratio pose problems in obtaining uniform coating over CNTs [240]. Zeng et al. [241] showed that side wall functionalization, by remarkably modifying the wettability and by entrapping more catalytic ions on the CNT surface, helps in achieving a dense and uniform coating. Functional groups (such as -COOH, -C=O,-OH) attached on the surface also help to overcome the Van der Waals force between the CNTs during plating and promote dispersion with ultrasonication. It has been observed that a high density of catalytic sites and a low deposition rate are the critical parameters to obtain better coatings on CNTs [238, 239].

Several attempts were made to coat CNTs with Ag [240], Ni-P[239, 241, 242, 243], Ni-N [244], Ni[245], Cu[246, 247], Co[238] and Au[248] by the electroless method. Ni-P layers on CNTs (Fig. 2.10) are usually amorphous and are heat treated above 400 ^{o}C to achieve a nanocrystalline microstructure (Fig. 2.11) [242, 243].

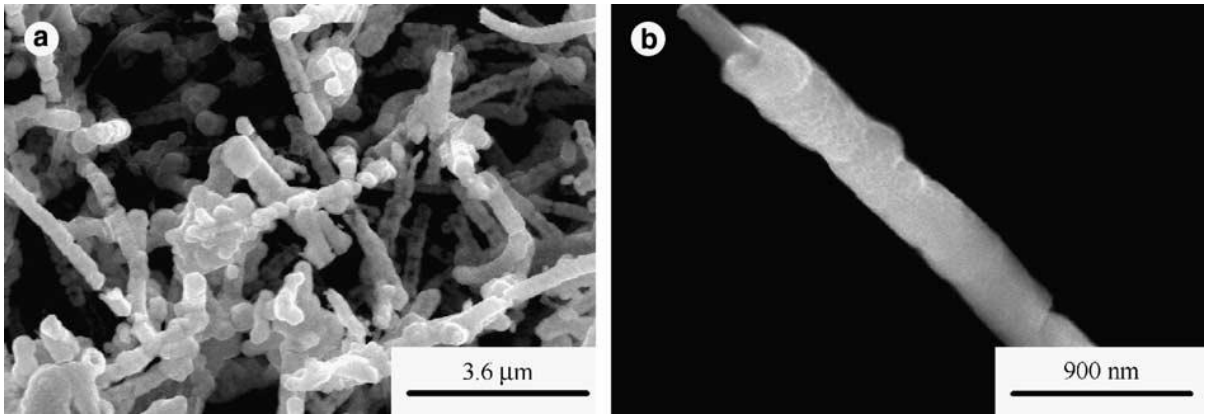

Fig. 2.10 SEM images of Ni–P-coated MWCNTs by the electroless deposition: (a) low magnification (b) higher magnification [243]

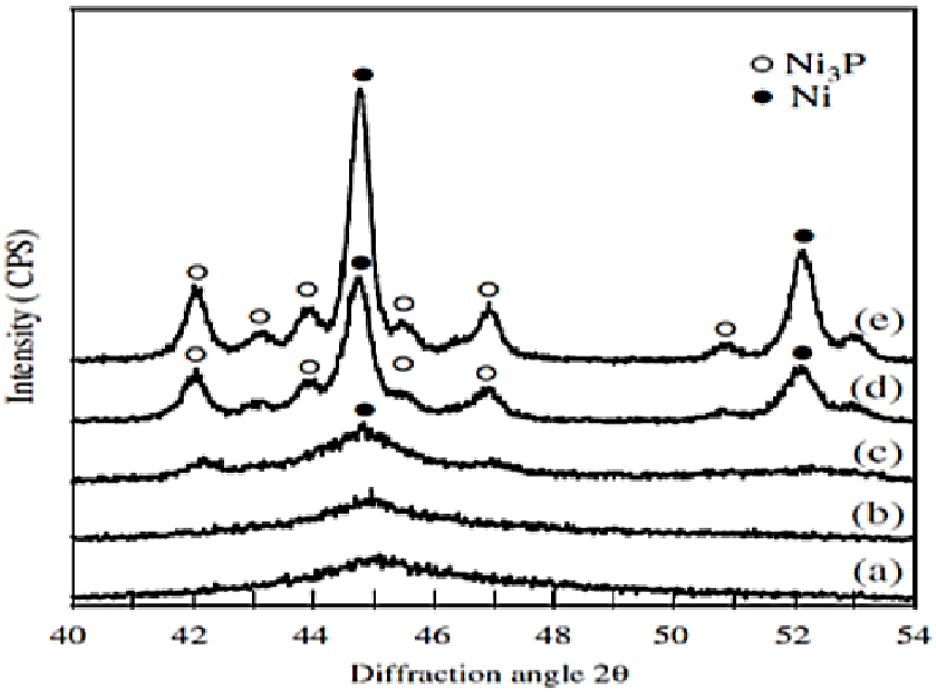

Fig. 2.11 XRD patterns of MWCNTs with Ni–P layers: (a) as-coated and (b–d) under heat-treatment at different temperature. (b) 200^{o}C, (c) 330^{o}C, (d) 400^{o}C, and (e) 480^{o}C [243]

Xue et al. [249] wrapped CNTs with Ni-Fe-P alloy layers by an electroless technique and showed that heat treatment is mandatory to realise crystallinity in magnetic coatings like Ni-P films.

Chen et al. [238] plated CNTs with Co and improved the coating continuity by heating them in a quartz tube at 600 ^{o}C in an H_2 atmosphere. In general, the performance of the electroless plated magnetic layers on CNTs was improved after heat treatment.

Composite coatings containing Ni-P and CNTs can be prepared by an electroless co-deposition method on metallic substrates like copper [250, 251], steel [252] and ceramic

substrates [253]. It has been showed that these coatings display remarkable wear resistance and CNT addition promotes crystallinity in Ni-P deposits and reduces phosphorus content in the coating. Mechanical performance of composite coatings prepared after activating the CNTs are inferior to those prepared without any activation. It is also possible to obtain quaternary composite coatings on substrates by an electroless method by varying the bath components and operating conditions [254].

SiC whisker reinforced copper composites with a large volume fraction of fillers (20-50 vol%) were prepared by sintering the electroless plated SiC whiskers [255]. Yih et al. metallised SiC whiskers with Cu by electroless plating and subsequently electrodeposited with Cu to prepare composites by a coated filler method [256]. Jiang et al. deposited a Co layer on SiC whiskers by electroless plating and transformed the amorphous aggregates to crystalline clusters by heat treating the SiC_w/Co composite in a hydrogen atmosphere at 500^{o}C (Fig. 2.12 and 2.13) [236].

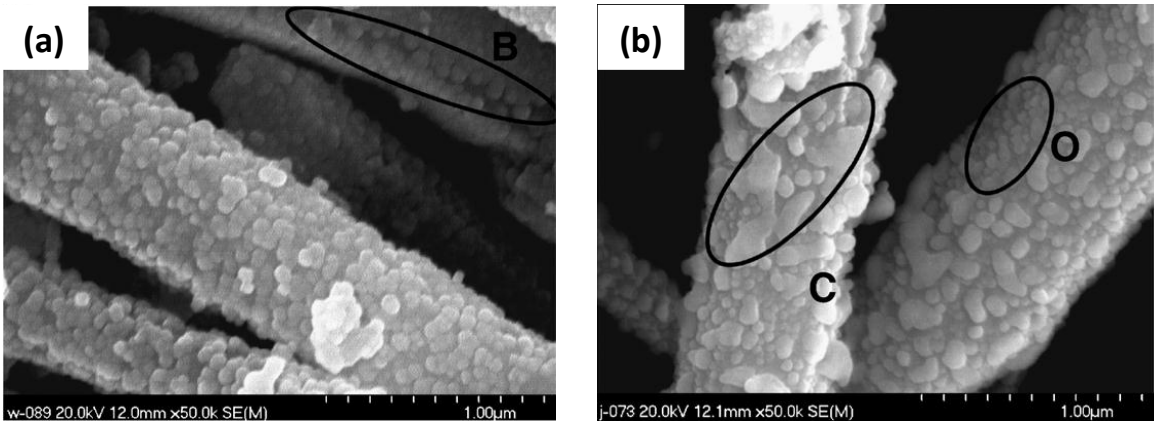

Fig. 2.12 SEM image of SiC_w/Co nanocomposite powders: (a) before; and (b) after heat treatment [236]

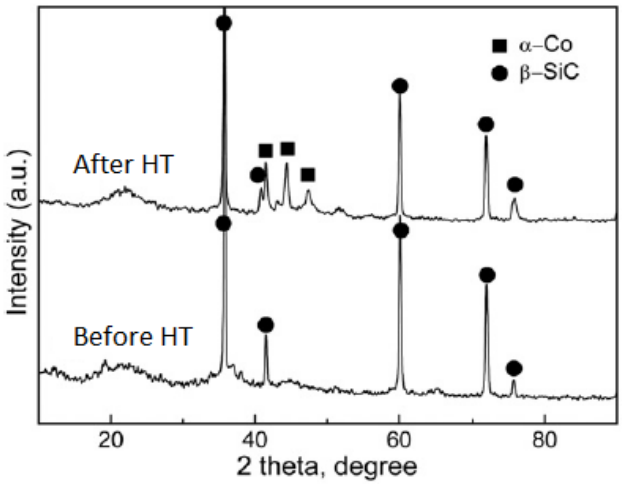

Fig. 2.13 XRD patterns of SiC_w/Co nanocomposite powders, before and after heat treatment [236]

SiC whiskers were also coated with Ni by an electroless plating method to enhance the wetting characteristics of SiC reinforcement with Al matrix [197]. The electroless method has also been employed to prepare short-fibre composites by co-depositing potassium titanate whiskers with Ni-P [257].

References

1 R. S. Sundar and S. C. Deevi, Soft magnetic FeCo alloys: alloy development, processing, and properties, *Inter. Mater. Rev.* **50**, 157-192 (2005)

2 R.E. Quigley: Proc. of IEEE Applied Power Electronics Conf. 'More electric aircraft', 1993. pp. 906-911.

3 R.I. Jones: Proc. of the Institution of Mech. Engineers, Part G: J of Aerospace Engineering, 2002 vol. 216 pp. 259-269

4 R.T. Fingers, J.E Coate, R.E Dowling: Proc. of Intersociety Energy Conversion Engineering Conf., vol.1, 1997. pp. 563-568

5 N. S. Stoloff and R. G. Davies, The plastic deformation of ordered FeCo and Fe_3Al alloys, *Acta Metall.* **12**, 473–85 (1964)

6 J. M. MacLaren, T. C. Schulthess, W. H. Butler, R. Sutton and M. McHenry, Electronic structure, exchange interactions, and Curie temperature of FeCo, *J. Appl. Phys.* **85**, 4833–35 (1999)

7 T. Nishizawa, K. Ishida, T.B. Massalski (Ed.), Binary alloy phase diagrams, vol. 2 (2nd ed.), ASM International, Metal Park (OH) (1990), p. 1186

8 C.W. Chen, Magnetism and metallurgy of soft magnetic materials, North-Holland Publishing Company, Amsterdam (1977)

9 R. V. Major and V. Samadian, Physical metallurgy and properties of a new high saturation Co-Fe alloy, *J. Mater. Eng.* **11**, 27–30 (1989)

10 L. Zhao and I. Baker, Extrusion processing of FeCo, *J. Mater. Sci.* **29**, 742–748 (1994)

11 H. Hosoda, S. Miyazaki, K. Inoue, T. Fukui, K. Mizuuchi, Y. Mishima and T. Susuku, Cold rolling of B2 intermetallics, *J. Alloys Comp.* **302**, 266–273 (2000)

12 D. W. Clegg and R. A. Buckley, The disorder → order transformation in iron-cobalt-based alloys, *Metal Science Journal* **7**, 48-54 (1973)

13 K. K. Bogma, *Fiz. Met. Metalloved.* **22**, 148–151 (1966)

14 R. C. Hall, *Trans. TMS-AIME* **218**, 268–270 (1960)

15 R. H. Yu, S. Basu, R.Y. Zhang, A. Parvizi-Marjidi, K. M. Unruh and J. Q. Xiao, High temperature soft magnetic materials: FeCo alloys and composites, *IEEE Trans Magn* **36(5)**, 3388–3393 (2000)

16 L. Zhao and I. Baker, The effect of grain size and Fe:Co ratio on the room temperature yielding of FeCo, *Acta metall. mater.* **42,** 1953-1958 (1994)

17 T. Sourmail, Near equiatomic FeCo alloys: Constitution, mechanical and magnetic properties, *Prog. Mater. Sci.* **50,** 816–880 (2005)

18 K. Kawahara, Effect of additive elements on cold workability in FeCo alloys, *J. Mater. Sci.* **18**, 1709-18 (1983)

19 L. Zhao, I. Baker and E.P. George, Room temperature fracture of FeCo, *Mater. Res. Symp. Proc.* **288**, 501–506(1993)

20 J.H. White and C.V. Wahl, U.S. Patent 1862559, 1932

21 K. Kawahara, Effect of carbon on mechanical properties in $Fe_{0·5}Co_{0·5}$ alloys, *J. Mater. Sci*. **18**, 2048-55 (1983)
22 H.C. Fielder and A.M. Davies, The formation of Gamma Phase in Vanadium Permendur, *Met. Trans.* **1**, 1036-37 (1970).
23 A.I.C. Persiano and R. D. Rawlings, Effect of niobium additions on the structure and magnetic properties of equiatomic iron-cobalt alloys, *J. Mater. Sci.* **26**, 4026-32 (1991)
24 R.S. Sundar and S.C. Deevi, Influence of alloying elements on the mechanical properties of FeCo–V alloys, *Intermetallics* **12**, 921–27 (2004)
25 K. Kawahara and M. Uehara, A possibility for developing high strength soft magnetic materials in FeCo-X alloys, *J. Mater. Sci.* **19**, 2575- 81 (1984)
26 M. R. Pinnel and J. E. Bennett, Influence of thermal treatments on the mechanical properties of an Fe-Co-V alloy, *Acta Metall.* **24**, 1095-1106 (1976)
27 T. Sourmail, Evolution of strength and coercivity during annealing of FeCo based alloys, *Scripta Mater.* **51,** 589-91 **(**2004)
28 D.R. Thornburg, High strength high ductility cobalt iron alloys, *J. Appl. Phys.* **40**, 1579- 80 (1969)
29 E.P. George, A.N. Gubbi, I. Baker and L. Robertson, Mechanical properties of soft magnetic FeCo alloys, *Mater. Sci. Eng., A* **329–331**, 325–33 (2002)
30 A. Duckham, D.Z. Zhang, D. Liang, V. Luzin, R.C. Cammarata, R.L. Leheny, C.L. Chien and T.P. Weihs, Temperature dependent mechanical properties of ultra-fine grained FeCo–2V, *Acta Mater.* **51**, 4083–93 (2003)
31 R. H. Yu, S. Basu, L. Ren, Y. Zhang, A. Parvizi-Majidi, K. M. Unruh, and J. Q. Xiao, High Temperature Soft Magnetic Materials: FeCo Alloys and Composites, *IEEE Trans. Mag.* **36[5]**, 3388-93 (2000)
32 R.S. Sundar, S.C. Deevi and B.V. Reddy, High strength FeCo–V intermetallic alloy: Electrical and magnetic properties, *J. Mater. Res.* **20**, 1515-22 (2005)
33 A. Inoue, B.L. Shen and C.T. Chang, Fe- and Co-based bulk glassy alloys with ultrahigh strength of over 4000 MPa, *Intermetallics* **14**, 936–44 (2006)
34 A.H. Taghvaei, A. Ebrahimi, M. Ghaffari and K. Janghorban, Magnetic properties of iron-based soft magnetic composites with MgO coating obtained by sol–gel method, *J. Magn. Magn. Mater.* **322**, 808–13 (2010)
35 A.H. Taghvaei, A. Ebrahimi, M. Ghaffari and K. Janghorban, Investigating the magnetic properties of soft magnetic composites based on mechanically alloyed nanocrystalline Fe–5 wt% Ni powders, *J. Magn. Magn. Mater.* **323**, 150–56 (2011)
36 H. Shokrollahi and K. Janghorban, Soft magnetic composite materials (SMCs), *J. Mater. Process. Techno.* **189,** 1–12 (2007)
37 B. Williams, Powder Metallurgy Permanent Magnets and their Applications, IPMD 15th Edition 2012-201, 4 pages
38 F. Hanejko, H. Rutz, C. Oliver, Effects of Processing and Materials on Soft Magnetic Performance of Powder Metallurgy Parts, Advances in Powder Metallurgy & Particulate Materials, 1992, Vol. 6, pp 375-404, Metal Powder Industries Federation, Princeton, NJ
39 J.A. Bas, J.A. Calero and M.J. Dougan, Sintered soft magnetic materials. Properties and applications, *J. Magn. Magn. Mater.***254–255**, 391–98 (2003)
40 A. Silva, P. Wendhausen, R. Machado and W. Ristow Jr, Magnetic properties obtained for Fe-50Co alloy produced by MIM with elemental powders, *Mater. Sci. Forum* **534-536,** 1353-56 (2007).

41 P.W. Lee, ASM Handbook, volume 7, *Powder metal Technologies and applications*; pg.1009, ed. American Society for Metals, (1998)

42 W. Yamagishi, K. Hashimoto, T. Sato, S. Ogawa and Z. Henmi, Magnetic properties of Fe-Co alloys produced by powder metallurgy, *IEEE Trans.Mag.* **Mag-22 (5)**, 641-643 (1986).

43 Z. Turgut, M. Huang, J.C. Horwath, and R.T. Fingers, High strength bulk Fe–Co alloys produced by powder metallurgy, *J App. Phys.* **103**, 07E7241-3 (2008)

44 L. Minier, S.L Gallet, Yu. Grin and F. Bernard, A comparative study of nickel and alumina sintering using spark plasma sintering, *Mater. Chem.& Phys.* **134,** 243-53 (2012)

45 J.R. Groza and A. Zavaliangos, Sintering activation by external electrical field, *Mater. Sci. Eng., A* **287**, 171–77 (2000)

46 M. Nygren and Z. Shen, Spark Plasma Sintering: Possibilities and Limitations, *Key Eng. Mater.* **264-268,** 719-724 (2004).

47 V. Mamedov, Spark plasma sintering as advanced PM sintering method, *Powder Metall.* **45 [4],** 322-28 (2002).

48 M. Eriksson, M. Radwan and Z. Shen, Spark plasma sintering of WC, cemented carbide and functional graded materials, *Int. J. of Refract. Met.Hard Mater.* **36**, 31-37 (2013).

49 B. Mei and Y. Miyamoto, Preparation of Ti-Al Intermetallic Compounds by Spark Plasma Sintering, *Metall. Mater. Trans. A* **32A**, 843-847 (2000).

50 Q. Jiang, F. Liu, H. Yan, H. Ning, Z. Libor, Q. Zhang, M. Cain, and M.J. Reece, Magneto-Electric Properties of Multiferroic Pb(Zr0.52Ti0.48)O3–NiFe2O4 Nanoceramic Composites, *J. Am. Ceram. Soc.* **94 [8]**, 2311–14 (2011).

51 Robles-Hernández, C. Francisco and H. A. Calderon, Nanostructured metal composites reinforced with fullerenes, *JOM* 62 [2], 63-68 (2010)

52 D. Sebayang, D. S. Khaerudini, H. Saryanto, M.A. Othman, M. H Saleh, D. Fredrick, and P. Untoro, Microstructure and Mechanical Properties of Nanocrystalline FeCr Alloy Prepared by Spark Plasma Sintering, *Appl. Mechanics and Mater.* **52-54,** 2197-2202 (2011).

53 Z. Shen, E. Adolfsson, M. Nygren, L. Gao, H. Kawaoka and K. Niihara, Dense Hydroxyapatite-Zirconia Ceramic Composites with High Strength for Biological Applications, *Adv. Mater.* **13**, 214-216 (2001).

54 D. Fabrègue, B. Mouawad, C. Buttay, M. Soueidan, A. Lamontagne, R. Forte, M. Perez, L. Courtois, C. Landron, E. Maire and V. Massardier-Jourdan, Elaboration of architectured materials by spark plasma sintering, *Mater. Sci. Forum* **706-709,** 1885-92 (2012).

55 J.L. Ning, D.M. Jiang, K.H. Kim and K.B. Shim, Influence of texture on electrical properties of ZnO ceramicsprepared by extrusion and spark plasma sintering, *Ceramics International* **33,** 107–14 (2007).

56 Z. Xiao, C. Tang, H. Zhao, D. Zhang and Y. Li, Effects of sintering temperature on microstructure and property evolution of $Fe_{81}Cu_2Nb_3Si_{14}$ soft magnetic materials fabricated from amorphous melt-spun ribbons by spark plasma sintering technique, *J. Non-Cryst. Solids* **358[1]**, 114-18 (2012).

57 M. Mulukutla, A. Singh and S.P. Harinkar, Spark Plasma Sintering for Multi-scale Surface Engineering of Materials, *JOM* **62 [6]**, 65-71 (2010).

58 Z.A. Munir, U. Anselmi-Tamburini and M. Ohyanagi, The effect of electric field and pressure on the synthesis and consolidation of materials: a review of the spark plasma sintering method. *J. Mater. Sci.* **41,** 763–77 (2006).

59 K.A. Khor, L.G. Yu, O. Andersen and G. Stephani, Effect of spark plasma sintering (SPS) on the microstructure and mechanical properties of randomly packed hollow sphere (RHS) cell wall, *Mater. Sci. Eng. A* **356**, 130-35 (2003).

60 M. Omori, Sintering, consolidation, reaction and crystal growth by the spark plasma system, *Mater. Sci. Eng. A* **287**, 183–88 (2000).

61 S.W. Wang, L.D. Chen, Y.S. Kang, M. Niino and T. Hirai, Effect of plasma activated sintering (PAS) parameters on densification of copper powder, *Mater. Res. Bull.* **35** 619–28 (2000).

62 D.M. Hulbert, A. Anders, J. Andersson, E.J. Lavernia and A.K. Mukherjee, A discussion on the absence of plasma in spark plasma sintering, *Scripta Mater.* **60**, 835–38 (2009)

63 T. H. Noh, M.B. Lee, H.J. Kim, and I.K. Kang, Relationship between crystallization process and magnetic properties of Fe-(Cu-Nb)-Si-B amorphous alloys, *J. Appl. Phys.* **67 [9]**, 5568- 70 (1990).

64 Z. Zhao, C. Chang, A. Makino, A. Okubo and A. Inoue, Preparation of bulk glassy $Fe_{76}Si_9B_{10}P_5$ as a soft magnetic material by spark plasma sintering, *Mater.Trans.* **50[3]**, 487-89 (2009).

65 B. Shen, H. Kimura, A. Inoue, M. Omori and A. Okubo, Preparation of Fe65Co10Ga5P12C4B4 Bulk Glassy Alloy with Good Soft Magnetic Properties by Spark-Plasma Sintering of Glassy Powder, *Mater. Trans.* **43[8]**, 1961-65 (2002)

66 R. Yamada, N. Yodoshi, A. Kawasaki and R. Watanabe, Consolidation of Fe-Co Based Metallic Glassy Powder by SPS Method, *J. Japan Inst. Metals* **73[4]**, 299-305 (2009).

67 G. Xie, D.V. Louzguine-Luzgin, L. Song, H. Kimura and A. Inoue, Dual phase metallic glassy composites with large-size and ultra-high strength fabricated by spark plasma sintering, *Intermetallics* **17**, 512–16 (2009).

68 H.W. Zhang, R. Gopalan, T. Mukai and K. Hono, Fabrication of bulk nanocrystalline Fe–C alloy by spark plasma sintering of mechanically milled powder, *Scripta Mater.* **53**, 863–868 (2005).

69 G. Herzer, Soft Magnetic Nanocrystalline Materials, *Scripta Metallurgica et Materialia* **33**, 1741-56 (1995).

70 M.A. Meyers, A. Mishra and D.J. Benson, Mechanical properties of nanocrystalline materials, *Prog. Mater. Sci.* **51**, 427–556 (2006).

71 M.E. McHenry, M.A. Willard and D.E. Laughlin, Amorphous and nanocrystalline materials for applications as soft magnets, *Prog. Mater. Sci.* **44,** 291–433 (1999).

72 M.E. McHenry and D.E. Laughlin, Nano-scale materials development for future magnetic applications, *Acta Mater.* **48,** 223–38 (2000).

73 F. Fellah, S. M. Cherif, K. Bouziane, F. Schoenstein, N. Jouini, and G. Dirras, Magnetic properties of ultrafine-grained cobalt samples obtained from consolidated nanopowders, *Phys. Status Solidi A* **208[8],** 1942-49 (2011).

74 L.H. Bac, H.J. Ryu, B.K. Kim, J.S. Kim and J.C Kim, Production and determination of the magnetic properties of the Fe-36Ni nanopowder via electrical explosion of wire in water and compacted alloy, *Journal of Nanoscience and Nanotechnology* **11[7]**, 6433-36 (2011).

75 R. Nicula, V.D. Cojocaru, M. Stir, J. Hennicke and E. Burkel, High-energy ball-milling synthesis and densification of Fe–Co alloy nanopowders by field-activated sintering (FAST), *J. Alloys Compd* **434–435**, 362–66 (2007).

76 Y.D. Kim, J.Y. Chung, J. Kim and H. Jeon, Formation of nanocrystalline Fe–Co powders produced by mechanical alloying, *Mater. Sci. & Engg.* **A291**, 17–21 (2000).

77 A. Kojima, T. Mizushima, A. Makino, A. Inoue and T. Masumoto, Soft magnetic properties of bulk nanocrystalline $Fea_0Zr_7B_3$ alloys consolidated by spark-plasma sintering, *Journal of the Japan Society of Powder and Powder Metallurgy* **43[5]**, 613-18 (1996).

78 S. Gururaja, M. Taya and Y.S. Kang, Design of ferromagnetic shape memory alloy composite made of Fe and TiNi particles, *J Appl. Phys.* **102**, 064910-1-6 (2007).

79 H.R. Cha, C.H. Yun, H-T Son and J.I. Cho, The improvement of permeability and strength in soft magnetic composites motor core using spark plasma sintering process, *Adv. Mater. Res.* **26-28**, 609-12 (2007).

80 S.Ishihara, W. Zhang, H. Kimura, M. Omori and A. Inoue, Consolidation of Fe-Co-Nd-Dy-B glassy powders by spark-plasma sintering and magnetic properties of the consolidated alloys, *Mater. Trans.* **44[1]**, 138-43 (2003).

81 T. Saito, Structures and magnetic properties of Sm-Fe-N bulk magnets produced by the spark plasma sintering method, *J. Mater. Res.* **22[11]**, 3130-36 (2007).

82 M. Grigoraş, M. Lostun, N. Lupu and H. Chiriac, NdFeB/αFe Nanocomposite Permanent Magnets with Enhanced Properties Prepared by Spark Plasma Sintering, *Mater. Sci. Forum* **672**, 229-32 (2011).

83 G. Jing, L. Ying, L. Jun, M. Yilong, D. Huilong and G. Shengji, Preparation of Nd-Fe-B/α-Fe nano-composite magnets by chemical vapor deposition, *Rare Metal Mater. Engg.* **39[6]**, 1121-24 (2010).

84 K.P. Su, Z.W. Liu, H.Y. Yu, X.C. Zhong, W.Q. Qiu and D.C. Zeng, A feasible approach for preparing remanence enhanced NdFeB based permanent magnetic composites, *J Appl. Phys.* **109[7]**, 07A710-1-3 (2011).

85 N. Lupu, M. Grigoras, M. Lostun, and H. Chiriac, $Nd_2Fe_{14}B$/soft magnetic wires nanocomposite magnets with enhanced properties, *J Appl. Phys.* **105**, 07A738-1-3 (2009).

86 N. Millot, S. Le Gallet, D. Aymes, F. Bernard and Y. Grin, Spark plasma sintering of cobalt ferrite nanopowders prepared by coprecipitation and hydrothermal synthesis, *J. Eur. Ceram. Soc.* **27**, 921–26 (2007).

87 S. Imine, F. Schoenstein, S. Mercone, M. Zaghrioui, N. Bettahar and N. Jouini, Bottom-up and new compaction processes: A way to tunable properties of nanostructured cobalt ferrite ceramics, *J. Eur. Ceram. Soc.* **31**, 2943–55 (2011).

88 M. Yue, J. X. Zhang, H. Zeng, and K. J. Wang, Preparation, microstructure, and magnetic properties of bulk nanocrystalline Gd metal, *Appl. Phys. Lett.* **89**, 232504-1-3 (2006).

89 S. Iijima, Helical microtubes of graphitic carbon, *Nature* **354**, 56–58 (1991).

90 S.G. Louie, "Electronic Properties, Junctions, and Defects of Carbon Nanotubes", in *Carbon Nanotubes*, *Topics in Applied Physics* 80, eds. M.S. Dresselhaus, G. Dresselhaus, and P. Avouris (Springer-Verlag, Heidelberg, 2001), p. 113.

91 T.W. Odom, J.-L. Huang, P. Kim and C. M. Lieber, Atomic structure and electronic properties of single-walled carbon nanotubes, *Nature* **391**, 62–64 (1998).

92 P. Chen, J. Lin and K. L. Tan, Carbon Nanotubes: A Future Material of Life, *IUBMB Life* **49**, 105–08 (2000).

93 J.-P. Salvetat, J.-M. Bonard, N.H. Thomson, A.J. Kulik, L. Forr´o, W. Benoit and L. Zuppiroli, Mechanical properties of carbon nanotubes, *Appl. Phys. A* **69**, 255–60 (1999).

94 L. An, L. Feng and C. Lu, Mechanical Properties and Applications of Carbon Nanotubes, *Adv. Mater. Res.* **295-297**, 1516-21 (2011).

95 J. Stein, B. Lenczowski, N. Fre´ty and E. Anglaret, Mechanical reinforcement of a high-performance aluminium alloy AA5083 with homogeneously dispersed multi-walled carbon nanotubes, *Carbon* **50,** 2264-72 (2012).

96 M.F. Yu, O. Lourie, M.J. Dyer, K. Moloni, T.F. Kelly and R.S. Ruoff, Strength and breaking mechanism of multiwalled carbon nanotubes under tensile load, *Science* **287**, 637–40 (2000).

97 B.G. Demczyk, Y.M. Wang, J. Cumings, M. Hetman, W. Han, A. Zettl and R.O. Ritchie, Direct mechanical measurement of the tensile strength and elastic modulus of multiwalled carbon nanotubes, *Mater. Sci. Eng., A* **334**, 173–78 (2002).

98 J.H. Lehman, M. Terrones, E. Mansfield, K.E. Hurst and V. Meunier, Evaluating the characteristics of multiwall carbon Nanotubes, *Carbon* **49**, 2581-602 (2011).

99 R.H. Baughman, A.A. Zakhidov and W.A de Heer, Carbon Nanotubes- the route toward applications, *Science* **297**, 787-792 (2002).

100 H. Dai, Carbon nanotubes: opportunities and challenges, *Surface Sci.* 500, 218–41 (2002).

101 W. Lu, M. Zu, J-H Byun, B-S Kim and T-W Chou, State of the art of carbon nanotube fibers: Opportunities and challenges, *Adv. Mater.* **24**, 1805-33 (2012).

102 E.T. Thostenson, Z Ren and T-W Chou, Advances in the science and technology of carbon nanotubes and their composites: a review, *Comp. Sci Technol.* **61,** 1899–1912 (2001).

103 S. Bal and S.S. Samal, Carbon nanotube reinforced polymer composites–A state of the art, *Bull. Mater. Sci.* **30**, 379–86 (2007).

104 R. Andrews and M.C. Weisenberger, Carbon nanotube polymer composites, *Current Opinion in Solid State and Materials Science* **8**, 31–37 (2004).

105 P.J.F. Harris, Carbon nanotube composites, *Inter. Mater. Rev.* **49**, 31-43 (2004).

106 W.A. Curtin and B.W. Sheldon, CNT-reinforced ceramics and metals, *Mater. Today*, 44-49 (2004).

107 J. Cho, A.R. Boccaccini and M.S.P. Shaffer, Ceramic matrix composites containing carbon nanotubes, *J. Mater. Sci.* **44**, 1934–51 (2009).

108 J. Cho, F. Inam, M.J. Reece, Z. Chlup, I. Dlouhy, M.S.P. Shaffer and A.R. Boccaccini, Carbon nanotubes: do they toughen brittle matrices?, *J Mater. Sci.* **46**, 4770-79 (2011).

109 A. Peigney, Tougher ceramics with nanotubes, *Nature Mater.* **2**, 15-16 (2003).

110 J.W. Ning, J.J. Zhang, Y.B. Pan and J.K. Guo, Fabrication and mechanical properties of SiO_2 matrix composites reinforced by carbon nanotube, *Mater. Sci. Eng., A* **357 [1–2]**, 392–396 (2003).

111 A.G. Evans and F.W. Zok, The physics and mechanics of fibre-reinforced brittle matrix composites, *J. Mater. Sci.* **29**, 3857-96 (1994).

112 A. Peigney, F.L. Garcia, C. Estournes, A. Weibel and C. Laurent, Toughening and hardening in double-walled carbon nanotube/nanostructured magnesia composites, *Carbon* **48**, 1952-60 (2010).

113 C.B. Mo, S.I. Cha, K.T. Kim, K.H. Lee, S.H. Hong, Fabrication of carbon nanotube reinforced alumina matrix nanocomposite by sol–gel process, *Mater. Sci. Eng., A* **395 [1–2]**, 124–28 (2005).

114 E. Flahaut, A. Peighey, Ch. Laurent, Ch. Marliere, F. Chastel and A. Rousset. Carbon nanotube–metal–oxide nanocomposites: microstructure, electrical conductivity and mechanical properties. *Acta Mater.* **48**, 3803–12 (2000).

115 S. Guo, R. Sivakumar and Y. Kagawa, Multiwall CarbonNanotube-SiO2 Nanocomposites: Sintering, Elastic Properties, and Fracture Toughness, *Adv. Engg. Mater.* **9**, 84-87 (2007).

116 J.P. Fan, D.Q. Zhao, M.S. Wu, Z.N. Xu and J. Song, Preparation and microstructure of multi-wall carbon nanotubes-toughened Al_2O_3 composite, *J. Am Ceram Soc* **89[2]**, 750–53 (2006).

117 S.C. Zhang, W.G. Fahrenholtz, G.E. Hilmas, and E.J. Yadlowsky, Pressureless sintering of carbon nanotube–Al2O3 composites, *J. Eur. Ceram. Soc.* **30**, 1373–80 (2010)

118 J-W. An, D-H. You and D-S. Lim, Tribological properties of hot-pressed alumina-CNT composites,*Wear* **255** 677–81 (2003)

119 R. Sivakumar, S. Guo, T. Nishimura and Y. Kagawa, Thermal conductivity in multi-wall carbon nanotube/silica-based Nanocomposites, *Scripta Mater.* **56**, 265–68 (2007).

120 G.D. Zhan, J.D. Kuntz, J.L. Wan and A.K. Mukherjee, Single-wall carbon nanotubes as attractive toughening agents in alumina-based nanocomposites, *Nature Mater.* **2**, 38–42 (2003).

121 Y. Morisada, Y. Miyamoto, Y. Takaura, K. Hirota and N. Tamari, Mechanical properties of SiC composites incorporating SiC-coated multi-walled carbon nanotubes, *Inter. J Refract. Met. Hard Mater.* **25**, 322–27 (2007).

122 Y-F. Zhu, L. Shi, C. Zhang, X-Z. Yang and J. Liang, Preparation and properties of alumina composites modified by electric field-induced alignment of carbon nanotubes, *Appl. Phys. A* 89, 761-67 (2007).

123 Z.H. Xia, J. Lou and W.A. Curtin, A multiscale experiment on the tribological behaviour of aligned carbon nanotube/ceramic composites, *Scripta Mater.* **58**, 223–226 (2008).

124 C. Balazsi, B. Fenyi, N. Hegman, Z. Kover, F. Weber, Z. Vertesy, Z. Konya, I. Kiricsi, L.P. Biro and Arato P Development of CNT/Si_3N_4 composites with improved mechanical and electrical properties, *Composites* B **37**, 418–24 (2006).

125 F. Inam, H. Yan, T. Peijs and M.J. Reece, The sintering and grain growth behaviour of ceramic–carbon nanotube nanocomposites, *Compos. Sci. Tech.* **70**, 947–52 (2010).

126 E. Neubauer, M. Kitzmantel, M. Hulman and P. Angerer, Potential and challenges of metal-matrix-composites reinforced with carbon nanofibers and carbon nanotubes, *Composites Sci. & Tech.* **70**, 2228–36 (2010).

127 S. R. Bakshi, D. Lahiri and A. Agarwal, Carbon nanotube reinforced metal matrix composites – a review, *Inter. Mater. Rev.* **55 (1)**, 41-64 (2010).

128 J. Liao and M-J. Tan, Mixing of carbon nanotubes (CNTs) and aluminum powder for powder metallurgy use, *Powder Technology* **208**, 42–48 (2011).

129 T. Noguchi, A. Magario, S. Fukazawa, S. Shimizu, J. Beppu and M. Seki, Carbon nanotube/aluminium composites with uniform dispersion, *Mater Trans.* **45**, 602–04 (2004).

130 H. Kwon, M. Estili, K. Takagi, T. Miyazaki and A. Kawasaki, Combination of hot extrusion and spark plasma sintering for producing carbon nanotube reinforced aluminium matrix composites, *Carbon* **47,** 570-77 (2009).

131 C. He, N. Zhao, C. Shi, X. Du, J. Li, H. Li, and Q. Cui, An Approach to Obtaining Homogeneously Dispersed Carbon Nanotubes in Al Powders for Preparing Reinforced Al-Matrix Composites, *Adv. Mater.* **19**, 1128-32 (2007).

132 T. Laha, Y. Liu, and A. Agarwal, Carbon Nanotube Reinforced Aluminum Nanocomposite via Plasma and High Velocity Oxy -Fuel Spray Forming, *J. Nanosci. Nanotechnol.* **7**, 515-24 (2007).

133 S. R. Bakshi, V. Singh, K. Balani, D. G. McCartney, S. Seal and A. Agarwal, Carbon nanotube reinforced aluminum composite coating via cold spraying, *Surface & Coatings Tech.* **202**, 5162–69 (2008).

134 H. Kwon, M. Estili, K. Takagi, T. Miyazaki and A. Kawasaki, Combination of hot extrusion and spark plasma sintering for producing carbon nanotube reinforced aluminium matrix composites, *Carbon* **47**, 570–77 (2009).

135 C.S. Goh, J. Wei, L.C. Lee and M. Gupta, Ductility improvement and fatigue studies in Mg-CNT nanocomposites, *Compos. Sci. Tech.* **68**, 1432–39 (2008).

136 E. Carreño-Morelli, J. Yang, E. Couteau, K. Hernadi, J. W. Seo, C. Bonjour, L. Forró, and R. Schaller, Carbon nanotube/magnesium composites, *Phys. Status Solidi A* **201[8]**, R53– R55 (2004).

137 K. Kondoh, T. Threrujirapapong, H. Imai, J. Umeda and B. Fugetsu, Characteristics of powder metallurgy pure titanium matrix composite reinforced with multi-wall carbon nanotubes, *Compos. Sci. Tech.* **69**, 1077–81 (2009).

138 F. Xue, S. Jiehe, F. Yan and C. Wei, Preparation and elevated temperature compressive properties of multi-walled carbon nanotube reinforced Ti composites, *Mater. Sci. Eng., A* **527**, 1586–89 (2010).

139 Y. Feng, H.L. Yuan and M. Zhang, Fabrication and properties of silver-matrix composites reinforced by carbon nanotubes, *Mater. Charact.* **55**, 211–18 (2005).

140 S.I. Cha, K.T. Kim, S.N Arshad, C.B. Mo and S.H. Hong, Extraordinary Strengthening Effect of Carbon Nanotubes in Metal-Matrix Nanocomposites Processed by Molecular-Level Mixing, *Adv. Mater.* **17**, 1377-81 (2005).

141 K.T. Kim, S.I. Cha, S.H. Hong and S.H. Hong, Microstructures and tensile behavior of carbon nanotube reinforced Cu matrix nanocomposites, *Mater. Sci. Eng., A* **430**, 27–33 (2006).

142 S. Arai, T. Saito and M. Endo, Low-Internal-Stress Nickel Multiwalled Carbon Nanotube Composite Electrodeposited from a Sulfamate Bath, *J. Electrochem. Soc.* **154**, D530-D533 (2007).

143 Y. Hwang, A. Neira, T.W. Scharf, J. Tiley and R. Banerjee, Laser-deposited carbon nanotube reinforced nickel matrix composites, *Scripta Mater.* **59**, 487–90 (2008).

144 W.C. Sun, Effects of CNT concentration and heat treatment on micro-hardness of Ni-P-CNTs composite coatings, *Mater. Sci. Forum* **694**, 855-59 (2011).

145 B.M. Praveen, T.V. Venkatesha, Y. Arthoba Naik and K. Prashantha, Corrosion studies of carbon nanotubes–Zn composite coating, *Surf. Coat. Technol.* **201**, 5836-42 (2007).

146 S.M.L. Nai, J. Wei and M. Gupta, Lead-free solder reinforced with multiwalled carbon nanotubes, *J. Elec. Mater.* **35 (7)**, 1518-22 (2006).

147 D. Kaewsai, A. Watcharapasorn , P. Singjai, S. Wirojanupatump, P. Niranatlumpong, S. Jiansirisomboon, Thermal sprayed stainless steel/carbon nanotube composite coatings, *Surf. Coat. Technol.* **205**, 2104–12 (2010).

148 L-X. Pang, K-N. Sun, S Ren, C. Sun, R-H. Fan and Z-H. Lu, Fabrication and microstructure of Fe3Al matrix composite reinforced by carbon nanotube, *Mater. Sci. Engg., A* **447**, 146–49 (2007).

149 Z. Bian, M.X. Pan, Y. Zhang and W.H. Wang, Carbon nanotube reinforced $Zr_{52.5}Cu_{14.6}Al_{10}Ti_5$ bulk metallic glass composites, *Appl. Phys. Lett.* **81 (25),** 4739–41 (2002).

150 L.A. Girifalco, M. Hodak, and R.S. Lee, Carbon nanotubes, buckyballs, ropes, and a universal graphitic potential, *Phys. Rev. B* **62**, 13104-10 (2000).

151 R. Perez-Bustamante, I. Estrada-Guel, W. Antunez-Flores, M. Miki-Yoshida, P.J. Ferreira and R. Martinez-Sanchez, Novel Al-matrix nanocomposites reinforced with multi-wall carbon nanotubes, *J. Alloys Compd.* **450**, 323–26 (2008).

152 L. Jiang, G. Fan, Z. Li, X. Kai, D. Zhang, Z. Chen, S. Humphries, G. Heness and W.Y. Yeung, An approach to the uniform dispersion of a high volume fraction of carbon nanotubes in aluminum powder, *Carbon* **49** 1965-71 (2011).

153 D.A. Mortimer and M. Nicholas, The wetting of carbon by copper and copper alloys, *J. Mater. Sci.* **5**, 149-55 (1970).

154 B.S. Lim, C.J. Kim, B.J. Kim, U.T. Shim, S.Y. Oh, B.H. Sung, J.H. Choi and S.H. Baik, The effects of interfacial bonding on mechanical properties of single-walled carbon nanotube reinforced copper matrix nanocomposites, *Nanotechnology* **17**, 5759–64 (2006).

155 P. Quang, Y.G. Jeong, S.H. Hong and H.S. Kim, Equal channel angular pressing of carbon nanotube reinforced metal matrix nanocomposites, *Key Eng. Mater.* 326-28, 325-28 (2006).

156 A.M.K. Esawi, K. Morsi, A. Sayed, A.A. Gawad and P. Borah, Fabrication and properties of dispersed carbon nanotube–aluminum composites, *Mater. Sci. Eng., A* **508**, 167-173 (2009).

157 P. Quang, Y.G. Jeong, S.C. Yoon, S.H. Hong and H.S. Kima, Consolidation of 1 vol.% carbon nanotube reinforced metal matrix nanocomposites via equal channel angular pressing, *J. Mater. Proc. Technol.* 187–188, 318–332 (2007).

158 H. Uozumi, K. Kobayashi, K. Nakanishi, T. Matsunaga, K. Shinozaki, H. Sakamoto, T. Tsukada, C. Masuda and M. Yoshida, Fabrication process of carbon nanotube/light metal matrix composites by squeeze casting, *Mat. Sci. Eng., A* **495**, 282–87 (2008).

159 K.D. Ausman, R. Piner, O. Lourie, R.S. Ruoff and M. Korobov, Organic Solvent Dispersions of Single-Walled Carbon Nanotubes: Toward Solutions of Pristine Nanotubes, *J. Phys. Chem. B* **104**, 8911-15 (2000).

160 H.T. Ham, Y.S. Choi and I.J. Chung, An explanation of dispersion states of single-walled carbon nanotubes in solvents and aqueous surfactant solutions using solubility parameters, *J. Colloid Interface Sci.* **286**, 216-23 (2005).

161 L. Vaisman, H.D. Wagner and G. Marom, The role of surfactants in dispersion of carbon nanotubes, *Adv. Colloid Interface Sci.* **128–130**, 37–46 (2006).

162 A. Felten, C. Bittencourt, J.J. Pireaux, G. Van Lier, and J. C. Charlier, Radio-frequency plasma functionalization of carbon nanotubes surface O2, NH3, and CF4 treatments, *J. Appl. Phys.* **98**, 074308-1-9 (2005).

163 K.H. An, J.G Heo, K.G Jeon, D.J Bae, C. Jo, C. W Yang, C-Y. Park, Y. H. Lee, Y.S. Lee and Y.S. Chung, X-ray photoemission spectroscopy study of fluorinated single-walled carbon nanotubes, *Appl. Phys. Lett.* **80**, 4235-37 (2002).

164 U. Dettlaff-Weglikowska, J-M. Benoit, P-W. Chiu, R. Graupner, S. Lebedkin and S. Roth, Chemical functionalization of single walled carbon nanotubes, *Curr. Appl. Phys.* **2**, 497–501 (2002).

165 J. Gonález-Julián, P. Miranzo, M.I. Osendi and M. Belmonte, Carbon nanotubes functionalization process for developing ceramic matrix nanocomposites, *J. Mater. Chem.* **21**, 6063-71 (2011).

166 Q. Zeng, Metal coated functionalised single-walled carbon nanotubes for composite applications, PhD thesis, Rice University, 2008

167 Ch. Guiderdoni, C. Estourne`s, A. Peigney, A. Weibel, V. Turq and Ch. Laurent, The preparation of double-walled carbon nanotube/Cu composites by spark plasma sintering, and their hardness and friction properties, *Carbon* **49**, 4535-43 (2011).

168 C. Kim, B. Lim, B. Kim, U. Shim, S. Oh, B. Sung, J. Choi, J. Ki and S. Baik, Strengthening of copper matrix composites by nickel-coated single-walled carbon nanotube reinforcements, *Synthetic Metals* **159**, 424–29 (2009).

169 A. Jitianu, T. Cacciaguerra, R. Benoit, S. Delpeux, F. Béguin and S. Bonnamy, Synthesis and characterization of carbon nanotubes-TiO_2 nanocomposites, *Carbon* **42**, 1147-51 (2004).

170 Y.J. Zhang, Q. Zhang, Y.B. Li, N.L. Wang and J. Zhu, Coating of carbon nanotubes with tungsten by physical vapor deposition, *Solid State Commun.* **115**, 51–55 (2000).

171 S. Dag, E. Durgun and S. Ciraci, High-conducting magnetic nanowires obtained from uniform titanium-covered carbon nanotubes, *Phys. Rev. B* 69, 121407-1-4 (2004).

172 J.D. Kim, B.S. Kang, T.W. Noh, J.G. Yoon, S.I. Baik and Y.W. Kim, Controlling the nanostructure of RuO_2/carbon nanotube composites by gas annealing, *J. Electrochem. Soc.* **152**, 23–25 (2005).

173 Q. Kuang, S-F. Li, Z-X. Xie, S-C. Lin, X-H. Zhang, S-Y. Xie, R-B. Huang and L-S. Zheng, Controllable fabrication of SnO2-coated multiwalled carbon nanotubes by chemical vapor deposition, *Carbon* **44**, 1166–72 (2006).

174 F. Zhao, H. Duan, W. Wang and J. Wang, Synthesis and characterization of magnetic Fe/CNTs composites with controllable Fe nanoparticle concentration, *Physica B* **407**, 2495–99 (2012).

175 B. Liu and J.Y. Lee, Ordered Alignment of CdS Nanocrystals on MWCNTs without Surface Modification, *J. Phys. Chem. B* **109**, 23783-86 (2005).

176 J-H. Nie, C-C. Jia, N. Shi, Y-F. Zhang, Y. Li and X. Jia, Aluminum matrix composites reinforced by molybdenum-coated carbon nanotubes, *IOM*^{3} **18**, 695-702 (2011).

177 N. Junhui, J. Xian, J. Chengchang, L. Yi, Z. Yafeng, and S. Na, Friction and wear properties of copper matrix composites reinforced by tungsten- coated carbon nanotubes, *Rare metals* **30**, 657-63 (2011).

178 K.T. Kim, S.I. Cha, T. Gemming, J. Eckert and S. H. Hong, The Role of Interfacial Oxygen Atoms in the Enhanced Mechanical Properties of Carbon-Nanotube-Reinforced Metal Matrix Nanocomposites, *Small* **4(11)**, 1936-40 (2008).

179 S.I. Cha, K.T. Kim, S.N. Arshad, C.B. Mo, K.H. Lee and S.H. Hong, Field-Emission Behavior of a Carbon-Nanotube-Implanted Co Nanocomposite Fabricated from Pearl-Necklace-Structured Carbon Nanotube/Co Powders, *Adv. Mater.* **18**, 553-58 (2006).

180 W.X. Chen, J.Y. Lee and Z. Liu, The nanocomposites of carbon nanotube with Sb and $SnSb_{0.5}$ as Li-ion battery anodes, *Carbon* **41**, 959–66 (2003).

181 J.J. Petrovic, J.V. Milewski, D.L. Rohr and F.D. Gac, Tensile mechanical properties of SiC whiskers, *J. Mater. Sci.* **20**, 1167-77 (1985).

182 D. Jianxin, L. Lili, L. Jianhua, Z. Jinlong and Y. Xuefeng, Failure mechanisms of TiB_2 particle and SiC whisker reinforced Al_2O_3 ceramic cutting tools when machining nickel-based alloys, *Inter. J. Machine Tools and Manufacture* 45, 1393–1401 (2005).

183 A.C. Solomah and W. Reichert, Mechanical properties, thermal shock resistance and thermal stability of zirconia-toughened alumina-10 vol% silicon carbide whisker ceramic matrix composite, *J. Am. Ceram. Soc.* **73 (3)**, 740-743 (1990).

184 S.R. Nutt, P. Lipetzky and P.F. Becher, Creep Deformation of Alumina-SiC Composites, *Mater. Sci. Eng., A* 126, 165 - 72 (1990).

185 V. Garnier, G. Fantozzi, D. Nguyen, J. Dubois and G. Thollet, Influence of SiC whisker morphology and nature of SiC/Al2O3 interface on thermomechanical properties of SiC reinforced Al2O3 composites, *J. Am. Ceram. Soc.* **25**, 3485-93 (2005).

186 M. Ruehle, B.J. Dalglesish and A.G. Evans, On the toughening of ceramics by whiskers, *Scripta Metallur.* **21**, 681-86 (1987).

187 P.F. Becher, C.H. Hsueh, P. Angelini and T.N. Tiegs, Theoretical and experimental analysis of the toughening behaviour of whisker reinforcement in ceramic matrix composites, *Mat. Sci. Eng., A* **107**, 257-59 (1989).

188 G.H. Campbell, M. Rühle, B.J. Dalgleish, A.G. Evans, Whisker Toughening: A Comparison Between Aluminum Oxide and Silicon Nitride Toughened with Silicon Carbide, *J. Am. Ceram. Soc.***73[3]**, 521–30 (1990).

189 P.F. Becher, C-H. Hsueh, P. Angelini and T.N. Tiegs, Toughening Behavior in Whisker-Reinforced Ceramic Matrix Composites, *J. Am. Ceram. Soc.* **71[12]**, 1050–61 (1988).

190 A.C. Solomah, W. Reichert, V. Rondinella, L. Esposito and E. Toscano, Mechanical Properties, Thermal Shock Resistance, and Thermal Stability of Zirconia-Toughened Alumina-10 vol% Silicon Carbide Whisker Ceramic Matrix Composite, *J. Am. Ceram. Soc.* **73[3],** 740–43 (1990).

191 P. Go, C. Sung, J.J. Kostetsky and T. Vasilos, Silicon nitride matrix composites with unidirectional silicon carbide whisker reinforcement, *J. Mater. Sci.* **37**, 2587-90 (2002).

192 R.J. Arsenault, L. Wang and C.R. Feng, Strengthening of composites due to microstructural changes in the matrix, *Acta Metall. Mater.* **39**, 47–57 (1991).

193 B-C. Ko and Y-C. Yoo, The effect of aging treatment on the microstructure and mechanical properties of AA2124 hybrid composites reinforced with both SiC whiskers and SiC particles, *Comp. Sci. Technol.* **59**, 775-79 (1999).

194 K. Ohori, H. Watanabe and Y. Takeuchi, Silicon carbide whisker reinforced aluminium composites-fabrication and properties, *Mater. Sci. and Tech.* **3**, 57-60 (1987).

195 W. Zhang, D. Wang, Z. Yao and M. Gu, Microstructural evolution in Cold-Rolled Squeeze Cast SiC_w/Al composites during annealing, *J. Mater. Sci. Tech.* **20**, 318-22 (2004).

196 Y. Iwai, H. Yoneda and T. Honda, Sliding wear behavior of Sic whisker-reinforced aluminium composite, *Wear* **181-83**, 594-602 (1995).

197 Y. Chen and D.D.L. Chung, Aluminium-matrix silicon carbide whisker composites fabricated by pressureless infiltration, *J. Mater. Sci.* **31**, 407-12 (1996).

198 S-Y. Chang, K-S. Lee, S K. Ryu, K-T. Park and D.H. Shin, Effect of Equal Channel Angular Pressing on the Distribution of Reinforcements in the Discontinuous Metal Matrix Composites, *Mater. Trans.* **43[4]**, 757-61 (2002).

199 D.F. Hasson, S.M. Hoover and C.R. Crowe, Effect of thermal treatment on the mechanical and toughness properties of extruded SiC_w/aluminium 6061 metal matrix composites, *J. Mater. Sci.* **20**, 4147-54 (1985).

200 M. Zheng, K. Wu and C. Yao, Effect of interfacial reaction on mechanical behavior of SiCw/AZ91 magnesium matrix composites, *Mat. Sci. and Engg A* **318**, 50–56 (2001).

201 Y. Feng, X. Zhou, Z. Min and W. Kun, Superplasticity and texture of SiC whiskers in a magnesium-based composite, *Scripta Mater.* **53**, 361-65 (2005).

202 Y. Chen and D.D.L. Chung, Brass-matrix silicon carbide whisker composites prepared by powder metallurgy, *J. Mater. Sci.* **34**, 359-64 (1999).

203 C. Schuh and D.C. Dunand, Load transfer during transformation superplasticity of Ti-6Al-4V/ TiB whisker reinforced composites, *Scripta Mater.* **45**, 631-38 (2001).

204 V.S.R. Murthy, K. Srikanth and C.B. Raju, Abrasive wear behaviour of SiC whisker-reinforced silicate matrix composites, *Wear* **223**, 79–92 (1998).

205 C. Poletti, M. Balog, T. Schubert, V. Liedtke, C. Edtmaier, Production of titanium matrix composites reinforced with SiC particles, *Compos. Sci. Technol.* **68**, 2171–77 (2008).

206 N.J. Fei, L. Katgerman, W.H. Kool, Production of SiC particulate reinforced aluminium composites by melt spinning, *J. Mater. Sci.* **29[24]**, 6439-44 (1994).

207 R.M. Aikin. Jr, The Mechanical Properties of In-Situ Composites, *JOM* **49 [8]**, 35-39 (1997).

208 C.Sun, M. Song, Z. Wang, Y.He, Effect of Particle Size on the Microstructures and Mechanical Properties of SiC-Reinforced Pure Aluminum Composites, *J. Mater. Eng. Perform.* **20[9]**, 1606-12 (2011)

209 B. Inem and G. Pollard, Interface structure and fractography of a magnesium-alloy, metal-matrix composite reinforced with SiC particles, *J. Mater. Sci.* **28[16]**, 4427-4434 (1993).

210 M.S.B. Selamat, L.M.Watson and T.N.Baker, XRD and XPS studies on surface MMC layer of SiC reinforced Ti–6Al–4V alloy, *J. Mat. Proc. Tech.* **142**, 725-737 (2003).

211 M. Lei and H. Ledbetter, "Communications: elastic constants of SiCp/Al: measurements and modeling", *Metall. Mater. Trans.* **25A**, 2832-2835 (1994).

212 M. Manoharan and J.J Lewandowski, Crack initiation and growth toughness of an aluminium metal matrix composite, *Acta Metall. Mater.* **38**, 489-496 (1990).

213 J. Yang, C. Cady, M.S. Hu, F. Zok, R. Mehrabian and A.G Evans, Effects of damage on the flow strength and ductility of a ductile Al alloy reinforced with SiC particulates, *Acta Metall. Mater.* **38**, 2613-19 (1990).

214 T.W. Clyne, Metal Matrix Composites: Matrices and Processing in Encyclopaedia of Materials: Science and Technology,§3.7.12 "Composites: MMC, CMC, PMC", Mortensen, A. (ed.), Elsevier (2001).

215 T.W. Clyne and F.R Jones, Composites: Interfaces in Encyclopaedia of Materials: Science and Technology,*§*3.7.17 "Composites: MMC, CMC, PMC", Mortensen, A. (ed.), Elsevier (2001)

216 S. Ochiai and K. Osamura, Influences of matrix ductility, interfacial bonding strength, and fiber volume fraction on tensile strength of unidirectional metal matrix composite, *Metall. Trans. A* **21**, 971-77 (1990)

217 S.J. Sun and M.D. Zhang, Interface characteristics and mechanical properties of carbon fibre reinforced copper composites, *J. Mater. Sci.* **26**, 5762–66 (1991).

218 V. Garibay-Febles, H. A. Calderon, F. C. Robles-Hernández, M. Umemoto and K. Masuyama, J. G. Cabañas-Moreno, Production and Characterization of (Al, Fe)-C (Graphite or Fullerene) Composites Prepared by Mechanical Alloying, *Mater. Manuf. Processes* **15[4]**, 547-67 (2000).

219 R.B. Bhagat, Growth kinetics of interface intermetallic compounds in stainless steel fibre reinforced aluminium matrix composites, *J. Mater. Sci.* **24[4]**, 1496-502 (1989).

220 X. Zhang, G. Lu, M.J. Hoffmann and R. Metselaar, Properties and Interface Structures of Ni and Ni-Ti Alloy Toughened A1203 Ceramic Composites, *J. Euro. Ceram. Soc.***15**, 225-32 (1995).

221 L. Ci, Z. Ryu, N-Y. Jin-Phillipp and M. Rühle, Investigation of the interfacial reaction between multi-walled carbon nanotubes and aluminium, *Acta Mater.* **54**, 5367-75 (2006).

222 K. Kondoh, T. Threrujirapapong, H. Imai, J. Umeda, and B. Fugetsu, CNTs/TiC Reinforced Titanium Matrix Nanocomposites via Powder Metallurgy and Its Microstructural and Mechanical Properties, *J. of Nanomaterials* **2008**, Article ID 127538, 4 pages, (2008).

223 H. Fukuda, K. Kondoh, J. Umeda and B. Fugetsu, Fabrication of magnesium based composites reinforced with carbon nanotubes having superior mechanical properties, *Mater. Chem. Phys.* **127**, 451-58 (2011).

224 G. Requena, D. Telfser, C. Hörist, H.P. Degischer, Creep behaviour of AA 6061 metal matrix composite alloy and AA 6061, *Mater. Sci. Technol.* **18[5]**, 515-521(2002)

225 Y. Tang, L. Liu, W. Li, B. Shen and W. Hu, Interface characteristics and mechanical properties of short carbon fibers/Al composites with different coatings, *Appl. Surf. Sci.* **255**, 4393–400 (2009).

226 T.P.D. Rajan, R.M. Pillai, B.C. Pai, Reinforcement coatings and interfaces in aluminium metal matrix composites, *J. Mater. Sci.* **33**, 3491-503 (1998).

227 A. Brenner and G.E. Riddell, *Proc. Amer. Electroplaters Soc.* **33**, p16 (1946).

228 A. Brenner and G.E. Riddell, *J. Res. Nat. Bus. Stand.* **39**, 385-395 (1946).

229 P. Sahoo and S.K. Das, Tribology of electroless nickel coatings – A review, *Mater. Des.* **32**, 1760–75 (2011).

230 G.O. Mallory and J.B. Hadju, Electroless plating: fundamentals and applications. Orlando: AESF; 1991.

231 W. Riedel, Electroless Nickel Plating, ASM International, Metals Park, Ohio, and Finishing Publications Ltd, Stevenage, England, 1991

232 J. R. Henry, Electroless (Autocatalytic) Plating. WEAR-COTE International, Rock Island, Ill.; www.wear-cote.com

233 L.M. Ang, T.S.A. Hor, G.Q. Xu, C.H. Tung, S.P. Zhao and J.L.S. Wang, Electroless Plating of Metals onto Carbon Nanotubes Activated by a Single-Step Activation Method, *Chem. Mater.* **11**, 2115-18 (1999).

234 L.M. Ang, T.S.A. Hor, G.Q. Xu, C.H. Tung, S.P. Zhao and J.L.S. Wang, Decoration of activated carbon nanotubes with copper and nickel, *Carbon* **38**, 363–72 (2000).

235 N.B. Baba, W. Waugh and A.M. Davidson, Manufacture of Electroless Nickel/YSZ Composite Coatings, *World Academy of Sci. Engg. and Tech.* **49**, 715-20 (2009).

236 J.T. Jiang, L. Zhen, C.Y. Xu and W.Z. Shao, Microstructure evolution of cobalt coating electroless plated on SiC whisker during electroless plating and heat treatment, *Surf. Coat. Technol.* **201**, 6059–62 (2007).

237 L. Wilson, E.E. Kalu, L. Martin and M.E. McHenry, Decoration of carbon nanotubes with iron–cobalt (FeCo) alloy using polymer-stabilization and electroless deposition techniques for thermotherapy applications, *J. Mater. Chem.* **22**, 595–601 (2012).

238 X. Chen, J. Xia, J. Peng, W. Li and S. Xie, Carbon-nanotube metal-matrix composites prepared by electroless plating, *Comp. Sci. Techol.* **60**, 301-306 (2000).

239 Q. Li, S. Fan, W. Han, C. Sun and W. Liang, Coating of Carbon Nanotube with Nickel by Electroless Plating Method, *Jpn. J. Appl. Phys.* **36**, L501-L503 (1997).

240 Y. Feng and H. Yuan, Electroless plating of carbon nanotubes with silver, *J. Mater. Sci.* **39**, 3241-43 (2004).

241 Q. Zeng, J. Luna, Y. Bayazitoglu, K. Wilson, M. Aimam and E.V. Barrera, Metal coated functionalised single-walled carbon nanotubes for composite application, *Mater. Sci. Forum* **561-565**, 655-658 (2007).

242 W. Li, H. Jin, Y. Hao, T. Chen, J. Dai, and Q. Wang, The Microstructure of Ni Layer on Single-Walled Carbon Nanotubes Prepared by an Electroless Coating Process, *J. of Nanomater.* **2011**, 1-5 (2010).

243 F. Wang, S. Arai and M. Endo, The preparation of multi-walled carbon nanotubes with a Ni–P coating by an electroless deposition process, *Carbon* **43**, 1716-21 (2005).

244 D-L. Zhao, X. Li, Z-M. Shen, Microwave absorbing property and complex permittivity and permeability of epoxy composites containing Ni-coated and Ag filled carbon nanotubes, *Comp. Sci. Technol.* **68**, 2902–08 (2008).

245 S. Arai, M. Kobayashi, T. Yamamoto and M. Endo, Pure-Nickel-Coated Multiwalled Carbon Nanotubes Prepared by Electroless Deposition, *Electrochem. Solid-State Lett.* **13[12]**, D94-D96 (2010).

246 W.M. Daoush, B.K. Lim, C.B. Mo, D.H. Nam and S.H. Hong, Electrical and mechanical properties of carbon nanotube reinforced copper nanocomposites fabricated by electroless deposition process, *Mater. Sci. Eng., A* **513–514**, 247–253 (2009).

247 Y. Peng and Q. Chen, Ultrasonic-assisted fabrication of highly dispersed copper/multi-walled carbon nanotube nanowires, *Colloids Surf., A* **342**, 132–35 (2009).

248 W. Lü, X. Ma, N. Lun and S. Wen, Decoration of carbon nanotubes with gold nanoparticles for catalytic applications, *MRS Symp. Proc.* **820**, 75-80 (2004).

249 R-J. Xue and Y-C. Wu, Mechanism and Microstructure of Electroless Ni-Fe-P Plating on CNTs, *J China Univ Mining and Technol*, **17[3]**, 424-27 (2007).

250 M. Alishahi, S.M. Monirvaghefi, A Saatchi and S.M Hosseini, The effect of carbon nanotubes on the corrosion and tribological behavior of electroless Ni–P–CNT composite coating, *Appl. Surf. Sci.* **258**, 2439-46 (2011).

251 T. Li, S. Qu, Z. Li, W. Tao, M. Wang, Investigation of the mechanical properties of the Ni–P–CNTs coated copper composite materials: Experiments and modelling, *Mater. Sci. and Engg. A* **500**, 182–87 (2009).

252 X.Q. Wang, M. Wang, Z.H. Li, H.B. Zhu, F.F. Wang, S.L. He, B.X. Han and P.M. He, Synthesis and the performance of carbon nanotubes-(Ni-P) composites, *Acta Materiae Compositae Sinica* **20**, 142–46 (2003).

253 F-H. Wang, T-C. Lin, S-D. Tzeng and C-T. Chou, Field emission properties of carbon nanotube cathodes produced using composite plating, *Appl. Surf. Sci.* **256**, 7600-05 (2010).

254 W. Yucheng, R. Rong, W. Fengtao, Y. Zaoshi, W. Tugen and H. Xiaoye, Preparation and characterization of Ni–Cu–P/CNTs quaternary electroless composite coating, *Mater. Res. Bull.* **43**, 3425-32 (2008).

255 S-Y. Chang and S-J. Lin, Fabrication of SiC_w reinforced copper matrix composite by electroless copper plating, *Scripta Mater.* **35[2]**, 225-31 (1996).

256 P. Yih and D.D.L Chung, Silicon carbide whisker copper-matrix composites fabricated by hot pressing copper coated whiskers, *J. Mater. Sci.* **31**, 399-406 (1996).

257 Y. Jin and L. Hua, Preparation and tribological properties of Ni-P electroless composite coating containing Potassium Titanate whisker, *J. Mater. Sci. Technol.* **23[3]**, 387-91 (2007).

Chapter 3
Experimental Procedure

3.1 Introduction

This chapter outlines the procedure employed to prepare Fe-Co materials with and without SiC particulates, whiskers and carbon nanotubes by spark plasma sintering and for their characterisation. The methodologies are described under five different sections: electroless plating of fillers and their characterisation, characterisation of matrix alloy powder, mixing of coated and uncoated fillers with Fe-Co, spark plasma sintering of monolithic and composite materials and the magnetic and mechanical testing of the compacts.

The methods followed to decorate SiC particulates, SiC whisker and CNTs with copper, Ni-P, cobalt and duplex (Ni-P and copper) layers by electroless plating and the details of the equipment used to characterise the plated particles are discussed in the first section.

In the second section, the characterisation details of the as-received Fe-Co alloy particles are explained.

In section three, the process of dispersing the coated and uncoated filler materials with Fe-Co powder is explained in greater detail, as it varied with the type of fillers.

In the following section, the trials performed on the compaction of unreinforced Fe-Co alloy by varying the sintering parameters such as temperature, pressure and time to find the optimum sintering conditions for the composite fabrication are delineated. This section also explains the details of the additional compacts prepared without any filler materials to study the influence of other possible sintering variables such as heating rate, cooling rate, temperature at which the pressure was applied and released, magnetic behaviour (sintering around the Curie temperature of the material) and post heat treatments on final magnetic properties of Fe-Co alloy.

The structural, magnetic and mechanical characterisation details of all the compact materials are delineated in the final part of this chapter.

3.2 Electroless plating of fillers and their characterisation

3.2.1 Electroless plating of SiC particles and whiskers

3.2.1.1 Pre-treatments

The SiC particles and whiskers were purchased from Goodfellow Cambridge Ltd., UK. The average size of SiC particles as declared by the supplier was 20 µm. The diameter

and length of SiC whiskers, as stated by the provider were 0.45-0.65 and 5-80 μm respectively.

The SiC fillers were thoroughly cleaned in acetone under ultrasonic agitation for 15 minutes. They were etched with 16M nitric acid solution for 15 minutes under ultrasonic agitation to roughen the particle surface. The surface roughness was believed to help to achieve more uniform electroless coating by fixing more catalytic species on the particle's surface in the subsequent pre-treatment steps and to improve coating adherence. After acid treatment, the fillers were thoroughly washed with de-ionised water (5-6 times) until the pH of water read 7.0. The pH of all the solutions used in this research were measured using a pocket pH Tester fabricated by Oakton Instruments with 0.1 pH resolution. The pH meter was calibrated under National Institute of Standards and Technology (NIST) buffer set standard using 6.86, 4.01, 9.18 buffer solutions. The SiC particles were allowed to settle under gravity, separated and dried. The SiC whiskers, being finer than SiC particles, posed problems during separation by suspending in the solution. The SiC whiskers were separated from the solution by centrifuging the suspension for 10 minutes at 3000 rpm with a Heraeus Varifuge 3.0 centrifuge, which could house 15 ml test tubes (48 nos.) and 50 ml test tubes (8 nos.). The washing and centrifugation were repeated until the pH of the colloid read 7.0.

The etched fillers were treated with sensitisation solution containing 2 g of $SnCl_2$. H_2O in 4 ml of HCl + 100 ml of de-ionised water under magnetic stirring for 30 minutes at room temperature to introduce Sn atoms on the ceramic particle surface. The particles and whiskers were then washed thoroughly in de-ionised water until the pH of the water read 7 as discussed above. The particles with a Sn layer were dried and introduced into an activation bath containing 0.025 g of $PdCl_2$ in 0.25 ml of HCl+100 ml of de-ionised water and magnetically stirred for 30 minutes at room temperature. The particles were washed four times and dried. The whiskers were washed until the pH value became neutral and dried in an oven at 70^oC for 24 hrs under atmospheric conditions. Around 200 ml and 600 ml of sensitisation and activation solutions were used to treat 5.0 g of SiC particles and 2.0 g of SiC whiskers respectively.

A schematic diagram summarising the key pre-treatment steps for the electroless plating of SiC particles and whiskers is shown in Fig. 3.1

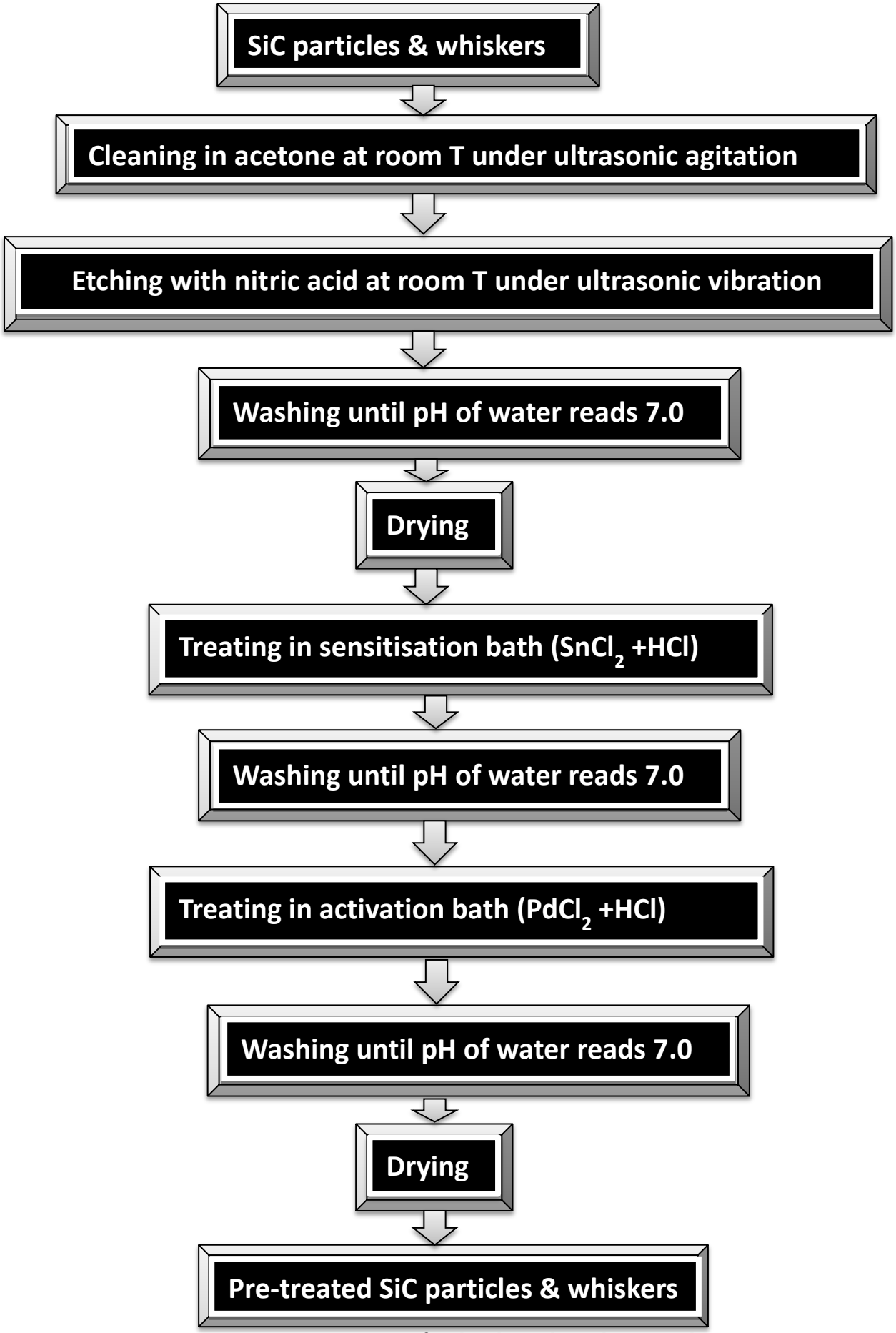

Fig. 3.1 Key pre-treatment steps for the electroless plating (Schematic)

3.2.1.2 Electroless copper plating of SiC particles

The copper plating bath was prepared by mixing a metallic ion source (copper sulphate), reducing agent (formaldehyde), complexing agent (sodium potassium tartrate or Rochelle salt) and alkalinity reserve (sodium hydroxide) in de-ionised water [1]. The procedure for the preparation is outlined below,

(i) About 3.6 g of $CuSO_4.5H_2O$ and 9.6 g of sodium potassium tartrate were taken separately in two different beakers each containing 100 ml of de-ionised water. The solutions were ultrasonically agitated until the salt dissolved completely in both the beakers.

(ii) The salt solutions were mixed together and ultrasonically agitated for 10 minutes.

(iii) Formaldehyde (4 ml) was added to the mixture and thoroughly blended.

(iv) Conc. sodium hydroxide solution, prepared by dissolving sodium hydroxide pellets in a small amount of de-ionised water, was added in drops to the mixture until the pH of the solution read 12.5.

About 2.4 g of catalyst solution treated particles was added into 200 ml of plating bath. The bath was continuously stirred using a magnetic stirrer at 300 rpm. The commencement of plating reactions was identified by the sharp change of solution colour from blue to dark black. The plating time was counted from the moment the colour changed. The particles were plated for 5 minutes, washed with de-ionised water 3 times and dried in an oven at 100^oC.

3.2.1.3 Electroless cobalt plating of SiC particles

The cobalt plating bath was prepared by mixing metallic ion source (cobalt (II) sulphate), reducing agent (sodium hypophosphite), complexing agent (tri-sodium citrate), stabilizer (Boric acid) and alkalinity reserve (sodium hydroxide) in de-ionised water [2].

(i) About 5.0 g of $CoSO_4{\cdot}7H_2O$ and 5.0 g of sodium phosphite ($NaH_2PO_2.H_2O$), 10.0 g of tri-sodium citrate ($Na_3C_6H_5O_7.H_2O$) and 5.0 g of boric acid were taken separately in two different beakers each containing 100 ml of de-ionised water. The solutions were ultrasonically agitated until the salts dissolved completely in both the beakers.

(ii) The salt solutions were mixed together and ultrasonically agitated for 10 minutes.

(iii) Conc. sodium hydroxide solution, which was prepared by dissolving sodium hydroxide pellets in de-ionised water, was added in drops to the mixture until the pH of the solution read 9.2.

The cobalt plating bath was heated to 55 ^{o}C and agitated using a magnetic stirrer with heater. After adding the catalyst solution treated particles in the plating bath, the commencement of the plating reaction was marked by the change in the solution colour from violet to dark black. The plating time, which was counted from the moment the colour changed, was 30 minutes. The cobalt coated particles, being magnetic, were attracted towards the stir bar when the stirrer was turned off. The coated particles were collected, washed and dried.

3.2.1.4 Electroless Ni-P plating of SiC particles using an acidic bath

About 1.2 g of sensitised and activated SiC particles were added in 100 ml of magnetically stirred electroless nickel plating solution (formulated by M/s Schlötter Chemical technology under the tradename Slotonip 1850) maintained at 85^{o}C. The commencement of the plating reaction was marked by vigorous bubbling. After plating the particles for 10.0 minutes, the solution with coated particles was poured into de-ionised water to arrest the reaction. The coated particles that settled at the bottom were filtered and washed thoroughly in de-ionised water. The particles were dried at 100^{o}C for 10 minutes in an oven.

3.2.1.5 Electroless Ni-P plating of SiC particles using an alkaline bath

The Ni plating bath was prepared by dissolving nickel sulphate, sodium hypophosphite, tri-sodium citrate and ammonium hydroxide in de-ionised water [3]. The preparation procedure is outlined below,

(i) About 4.0 g of $NiSO_4{\cdot}7H_2O$ and 6.0 g of sodium phosphite ($NaH_2PO_2.H_2O$), 2.0 g of tri-sodium citrate ($Na_3C_6H_5O_7.H_2O$) and 6.0 g of ammonium chloride were taken separately in two different beakers, each containing 100 ml of de-ionised water. The solutions were ultrasonically agitated until the salts in both the beakers were dissolved completely.

(ii) The salt solutions were mixed together and ultrasonically agitated for 10 minutes. The pH meter displayed 5.2 for the mixture.

(iii) Ammonium hydroxide (2.0 M ammonia water) was added in drops to the mixture until the pH of the solution surge to 8.6.

The pre-treated SiC particles (1.2 g) were added to the plating bath maintained at 50^{o}C and agitated magnetically using a hot plate/magnetic stirrer. The commencement of the plating was marked by vigorous bubbling. The plating was done for 10 minutes and the plated particles were washed and dried.

3.2.1.6 Electroless Ni-P plating on Cu plated particles (duplex plating)

About 1.2 g of copper coated SiC particles were added in 100 ml of Slotonip 1850 nickel plating solution maintained at 85^{o}C and magnetically stirred at 300 rpm. The plating, which started instantly with effervescence, was performed for 10 minutes. The coated sediment was washed thoroughly in de-ionised water and dried.

3.2.1.7 Electroless copper plating of SiC whiskers

The plating solution was prepared as described above for SiC particles. The catalyst solution treated SiC whiskers (0.08g) were placed in a small beaker with 10 ml of de-ionised water and ultrasonically stirred to disperse them. The suspension was poured into 200 ml of Cu plating bath, which was stirred by a magnetic stirrer at 300 rpm. On adding the whiskers, the solution turned milky blue. The commencement of plating was marked by a sharp colour change to deep blue. After plating for 10 minutes, the turbid bath with coated SiC whisker was poured into a beaker containing de-ionised water. The coated SiC whiskers were collected, washed 3 times in de-ionised water and dried in an oven at 80^{o}C under atmospheric conditions overnight. The same procedure was repeated to plate 0.16 and 0.4 g of SiC whiskers in 400 ml and 300 ml of plating bath respectively. Only 300 ml of plating solution was used to plate the latter large quantity of whiskers in order to reduce the amount of copper deposited on the whisker surface. This will reduce the amount of copper introduced into the composite. The 0.4 g of whiskers that was coated with copper was divided in a ratio of 2:3 to prepare composites with 2 and 3 vol % of copper coated whiskers respectively.

3.2.1.8 Electroless Ni-P plating of SiC whiskers

About 200, 500 and 300 ml of alkaline Ni plating baths were prepared as discussed before for SiC particles to plate 0.08, 0.16 and 0.4 g of pre-treated SiC whiskers, respectively. The solution became milky green on addition of SiC whiskers and turned into grey colour with effervescence once the reaction started. The whiskers were plated at 50^{o}C under magnetic stirring to ensure uniform supply of Ni^{+} ions near the catalytic surface. The plated whiskers were filtered, washed and dried as explained before. As mentioned for Cu coated whiskers, the 0.4 g of Ni-P plated whiskers was coated and divided in a ratio of 2 to 3 to prepare the respective composites.

3.2.1.9 Electroless cobalt plating of SiC whiskers

About 200, 400 and 300 ml of Co plating bath was made to treat 0.08, 0.16, 0.24 g of SiC whiskers. This electroless plating was performed for 30 minutes at 50^{o}C under magnetic stirring. The bubbling during Co plating was less vigorous than Cu and Ni plating and was

continuous for long time. This was due to the lesser plating rate of cobalt over the other two coatings.

3.2.2 Electroless plating of CNTs

The oxygen functionalised multi-walled CNTs were supplied by M/s Haydale Ltd, U.K.

3.2.2.1 Pre-treatments

About 1.5 g of CNTs were treated in 600 ml of palladium and tin colloidal catalyst solution (Tradename: UNIPHASE PHP) supplied by M/s Schlötter Chemical Technology under ultrasonic agitation at 35^{o}C to impart nucleation sites. The catalyst solution with CNTs was sonicated with a Vibra-Cell™ VCX 750 ultrasonic probe purchased from JENCONS, a VWR Division, to disperse the CNTs. The CNTs were then washed thoroughly with de-ionised water until the pH of water reads 7.0. In contrast to conventional catalytic treatment involving two steps, Pd centres can be introduced on CNTs in a single step with Uniphase solution. Similar in the case of SiC whiskers, the suspension problem because of the low density of CNTs (~ 1.3-1.4 g cm^{-3}) was overcome by centrifugation. The pre-treated CNTs were dried in an oven for 24 hrs at 70 ^{o}C.

3.2.2.2 Electroless Ni-P plating of CNTs

The alkaline Ni-P electroless plating baths were prepared as explained for SiC particles; the pre-treated CNTs were plated at 40^{o}C for 10 minutes under ultrasonic agitation. The plated CNTs were washed thoroughly in de-ionised water and were separated by centrifugation. The resulting wet CNTs were dried in an oven with ethanol for 24 hrs at 70 ^{o}C in atmospheric condition.

3.2.3 Characterisation of as-received and coated fillers

3.2.3.1 Morphological and spectroscopic studies

The surface morphology and chemical composition of the plated particles and fibers were examined using a scanning electron microscope (supplied by Nanotechnology Systems, Carl Zeiss) with an EDX attachment (supplied by Oxford Instruments).

The plated particles and fibers were sprinkled/spread on carbon adhesive tapes, which were stuck to a 12.5 mm diameter aluminium stubs. The uncoated SiC particles and whiskers were coated with a layer of carbon to avoid charge build-up during analysis. The aluminium stubs containing the particles were introduced into the SEM system and were exposed to a beam of high energy electrons from a field emission gun (FEG), which comprises of a very

fine single crystal of tungsten. The secondary electrons emitted as a result of electron-sample interaction were used to obtain the topographical information. The X-ray photons emitted from the selected area of the sample were analysed by a liquid nitrogen cooled Si-Li detector in the EDX arrangement to get spectroscopic details.

The number of walls, wall thickness and morphology of the as-received CNTs and coating thickness of the plated ones were characterised using a high resolution JEM-2100 LaB6 Transmission Electron Microscope. The composition analysis of the coating was performed using an EDS NanoAnalysis attachment (X-max) with INCA software supplied by Oxford instruments.

3.2.3.2 Phase characterisation of the coatings

The diffraction study was performed on the coated and uncoated SiC particles and CNTs to acquire information about the phases present in the coating. The analysis was carried out with a monochromatic radiation of Cu K_α ($\lambda = 0.154$ nm) using an X-ray diffractometer (PANalytical, XPERT Pro) operated at a voltage and current of 40 kV and 40 mA respectively. All the samples were scanned at the rate of 0.5 $^o2\theta$/min for the 2θ values range between 30° and 90°. The diffractograms obtained were compared with the known patterns in the Joint Committee on Powder Diffraction Standards (JCPDS) database to determine the crystallographic phases present in the coatings.

3.2.3.3 Raman spectroscopy of as-received and coated CNTs

The as-received multi-walled carbon nanotubes in the untreated and oxygen plasma functionalised states and the electroless Ni-P plated CNTs were studied using a Renishaw inVia Raman microscope to assess their quality. The carbonaceous samples were excited with a 514 nm argon laser with the power and spot size maintained at 12.5 mW and 5 µm, respectively. The Raman spectra spanning between 100 and 3200 cm^{-1} was obtained three times for each sample after 15 accumulations.

3.2.3.4 Thermal stability of Ni-P plated CNTs

The thermal stability of Ni-P plated CNTs was assessed by recording the heat flow and weight loss of the material using an integrated differential scanning calorimeter and thermogravimetric analyser (Perkin Elmer TGA/DTA/DSC 7). The characterisation was performed by heating 60 mg of plated nanotubes from 30 to 900^{o}C in an alumina crucible at the rate of 10^{o}C/min in N_2 atmosphere.

3.3 Characterisation of Fe-Co alloy powders

Gas atomised Fe-50%Co-0.2% Si powder with average particle size of 9.5- 11 microns (as defined by the supplier) was obtained from Sandvik Osprey Powder group.

3.3.1 Density measurements

The density of Fe-Co powders was measured using the AccuPyc II 1340 gas displacement density analyzer supplied by Micromeritics Instrument Corporation. The schematic of the gas pycnometer instrument is shown in Fig. 3.2.

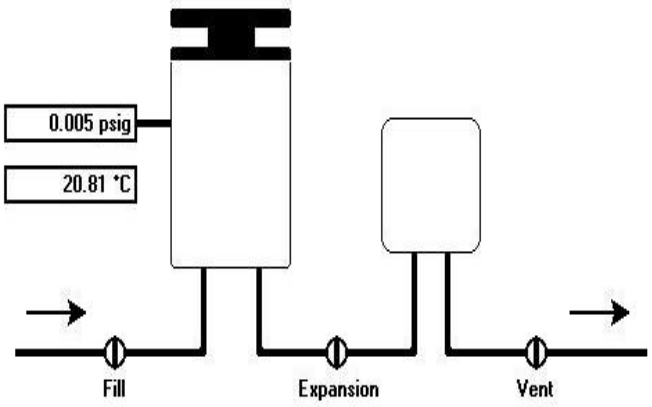

Fig. 3.2 Schematic of helium pycnometer

The gas pycnometer consists of two chambers - one with a removable gas tight lid and second with a fixed, known internal volume. The density was calculated by measuring the volume of helium gas displaced by the known mass of the powder present in the first chamber to the adjustant chamber. The density measurements were repeated ten times by a set program and the average and standard deviation values were reported.

3.3.2 Confirmatory test for chemical composition of matrix powder

The elemental composition of the starting powder was confirmed using Inductively Coupled Plasma Optical Emission Spectroscopy (ICP-OES analysis). The analysis was performed by the chemical analysis team at Ceram Research Limited, Staffordshire, U.K. About 1 g of the powder sample was treated with 12 ml of aqua regia and 2 ml of hydrofluoric acid to ensure the dissolution of silicon and rare earth elements, if any were present. The solution samples were introduced into the plasma in a process that desolates, ionises, and excites them. The constituent elements were identified by their characteristic emission lines, and quantified by the intensity of the lines.

3.3.3 Particle size distribution

The size distribution of the Fe-Co powder was measured using Malvern Mastersizer 3000 laser diffraction particle size analyzer. The working principle of the Mastersizer is schematically shown in Fig. 3.3. The powder was dispersed in de-ionised water using the Hydro EV dispersion unit attached to the system, which has a dip-in centrifugal pump and a stirrer. A laser beam was passed through the dispersed particulate sample and the size distribution of the particles was calculated by the Mastersizer 3000 software from the resulting diffraction pattern. The particle refractive index and absorption index entered in the program for analysing the Fe-Co powder were 2.3 and 0.1 respectively.

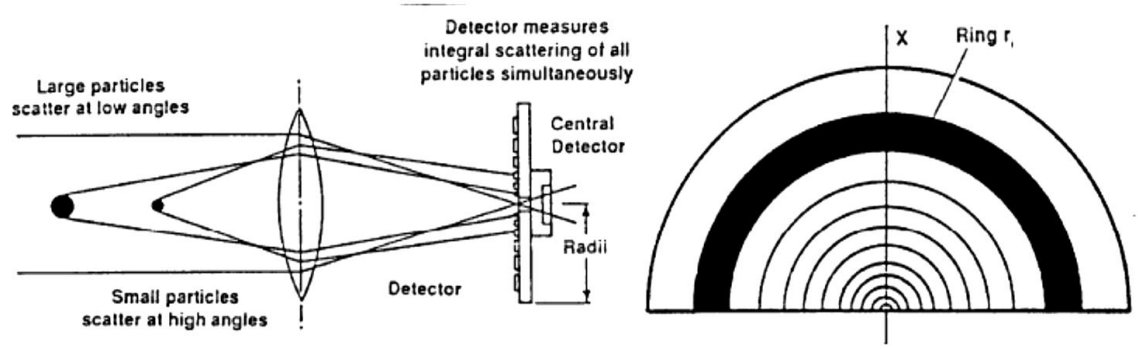

Fig. 3.3 Working principle of Malvern Mastersizer (Schematic)

3.3.4 Morphological characterisation

The size, shape and size distribution of the as-procured powder were examined using a scanning electron microscope (supplied by Nanotechnology Systems, Carl Zeiss).

3.3.5 Thermal analysis

The phase transitions of the Fe-Co powder in the temperature range of 30-1050^{o}C were studied using a differential scanning calorimeter (Perkin Elmer TGA/DTA/DSC 7). Analysis was carried out by heating and cooling 145 mg of Fe-Co powder in an alumina crucible at the rate of 5 and 10^{o}C/min in N_2 atmosphere.

3.4 Mixing of coated and as-received fillers with Fe-Co powder

3.4.1 Materials with SiC particles

The coated and uncoated SiC particles were blended with 20 g of Fe-50% Co powder using a Spectromill ball pestle impact grinder (Model 1100) as shown in Fig. 3.4, supplied by Chemplex Industries Inc.. The amount of particles taken to prepare composites with 5 and 10

vol% particulates is summarised in Table 3.1. The powders were taken in a stainless steel communition vial (84mm length x 38 mm diameter) with concave interior ends and blended for 1 hr. The mixing was done without ball pestles to minimize the damage to the coatings and breakage of brittle SiC particles.

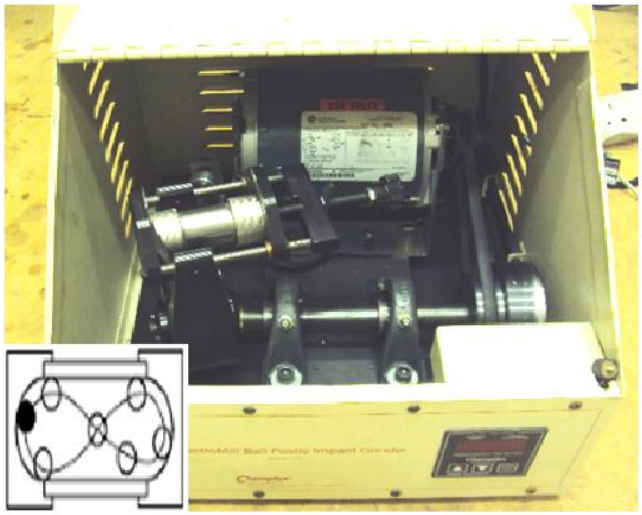

Fig. 3.4 SpectroMill ball pestle impact grinder used for mixing with an inset showing the travel path configuration of ball pestles

Table 3.1 *Weight of SiC particles taken for preparing composites*

Composites with	Weight of SiC particles (g)				
	Uncoated	Cu coated	Ni-P coated	Co coated	Duplex coated
5 vol% particles	0.4	0.45	0.6	0.5	0.5
10 vol% particles	0.8	0.89	1.2	1.0	1.0

3.4.2 Materials with SiC whiskers

In the case of whiskers, the coated and uncoated whiskers were dispersed in ethanol under ultrasonic agitation. About 20.3 g of Fe-Co powder was added to each solution bearing SiC whiskers and the slurry was sonicated for 30 minutes. The slurry was then heated in an oven at 60^{o}C to evaporate off ethanol. The dried powders were blended in the ball mill for 1 hr without ball pestles. The amount of uncoated and coated whiskers taken to prepare the mixture is summarised in Table 3.2.

Table 3.2 *Weight of SiC whiskers taken for preparing composites*

Composites with	Initial weight of whiskers taken (g)- final weight of whiskers after coating (g)			
	1 vol%	2 vol% Thin coating	2 vol% Thick coating	3 vol%
Uncoated SiC whiskers	0.08	0.16		0.24
Cu coated SiC whiskers	0.08-0.5	0.16-0.46	0.16-0.92	0.24-0.69
Ni-P coated SiC whiskers	0.08-0.5	0.16-0.72	0.16-1.5	0.24-1.04
Co coated SiC whiskers	0.08-0.44	0.16-1.02		0.24-0.72

3.4.3 Materials with carbon nanotubes

For CNTs, two different methods were employed to mix uncoated CNTs with metal powders. About 0.015, 0.03, 0.045, 0.06, 0.09, 0.15 g of as-received CNTs were dispersed in dimethylformamide (DMF) under ultrasonic agitation for 90 minutes. About 20.3 g of Fe-Co powder was added in each suspension and the slurry was sonicated for 30 minutes. The slurry was heated with a hot plate maintained at 150^{o}C to vaporise DMF in a fume cupboard. The Fe-Co CNT mixture was dry milled in the ball pestle impact grinder with ball to powder ratio of (BPR) ~1:1 for 1 hr. In the alternative method, 20 g of Fe-Co powders were dry ball milled with different volume fractions (1, 1.5, 2, 3, 5 and 10 vol%) of CNTs in the ball mill with BPR 1:1 for 1 hr without any prior colloidal processing. Hereafter, the former mixing route will be denoted as B method and the latter as U+B method.

Two different routes were followed to mix CNTs decorated with Ni-P layer with Fe-Co powders. In the first method, 1.5 and 3 vol % of coated CNTs were dispersed in 100 ml of ethanol by ultrasonication for 7 hrs and mixed with 20.3 g of metal powders. The slurry, after sonicating for 30 minutes, was dried in an oven at 60^{o}C for 12 hrs to evaporate ethanol. The powder mixture was then blended without ball pestles for 1 hr in the ball mill. In the other method, after colloidal processing, the coated CNTs and Fe-Co powders were dried and mixed by ball milling the mixture with BPR ~1:1 for 1 hr.

3.5 Spark plasma sintering of monolithic Fe-Co alloy and its composites

Sintering of Fe-Co powders was carried out using the spark plasma sintering facility (HPD 25/1 FCT, Germany) at Queen Mary, University of London (Fig. 3.5). A schematic outline depicting the main parts of the sintering system is shown in Fig. 3.6(a). The metal powder or powder mixture was placed in a 30 mm graphite die fitted with the lower punch and lined with graphite paper. The powder was uniaxially pressed with a manual Perkin Elmer hydraulic press after fitting the upper punch. The schematic of die set, fitted with upper and lower conical protection plates was wrapped with graphite wool for thermal insulation as shown in Fig. 3.6(b). The temperature was measured using an optical pyrometer inserted through a 10 mm diameter hole in the upper half of the die set. The pressure was applied through water a cooled steel ram using a hydraulic press. The DC pulse current was on for 15 ms and off for 5 ms.

3.5.1 Monolithic materials prepared to find optimum SPS parameters

Spark plasma sintering was carried out under vacuum at different temperatures ranging between 700-950^{o}C by soaking for different periods ranging between 2-30 minutes under 40, 80 and 100 MPa pressure. The details of the sintering variables used to prepare samples to predict the optimum parameters are summarised in Table 3.3. All the samples were heated to the sintering temperature at a constant rate of 100 ^{o}C/min. Once the die set with the packed powder was introduced into the sintering system, it was pressed by at least a minimum load of 5 kN (7 MPa) throughout the sintering cycle. Two different sets of samples were prepared by varying the starting point of the pressure application from the minimum pressure level (7 MPa) to the desired level. For the first set of samples, the pressure was applied when the pyrometer read 450^{o}C and it was gradually increased to the desired value. The second set of samples was prepared by applying the pressure at 750^{o}C and increasing it to the required level. After sintering, the pressure from the set value was reduced to 7 MPa in 1 minute. All the compacts were cooled in the sintering furnace by convective heat exchange with the water circulating in the copper alloy ducts inside the steel ram. The compacts were taken out using the manual hydraulic press.

Table 3.3 *Summary of experiments performed to predict optimum sintering variables*

Sintering temperature (^oC)	Soaking time (min)	Sintering pressure (MPa)	Temperature at which the additional pressure was applied (^oC)
700	5	80	450
	10	80	
	30	80	
	10	100	
800	2	80	750
	5	80	
	10	80	
	30	80	
	10	100	
900	2	40	750
	5	40	
	2	80	
	5	80	
	10	80	
	30	80	
950	2	40	750

Fig. 3.5 SPS furnace in Nanoforce Technology Limited, London,

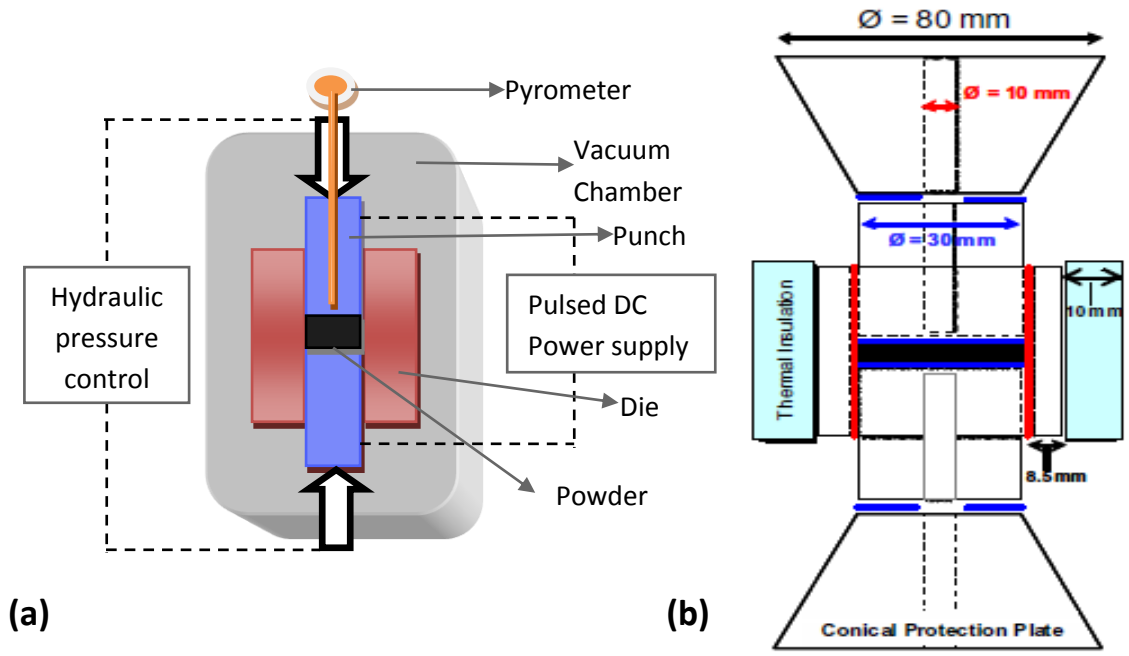

Fig. 3.6 (a) Schematic of the SPS system; (b) Diagram showing the parts and dimensions of the die-punch assembly

3.5.2 Monolithic samples prepared to study the effects of SPS variables and post heat treatments on magnetic properties

As shown in Fig. 3.7 and Fig. 3.8 and summarised in Table 3.4, unreinforced samples were prepared to study the influence of the following variables related to the mechanical pressure on the magnetic properties.

a) Temperature at which the pressure was applied
b) Amount of pressure applied
c) Rate at which the pressure was applied

In all the above experiments, heating rate, sintering temperature and soaking time were maintained at 100^{o}C/min, 900 ^{o}C and 2 min respectively. All the samples were pressed by a minimum force of 5 kN (7 MPa) throughout the sintering cycle. As the heating rate was fixed, the pressure application rate was changed by varying one of the following variables (a) the temperature at which the pressure application was started, (b) the temperature at which the set pressure was reached, and (c) the maximum pressure applied. Hereafter, all monolithic samples prepared to study the influence of pressure were designated with MLP.

Table 3.4 *Summary of the experiments performed to study the influence of sintering pressure and the rate and temperature of their application*

Sample designation	Sintering pressure (MPa)	Temperature at which pressure application started (^{o}C)	Temperature at which maximum pressure was reached (^{o}C)
MLP1	40	600	650
MLP2			700
MLP3	80		650
MLP4			700
MLP5	40	800	850
MLP6	80		
MLP7	40		900
MLP8	80	600	800
MLP9			850
MLP10			900
MLP11	80	450	900
MLP12		750	

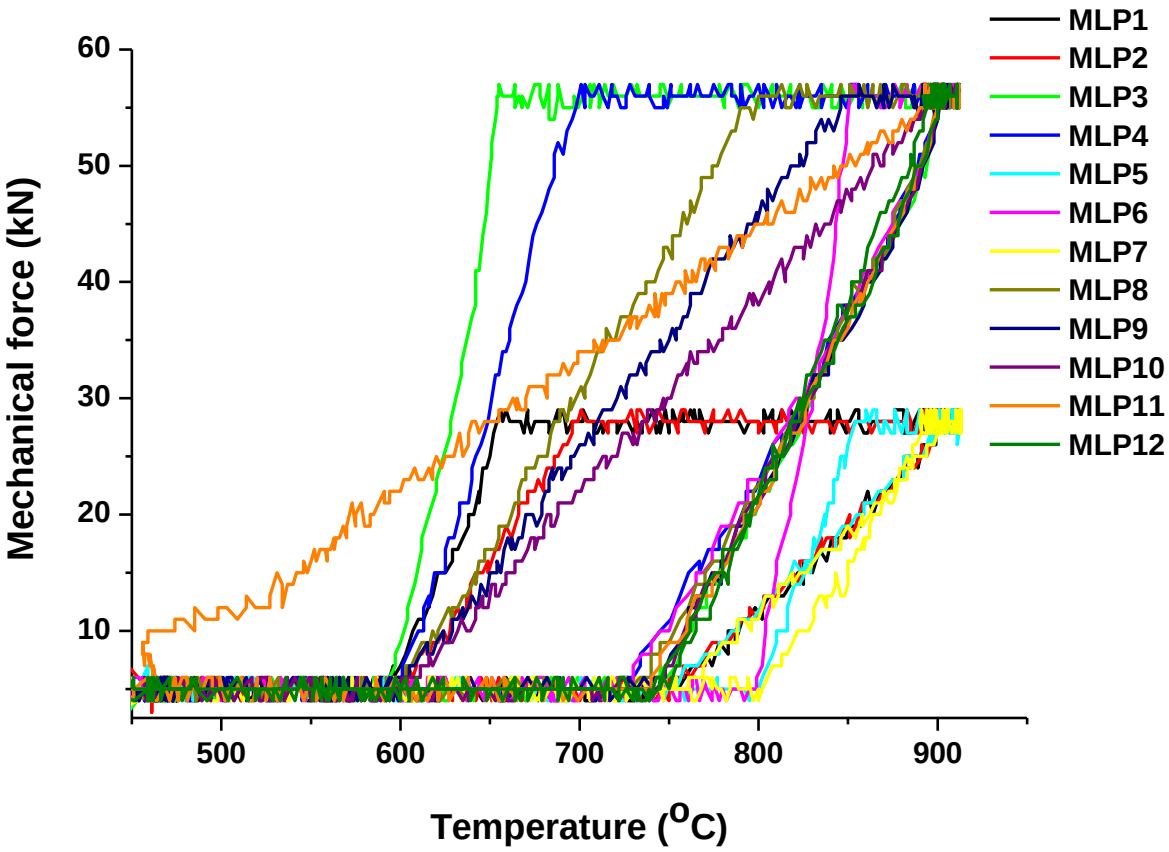

Fig. 3.7 Mechanical force vs temperature plots for the experiments performed to study the influence of sintering pressure and the rate and temperature of their application

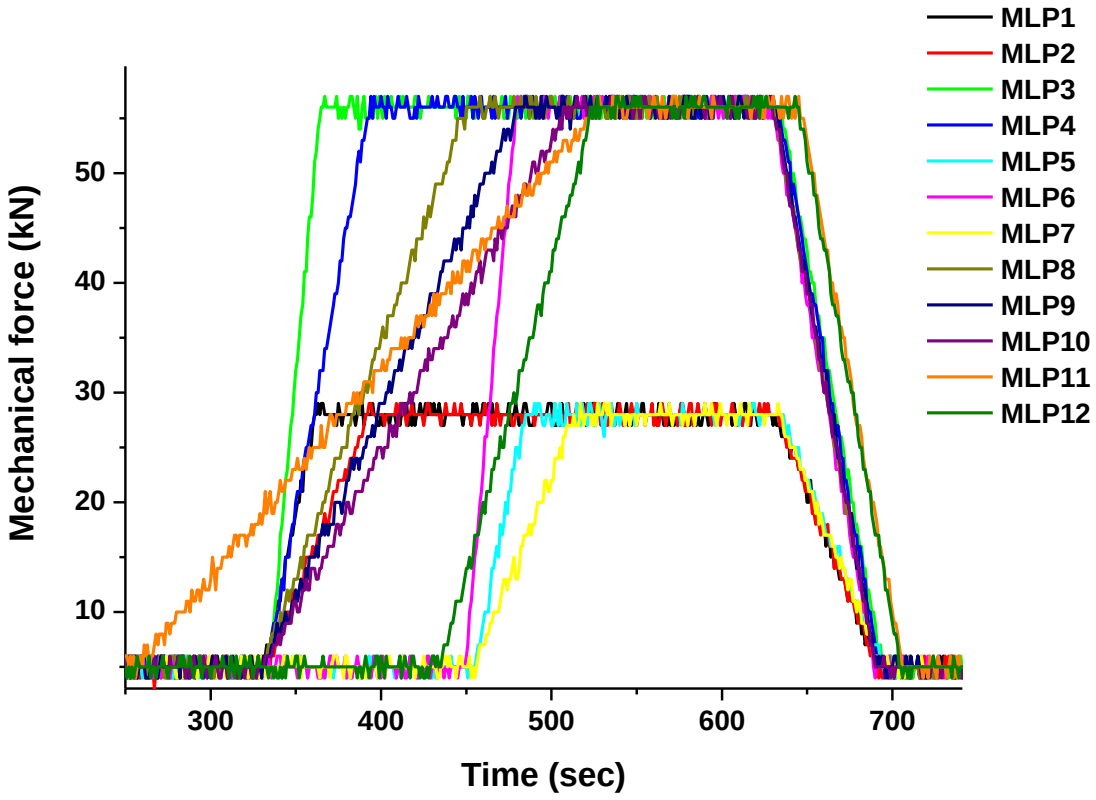

Fig. 3.8 Mechanical force Vs time plots for the experiments performed to study the influence of sintering pressure and the rate and temperature of their application

Four monolithic samples were prepared by maintaining the heating rates as 50, 100, 250 and 500^{o}C/min to 900^{o}C, with the mechanical pressure and soaking time set constant as 7 MPa and 2 mins respectively. The mechanical pressure was set to be minimum (7 MPa) to ensure that the particles are under good electrical and thermal contact and to differentiate the effects of heating rate from other variables.

The importance of magnetic behaviour of Fe-Co on spark plasma sinterability was studied by compacting the powders at different temperatures above and below the Curie temperature. After confirming the Curie temperature as 990^{o}C with the DSC measurements, the sintering was done at 900, 950, 1000, 1050 and 1100 ^{o}C under a minimum pressure of 7 MPa as explained before. The soaking time and heating rate were maintained at 2 minutes and 100 ^{o}C/min, respectively.

Four unreinforced Fe-Co samples were prepared to study the influence of post heat treatment on magnetic properties. Sintering variables such as heating rate, sintering temperature, mechanical pressure, temperature of application of pressure, soaking time were

maintained constant in all the four samples as 100^{o}C/min, 900^{o}C, 80 MPa, 450^{o}C, 2 mins respectively. The samples were heated in a vacuum furnace at the rate of 250^{o}C/hr and held at 500, 700, 900 and 1050^{o}C for 1, 5 hrs and cooled in the furnace to room temperature.

Three monolithic samples were sintered by setting the cooling rate at 100, 50 and 10 ^{o}C/min, with the sintering temperature, pressure, soaking time and heating rate maintained as 900^{o}C, 80 MPa, 11 minutes and 100^{o}C/min respectively. A longer soaking time (11 min) was chosen to ensure temperature homogeneity in the entire sintering mass. The pressure was removed completely in 1 minute from 80 MPa to 7 MPa to isolate the effects of cooling rate from other parameters. The influence of temperature at which the pressure was released on final properties was also examined by removing the pressure at 900, 600 and 450 ^{o}C and by managing other parameter constants.

The possibility of any texture development in the magnetic Fe-Co alloy sintered by SPS was investigated by measuring the magnetic properties in all the three directions. For this, two cube samples (15.3 mm) were used, which were cut from thick cylindrical samples produced by sintering 90 g of powder at 900 and 1050^{o}C for 5 minutes by applying a uniaxial pressure of 80 MPa.

3.5.3 Sintering of composite materials

The sintering temperature and pressure employed for composite fabrication were 900^{o}C and 80 MPa, respectively. The soaking time varied between 2 -5 minutes. The reasons for choosing the aforementioned parameters are discussed in detail in Section 4.12.

3.6 Characterisation of compacts

3.6.1 Microstructural and spectroscopic characterisation

After sintering, the surface of the compact was ground with 80 grit SiC cloth to remove the graphite layer. The density of the sintered samples was measured using Archimedes' immersion method with water. The graphite free cylindrical compacts were cut along the dotted lines using wire EDM as shown in Fig. 3.9. The rectangular sample in the centre and one of the arc segments at the ends were used respectively for magnetic testing and microstructural characterisation. The cross section of the arc segment was ground and polished with discs embedded with 15, 9, 3 and 1µm sized abrasives. The polished surface was examined under optical microscope and scanning electron microscope to examine the shape, size and distribution of pores. After the initial inspection, the sample was etched with Nital, containing 90% ethanol and 10% HCl, to reveal the grain structure. The following

procedure was employed to etch the polished sample: wet the polished surface with iso-proponal; immerse the sample with the face up into the etchant for 30 sec and slightly agitate; rinse it with iso-proponal; and dry with a stream of warm air. The optical microscopy and scanning electron microscopy was performed immediately after drying to prevent drying stains, which may be formed when cleaning and etching liquids are gradually released by the pores. In the case of composites with coated fillers, point, area and line EDX analysis were performed to obtain compositional details.

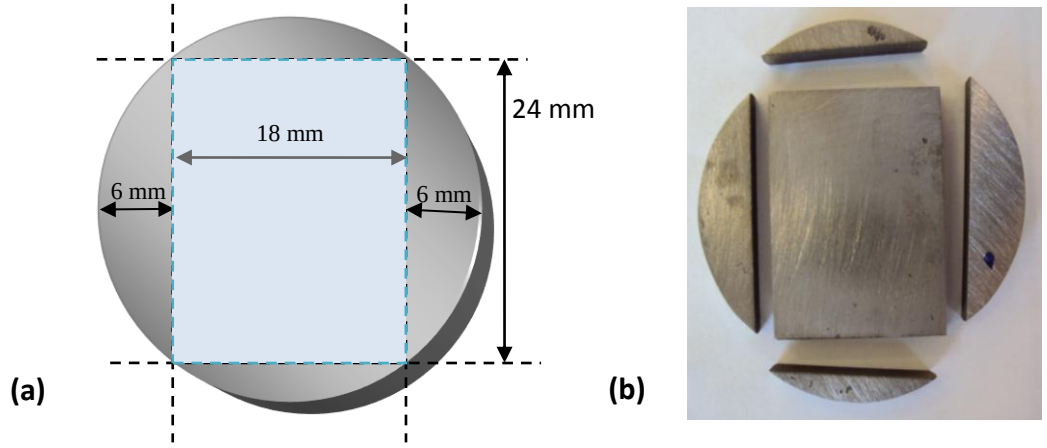

Fig. 3.9(a) Schematic showing the lines along which the sample was cut (b) image of a sample cut by EDM

3.6.2 Crystallograpic structural characterisation

The crystal structural characteristics of a few selected CNT reinforced composites were studied using a Philips PW1710 Automated Powder Diffractometer, which uses Cu Kα radiation. The X-ray tube was operated at 35kV and 40mA and the scanning was done between 2 and 80 °2θ at a speed of 0.01 °2θ/s. The phases present were identified using Philips PC-Identify software.

In Fe-Co alloys, long range ordering plays an important role in dictating the magnetic and mechanical properties. Among the experimental techniques used to assess ordering, one is the direct comparison of the intensity of characteristic superlattice lines and fundamental lines present in the X-ray histogram of an ordered solid solution [4], [5]. Since the atomic numbers of Fe and Co are 26 and 27 respectively, the structure factor, one of the six factors affecting the relative intensity of the diffraction lines is nearly equal for both the elements. On ignoring the minor variations due to other factors such as polarization factor, multiplicity factor, Lorentz factor, absorption factor and temperature factor [6], the intensity of the superlattice line is generally proportional to $(f_{Fe} - f_{Co})^2$, where f_{Fe}=26 and f_{Co}=27 are atomic scattering factors of Fe and Co respectively. The problem of reduction in the intensity

of superlattice reflection was overcome by exploiting the anomalous scattering effects that occur when the wavelength of an incident radiation is nearly equal to the wavelength of the K adsorption edge of the scattering element [6]. Therefore, most studies on ordering in Fe-Co alloys use Co or Fe Kα radiations, which can enhance the intensity of superlattice lines by an order of magnitude. X-ray diffraction histograms were also obtained for selected compacts with and without fillers in the as-prepared and heat treated conditions using Siemens D500 diffractometer with cobalt X-ray source available at Department of Materials Science and Engineering, University of Sheffield. The X-ray tube was operated at 40kV and 30mA and the scanning was done between 30 and 130 °2θ at a scan speed of 0.75 °2θ/min. To know about the ordered alloy characteristics, slow scan experiments (0.02 $^{o}2\theta$ min^{-1}) were also performed on selected samples in the angular ranges of 34-39^{o} and 87-92^{o}, where (100) and (210) superlattice lines, respectively were expected to appear in Fe-Co alloys [7]. The International Center for Diffraction Data (ICDD) and SIeve+ 2012 software package was used to view the data. The phases present were identified by comparing the X–ray diffraction pattern against known reference materials in the ICDD's Powder Diffraction File (PDF-4+), 2012 edition.

3.6.3 Quasi DC magnetic testing

The DC magnetic characteristics of the sintered samples were studied using a DC permeameter developed at the Wolfson Centre for Magnetics, Cardiff University [8]. Samples with rectangular cross section, as shown in Fig. 3.10, were closely wound with a pick up coil of thin (approximately 0.01 mm) enamel coated copper wire at the centre. The number of turns was fixed at 10. The wire wound bar sample was placed between the pole pieces of an electromagnet and a closed magnetic circuit was formed. The pick-up coil was connected to an integrating fluxmeter to measure the magnetic flux density. Magnetic field strength was measured using a Gaussmeter with Hall probe. The fluxmeter and Gaussmeter were connected via a GPIB programmable input card. The outline of the measurement system is shown in Fig. 3.11. Before commencing the measurements, the sample was demagnetised by an alternating field technique (i.e) reducing the magnetic field from the peak value to zero at a certain frequency (usually 1 Hz) as explained by Jiles et al [9]. Test parameters including cross-section area of the sample, peak field required, magnetic path length, loop period and demagnetisation characteristics like demagnetisation time, amplitude and number of cycles were entered through a LabView interface, which aided in the construction of the hysteresis

loop from the Gaussmeter and fluxmeter readings by ramping the output current to the pre-defined H increments.

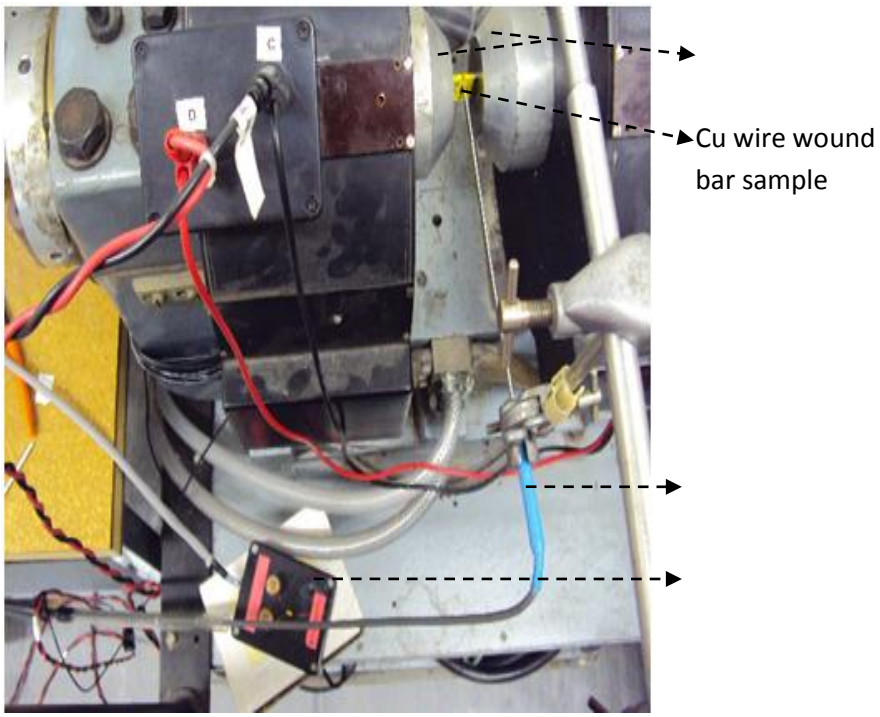

Fig. 3.10 Quasi DC magnetic property measurement of a sintered sample (image)

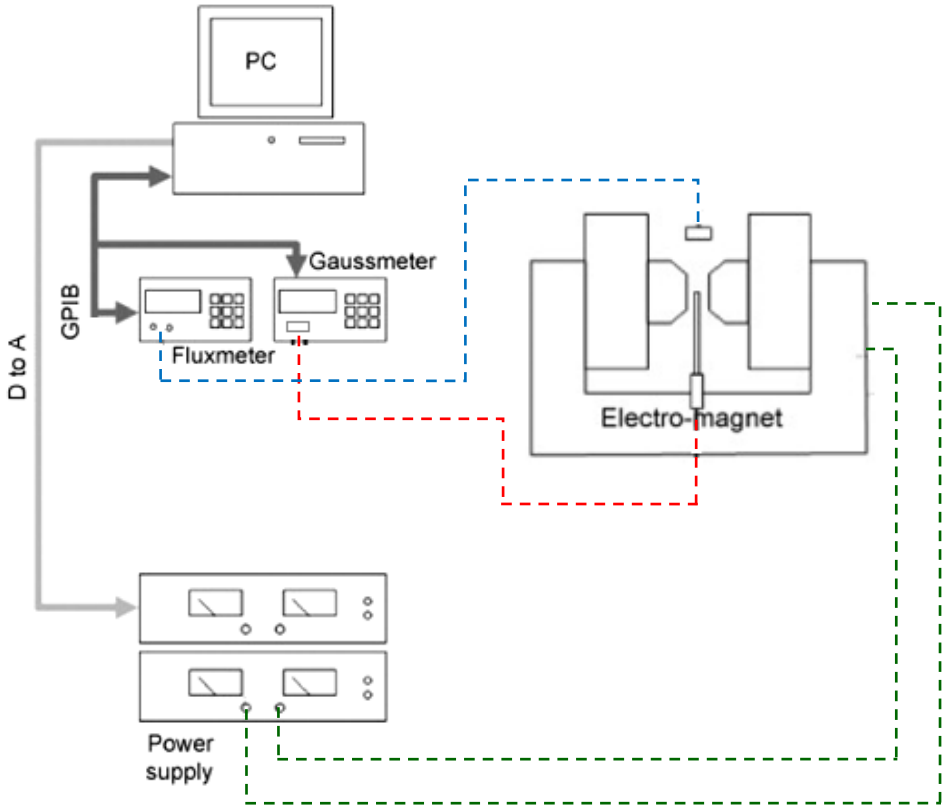

Fig. 3.11 Schematic diagram of the permeameter used for magnetic property measurement

3.6.3.1 Uncertainty in magnetic measurements

The uncertainties of the saturation induction and coercivity of the samples, as measured using the DC permeameter, were estimated according to the recommendations given in UKAS M3003 [10]. The parameters that have to be entered in the worksheet, as shown in Table 3.5 and 3.6, to estimate the standard uncertainty includes: values as mentioned in the calibration certificate (eg for rulers, mass balance) or calculated using the experimental methods (eg repeatability), divisor that is based on the probability distribution and sensitivity co-efficient (c_i) that can be experimentally determined from $\Delta y/\Delta x_i$ by varying the value of x_i. The uncertainity evaluation methodology is available elsewhere [11].

Table 3.5 *Uncertainty evaluation of B_{sat} of the SPS sintered compacts measured under DC conditions using a permeameter*

Source of uncertainty	± %	Probability distribution	Divisor	c_i	u_i ± %	v_i *or* v_{eff}
Fluxmeter cal, service uncert	0.2	Normal	2.0000	1	0.10000	∞
Cross section, width	0.025	Normal	2.0000	1	0.01250	∞
Cross section, thickness	0.025	Normal	2.0000	1	0.01250	∞
Repeatability, drift	0.01	Rectangular	1.7321	1	0.00577	
Repeatability, material	0.014	Rectangular	1.7321	1	0.00808	∞
Sum of squares					0.01041	
Combined uncertainty					0.10204	
Expanded uncertainty					0.20407	
Declared uncertainty in B_{sat} at a confidence level of 95 %					0.20000	

Table 3.6 *Uncertainty evaluation of H_c of the SPS sintered compacts measured under DC conditions using a permeameter*

Source of uncertainty	± %	Probability distribution	Divisor	c_i	u_i ± %	v_i *or* v_{eff}
Voltmeter calibration	0.010	Normal	2.0000	1	0.00500	∞
Standard resistor, 0.1 ohm	0.1	Normal	2.0000	1	0.05000	∞
Path length	0.025	Rectangular	1.7321	1	0.01443	∞
Ripple on DC supply	0.1	Rectangular	1.7321	1	0.05773	∞
Repeatability	0.2	Rectangular	1.7321	1	0.11547	2
Searching for Hc, incl in repeat	0	Rectangular	1.7321	1	0.00000	2
Sum of squares					0.01940	
Combined uncertainty					0.13928	
Expanded uncertainty					0.46102	
Declared uncertainty in *Hc* at a confidence level of 95 %					0.50000	

3.6.4 Mechanical testing

3.6.4.1 Hardness test

The hardness of the unreinforced and composite samples was measured at five different locations with a Vickers hardness tester (HTM 5027, Vickers Ltd., Crayford, Kent, England) under an applied load of 30 kg for 4 sec. The average length of the diagonal left by the square based pyramidal indenter in millimetres was used to calculate the Vickers hardness number using the formula,

$$\text{HV} = \frac{0.1891F}{d^2}$$

where, F is force applied in Newtons (294.20 N) and d in mm.

3.6.4.2 Three point bending test

After magnetic testing, the sintered samples with rectangular cross-section were cut into strip specimens of dimensions 3 mm x width x 24 mm as shown in Fig. 3.12. The width of the specimens varied between 3-3.5 mm depending on the thickness of the sintered samples. The three point bending experiments were conducted at room temperature in air using a Zwick/Roell Z050 electromechanical testing machine (supplied by Zwick Testing Machines Ltd.) with a 2 kN load cell. The specimen surface subjected to tension was polished with fine grit emery sheet to remove burrs, if any were introduced during cutting. The span and cross-head speed were maintained as 22 mm and 2mm/min respectively. The schematic experimental set-up is shown in Fig. 3.13. The bending strength of the specimen was calculated using the following formula [12],

$$\sigma_{max} = \frac{3P_{max}L}{2bd^2}$$

where, P_{max} is maximum load (N); L is the support span (22 mm); b is width of the specimen (mm); d is thickness of the specimen (mm)

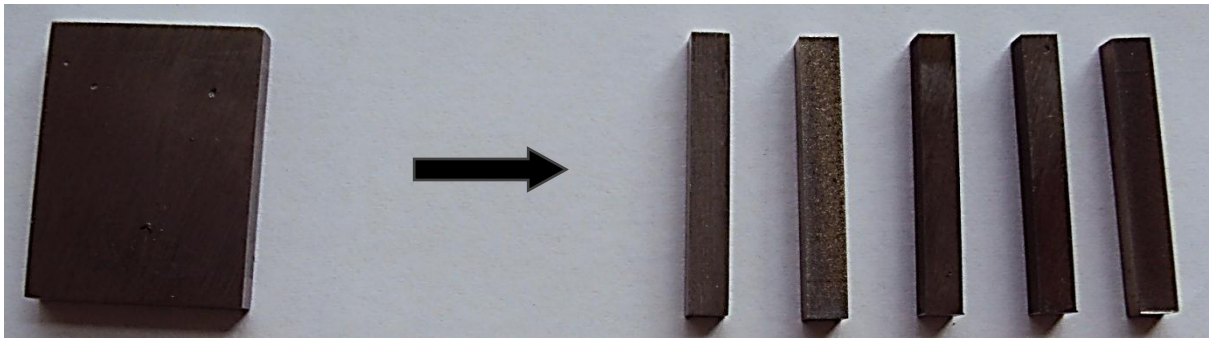

Fig. 3.12 Samples prepared for bending test

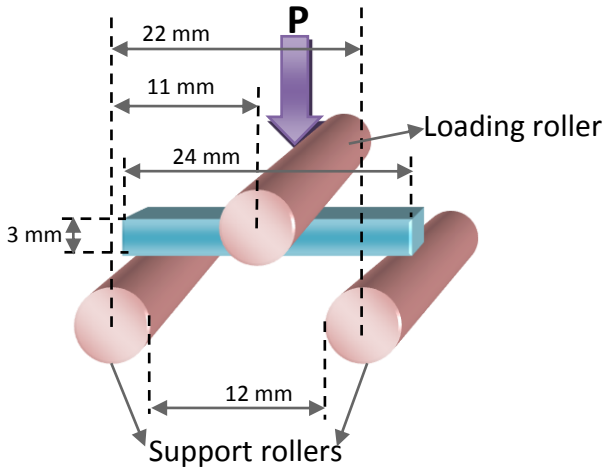

Fig. 3.13 Schematic of three point bending test set-up

The experiment was conducted for 5 samples in each case and the average bending strength and standard deviation were reported. The fractured surface of two randomly chosen failed samples in each set was examined using SEM (supplied by Nanotechnology Systems, Carl Zeiss) after ultrasonic cleaning to understand the mode of fracture and failure mechanisms. The fracture surfaces of the CNT composites were studied using a high resolution SEM (FEI Quanta 650 FEGSEM) available at School of Materials, The University of Manchester. The fractured surfaces of one randomly chosen sample in each CNT composites were studied using Raman spectroscopy to confirm the presence and structural integrity of carbon nanotubes [13]. The same instrument that was used to study the bare and coated CNTs was employed and the characterisations were performed at least at 7 different locations for each sample over a spectral range of 100-3200 cm^{-1}.

References

1. R. Sharma, R.C. Agarwala and V. Agarwala, Development of copper coatings on ceramic powder by electroless technique, *Appl. Surf. Sci.* **252**, 8487–93 (2006).
2. J.T. Jiang, L. Zhen, C.Y. Xu and W.Z. Shao, Microstructure evolution of cobalt coating electroless plated on SiC whisker during electroless plating and heat treatment, *Surf. Coat. Technol.* **201**, 6059–62 (2007).
3. L.B. Li, M.Z. An and G.H. Wu, Electroless deposition of nickel on the surface of silicon carbide/aluminum composites in alkaline bath, *Mater. Chem. Phys.* **94**, 159–64 (2005).
4. J. M. Loureiro, A. C. Batista, V. A. Khomchenko, B. F. O. Costa, G. Le Caër, Order-disorder phenomena from X-ray diffraction in FeCo alloys annealed and ground at high energy, *Powder Diffr.* **26 [3]**, 267-272(2011)

5. D. W. Clegg and R. A. Buckley, The disorder → order transformation in iron-cobalt-based alloys, *Metal Science Journal* **7**, 48-54 (1973)
6. B. D. Cullity, Elements of X-ray diffraction, Addison-Wesley publishing company, Inc., London, 383-95 (1978).
7. J. M. Loureiro, A. C. Batista, V. A. Khomchenko, B. F. O Costa and G. L. Caër, Order-disorder phenomena from X-ray diffraction in FeCo alloys annealed and ground at high energy, *Powder Diffr.* **26 [3]**, 267-272 (2011)
8. P. Anderson, A universal DC characterisation system for hard and soft magnetic materials, *J Magn. Magn. Mater.* **320**, e589–e593 (2008).
9. D.C. Jiles, D.L. Atherton, H.E. Lassen, D. Noble, J. deVette, and T. Astle, Microcomputer-based system for control of applied uniaxial stress and magnetic field, *Rev. Sci. Instrum.* **55 (11)**, 1843–48 (1984).
10. UKAS M3003, The expression of uncertainty and confidence in measurement, 1997
11. S. Somkun, Magnetostriction and magnetic anisotropy in non-oriented electrical steels and stator core laminations, PhD thesis, Cardiff University, 2010.
12. International Standards Organization. ISO 6872: Dental Ceramic. Geneva: ISO, 1995
13. F. Inam, H. Yan, M.J. Reece and T. Peijs, Structural and chemical stability of multiwall carbon nanotubes in sintered ceramic nanocomposite, *Advances in Applied Ceramics* **109**, 240-245 (2010).

Chapter 4

Results and discussion: Spark plasma sintering of monolithic Fe-Co alloy

4.1 Introduction

The Fe-50Co powders were sintered under different conditions such as maximum temperature, soaking time, maximum pressure applied, heating rate, cooling rate and temperature at which the pressure was applied and removed to find the optimum sintering parameters.

The density, microstructure, size distribution, chemical composition, crystallographic structure and thermal behaviour results of the as-received Fe-Co alloy powder, as characterised using a gas pycnometer, scanning electron microscope, particle size analyser, inductively coupled plasma- optical emission spectrometer, X-ray diffractometer and differential scanning calorimeter, respectively are presented and discussed in the first section of this chapter.

In the ensuing sections, the influences of the spark plasma sintering variables on the final magnetic and mechanical properties of the monolithic Fe-Co compacts are explained using the microstructural and crystallographic observations.

In the last section, the outcomes of the annealing treatments, which were performed on the sintered compacts, are described using the changes in the magnetic properties and X-ray diffraction results.

4.2 Characterisation of Fe-Co alloy powder

The Fe-Co powder was produced by gas atomisation to minimize the oxide content on the surface of the powders. The powder particles were found to be spherical with a wide size distribution ranging from around 1 µm to 20 µm (Fig. 4.1).

The density of the magnetic alloy powder was measured 10 times using a helium pycnometer. They were found to be distributed with a mean of 8.172 g/cm^3 and a standard deviation of 0.005 g/cc respectively.

The particle size as obtained using a laser diffraction Mastersizer showed a unimodal frequency distribution with a small amount of fines present as shown in Fig. 4.2. The shoulder in the left tail of the distribution curve indicated that there was a significant amount of particles with sizes nearer to one micron. The volume percentiles of the weighted particle

size distribution are usually reported as Dv X, where X represents the percentage below the reported particle size. The Dv 10, Dv 50 and Dv 90 of Fe-Co alloy powder were found to be 5.80, 14.1 and 28.8 µm, respectively.

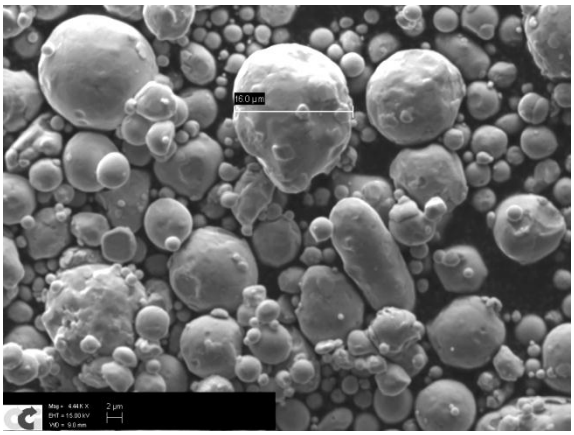

Fig. 4.1 SEM image of as-received Fe-Co alloy powder

The composition of the alloy powder, as mentioned by the powder supplier was Fe-50Co-0.2 Si. As the chemical composition of the alloy is one of the main variables that dictate the final properties, it was assessed using an inductively coupled plasma optical emission spectrometric analysis. The mean weight percentage of Co, Fe and Si present in the sample were determined to be 49.8, 49.9 and 0.18 respectively.

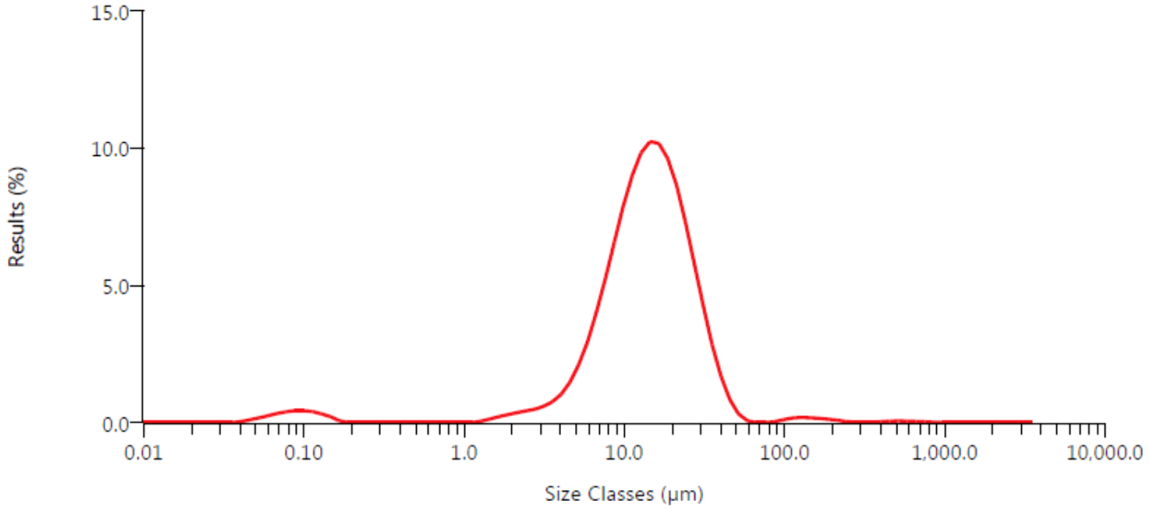

Fig. 4.2 Particle size distribution of Fe-Co alloy powder (frequency)

The XRD pattern of the as-received Fe-Co alloy powder is shown in Fig. 4.3(a). As the pattern displayed only the marked fundamental peaks, very slow scan XRD experiments were performed over the angular ranges of 34-39 and 87-92 $^{o}2\theta$, where the (100) and (210) superlattice lines, respectively, are expected to materialise in the spectra [1]. The absence of

the superlattice peaks even in the very slow scan spectra (Fig. 4.3(b)) confirmed that the as-received gas atomised powder was in the highly disordered state. This was due to the fast cooling rate during the gas atomisation process.

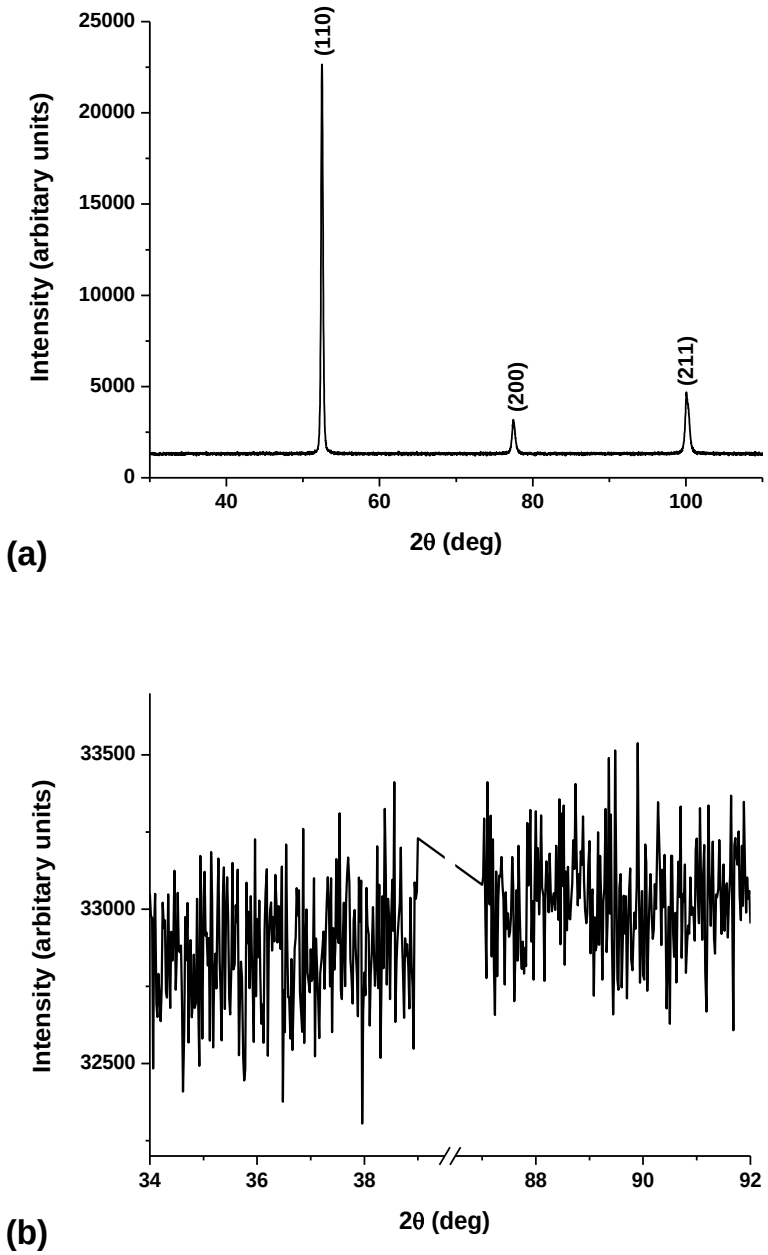

Fig. 4.3(a) XRD pattern obtained for as-received Fe-Co powder; (b) Results of the very slow scan XRD experiments performed at the shown narrow angular ranges to detect the superlattice lines

The results of the DSC experiments performed at two different heating and cooling rates are summarised in Fig. 4.4. Three different peaks of two natures (exothermic and endothermic) are observed in the scan corresponding to three phase transitions. The broad

exothermic peak observed distinctly in the fast scan (10°C/min) and less significantly in the slow scan (5°C/min) was due to the anomalous phase transformation associated with changes in heat capacity and lattice parameter [2]. The broad and shallow endothermic dip observed in the heating curves at 725°C could be related to the order-disorder phase transformation (T_{o-d}) (Fig. 2.1(a)). The relatively narrow endothermic dip noted in the heating curves at temperatures around 980 °C could be associated with the Curie transition (T_c) and α (bcc) - γ (fcc) phase transformation (Fig. 2.1(a)). It has to be noted that the order-disorder transformation temperature was not changed by the ramp rates, whereas α (bcc) - γ (fcc) transition was influenced by it. The endothermic (during heating) and exothermic (during cooling) peaks corresponding to α -γ transformation showed a thermal hysteresis. The hysteresis width varied with ramp rate as shown in Table 4.1. The results were processed using SETSOFT 2000 software and the heat released/absorbed during the transitions was obtained as shown in Fig. 4.5. The amount of heat absorbed during heating was marginally higher than the heat released during cooling.

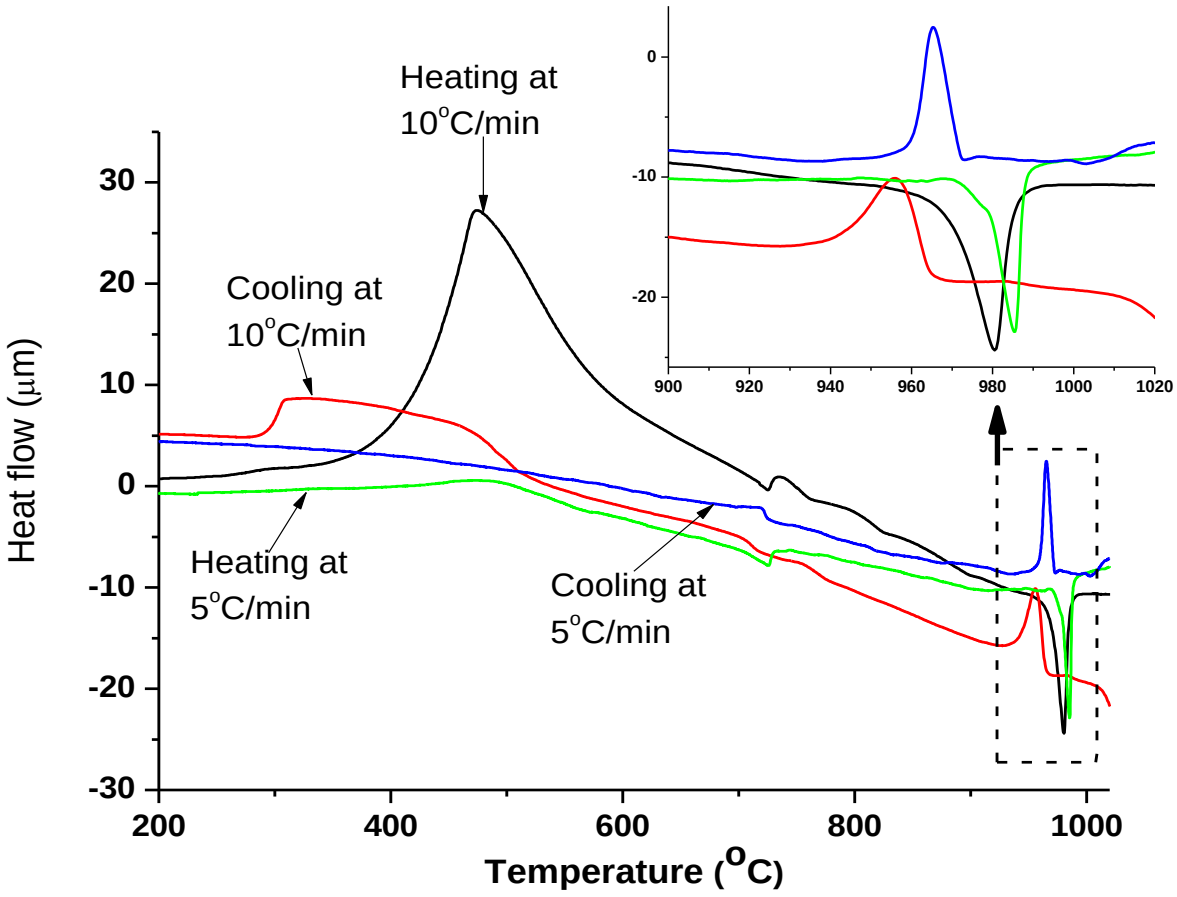

Fig. 4.4 DSC curves of Fe-Co alloy powder; inset is the enlarge image of the highlighted portion of the curve

Table 4.1 *Summary of DSC results of Fe-Co powder heated and cooled at two different rates*

Ramp rate	α – γ transformation (heating)		γ – α transformation (cooling)		Hysteresis width (^{o}C)
	Temp (^{o}C)	Heat absorbed (μV.s/mg)	Temp (^{o}C)	Heat released (μV.s/mg)	
10 ^{o}C/min	980	6.18	956	5.68	25
5 ^{o}C/min	986	7.01	966	6.81	20

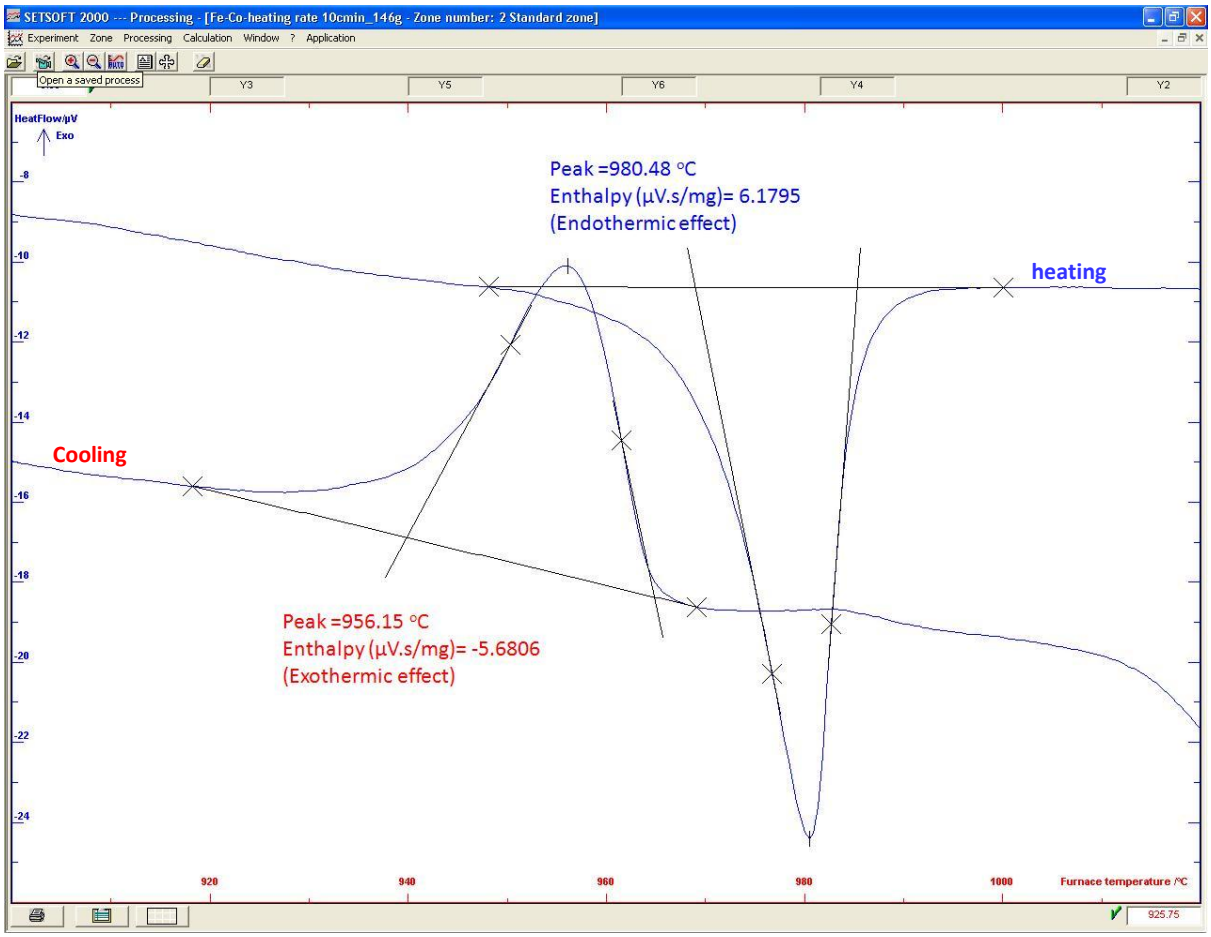

Fig. 4.5 Image showing the processing of DSC peaks near the Curie temperature of Fe-Co alloy powder using SETSOFT software and the results obtained

4.3 Effect of spark plasma sintering variables

It should be noted that for the materials sintered at 800, 900, and 950^{o}C, the mechanical pressure was applied when the pyrometer read 750^{o}C, whereas for those sintered at 700^{o}C, it was applied at 450^{o}C.

The magnetic and mechanical properties of monolithic samples compacted at different conditions are summarised in Table 4.2.

Table 4.2 *Magnetic and mechanical test results of the compacts prepared at different temperature-pressure-time combinations.*

Sintering parameters			Density (g/cc)	Coercivity (A/m)	Saturation induction (T)	Hardness (VHN)	Flexural strength (MPa)	
Temp. (^oC)	Pr. (MPa)	Time (min)					Mean	Std. deviation
700	80	5	7.82	1263	1.92	254±4	661	49
	80	10	7.86	1140	2.15	289±4	923	73
	80	30	8.07	1074	2.27	327±4	1188	21
	100	10	8.01	1185	2.23	309±4	1034	45
800	80	2	8.05	902	2.27	306±5	1120	33
	80	5	8.09	873	2.27	318±3	1143	61
	80	10	8.12	878	2.30	322±3	1118	55
	80	30	8.10	880	2.29	319±3	1132	68
	100	10	8.12	852	2.34	321±1	1098	73
900	40	2	7.97	816	2.30	296±5	1104	48
	40	5	8.10	785	2.31	302±3	1075	46
	80	2	8.09	795	2.33	321±4	1108	51
	80	5	8.14	788	2.34	312±3	1145	32
	80	10	8.13	779	2.32	302±5	1113	43
	80	30	8.13	768	2.31	299±1	1098	20
950	40	2	7.86	475	2.15	216±3	617	28

The optical micrographs of the materials sintered at different temperature-pressure-time combinations are shown in Fig. 4.6.

The materials that were sintered at 700^{o}C retained the spherical nature of the starting particles even after sintering for 30 minutes (Fig. 4.6(a) and (b)). However, those sintered at 800 and 900^{o}C showed grain structures with clear boundaries (Fig. 4.6(c)-(f)). It was very difficult to identify any significant microstructural difference in the compacts sintered for different durations at 800 and 900^{o}C. The optical micrographs of the compacts prepared at 950^{o}C displayed porous and coarse grain morphology (Fig. 4.6(g)).

4.3.1 Effect of sintering temperature

As shown in the bar chart (Fig. 4.7(a)), an increase in the sintering temperature up to 900^{o}C, with the other parameters maintained at a constant, increased the compact density. As a result, the mechanical properties and saturation induction were improved and the coercivity was decreased. The above statement holds true only if the dwelling time was short (< 5 minutes).

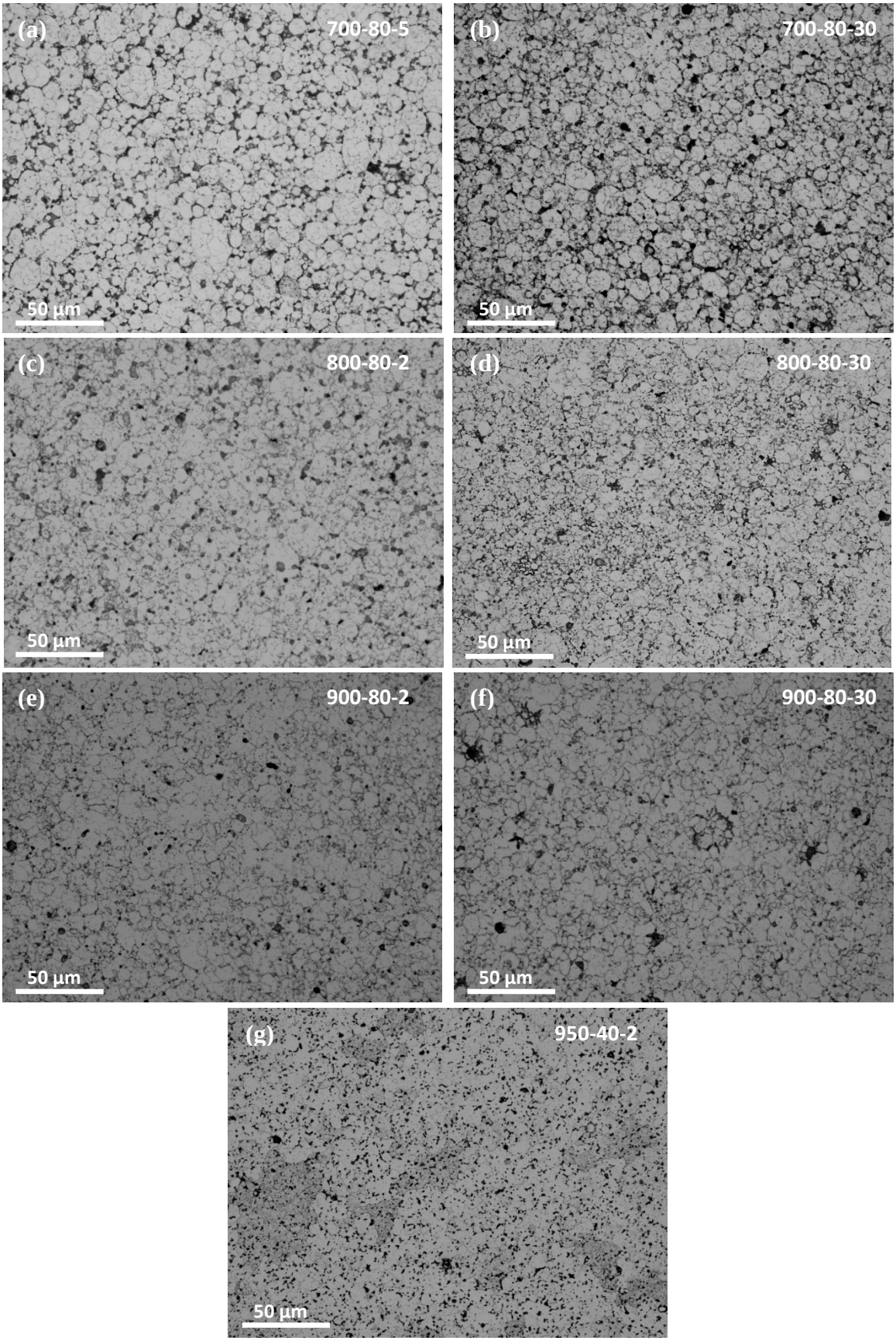

Fig. 4.6 Optical micrographs of Fe-Co alloy prepared at the shown temperature-pressure-time combinations

The variations in the magnetic and mechanical properties of the compacts prepared by soaking for longer durations at temperatures above and below $T_{o\text{-}d}$ will be discussed in the subsequent section. On increasing the maximum temperature to 950°C, the compact density was reduced. At temperatures higher than 900°C, there was a shift in the process mechanism from densification to grain growth, both of which are driven by the reduction in the total interfacial energy (Fig. 4.6(g)) as illustrated schematically in Fig. 4.7(b). Therefore, the mechanical properties, saturation induction and coercivity of the compact were significantly reduced when soaked at 950°C.

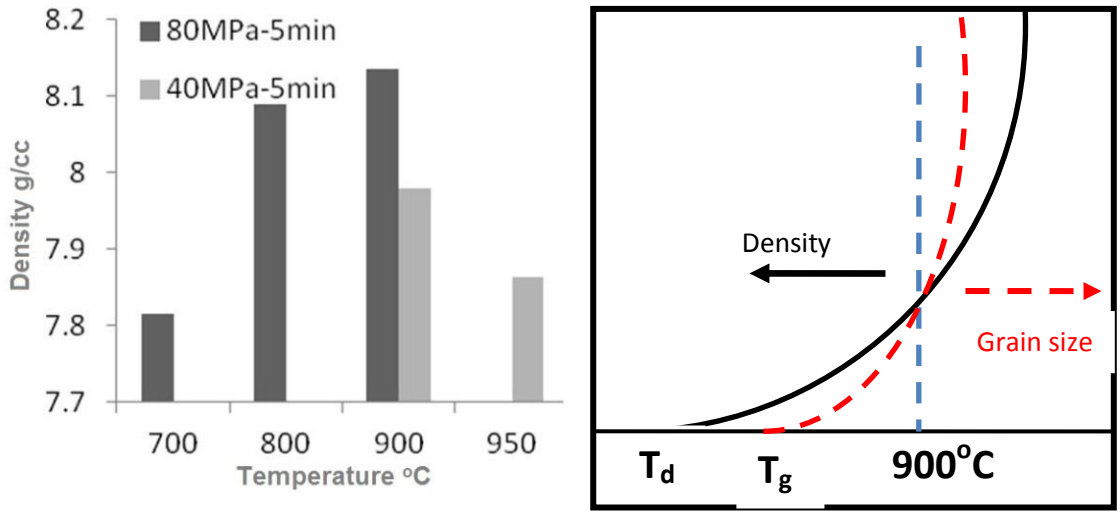

Fig. 4.7 (a) Effect of sintering temperature on density of compacts at two different pressure levels (theoretical density of the alloy is 8.17 g/cc; (b) Schematic drawing demonstrating the T dependence of the density and grain size; T_d and T_g are the onset temperature of densification and grain growth.

4.3.2 Effect of soaking time

The influences of dwelling time at different temperatures on the magnetic properties, bending strength and hardness are compared in Fig. 4.8, 4.9(a) and 4.9(b) respectively.

The bending strength of the materials that were processed for shorter durations at all temperatures were distributed over a wide range due to one or many of the following reasons: (a) inhomogenous microstructure due to the variation of temperature across the cross section of the compact during sintering, (b) different levels of porosity on the side which was subjected to tension during bending, and (c) inherent brittle nature of the material.

An increase in the sintering time at 700°C produced a significant improvement in the density values, and hence the flexural strength, hardness and saturation induction were increased and the coercive field was reduced. At 800°C, sintering for up to 10 minutes aided

in minimizing the porosity levels and hence a decrease in coercivity and an increase in saturation induction, and hardness were noticed. On increasing the soaking time to 30 minutes at 800^{o}C, no pronounced changes in the density, hardness, coercivity, bending strength and saturation induction were observed. The materials sintered for up to 5 minutes at 900^{o}C showed improvements in density values with the dwelling time and hence their magnetic and mechanical properties were improved with the soaking time. An increase in the dwelling time beyond 5 minutes at 900^{o}C produced no significant effects on the density of the compact. However, soaking the materials for longer durations (>5 minutes) at 900^{o}C had reduced the hardness, mean bending strength and coercivity because of the increase in the disordered alloy fractions in the sintered compact. These were in accord with the earlier findings that with the decrease in the degree of long range order (S), there would be a drop in the saturation induction, coercivity, hardness and mechanical strength [3], [4]. This was substantiated by the absence of superlattice lines in the XRD pattern on increasing the soaking time to 30 minutes at 900^{o}C (Fig. 4.10).

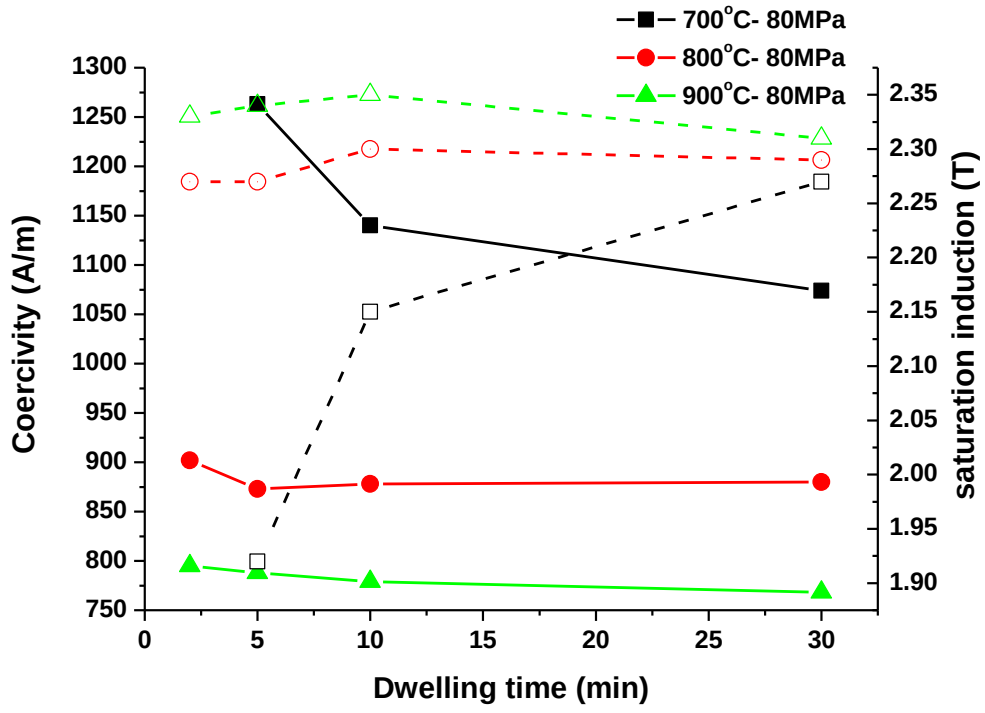

Fig.4.8 Variation of coercivity (shown by filled symbols) and saturation induction (shown by open symbols) with dwelling time at 700, 800 and 900^{o}C

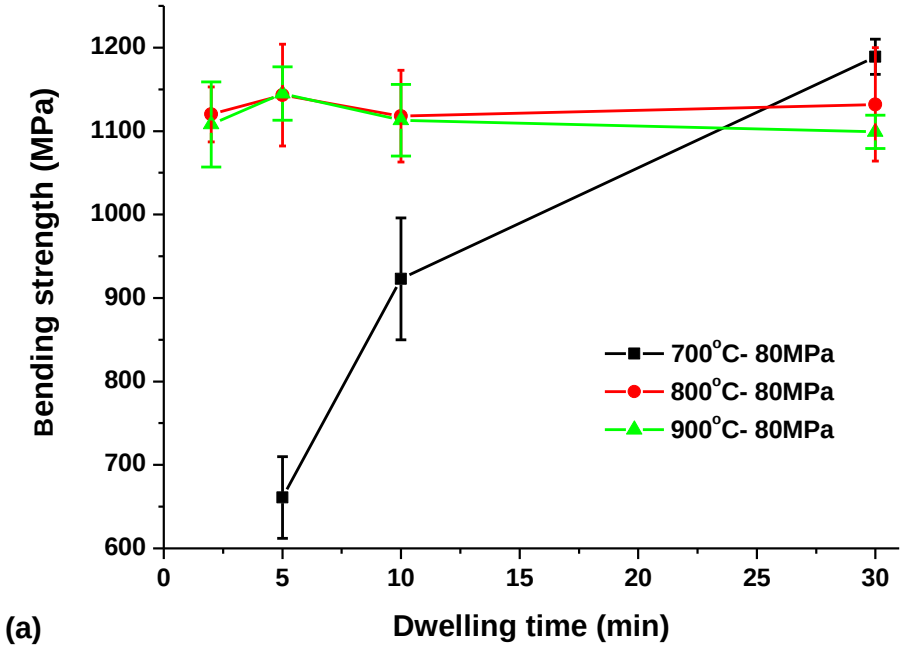

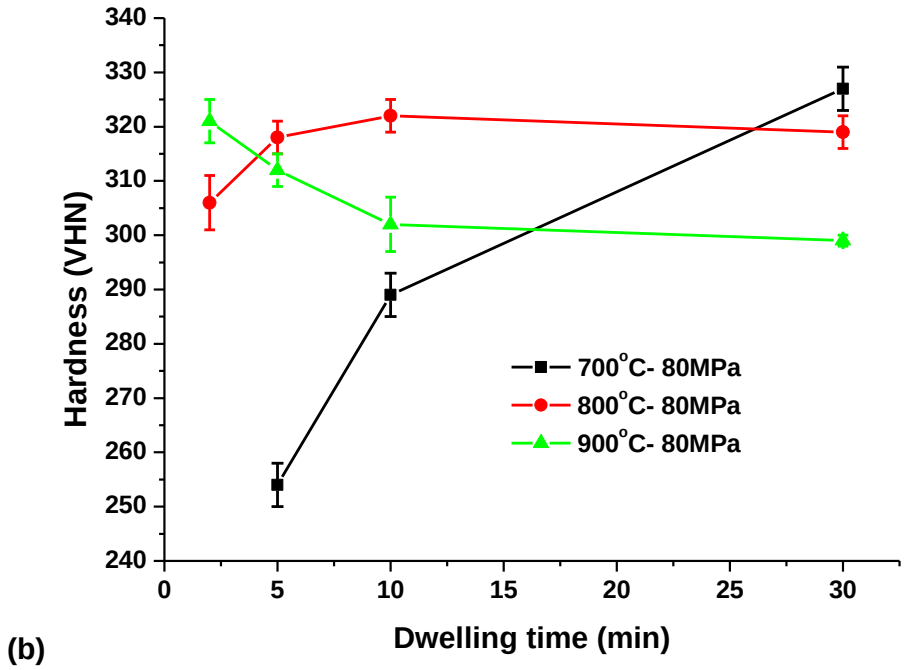

Fig.4.9 Plots showing the effects of dwelling time on: (a) bending strength; and (b) hardness at different temperatures and same pressure conditions

As shown by the drop in the intensity of superlattice lines (Fig. 4.10) and the mechanical properties, the volume fraction of the ordered structures in the samples soaked for 30 minutes at 900^{o}C was significantly lower than that soaked for the same duration at 800^{o}C. This was due to the increase in the disordering kinetics with the increase in the soaking

temperature above T_{o-d}. The materials sintered for longer durations at 700°C (i.e) below T_{o-d}, showed better mechanical properties than those sintered for similar durations at higher temperatures, say 800 and 900°C because of the increase in the volume fraction of ordered structures. With the increase in the sintering time, the compacts sintered at lower temperature (700°C) exhibited better mechanical properties than those heated to higher maximum temperatures (800 and 900°C) and this mechanical behaviour transition was due to the increase in disordering with the dwelling time at temperatures higher than $T_{o-d.}$

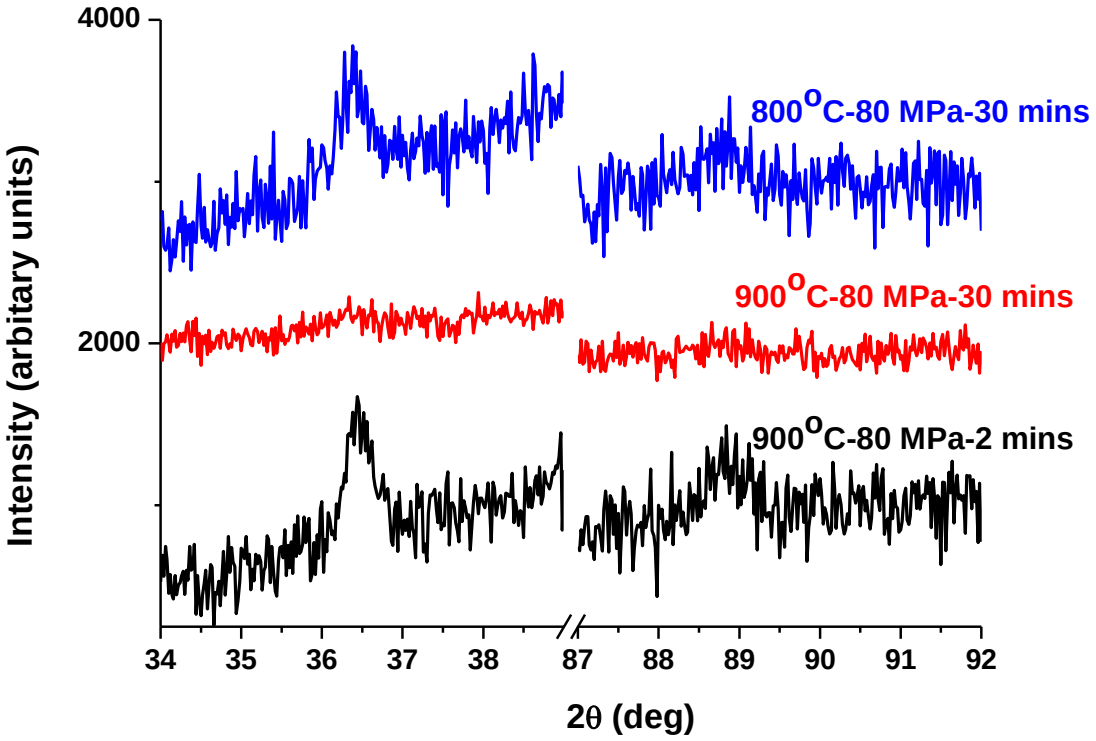

Fig. 4.10 Slow scan XRD result showing (100) and (210) superlattice reflections of Fe-Co compacts processed at the shown temperature-pressure-time combinations

4.3.3 Effect of sintering pressure

The employment of graphite dies and punches to contain and compact the powders restricted the mechanical pressure applied during sintering which could not to exceed 100 MPa.

It was evident that an increase in the pressure applied during compaction produced significant improvements in density at all sintering temperatures (Table 4.) and as a result, the saturation induction was improved. However, the role of pressure on coercivity was contradictory in materials sintered above and below T_{o-d}. An increase in sintering pressure

was found to change the coercivity marginally when the sintering temperature was above T_{o-d}, whereas, it significantly increased the coercive field when the temperature was lower than the transition temperature. The plausible factor that could explain the change in the magnetic behaviour with the sintering pressure at different temperatures was the difference in residual stresses. When the maximum temperature employed during sintering was higher (800, 900^{o}C), the stresses introduced due to mechanical pressing could have been relieved. At lower temperature sintering (700^{o}C), the thermal energy was not sufficient to relieve the internal stresses. Therefore, at 700^{o}C the stresses were believed to be retained in the material and they were increased with the increase in the mechanical pressure.

Depending on the mechanical pressure increments and the density improvements realised as a result, the mechanical hardness was increased. The hardness enhancements were marginal at 800 and 900^{o}C and significant at 700^{o}C. Other than in compacts that were sintered at 700^{o}C, which showed pronounced improvements in the flexural strength with mechanical pressure for the aforementioned reason, no notable change was observed in the compacts sintered at higher temperatures. As a precautionary measure to avoid the breakage of dies, all the composite materials were prepared by applying a mechanical pressure of 80 MPa.

4.3.4 Fractography of the bend test samples

Due to inefficient sintering at 700^{o}C for a shorter duration, the spherical morphology of the starting particles was retained, as displayed in the fractographic images (Fig. 4.11(a)). An increase in the soaking time at 700^{o}C improved the particle bonding and hence, well defined grain structures were formed (Fig. 4.11(b)). This contradicted the earlier observation using the optical microscopic images that sintering at 700^{o}C even for longer duration would retain the spherical shape of the powders (Fig. 4.6(a), (b)). The materials sintered for 2 minutes at 800^{o}C showed higher porosity levels on the fractured surfaces (Fig. 4.11(c)) than those sintered at 900^{o}C (Fig. 4.11(e)), which matched with the density findings (Table 4.2) . With the increase in the soaking time at 800^{o}C, the porosity content was reduced on the fractured surface. The samples sintered at 800 and 900^{o}C by soaking for 30 minutes displayed no significant differences in the fractographic features (Fig. 4.11(d) and (f)). On increasing the sintering temperature from 900 to 950^{o}C, the brittle fracture characteristic was completely changed from mostly intergranular mode (which occurs along grain boundaries and characterised by triple points, rock-candy or a faceted appearance) to transgranular type (typically described by cleavage steps, river patterns, feather markings and tongues) (Fig.

4.11(g)). The sample sintered at 950^{o}C exhibited large cleavage facets with river markings due to the large grain structures and pores left inside the grains due to ineffective sintering.

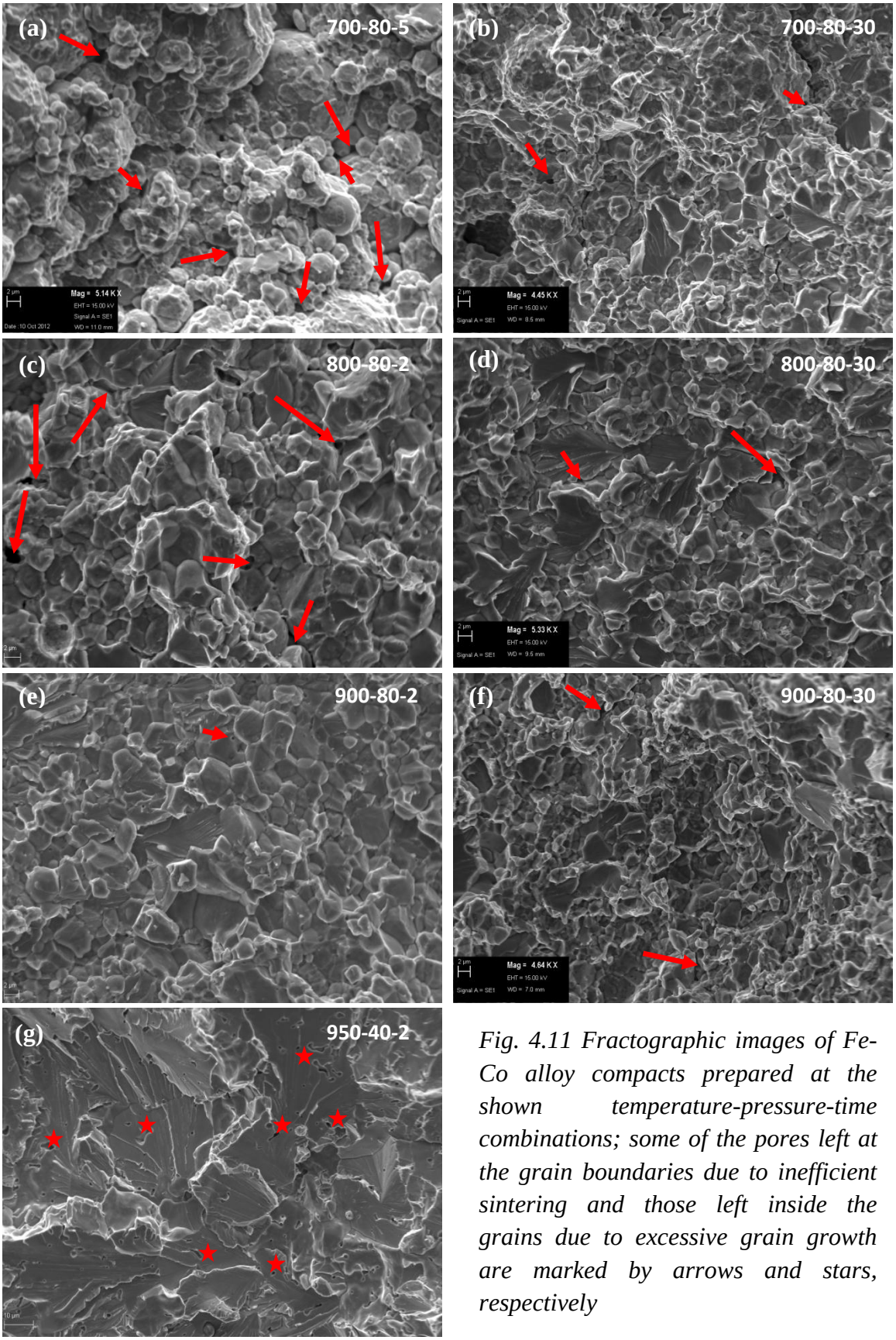

Fig. 4.11 Fractographic images of Fe-Co alloy compacts prepared at the shown temperature-pressure-time combinations; some of the pores left at the grain boundaries due to inefficient sintering and those left inside the grains due to excessive grain growth are marked by arrows and stars, respectively

4.4 Reproducibility of samples prepared by SPS

Two sets, of at least four samples each were sintered at 900^{o}C by soaking for 2 minutes under 80 MPa pressure. For one set, the mechanical pressure was applied when the pyrometer read 450 ^{o}C, whereas for the other it was applied at 750^{o}C. Each set of samples prepared under identical conditions showed nearly equal coercivity and saturation induction as shown in Fig. 4.12. This supported the reproducibility of samples prepared by SPS and the magnetic properties measured by a permeameter. The density and hardness of the all the nine samples were distributed within a narrow range between 8.12-8.13 g/cc and 312-320 VHN, respectively. Therefore, the structure insensitive saturation induction of the compacts, which varies only with density of the powder metallurgy processed monolithic materials, remained nearly constant. Hereafter, the samples that were consolidated by applying the mechanical pressure at 750 ^{o}C are referred as P-750 and those prepared by applying the pressure when the pyrometer read 450^{o}C are referred as P-450. The P-750 showed lower coercivity than P-450 (Fig. 4.12(b)). The variation of the slope of the curve or remanence could be due to the much higher sensitivity of the steep hysteresis curve to the internal stress in the materials. The P-750 showed: (a) an increase in the ordering fraction, as confirmed by the shift in the superlattice peaks (Fig. 4.13(a)); and (b) an increase in fine morphologies and/or lattice strain, as corroborated by the widening of fundamental peaks (Fig. 4.13(b)). The optical micrographs also displayed finer features for P-750 than P-450 (Fig. 4.14). The nearly equal full width half maximum (FWHM) of the superlattice lines (Fig. 4.13(a)) suggested that the size of the ordered domains (ε), which is calculated using the following Scherrer equation [5], was constant (23 nm).

$$\varepsilon = \frac{K\lambda}{\beta \cos\theta} \quad \ldots\ldots\ldots\ldots\ldots\ldots\ldots\ldots\ldots\ldots\ldots\ldots\ldots\ldots\ldots\ldots(1)$$

where, β is FWHM in radians;

λ is wavelength of Co K_{α} radiation (1.78896Å);

K ~ 1 for equiaxed small diffracting regions;

θ is Bragg angle.

All the aforementioned factors such as increase in ordered alloy fraction, fine morphologies and lattice strain will produce an increase in the coercivity. However, the coercivity of P-750 was consistently lower than that of P-450 by 60 A/m.

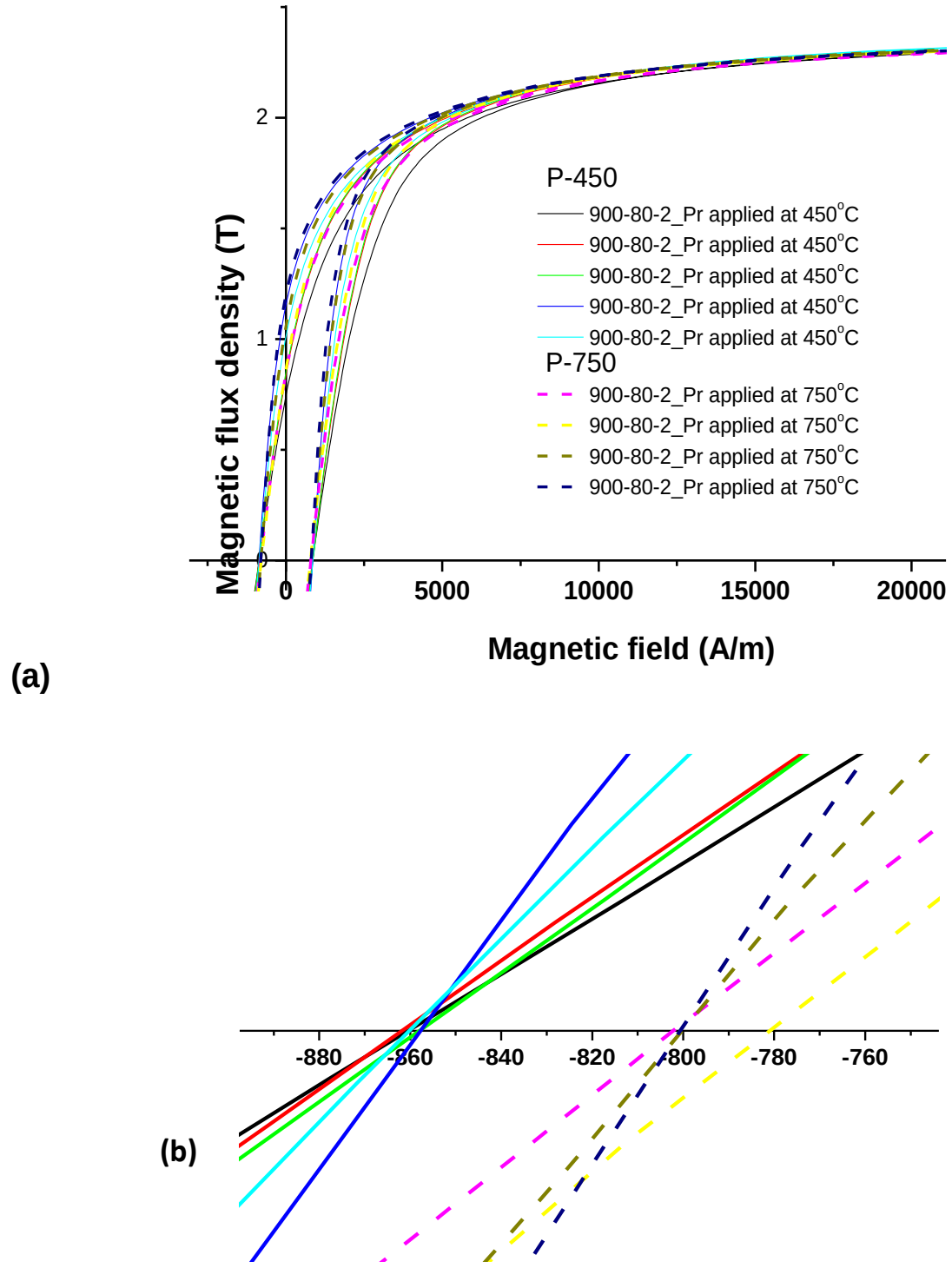

Fig. 4.12 (a) Magnetic hysteresis of P-450 and P-750; (b) enlarged diagram of the abscissa between -750 to -900 A/m shows their influence on coercivity of the compact.

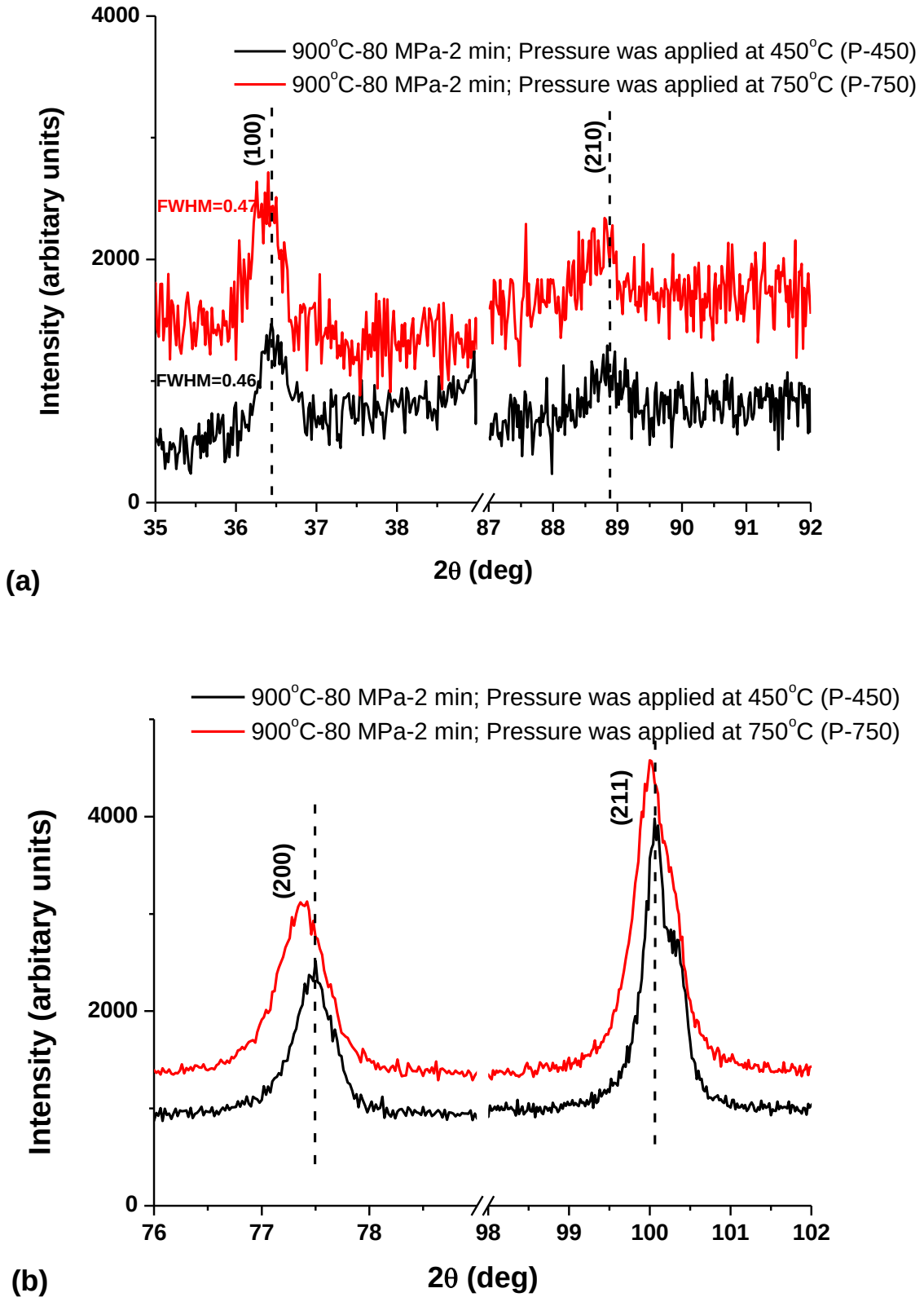

Fig. 4.13 XRD results of P-450 and P-750 showing: (a) (100) and (210) superlattice reflections; (b) (200) and (211) fundamental peaks

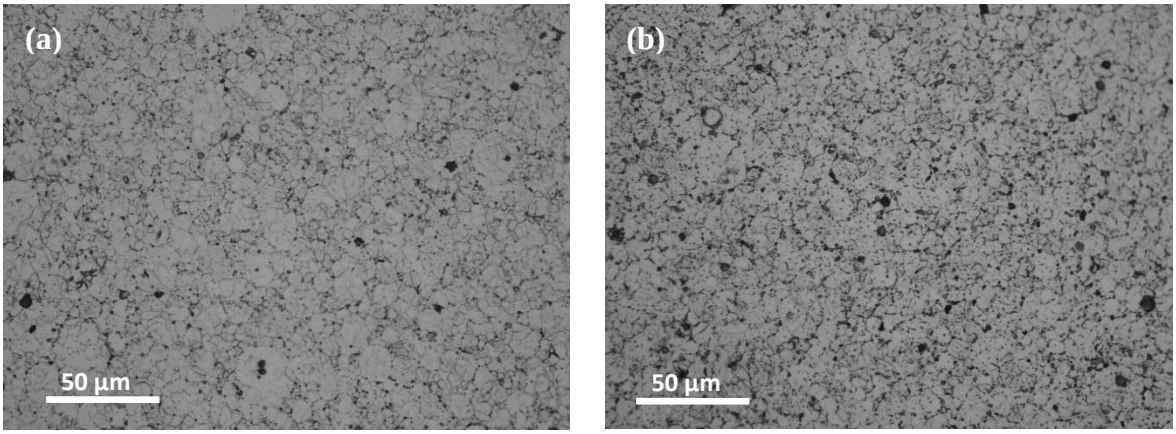

Fig. 4.14 Optical micrographs of: (a) P-450; and (b) P-750 sintered by soaking at 900°C for 2 minutes under 80 MPa pressure

One possible reason that could explain this anomalous coercivity is the presence of a larger volume fraction of fine single domain ordered crystallites in the $80T_{750}^{900}$ than in the $80T_{450}^{900}$ because below a critical size the coercivity of a magnetic material will start to fall [6]. Hertzer [7] showed that the magneto-crystalline anisotropy of the material that increases the coercivity would be significantly reduced when the diameter of the grain is less than the ferromagnetic exchange length (< 100 nm). Under minimum pressure (7 MPa) for three minutes in $80T_{750}^{900}$, the contact area between the particles was small. On the application of pulsed DC current, small ordered grains could have formed at the contact points below $T_{o\text{-}d}$ due to electrical discharge. Those fine grains would be disordered at 900°C. On cooling from 900°C, the disordered fine grain features were completely ordered because the ordered alloy nucleates at the grain boundaries [4]. However, the application of high pressure in $80T_{450}^{900}$ at lower temperatures increased the contact area between the particles. Therefore, the fine grain features that could cause coercivity reduction were reduced in those materials, as reflected by the microstructure and intensity and position of superlattice peaks.

4.5 Effect of sintering pressure variables

Monolithic Fe-Co compacts were prepared by changing the temperature at which the pressure was applied, the rate of pressure application and the maximum pressure to study their influence on the magnetic properties. The magnetic hysteresis response, coercivity and summary of the density and magnetic test results are showed in Fig. 4.15(a), 4.15(b) and Table 4.3, respectively. Corroborating the discussion in the previous section, all the compacts prepared by applying the full mechanical force (either 40 or 80 MPa) below the critical $T_{o\text{-}d}$ showed higher coercivity (highlighted by black oval in Fig. 4.15(b)) and those sintered by starting and finishing the pressure application, in addition to the minimum pressure (7 MPa),

above T_{o-d} displayed lower coercivity (emphasised by red ovals in Fig. 4.15(b)). Two of the three compacts fabricated by applying the force across T_{o-d} exhibited intermediate coercivity (marked by red squares in Fig. 4.15(b)).

Table 4.3 *Magnetic test results of the Fe-Co compacts prepared by varying the temperature at which the mechanical pressure was applied and the rate of pressure application*

Sample designation	Sintering pressure (MPa)	Temperature at which (^oC)		Density (g/cc)	Coercivity (A/m)	Saturation induction (T)
		pressure application was started	maximum pressure was attained			
MLP1	40	600 (below T_{o-d})	650	8.07	893	2.31
MLP2			700	8.06	862	2.28
MLP3	80		650	8.14	867	2.29
MLP4			700	8.12	876	2.29
MLP5	40	800 (above T_{o-d})	850	8.07	835	2.29
MLP6	80			8.14	847	2.30
MLP7	40		900	8.04	834	2.27
MLP8	80	600 (across T_{o-d})	800	8.11	857	2.31
MLP9			850	8.11	856	2.30
MLP10			900	8.11	834	2.31
MLP11	80	450	900	8.13	860	2.31
MLP12		750		8.13	801	2.31

Other than the materials prepared by applying 40 MPa pressure, all the other samples showed nearly equal compact density. Therefore, the saturation induction was found to vary in a narrow range (2.29-2.31T). When the pressure was applied above T_{o-d}, the coercivity of the compact was reduced irrespective of the pressure values and the density of the compact. On increasing the duration under a minimum pressure below T_{o-d}, the coercivity was reduced due to one or both of the reasons discussed in the previous section (Section 4.4). In all the three sets, the sample prepared with the lowest loading rate showed the lowest coercivity as emphasised by the black arrows in Fig. 4.15(b). In order to produce a Fe-Co compact with lower coercivity values in an SPS furnace, the pressure that was added to the minimum pressure (7 MPa) should be applied after 750^oC at the slowest possible rates.

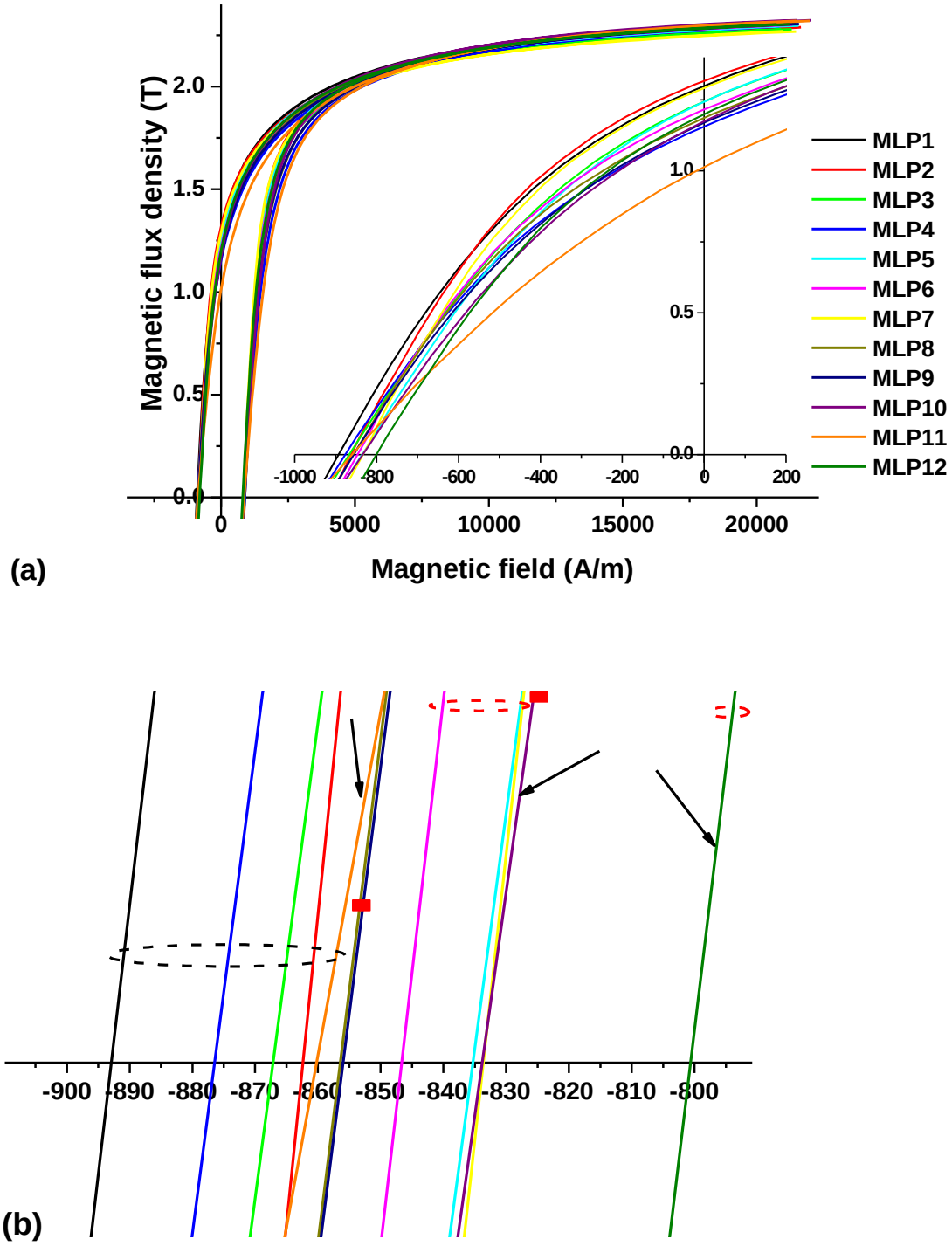

Fig. 4.15 (a) Magnetic hysteresis of the compacts prepared by varying the processing variables as shown in the Table 4.3; (b) enlarged diagram of the abscissa between -790 to -910 A/m shows their influence on coercivity; the curves enclosed/marked by black oval, red ovals and red squares were those of the compacts prepared by starting and finishing the force application above $T_{o\text{-}d}$, below $T_{o\text{-}d}$ and across $T_{o\text{-}d}$, respectively, with all the other sintering variables maintained constant.

4.6 Effect of heating rate

The materials were heated at different rates under a minimum and constant pressure to study its influence on final magnetic properties. In the presence of minimum pressure (7 MPa), the sintering current might have flown through the graphite dies because of the higher resistivity of the porous green compact. The samples were heated by the heat transferred from the heated graphite die set-up. The shrinkage curves superimposed on the heating curves is shown in Fig. 4.16. A positive pattern in the piston speed represents densification, whereas a negative one denotes expansion. Even though expansion of the graphite dies and the powder during heating could reduce the piston speed, significant positive piston speed values were noticed due to densification. Two different stages were noticed in the densification curve and the amplitude of the shrinkage curves in the first stage varied with the heating rates. A maximum positive speed was noticed for the sample heated at the highest heating rate (500^{o}C/min). The second sintering stage was observed during the start of cooling and it was denoted by nearly constant amplitude of the piston speed. As observed by Zhou et al. in spark plasma sintering experiments on alumina [8], during the early stages of sintering, rapid heating would result in a higher sintered density than slow heating.

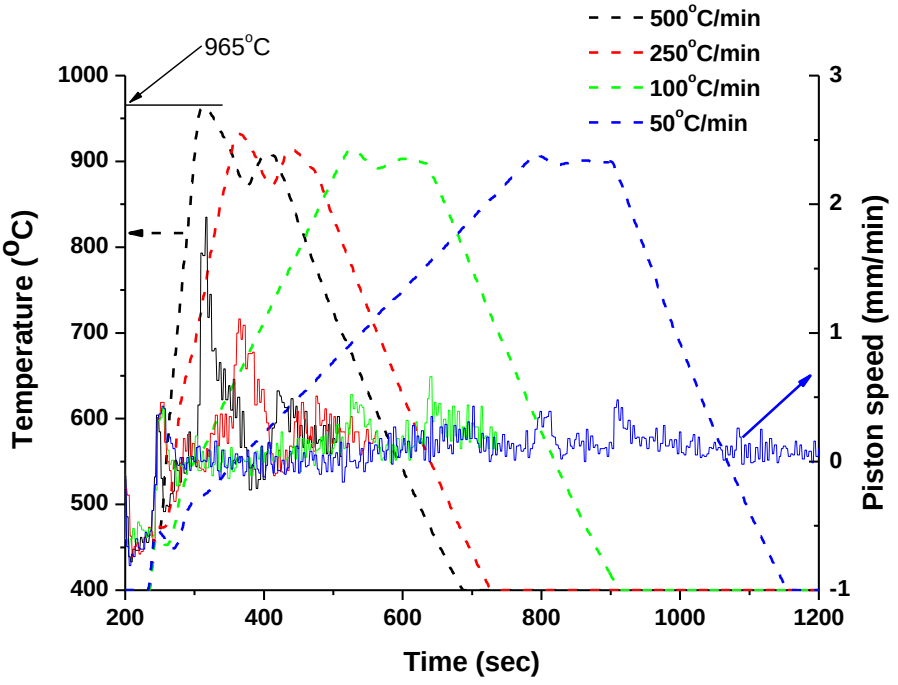

Fig. 4.16 Temperature and piston speed, as recorded by the SPS system, when the Fe-Co samples were heated at the displayed rates under a minimum pressure of 7 MPa; the profiles represented by broken lines are the heating curves, whereas those marked by solid lines are the corresponding shrinkage curves.

Other than in the sample heated at the slowest heating rate (50 ^{o}C/min), changes in the heating rate produced no pronounced changes in the magnetic induction (Fig. 4.17 and Table 4.4). The marginal variations in magnetic induction might be due to the insignificant density differences. Interestingly, the coercivity of the porous compact that was prepared by heating at 500^{o}C/min under 7 MPa pressure was lower than that of a dense compact prepared by heating at 100^{o}C/min (Table 4.4). This was due to the inability of the SPS system to control the temperature during the initial stages of soaking at high heating rates. The maximum temperature reached at the highest heating rate (500^{o}C/min) was 965^{o}C (Fig. 4.16). As a result, the competing grain growth might have favoured over densification and the resulting coarse microstructure reduced the magnetic hardness. The material heated at the slowest heating rate (50 ^{o}C/min) showed the highest magnetic induction and coercivity values (Fig. 4.17). Although density enhancement supported the magnetic induction improvement, the increase in the coercivity suggested that slower heating rates (≤ 50 ^{o}C/min) increased the volume fraction of long range ordered structures.

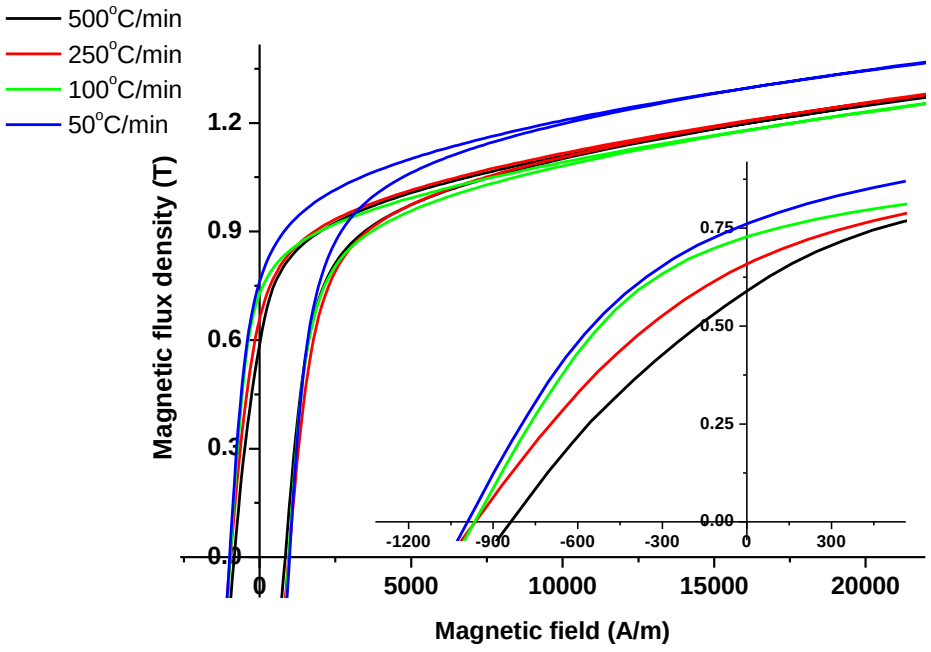

Fig. 4.17 Magnetic hysteresis curves of Fe-Co compacts prepared by heating at the shown rates; the inset is the enlarged image of the second quadrant to show their influence on remanence and coercivity.

Table 4.4 *Magnetic test results of Fe-Co compacts prepared by heating at the shown rates*

Heating rate (^{o}C/min)	Temp.-Pr.-time (^{o}C-MPa-min)	Density (g/cc)	Coercivity (A/m)	Induction at 20 kA/m (T)
500	900-7-2	6.45	838	1.25
250		6.49	964	1.26
100		6.55	966	1.23
50		6.61	991	1.35
100	900-80-2	8.12	862	2.3

4.7 Effect of cooling rate

The samples sintered under identical conditions were cooled controllably using the high current in the SPS furnace at three different rates to understand their effects on final properties. It was not possible to control the cooling rate higher than 200^{o}C/min by controlling the current flow in SPS. The density of the compact was not changed by the cooling rate as shown by the Archimedes results (Table 4.5) and optical micrographs (Fig. 4.18).

The material cooled at the highest rate (200^{o}C/min) exhibited higher coercivity than those cooled at relatively lower rates (100 and 50 ^{o}C/min) due to the increase in the locked-up stresses. Similar to the observations in the heating rate experiments, the material cooled at the lowest cooling rate (10^{o}C/min) showed the highest coercivity due to the increase in the long range order parameter (S). This was corroborated by the XRD results where the sample cooled at 10^{o}C/min showed a shift in the superlattice peak positions to lower angles because of the increase in the ordering fractions (Fig. 4.19). The reduction in the FWHM of the superlattice line for the samples cooled at 100^{o}C/min suggested that the sizes of the ordered domains were increased. A change in the long range order parameter (S) from 0 to 1 would produce only 4 % rise in the saturation induction values [9]. Therefore, the change in the ordering fractions, which was insignificant in these materials, was not highly reflected in the magnetic induction values.

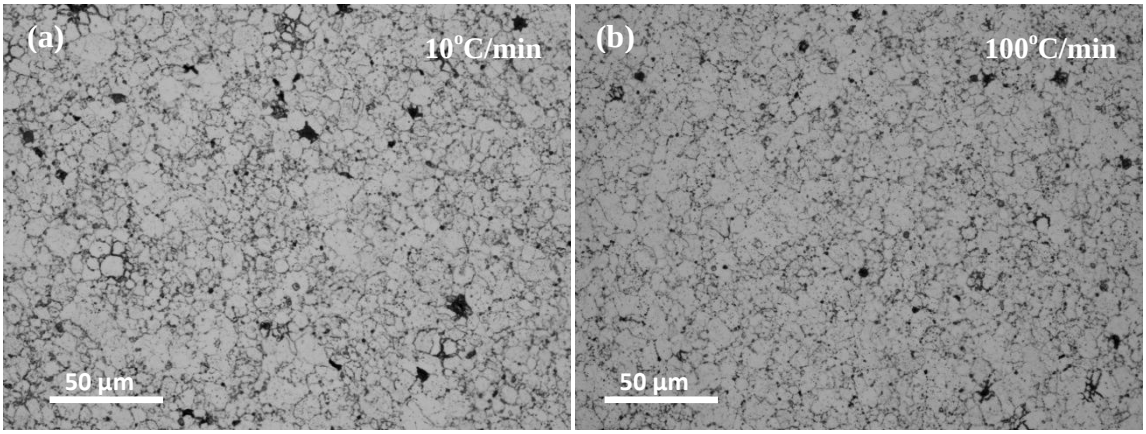

Fig. 4.18 Optical micrographs of Fe-Co compacts prepared by cooling at the displayed rates

Table 4.5 *Magnetic test results of Fe-Co compacts prepared by cooling at the shown rates following sintering*

Cooling rate (°C/min)	Density (g/cc)	Coercivity (A/m)	Saturation induction (T)
10	8.13	828	2.32
50	8.12	792	2.31
100	8.13	803	2.31
200	8.13	817	2.30

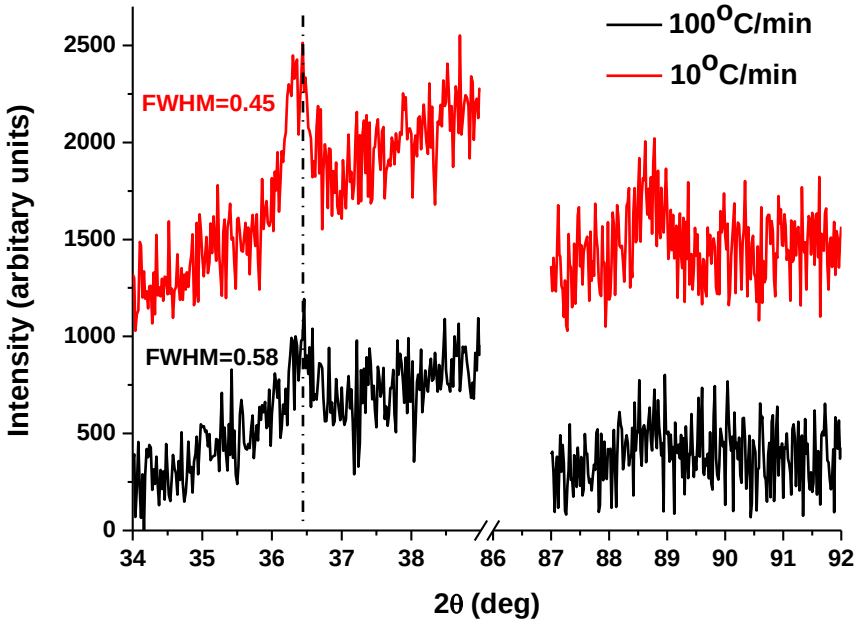

Fig. 4.19 Slow scan XRD result showing (100) and (210) superlattice reflection of Fe-Co compacts prepared by cooling at the shown rates

4.8 Effect of time of removal of mechanical force

Experiments were conducted to study the role of the temperature at which the mechanical pressure was removed during cooling. All the other sintering variables such as sintering temperature, pressure, soaking time, heating rate and cooling rate were maintained constant. Three samples were soaked at 900^{o}C for 11 minutes and the mechanical pressure was reduced from 80 MPa to 7 MPa when the pyrometer read 900, 600 and 450^{o}C. The latter two temperatures were below order-disorder transition temperature. From the hysteresis response, it is clear that the temperature at which the pressure was changed had a notable effect on the magnetic characteristics (Fig. 4.20).

It has to be noted that in the presence of mechanical pressure, the order-disorder transition in the dense compact during cooling was marked by a sudden rise in the sintering current (Fig. 4.21). The phase transitions were clearly shown in the SPS current profile in the presence of mechanical pressure due to the improved electrical contact. The coercivities of the materials for which the mechanical pressure was released below the transition temperature were increased and their remanences were reduced. This was either due to the increase in the residual stresses because of the constraint imposed by the mechanical pressure for the lattice expansion or due to the increase in the volume fraction of the long range ordered structures.

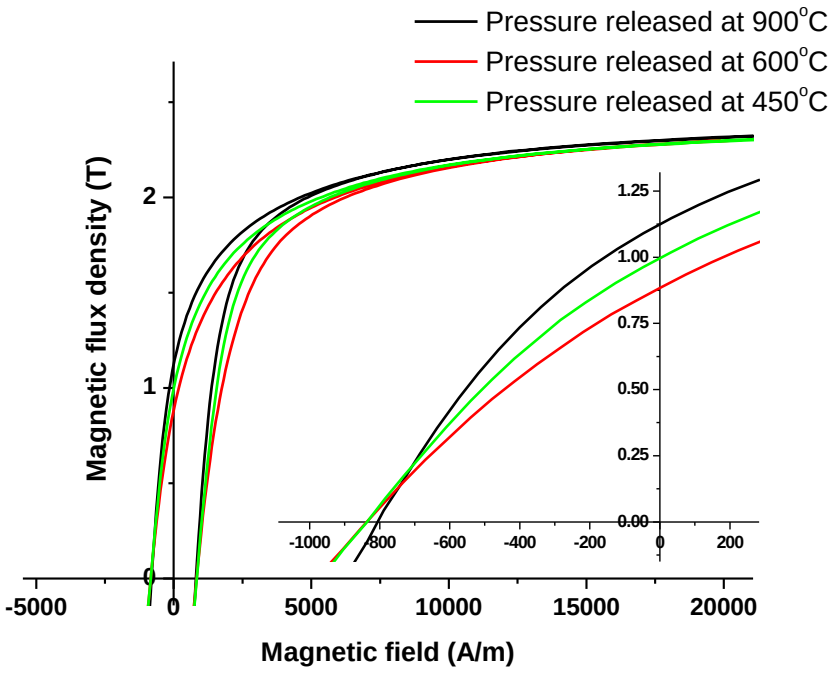

Fig. 4.20 Magnetic hysteresis curves of the monolithic compacts prepared by commencing the force removal, when the pyrometer read the displayed temperature; the inset is the enlarged image of the second quadrant to show their influence on remanence and coercivity

It was apparent that the magnetic and mechanical properties could be tuned by varying the temperature at which the mechanical pressure was applied and removed. By reducing the heating and cooling rates below the order-disorder transition temperature under pressure and high current, the volume fraction of the ordered structure can be increased.

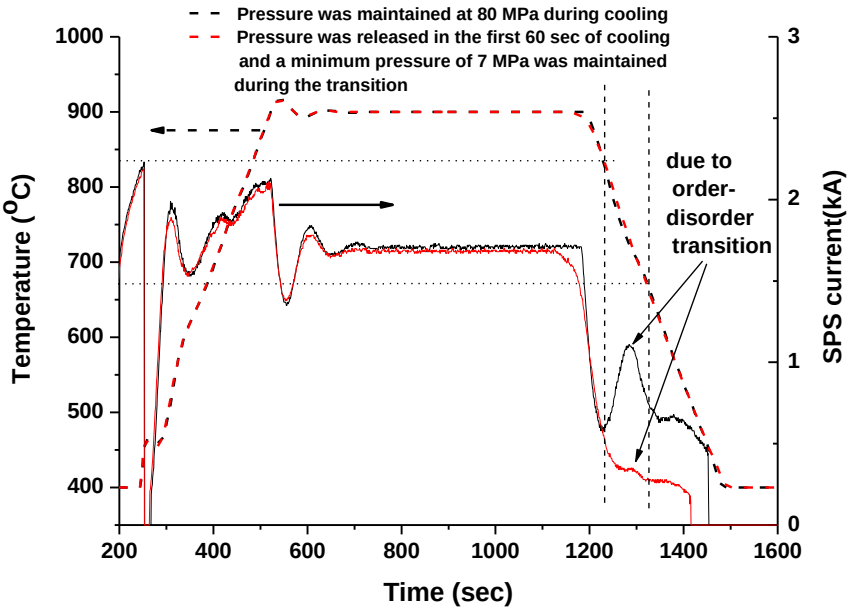

Fig. 4.21 Temperature and current profile, as recorded by the SPS system, showing the variation in the current flow during cooling at the disorder-order transition temperature in the presence of 80 MPa (black) and 7 MPa (red) mechanical pressure; the profiles represented by broken lines are the heating curves, whereas those marked by solid lines are the corresponding SPS current curves.

4.9 Anisotropy in Fe-Co compacts prepared by SPS

The possibility of anisotropy development during spark plasma sintering was investigated by preparing thick cylindrical compacts and by measuring their magnetic properties in all the three directions using cube samples cut out of them. The compacts were prepared at above and below the Curie transition temperature to examine whether their magnetic behaviour would cause any change in the final properties. From the coercivities, it was evident that spark plasma sintering of a ferromagnetic material induced anisotropy only when the whole sintering cycle was in the ferromagnetic regime (Table 4.6). When the maximum temperature was increased above the Curie transition, the properties were constant in all directions. The lowest coercivity along the direction of force application during sintering, in relation to the other two directions suggested that the current-magnetic spin interaction caused the easy direction to align along it. However, sintering a magnetic material

in the paramagnetic region, where the magnetic spins were completely absent, produced no preferred orientation and hence resulted in a material with isotropic magnetic properties. The reduction in the coercivity on increasing the sintering temperature was due to grain growth as evidenced from the optical micrographs (Fig. 4.22). The remanence of the cube samples sintered below Curie temperature varied over a wide range in all the three directions, whereas those prepared above T_c showed nearly equal remanence in all the three directions.

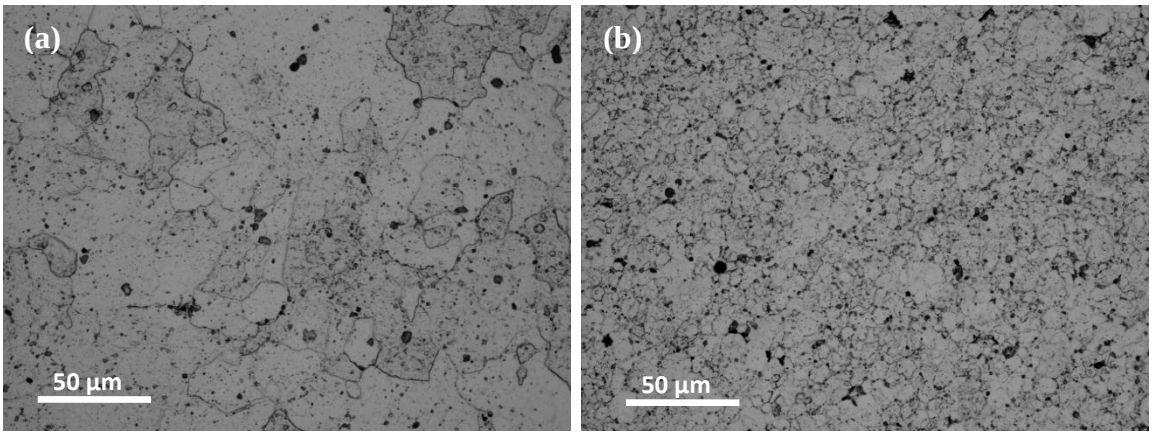

Fig. 4.22 Optical micrographs of thick Fe-Co compacts prepared by soaking at (a) 1050 ^oC; (b) 900 ^oC for 5 minutes under 80 MPa pressure.

Table 4.6 *Summary of the magnetic test results of the cube samples, as measured along the three directions*

Sample No	Direction to uniaxial force application	Density (g/cc)	Coercivity (A/m)	Remanence (T)	Saturation induction (T)
900-80-5	Parallel	8.10	829	0.94	2.29
	Perpendicular		902	0.75	2.28
	Perpendicular		896	1.07	2.28
1050-80-5	Parallel	8.09	474	0.45	2.27
	Perpendicular		482	0.46	2.27
	Perpendicular		471	0.49	2.27

4.10 Effect of heat treatments on the sintered compacts

Fe-Co compacts, sintered at 900^{o}C for 2 minutes under a mechanical pressure of 80 MPa were heat treated for 1, 5 and 10 hours in an inert atmosphere at temperatures below (500 and 700^{o}C) and above (900 and 1050^{o}C) order-disorder transition temperatures. Those experiments were performed to study the influence of post heat treatments on the evolution of long range ordered structures and in turn on the magnetic properties. An increase in the ordering fractions caused a shift in the superlattice positions to smaller angles 2θ because of the expansion of the lattice by ordering. Therefore shifts in peak positions to lower angles were noticed in both the (100) and (210) superlattice reflections (Fig. 4.23, 4.24).

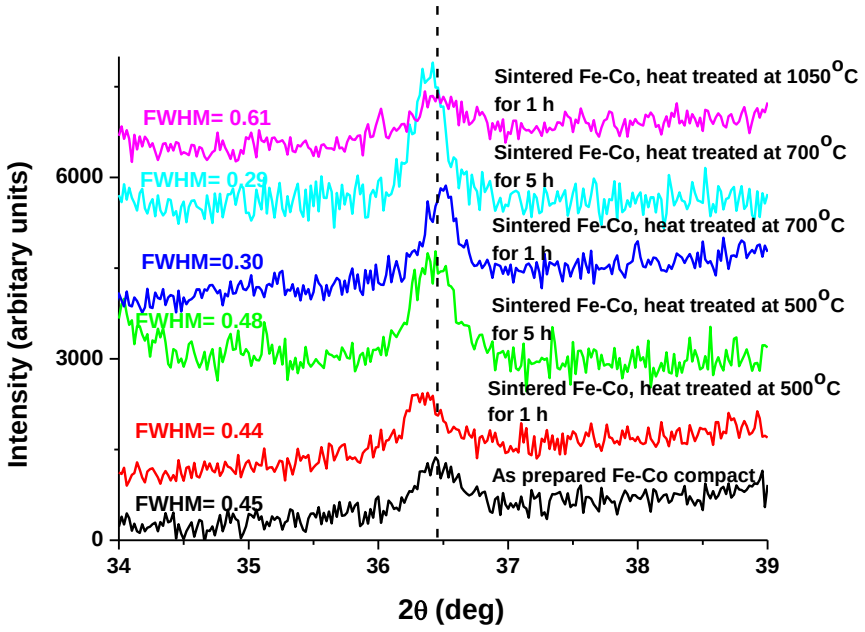

Fig. 4.23 Slow scan XRD result showing the (100) superlattice reflection of the as-sintered and heat treated Fe-Co compacts; the heat treatment conditions and the full width half maximum values of the peaks are depicted in the image

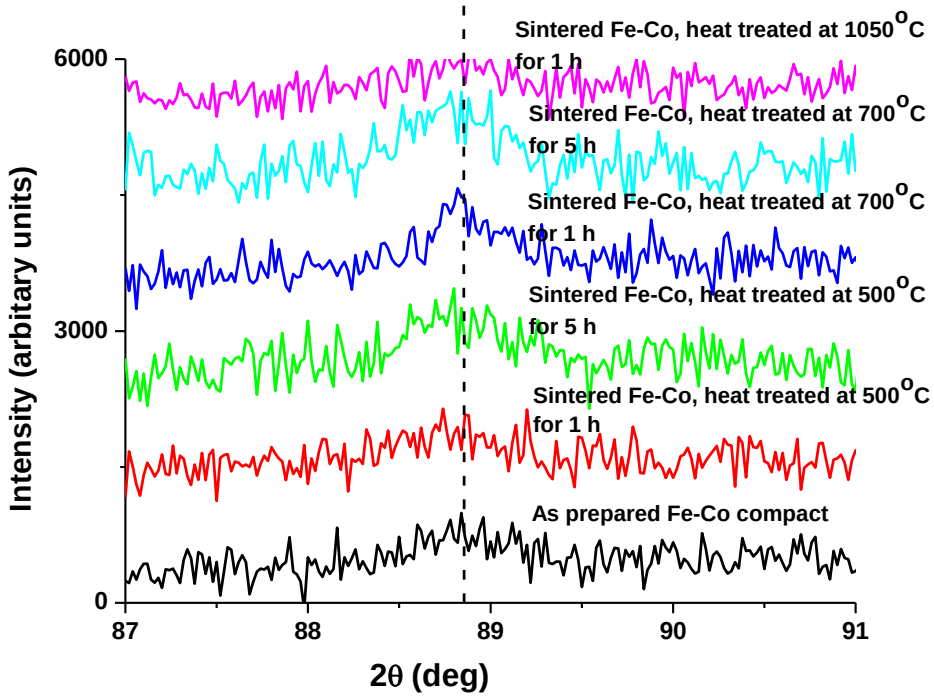

Fig. 4.24 Slow scan XRD result showing the (210) superlattice reflection of the as-sintered and heat treated Fe-Co compacts

The heat treatments of compacts at temperatures much lower than order-disorder transition temperature (at 500°C) did not produce any notable change in the full width half maximum (FWHM) of the superlattice lines (Fig. 4.23). This suggested that the anti-phase domain sizes were not changed. However, a reduction in the FWHM values was observed for

the samples sintered at a temperature close to the order-disorder temperature (i.e. at 700^{o}C) and it confirmed the increase in the size of the antiphase domains (Fig. 4.23). Heat treatment of Fe-Co at temperatures above the Curie point (990 ^{o}C) produced a reduction in the anti-phase domain sizes, as implied by the broad superlattice reflections and a fall in the intensity of superlattice lines. This implied that the nucleation and growth of antiphase domains were not favoured by the coarse grain morphology (Fig. 4.25). This could be because the grain boundaries act as the nucleation sites for the ordered alloy [10].

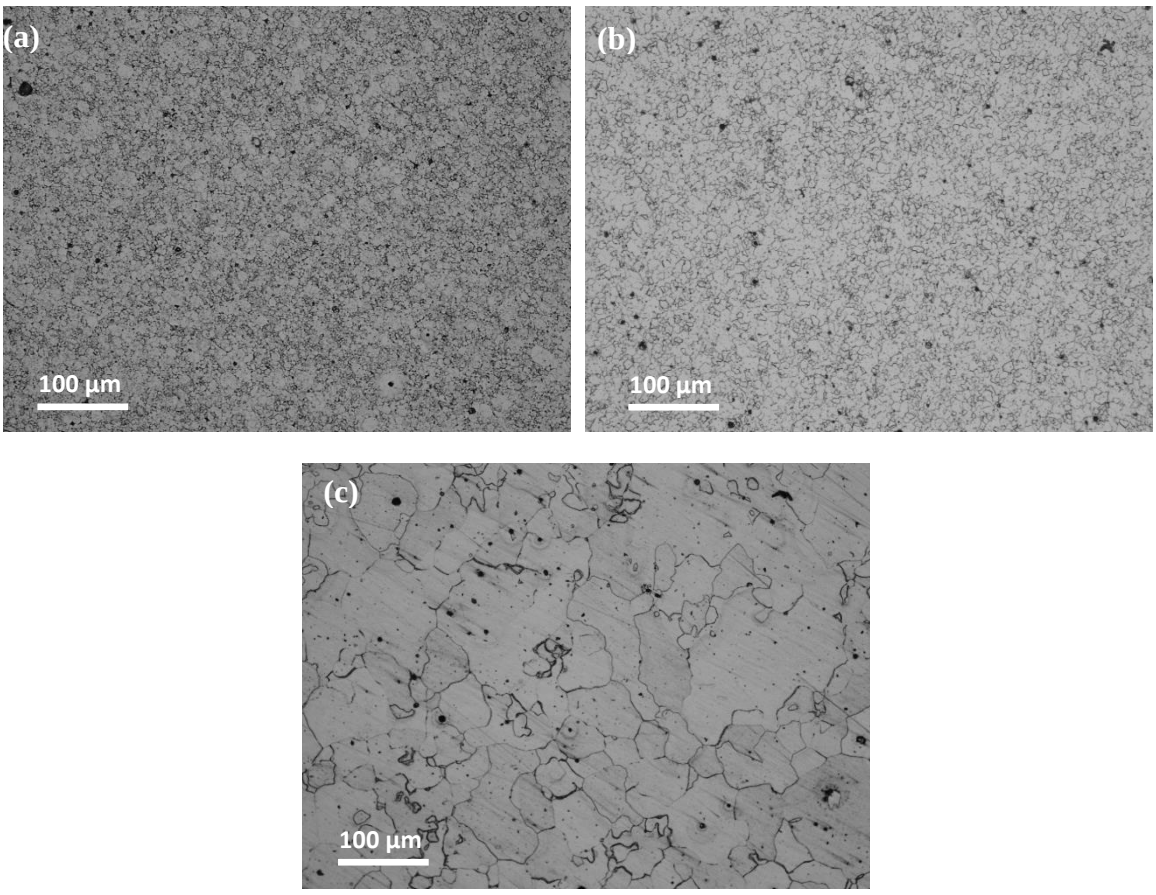

Fig. 4.25 Optical micrographs of Fe-Co compact: (a) in the as-prepared state; and after annealing treatments at: (b) 900 ^{o}C for 1 hour; and (c) 1050^{o}C for 1 hour

The hysteresis curves of the compacts heat treated for different durations at 500, 700, 900 and 1050^{o}C are compared in Fig. 4.26 (a), 4.26(b), 4.27(a) and 4.27(b), respectively. The saturation induction of the heat treated materials showed improvements, which was attributed either due to density enhancements or due to the increase in the ordering fractions. In the case of coercivity, improvements in compact density and grain growth reduce coercivity, whereas any increment in the long range order parameter increases coercivity. The materials heat

treated at temperatures below T_{o-d} showed an increase in coercivity and saturation induction due to the increase in the ordering fractions.

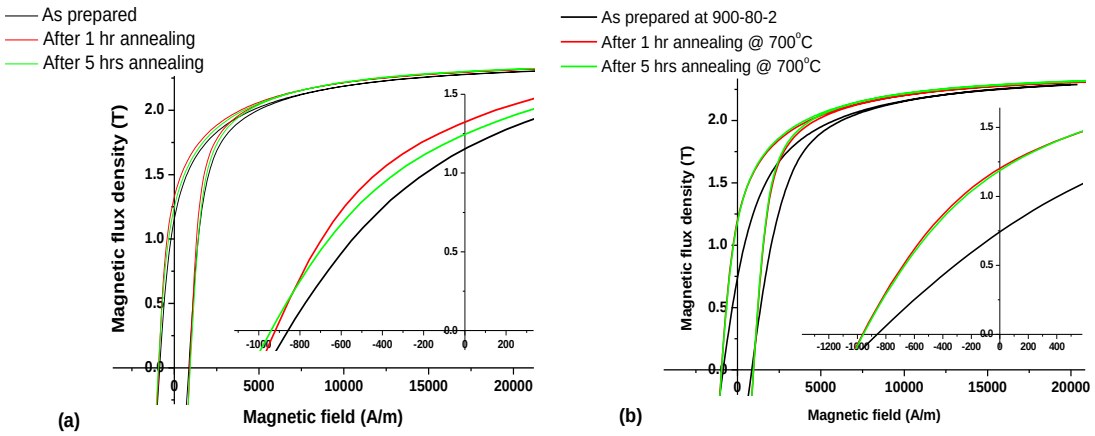

Fig. 4.26 Magnetic hysteresis curves of Fe-Co compact before and after annealing for the shown durations at: (a) 500 °C; (b) 700°C; the inset is the enlarged image of the second quadrant to show their influence on remanence and coercivity

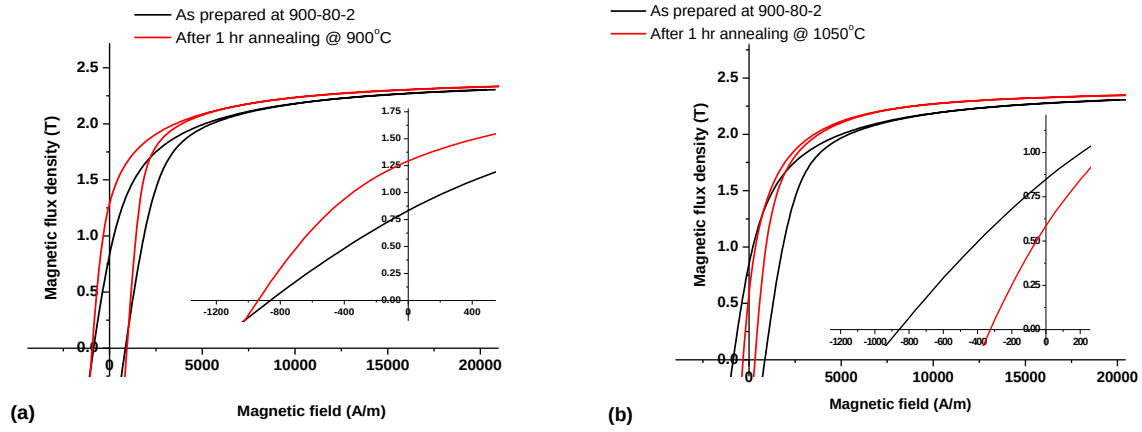

Fig. 4.27 Magnetic hysteresis curves of Fe-Co compact before and after annealing for the shown durations at: (a) 900 °C; (b)1050 °C; the inset is the enlarged image of the second quadrant to show their influence on remanence and coercivity

The compacts treated at 700°C formed the fully ordered structure in 1 hour as the coercivity, permeability and remanence remained constant on further heat treatment (Fig. 4.26(b)). However, the compact treated at 500°C showed a rise in coercivity and a fall in remanence and permeability with the soaking time (Fig. 4.26(a)). It suggested that complete ordering was not accomplished in 1 hour at 500°C due to the reduced ordering kinetics. The formation of new ordered domains increases the stresses in the material and hence, the remanence and permeability fell with soaking time. Although increases in the density and grain size favoured coercivity reduction in the sample heat treated at 900 °C for 1 hour (Fig.

4.25 (a), (b)), it was higher for the heat treated samples than the as-prepared ones. This was due to the ordering promoted by slow cooling of the sample in the annealing furnace. As a result, the coercivity increment was lower than the material treated at 700^{o}C. The increases in the density and ordering produced a rise in the saturation induction (Fig. 4.26(a)). On increasing the annealing temperature to 1050^{o}C, the saturation induction was increased and the coercivity was reduced significantly (Fig. 4.26(b). This could be due to the increase in density and grain size (Fig. 4.25 (a), (c)). Increases in ordering fraction, grain size, density and reduction in stresses produced a rise in the permeability, which was confirmed by the increase in the slope of the curve in the second quadrant (Fig. 4.27(b)).

4.11 FeCo based alloys processed by PM route

Table 4.7 summarises the attempts made to process FeCo based materials by powder metallurgy route and the saturation magnetisation and density values reported. It is evident that SPS helped to improve saturation induction values of the compacts formed from pre-alloyed powders significantly by improving the sintering density. FeCo materials processed under optimum SPS conditions, exhibit density values close to that of theoretical values. As a result, their magnetic induction is close to that of wrought alloys of similar composition, which is 2.4 T [4].

Table 4.7 *Saturation induction and density of FeCo based alloy processed by PM route*

Material	PM processing route	Density	Saturation induction (T)	Ref.
Fe-50 Co	metal injection moulding (MIM)	8.03 g/cc	1.69	[11]
Fe-49Co-2V	MIM	7.82 g/cc	1.82	[11]
Fe-50 wt% Co	Cold compaction followed by sintering	95% relative density	2.15	[12]
Fe-Co alloy	Not mentioned	8.0 g/cc	2	[13]
Fe-49Co-2V	Not mentioned	> 7.4 g/cc	2.0	[14]
Fe-50 Co	Not mentioned	> 7.4 g/cc	1.7	[14]
Fe- 49 wt %Co	SPS	8.14 g/cc (99.5% relative density)	2.34	This work

4.12 Optimization of SPS parameters for composite fabrication

From the magnetic and mechanical property results of the spark plasma sintered monolithic materials, it is clear that near-theoretical dense compacts of Fe-50Co can be prepared in shorter durations (2-5 mins) and with minimal grain growth when the maximum temperature was maintained as 900^{o}C. The employment of graphite dies limited the mechanical pressure applied during sintering to be 80 MPa. In order to minimize the interfacial reactions and to maintain the structural integrity of the CNTs, the composite mixtures containing CNTs were soaked at the maximum temperature for 2 minutes. The composite mixtures containing SiC particles and whiskers were dwelled at 900^{o}C for slightly long duration (5 minutes) to promote densification. For all the composite materials, the pressure was applied when the pyrometer read 450 ^{o}C and the heating rate was maintained at 100^{o}C/min. All the samples were cooled by the convectional heat transfer capability of the cooling water that flow through the steel rams.

References

1. J. M. Loureiro, A. C. Batista, V. A. Khomchenko, B. F. O. Costa, G. Le Caër, Order-disorder phenomena from X-ray diffraction in FeCo alloys annealed and ground at high energy, *Powder Diffr.* **26 [3]**, 267-272(2011)
2. Y. Ustinovshikov, S. Tresheva, Character of transformations in Fe–Co system, *Mat. Sci. Eng. A* **248**, 238–244(1998).
3. T. Fong, K. Sadananda and M. J. Marcinkowski, Effect of strain, temperature, and atomic order on slip deformation in FeCo, *Metal.Trans.* **5**, 1239–1247(1974)
4. R. S. Sundar and S. C. Deevi, Soft magnetic FeCo alloys: alloy development, processing, and properties, *Inter. Mater. Rev.* **50**, 157-192 (2005)
5. D.W Clegg and R.A Buckley, The disorder-order transformation in iron-cobalt- based alloys, *Met. Sci.* **7**, 48-54(1973)
6. B.D Cullity and C.D Graham, Introduction to magnetic materials, New Jersey, IEEE press and A John Wiley & sons, Inc., publisher, 2nd edition (2009), pp. 360-364
7. G. Herzer, Soft Magnetic Nanocrystalline Materials, *Scripta Metallurgica et Materialia* **33**, 1741-56 (1995)
8. Y. Zhou, K. Hirao, Y. Yamauchi and S. Kanzaki, Effects of heating rate and particle size on pulse electric current sintering of alumina, *Scripta Mater.* **48**, 1631–1636 (2003)
9. T Sourmail, Near equiatomic FeCo alloys: Constitution, mechanical and magnetic properties, *Prog. Mater. Sci.* **50**, 816–880 (2005)
10. M. Rajkovic and R.A Buckley, Ordering transformations in Fe-50Co based alloys, *Met. Sci.* **15**, 21-29 (1981)

11. A. Silva, P. Wendhausen, R. Machado and W. Ristow Jr, Magnetic properties obtained for Fe-50Co alloy produced by MIM with elemental powders, *Mater. Sci. Forum* **534-536** 1353-56 (2007).
12. W. Yamagishi, K. Hashimoto, T. Sato, S. Ogawa and Z. Henmi, Magnetic properties of Fe-Co alloys produced by powder metallurgy, *IEEE Trans. on Magnetics* **Mag-22**, 641-643 *(*1986).
13. J.A. Bas, J.A. Calero and M.J. Dougan, Sintered soft magnetic materials: Properties and applications, *Journal of Magnetism and Magnetic Materials* **254–255**, 391-398 (2003).
14. P.W. Lee, *ASM Handbook - Powder Metal Technologies and Applications* **7**, ed. (American Society for Metals, 1998) p 2523.

Chapter 5

Results and discussion: SiC particulate reinforced composites

5.1 Introduction

The influence of the addition of coated and uncoated particulates on the magnetic and mechanical behaviour of Fe-Co alloy is discussed in this chapter. This chapter begins with the discussion on the crystallographic features of the electroless copper, Ni-P, cobalt and duplex plated SiC particles using the diffractograms as obtained using XRD. It also delineates the microstructural, compositional and crystallographic differences in the sintered Fe-Co alloys with and without fillers using optical micrographs, SEM images, EDX line profiles and XRD diffractograms. The magnetic and mechanical responses of the composite and monolithic materials are explained in the later part of this chapter and are correlated with the microstructural, compositional and phase findings.

5.2 Characterisation of bare and coated SiC particles

5.2.1 Morphology of as-received particles

The SEM image of the SiC particles in the as-received condition is shown in Fig. 5.1. Morphologically, the particles were non-uniform in size with a broad size distribution (10 – 70 μm) and were irregular in shape with angular edges.

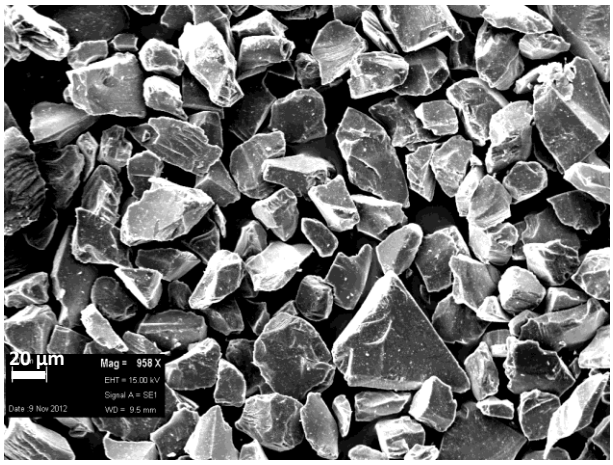

Fig. 5.1 SEM micrographs of as-received SiC particles

5.2.2 Crystallographic phases in the electroless plated particles

The XRD histograms of the uncoated and Cu, Ni-P, Co and duplex (Cu-(Ni-P)) coated SiC particles are compared in Fig. 5.2. The SiC substrate peaks in the copper, Ni-P and duplex plated particles were shifted to lower angles with respect to their position for the uncoated particles. This was due to the strong nature of the compressive stresses acting on the SiC surface in all the coated particles other than those with cobalt coating. An equivalent tensile stress would have been developed in the coating to compensate the compressive residual stresses. The broad hump in the XRD patterns of Ni-P (both prepared under acidic and alkaline conditions) and duplex plated particles confirmed the amorphous nature of the coatings, whereas the relatively sharp peaks for copper and cobalt plated particles corroborated their crystalline nature. It has been reported that phosphorus content in the Ni-P coating increases with the drop in the pH of the plating bath [1]. The EDX results of the coating confirmed that the phosphorus content in the Ni-P coating plated using an alkaline bath (pH 8.5) was less than that plated using an acidic bath (pH 4.5).

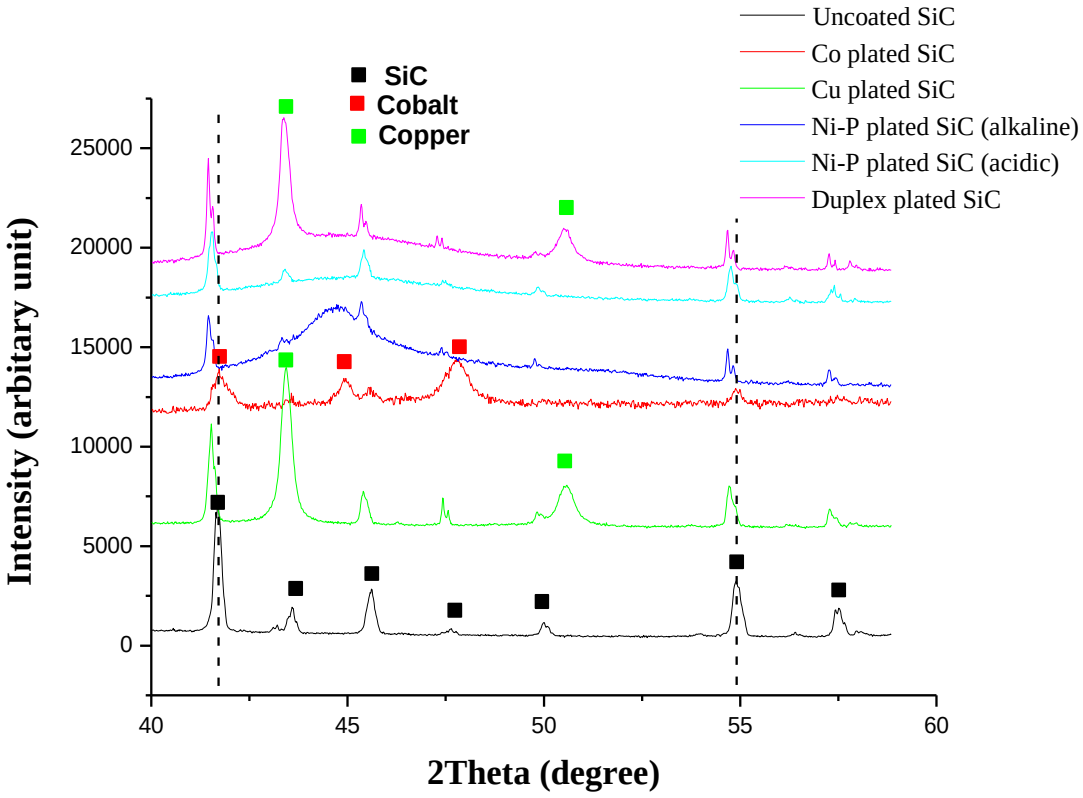

Fig. 5.2 X ray diffraction pattern of coated and uncoated SiC particles

5.2.3 Thermal stability of electroless Ni-P coatings

The DSC result of Ni-P plated particles using acidic and alkaline baths and uncoated particles are compared in Fig. 5.3. Similar to the report of Song et al. [1], two exothermic peaks at temperatures of 345 and 405^{o}C were observed for coated particles with lower phosphorus content. Hentschel et al.[2], related the first peak to structural transformations such as recovery and grain growth, and the chemical effects such as the segregation of P to Ni grain boundaries and the second peak to the crystallisation of the coating. In contrast, particles plated with Ni-P in the acidic bath showed a weak peak associated with structural and chemical effects and a sharp peak at about 345^{o}C corresponded to the decomposition of the amorphous Ni–P.

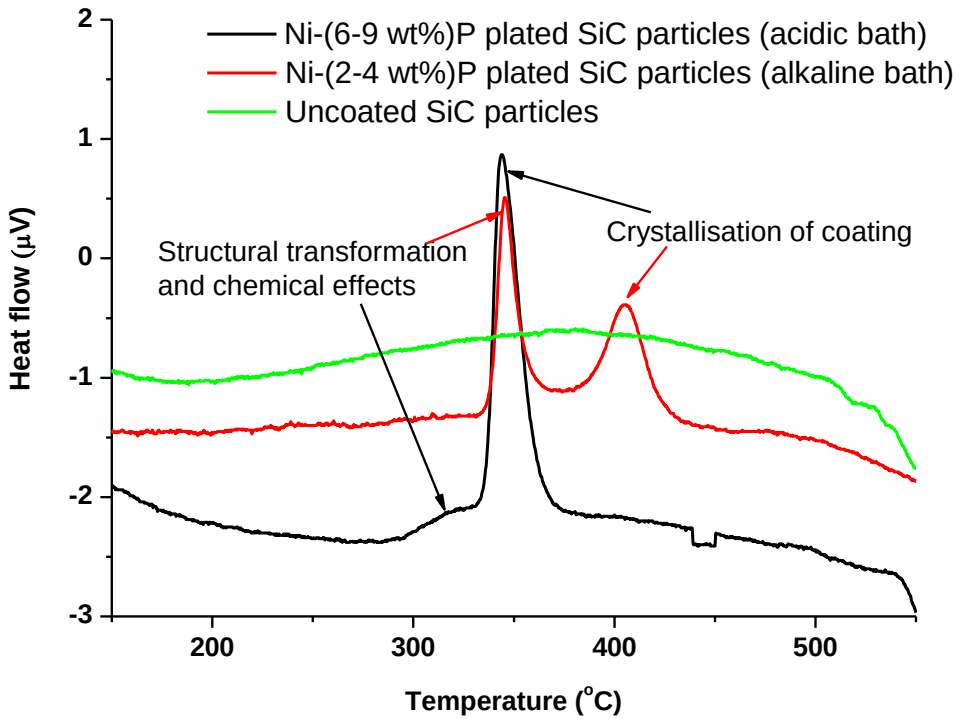

Fig. 5.3 DSC curves of SiC particles and Ni-P plated particles containing different amount of phosphorus

The X-ray diffractograms of the Ni-P coating prepared using the acidic and alkaline plating baths are compared with those for the corresponding heat treated particles in Fig. 5.4 and 5.5, respectively.

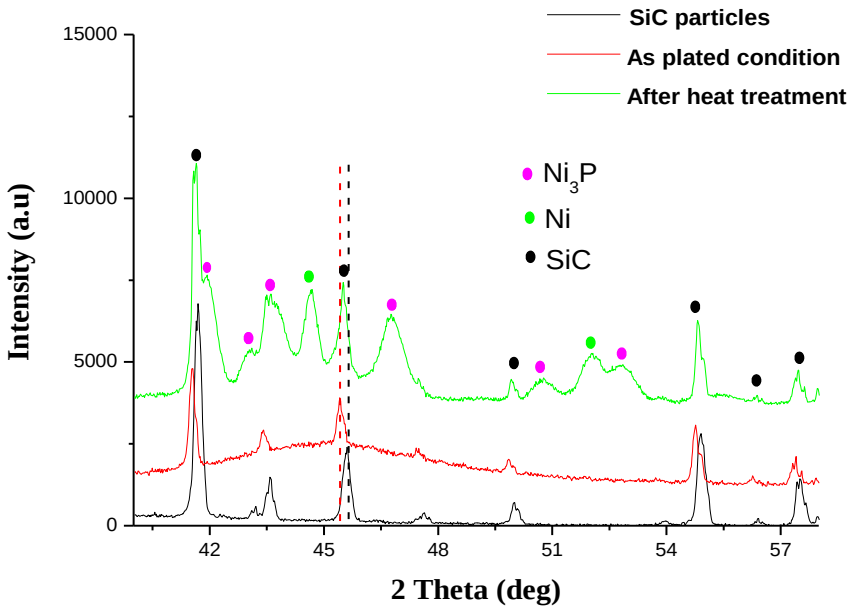

Fig. 5.4 X- ray diffractograms of SiC particles in the as-prepared under acidic condition and after thermal treatment at 350^{o}C for 1 hour.

Heat treatment at or above the temperature, where the exothermic peak is observed in the DSC scan, resulted in the decomposition of amorphous Ni-P coating into crystalline Ni and Ni_3P. The crystallisation of the coating caused a reduction in the residual stress levels on the SiC particle surface as evidenced by the shift in the XRD peaks of the substrate particles towards those of the uncoated particles.

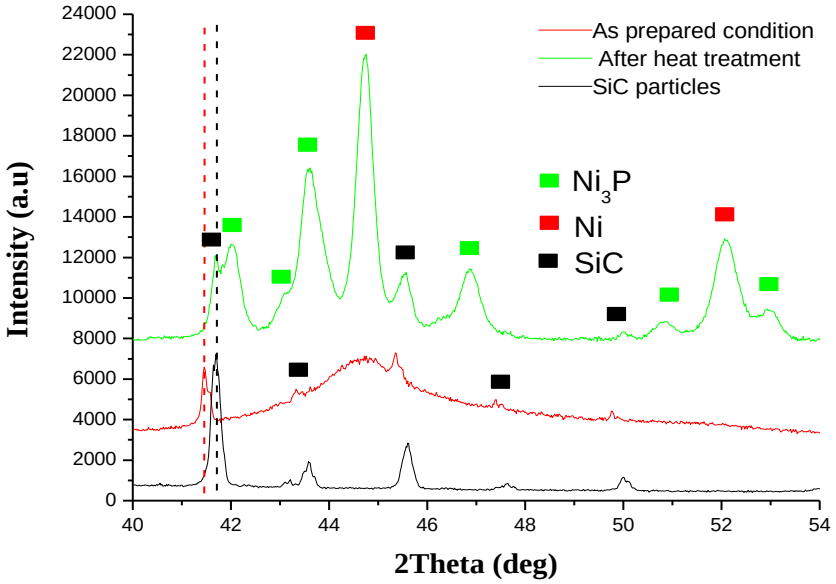

Fig. 5.5 X- ray diffractograms of SiC particles in the as-prepared under alkaline condition and after thermal treatment at 400^{o}C for 1 hour

5.3 Characterisation of monolithic and SiC particulate composite materials

5.3.1 Microstructure

The optical micrographs of Fe-Co alloy composites containing SiC particles in the as-polished and etched conditions are shown in Fig. 5.6 and 5.7, respectively.

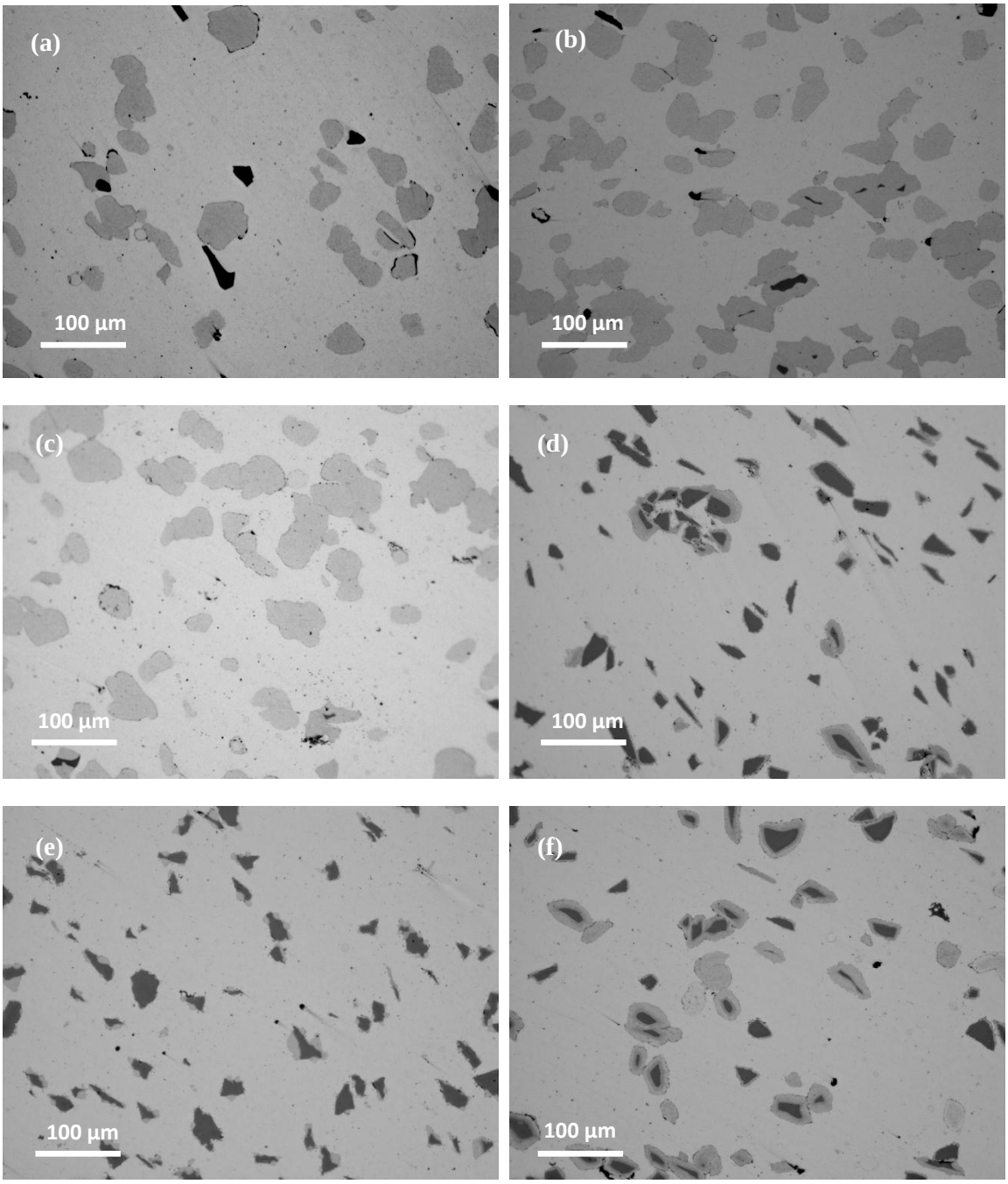

Fig. 5.6 Optical micrographs of Fe-Co composites with: (a) 5 vol % of uncoated; and 10 vol% of (b) uncoated; (c) copper coated; (d) Ni-P coated; (e) cobalt coated; (f) duplex coated SiC particles in the as-polished condition.

It was apparent that mixing in a ball mill without any grinding medium was sufficient to realise uniform distribution of particulates in the matrix material. The particulates with copper coating and without any coating appeared to be bigger and rounder (Fig. 5.6(a)-(c)), whereas those with Ni-P, Co and duplex coatings (Fig. 5.6(d)-(f)) showed the edges of angular particles and a distinct reaction zone at the particle-matrix interface. In composites containing 10 vol% of uncoated and copper coated particles, the reaction zone grew rapidly and even coalesced with that of the neighbouring particles (Fig. 5.6(a), (b)).

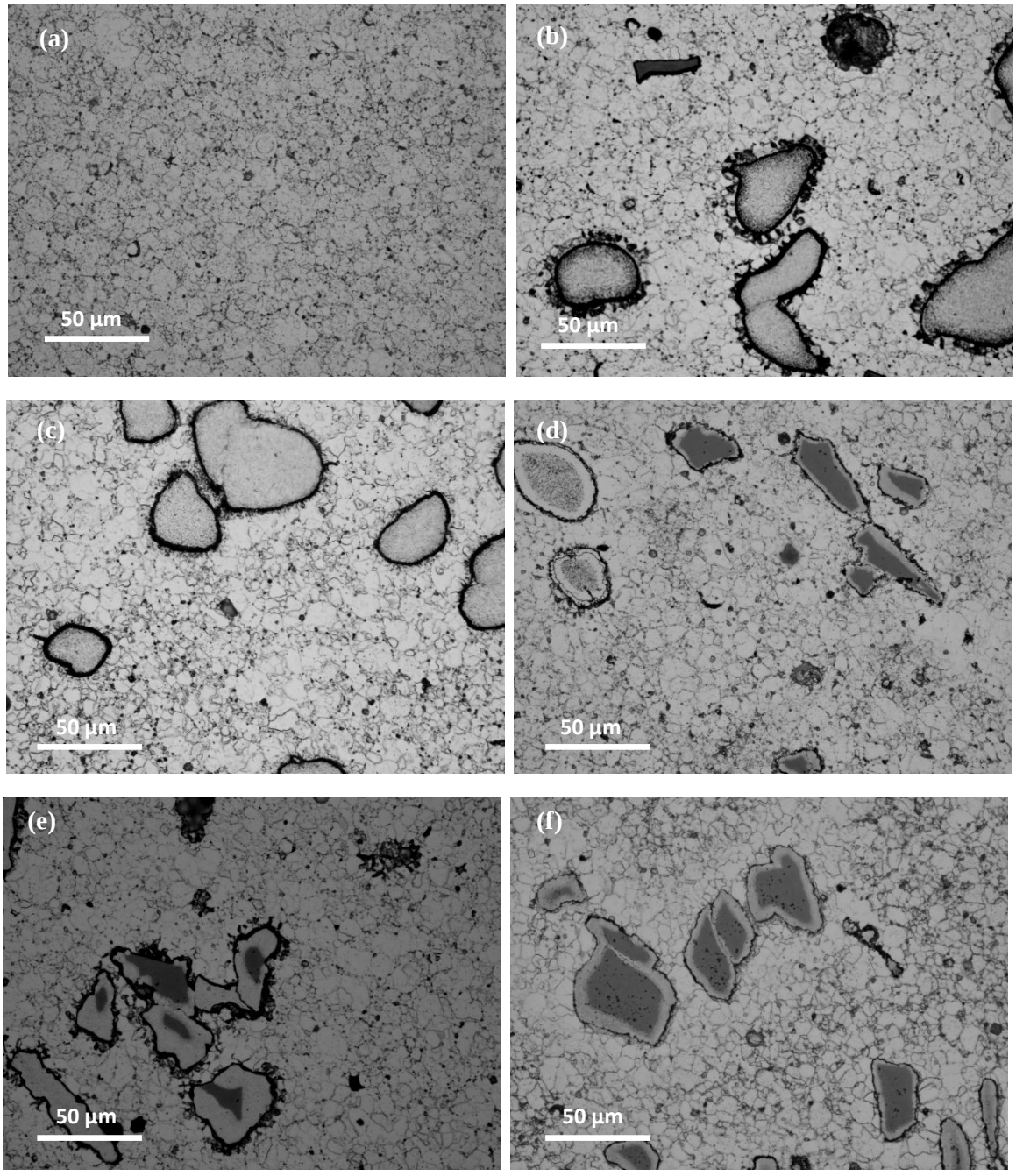

Fig. 5.7 Etched optical micrographs of (a) monolithic Fe-Co alloy and its composites with (b) uncoated and (c) copper (d) Ni-P (e) cobalt and (f) duplex plated particulates.

On etching (Fig. 5.7), the interfaces were etched preferentially compared to the matrix grain boundaries because of the smaller grain structures in the coating and the additional free energy associated with the interface. In the presence of non-conducting SiC particles, there was a reduction in the porosity levels and an increase in the grain size of the matrix material, in particular near the SiC particles. This may be due to localised rise in temperature because of the concentration of current in the regions adjacent to the non-conductive particles.

5.3.2 Particle/matrix interface

The EDX line profiles across a copper and Ni-P coated particle in the composites are shown in Fig. 5.8(a) and (b), respectively.

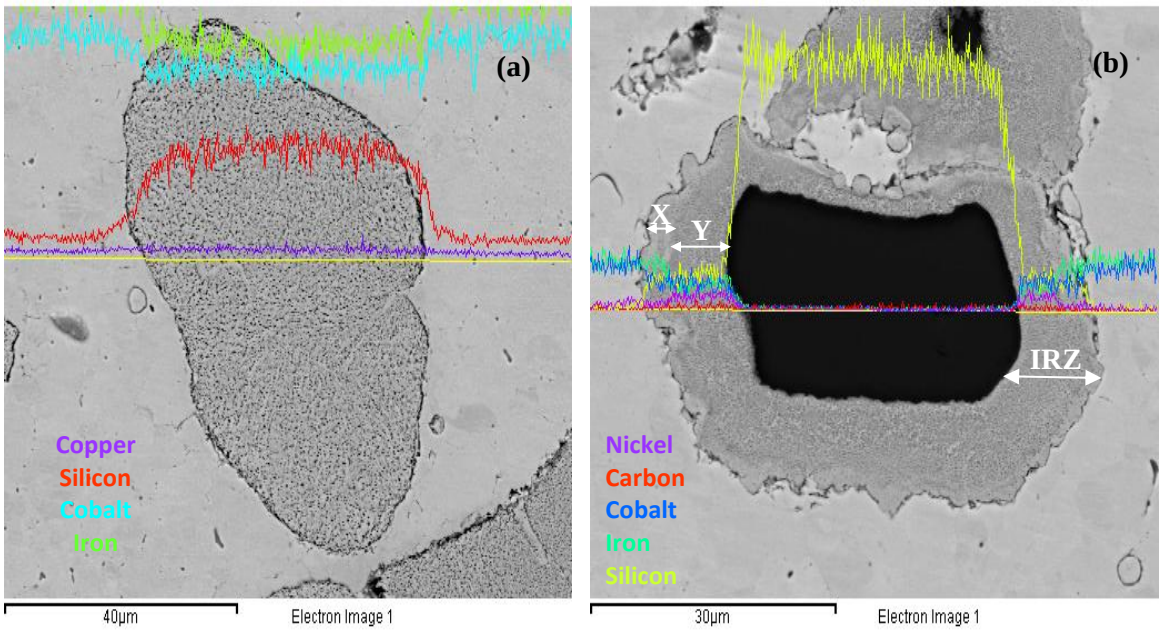

Fig. 5.8 SEM image with EDX line profile of composites with 10 vol% of: (a) copper; (b) Ni-P, where X and Y represent the regions with higher and lower Fe concentration, respectively in the interfacial reaction zone (IRZ).

The absence of Cu X-ray signal (Fig. 5.8(a)) suggested that it might have been dissolved into the matrix during sintering due to its low melting point or it might not be detectable due to its smaller thickness compared to other coatings. In composites with copper plated particles, the interface appeared to be porous unlike in other composites. In materials with Ni-P plated particulates, two distinct interfacial reaction regions were observed; one showing iron concentration which was same as that of the matrix (marked as X in Fig. 5.8(b)) and another with depleted iron and enriched Ni (marked as Y in Fig. 5.8(b)).

In materials with Co plated particles (Fig. 5.9(a)), the interface between the reaction zone and the matrix appeared to be smooth and continuous. Similar to Ni-P plated particles,

the reaction zone displayed two regions with different amounts of iron, as shown by the elemental mapping image formed by the Fe $K_{\alpha 1}$ radiation (Fig. 5.9(d)) compared to those mapped with Si $K_{\alpha 1}$ (Fig. 5.9(b)) and Co $K_{\alpha 1}$ signals (Fig. 5.9(c)). In duplex plated particulate composites (Fig. 5.10), the copper coating, unlike Ni-P coating was not continuous. Even though copper was present in the inner layer of the duplex coating, it was observed outside the Ni-P coating and in the interfacial reaction zone in the sintered material. This suggested that part of the copper coating was dissolved in the reaction zone and the rest was melted and raised above the interface.

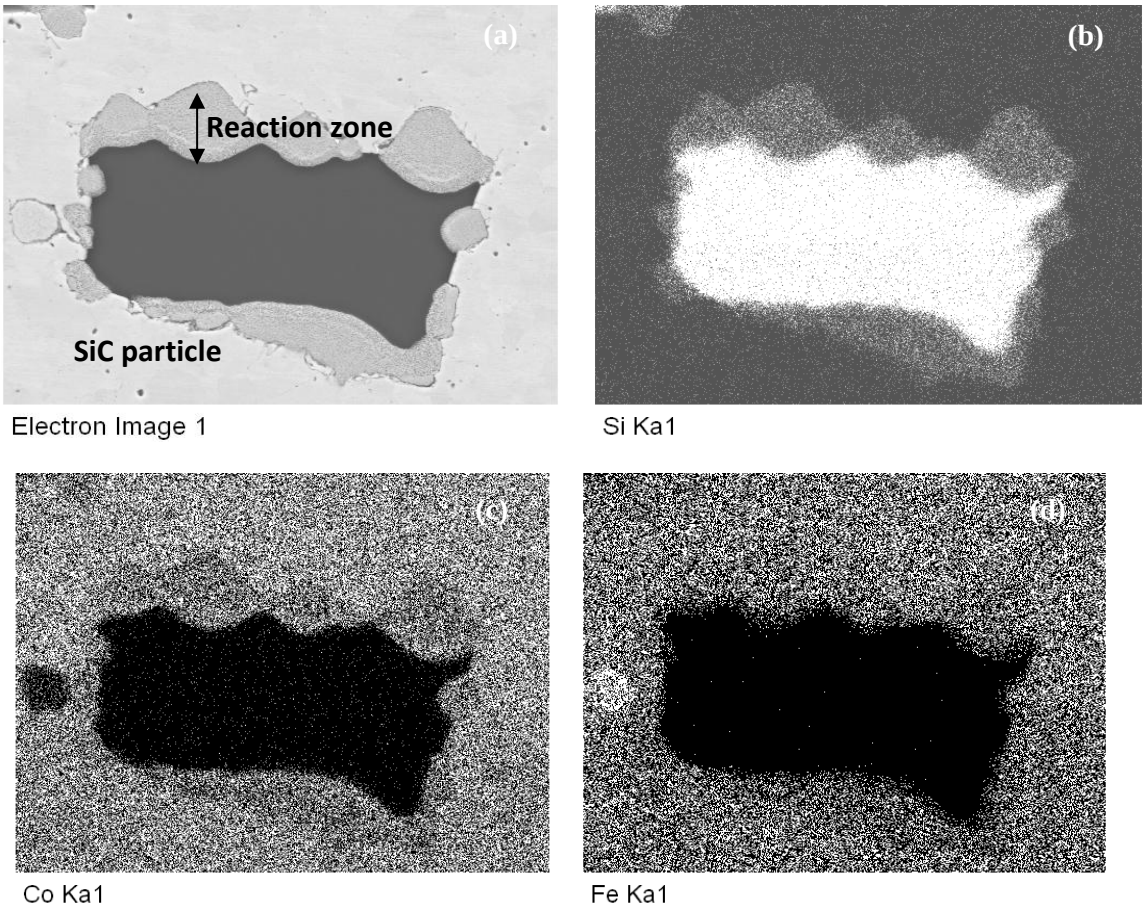

Fig. 5.9 (a) SEM image and (b-d) EDX elemental mapping image of Si, Co and Fe, respectively, of a cobalt plated particle in 10 vol% particulate composites

5.3.3 Crystallographic phases

The X-ray diffractograms of monolithic and composite materials are compared in Fig. 5.11. The absence of superlattice lines in the pattern corroborates the absence of long range ordered structures in the matrices [3]. Composites with uncoated and copper coated particulates showed less intense $FeCo_2Si$ phase peaks in the histogram. The absence of $FeCo_2Si$ shoulders near the Fe-Co alloy peaks in the patterns of other composites supported

the fact that duplex, Ni-P and Co coatings are effective in minimising the interfacial reaction during fabrication.

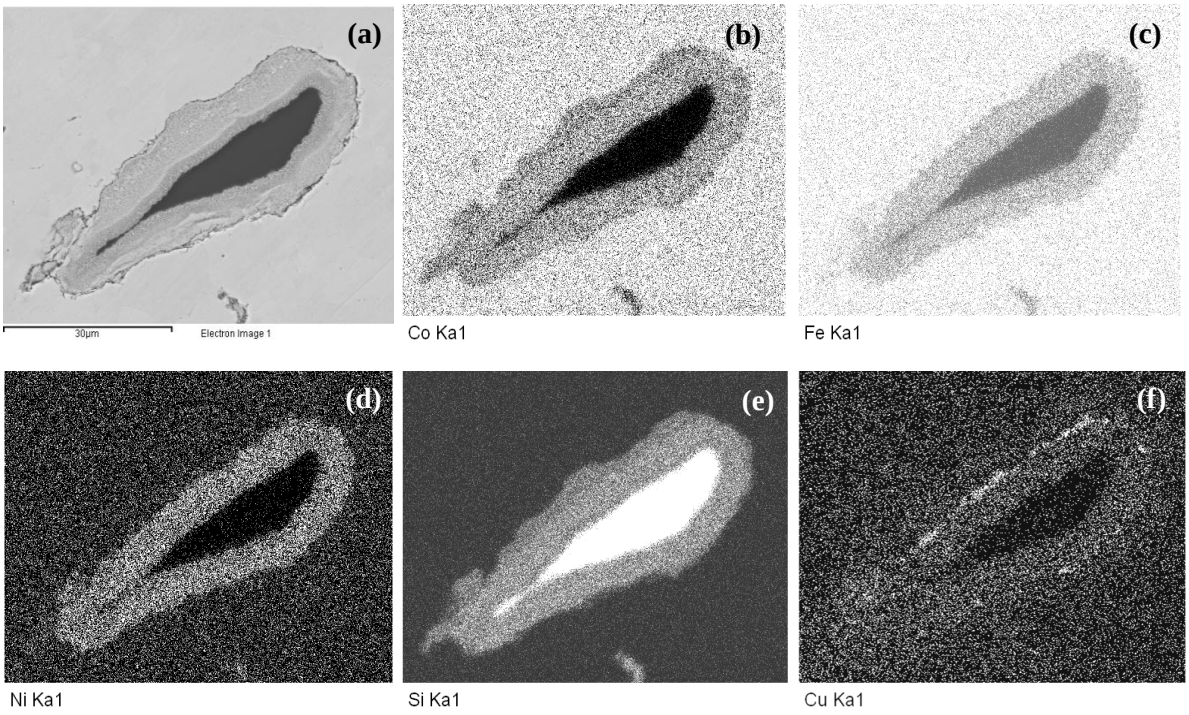

Fig. 5.10 SEM-EDX analysis of a duplex plated particle in 10 vol% composites: (a) SEM image (b-f) EDX elemental mapping pictures of Co, Fe, Ni, Si, Cu, respectively

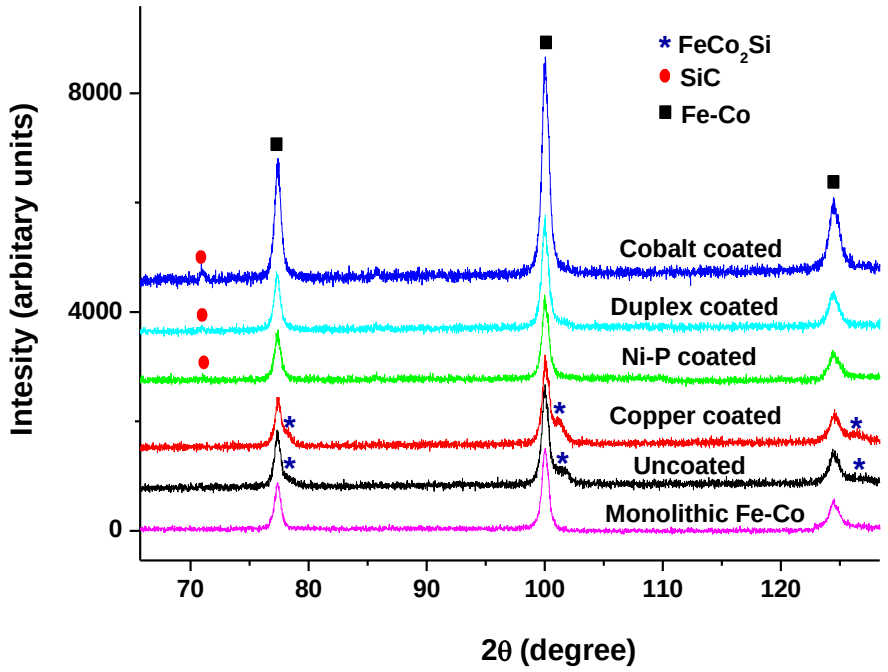

Fig. 5.11 XRD patterns of sintered monolithic and composites materials with 10 vol% particulates

5.4 Magnetic characterisation of monolithic and composite materials

The magnetic responses of materials with and without SiC particulates are compared in Fig. 5.12 and 5.13. The induction values at 20 kA/m and the coercivities of the composites and the monolithic material are summarised in Table I.

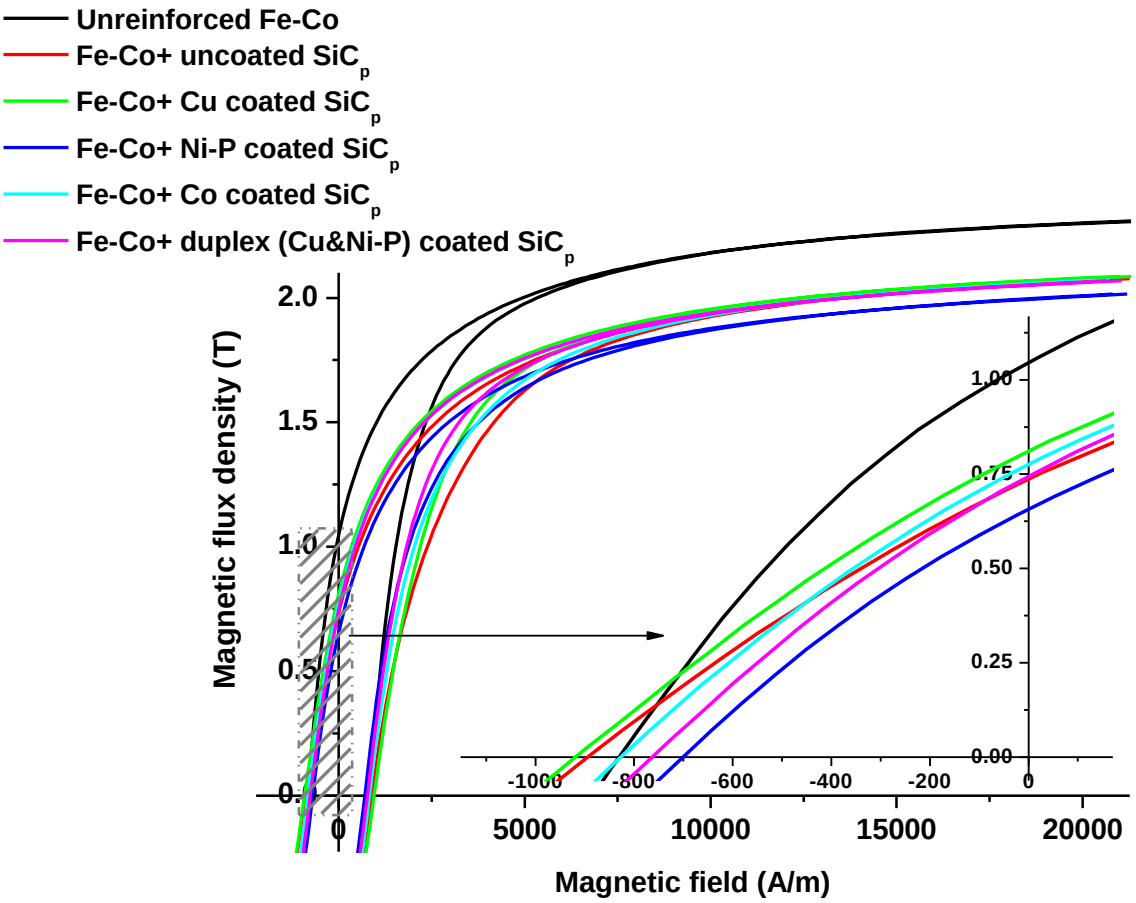

Fig. 5.12 Upper half of the hysteresis curve of unreinforced Fe-Co alloy and its composites with 5 vol% of reinforcements; the shaded area is enlarged and showed in the inset.

5.4.1 Structure insensitive magnetic properties

The saturation induction of a magnetic material, being insensitive to microstructure, depends on the chemical composition of the alloy. In powder metallurgy processed ordered magnetic alloys such as Fe-Co, additional factors that affect the saturation induction include density of the compact [4] and long range ordering fraction of the alloy [5]. The XRD results of the sintered materials confirm that there was no detectable long range ordered structures in any of the materials. The microstructure showed that there was no significant difference in the porosity levels. The addition of non-magnetic SiC particles caused a significant reduction

in the induction values compared to the material without fillers due to the dilution of the magnetic constituents. An increase in their volume fraction caused a further reduction for the same reason. Other than Ni-P plating, all the coatings had no substantial influence on the magnetic induction values in composites with 5 vol% particulates.

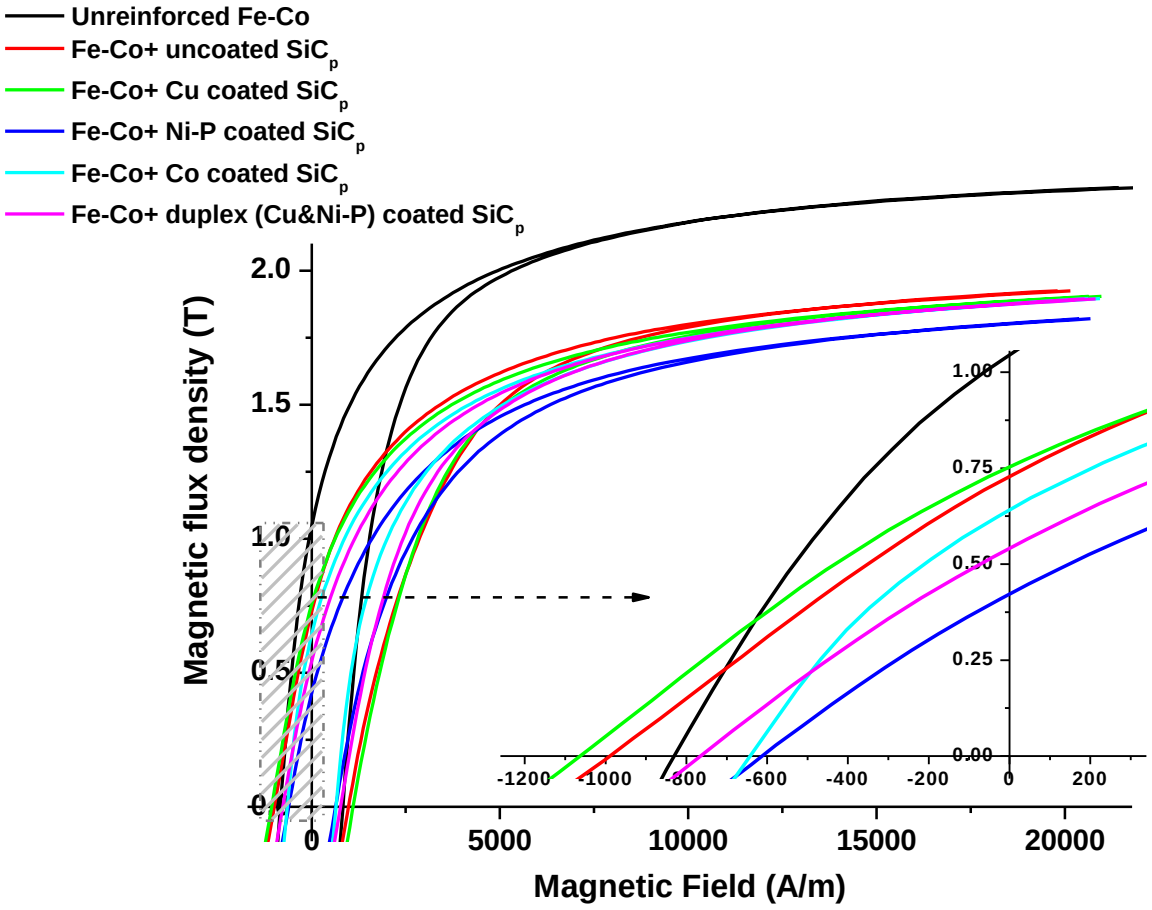

Fig. 5.13 Upper half of the hysteresis curve of unreinforced Fe-Co alloy and its composites with 10 vol% of reinforcements; the shaded area is enlarged and showed in the inset.

It is possible to differentiate the effects of coating by correlating the microstructure (Fig. 5.6) and XRD results (Fig. 5.11) with the magnetic induction values of 10 vol% composites (Table 5.1). Even though copper coated and uncoated particulates formed a porous and discontinuous interfacial reaction zone (IRZ) and produced more dilution by forming a thick IRZ, the ferromagnetic nature of $FeCo_2Si$ intermetallic helped in the retention of induction values comparable to those with better interfacial characteristics. $FeCo_2Si$ is a Heusler alloy with FCC structure and exhibits ferromagnetism due to double exchange mechanism between neighbouring magnetic ions (M_S=125 emu g^{-1}) [6]. The Ni-P coating on the particulates resulted in the reduction of magnetic induction values due to their inability to form a larger volume fraction of $FeCo_2Si$ and/or the lower saturation magnetisation values of

Ni compared to Fe and Co. The composites with duplex and Co plated particles, without forming $FeCo_2Si$ phase as high as in materials with copper plated and uncoated particulates, exhibited comparable magnetic induction because of better bonding and reduction in the overall porosity levels.

Table 5.1 *Summary of magnetic and mechanical testing results of monolithic and SiC particulate composite materials*

Sample details	Induction at 20 kA/m (T)	Coercivity (A/m)	Hardness (VHN)	Bending strength (MPa)	
				Mean	Std. deviation
Fe-Co	2.30	830	314±4	1148	35
Fe-Co composites with 5 vol% of					
Uncoated SiC	2.07	894	340 ± 8	760	39
Cu coated SiC	2.07	919	345 ± 5	712	24
Ni-P coated SiC	2.01	701	325 ± 4	871	33
Co coated SiC	2.07	826	330 ± 4	895	50
Duplex coated SiC	2.06	764	320 ± 2	782	55
Fe-Co composites with 10 vol% of					
Uncoated SiC	1.92	990	353 ± 4	569	19
Cu coated SiC	1.90	1063	344 ± 1	563	23
Ni-P coated SiC	1.81	612	346 ± 2	715	34
Co coated SiC	1.89	640	336 ± 1	967	11
Duplex coated SiC	1.89	764	332 ± 4	616	49

5.4.2 Structure sensitive magnetic properties

The factors affecting the structure sensitive coercivity in Fe-Co alloys include grain size, precipitate/second phase particle size and its distribution, internal stresses, state of order, texture, external stresses and test temperature. In powder metallurgy processed materials, effect of porosity is also significant because pores act as a source of internal demagnetising field.

The addition of fillers in Fe-Co alloys caused an increase or decrease in coercivity values depending on the amount of intermetallic compound formed at the interface. The introduction of copper coated and uncoated particulates promoted the formation of intermetallic compounds at the interface and resulted in an increase in the coercivity values. The copper coated particles were found to be more detrimental than those without any coating because of the elemental nature of copper in Fe-Co alloys [7]. The duplex, cobalt and Ni-P plating aided in the reduction of coercivity values due to one or more of the following reasons: (a) fewer (or zero) intermetallic compounds formed at the interface during

fabrication; (b) better bonding at the interface; (c) ferromagnetic nature of the coating; and (d) increase in the density and grain sizes due to the localised heating near the SiC particles as shown in the optical micrographs (Fig. 5.7). Co coating also aided in the improvement of structure-sensitive permeability values, as shown in the inset in Fig. 5.13. This may be due to one or more of the aforementioned reasons and/or because cobalt is one of the constituents of the matrix alloy. Interestingly, the coercivity of the materials with duplex coated fillers remained constant with increasing volume fraction of particulates. This suggested that the benefits realised by improving the density and by increasing the grain size near the duplex coated particles (Fig. 5.7(f)) were negated by the increase in the volume fraction of the particulates and coating.

5. 5 Hardness testing

The average Vickers hardness of the materials with and without dispersoids are summarised in Table 5.1. The introduction of hard SiC particles, with or without any coating, in the matrix alloy resulted in an increase in the hardness values. The increase in the hardness with volume fraction of filler was smaller due to the coarse nature of the particulates. The composites with copper coated and uncoated particulates, which formed $FeCo_2Si$ phase at the interface showed the highest hardness. The materials with the duplex coating showed the lowest hardness among the composites because of the coarsening of the microstructure near the particulates as shown in Fig 5.7(*f*).

5.6 Three point flexural testing

5.6.1 Flexural strength

The mean bending strength and standard deviation for the monolithic and composite materials are summarised in Table 5.1. The introduction of hard particles in the intermetallic Fe-Co alloy caused a reduction in the flexural strength values because the particles or the porous interface around the particles acted as crack initiation sites. However, the amount of the reduction was dictated by the type of coating over the fillers. The copper coated and uncoated particulate composites showed the lowest flexural strength due to the porous nature of the interface and formation of large amounts of detrimental interfacial phases during fabrication. The composites with duplex, Ni-P and cobalt plated particles, in the order mentioned, showed improvement in the flexural strength compared to the materials with uncoated and copper coated particulates. The factors that aid in the enhancement of flexural

strength in composites with Co plated SiC compared to those with uncoated fillers include better interfacial bonding and minimized interfacial compound formation at the interface.

5.6.2 Fractography

The SEM images displaying the fractographic features of the monolithic and composite materials are shown in Fig. 5.14.

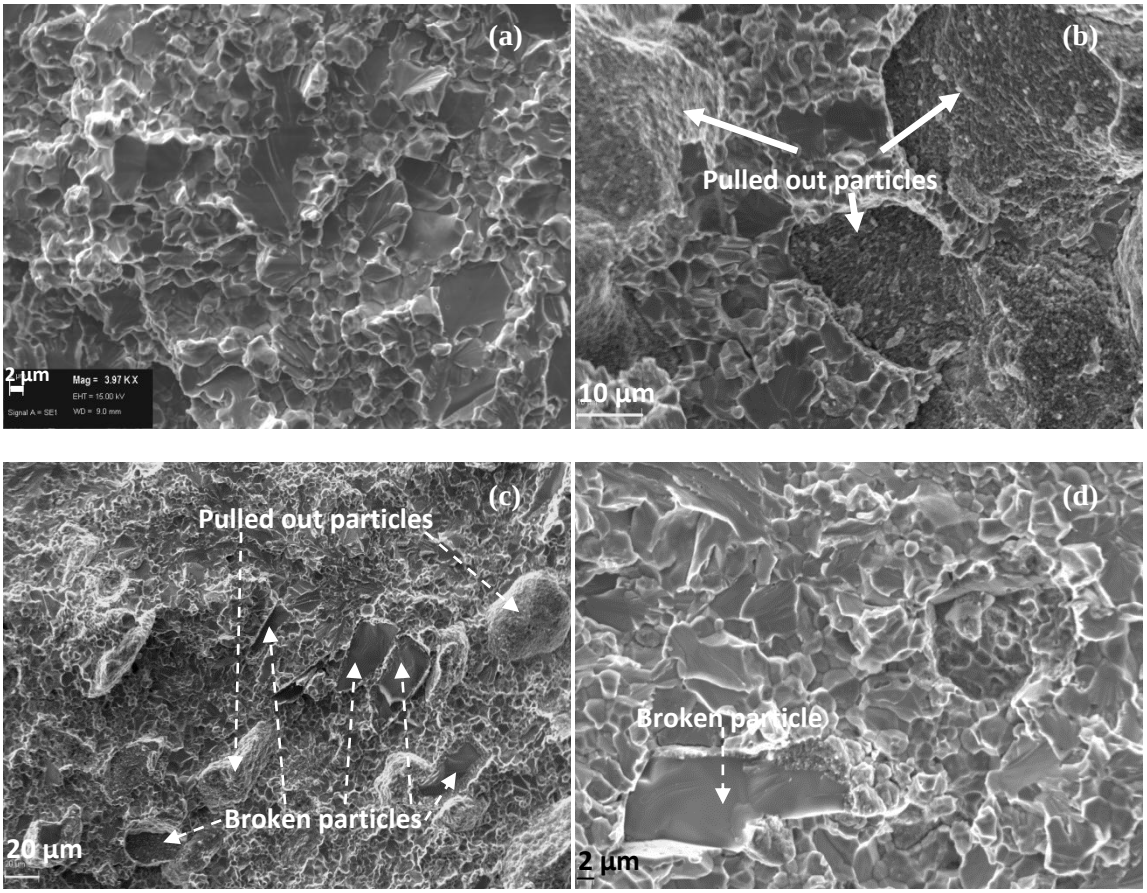

Fig. 5.14 SEM micrographs of fractured surface (a) Fe-Co alloy and its composites containing 10 vol% of SiC particles coated with (b) copper (c) Cu and Ni-P and (d) cobalt

The failed monolithic materials showed brittle transgranular fracture characteristics (Fig. 5.14(a)) as reported for ductile ordered and disordered Fe-Co alloys [8, 9]. However, Zhao et al. [10] reported intergranular fracture in Fe-Co alloys at room temperature with a rock candy feature and faceted appearance. The difference in the fracture behaviour may be related to the small grained microstructure or the presence of a small amount of silicon in the as-received Fe-Co alloy powders. The two damage mechanisms observed in the composite materials were SiC particle pullout/debonding and particle fracture. The composites with copper and uncoated particulates failed with particle pull out as shown in Fig. 5.14(b). Materials containing duplex coated and Ni-P plated particles showed a mixture of the two

fracture modes depending on the size of the particles. The smaller particles were fractured, while the larger particles were pulled out of the matrix (Fig. 5.14(c)). In case of composites with Co plated particles, the failure mechanism was predominantly particle fracture because of the better interfacial bonding (Fig. 5.14(d)).

References

1. J.Y. Song, J Yu, Residual stress measurements in electroless plated Ni–P films, *Thin Solid Films* **415**, 167–172(2002).
2. T.H. Hentschel, D. Isheim, R. Kirchheim, F. Müller, H. Kreye, Nanocrystalline Ni-3.6 at. % P and its transformation sequence studied by atom-probe field-ion microscopy, *Acta Mater.* **48**, 933-941(2000)
3. D.W. Clegg and R.A Buckley, The disorder-order transformation in iron-cobalt-based alloys, *Metal Science Journal* **7**, 48-54(1973).
4. F. Hanejko, H. Rutz and C. Oliver, Effects of Processing and Materials on Soft Magnetic Performance of Powder Metallurgy Parts, *Advances in Powder Metallurgy & Particulate Materials* **6**, 375-404 (1992), Metal Powder Industries Federation, Princeton, NJ
5. J.E. Goldman, R. Smoluchowski, Influence of order on the saturation magnetic moment, *Phys. Rev.* **75**, 310-311(1949).
6. V. Niculesu, T.J. Burch, K. Raj, J.I. Budnick, Properties of Heuler-type materials Fe_2TSi and $FeCo_2Si$, *J Mag. & Mag. Mater.* **5[1]**, 60-66(1977).
7. C.M. Orrock, PhD thesis, London University, 1986
8. K.R. Jordan, N.S. Stoloff, Plastic deformation and fracture in FeCo–2%V, *Trans Metal Soc AIME* **245**, 2027–34(1969).
9. T.L. Johnston, R.G. Davies, N.S. Stoloff, Slip character and the ductile to brittle transition of single phase solids, *Philos. Mag.* **12**, 305–17(1965).
10. L. Zhao, I. Baker and E.P. George, Room temperature fracture of FeCo, *Mater. Res. Symp. Proc.* **288**, 501–506(1993).

Chapter 6

Results and discussion: SiC whisker reinforced composites

6.1 Introduction

This chapter discusses the magnetic and mechanical behaviour of composites containing up to 5.5 vol% of as-procured and electroless Ni-P, Cu and Co plated SiC whiskers.

The morphology and the chemical composition of the coated whiskers, as studied using SEM with EDX attachment are presented. The microstructural, magnetic and phase characteristics of the composites with coated and as-received whiskers are compared with that of monoliths. The mechanical properties of the composites and monoliths are explained by correlating them with structure sensitive coercivity values and fractographic features, as obtained using SEM.

6.2 Characterisation of SiC whiskers

6.2.1 Morphology of as-received whiskers

From the SEM images of as-received SiC whiskers (Fig. 6.1), it is evident that the diameters and length of the whiskers corresponded with the supplier's specifications (diameter - 0.45-0.65 µm, length 5-80 µm). The surface of the whiskers appeared to be smooth with minimal granules.

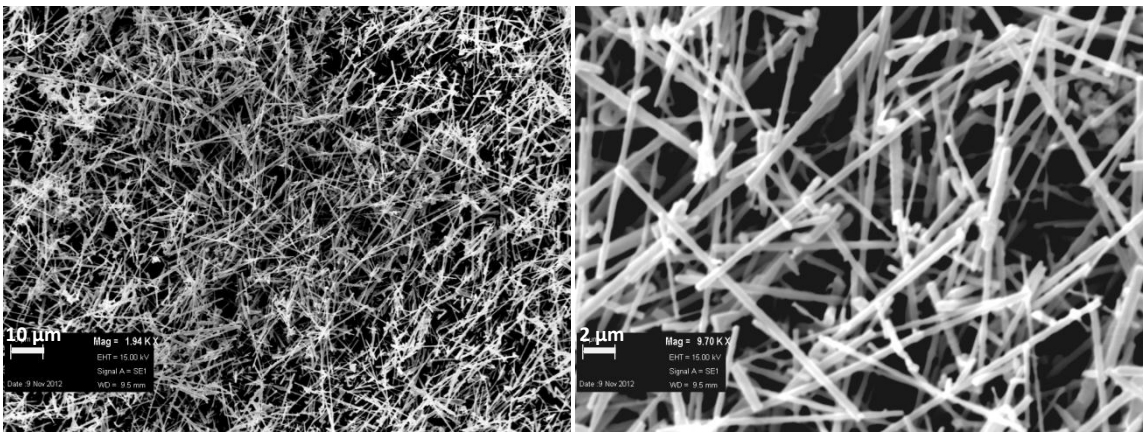

Fig. 6.1 SEM images of as-received SiC whiskers

6.2.2 Morphology and chemistry of electroless plated whiskers

Compositional point analysis was performed on the coated SiC whiskers. The SEM image showing the point of analysis and EDX spectrum of the Ni-P and copper coated whiskers are shown in Fig. 6.2 and 6.3, respectively. The presence of high intensity Ni, P and

copper peaks in the spectrum confirmed that the whiskers were coated with a thick layer of the respective coating. Song et al. [1] have previously shown that the crystallinity and phosphorus content of Ni-P coatings are dictated by the pH of the plating bath and the coating prepared at a pH of 8.5 would be amorphous and contain about 4 wt% of P. As exemplified by the SEM images of SiC whiskers plated with cobalt for 10 and 30 minutes (Fig. 6.4), the plating time played an important role in deciding the final thickness of the coating. In order to disperse the SiC whiskers effectively, the pH of the plating bath should be between 8 and 11 [2]. Therefore, it was possible to disperse whiskers effectively during Ni-P and cobalt coatings, which were done at a pH of 8.5 and 9.2, respectively. However, pH of the copper plating bath (>12) was not favourable to disperse the whiskers during plating.

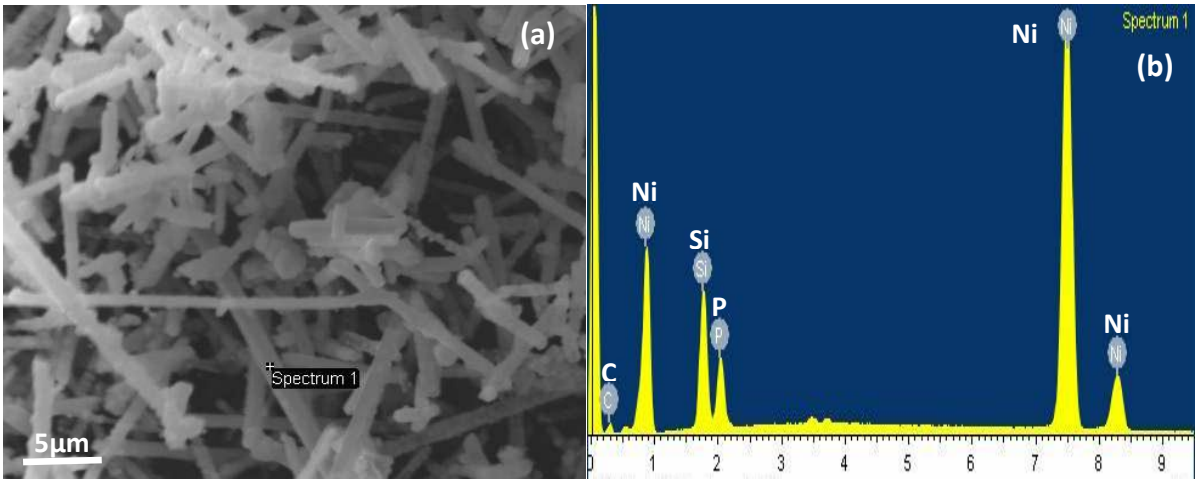

Fig. 6.2 (a) SEM image of Ni-P plated whiskers showing the point where the EDX analysis was performed; (b) EDX spectrum obtained

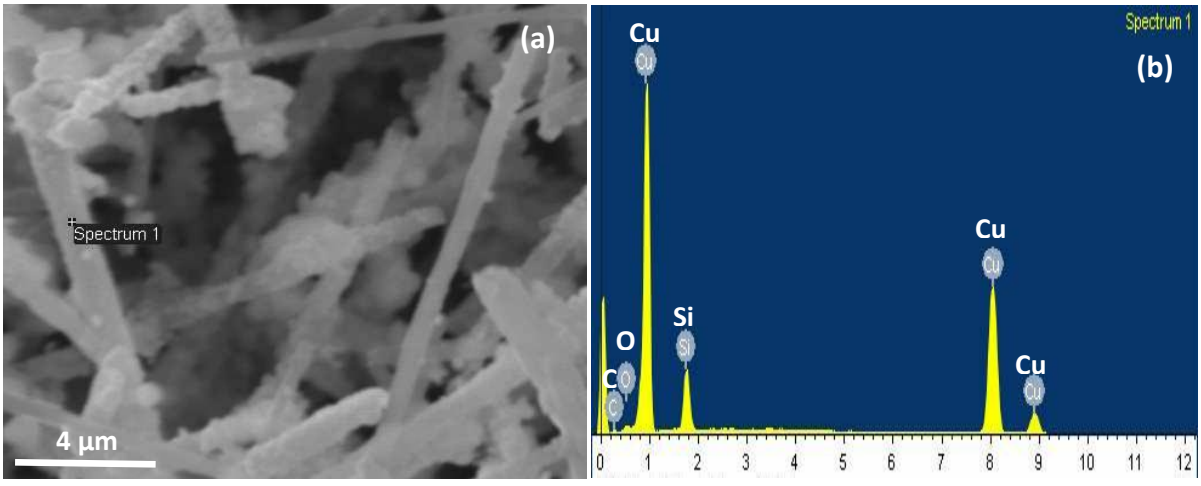

Fig. 6.3 (a) SEM image of copper plated whiskers showing the point where the EDX analysis was performed; (b) EDX spectrum obtained

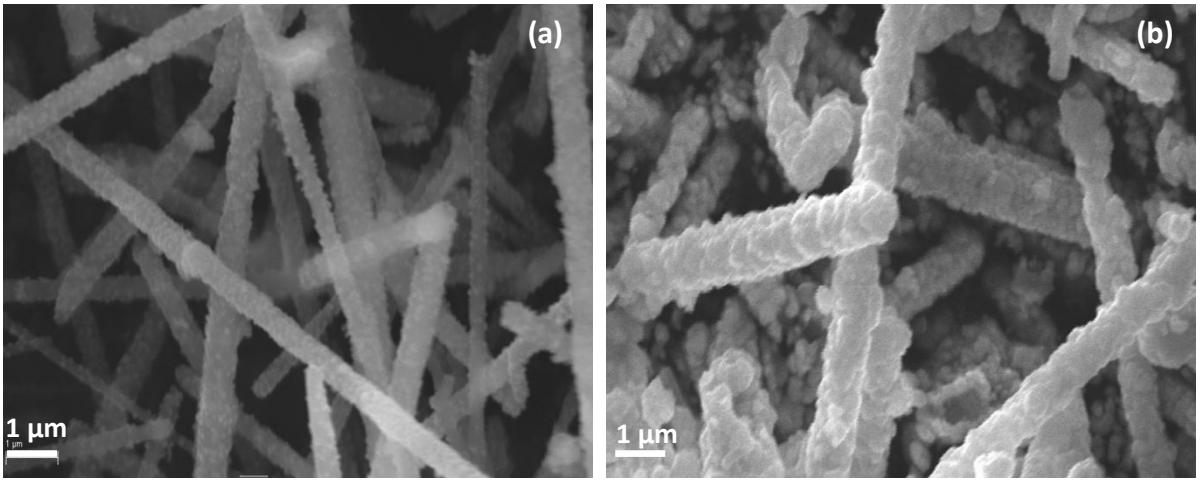

Fig. 6.4 SEM image of SiC whiskers plated with cobalt by an electroless method for (a) 10 minutes; and (b) 30 minutes.

6.3 Colloidal processing of composite mixtures

It has been showed that colloidal processing helps to disperse the SiC whiskers uniformly in the matrix with minimum disintegration of whiskers [3]. Colloidal processing involves dispersion of whiskers in a suitable liquid medium under magnetic or ultrasonic agitation, mixing of matrix powder in the slurry and drying to remove the liquid medium employed. The liquid media used are broadly classified as aqueous (containing water) and non-aqueous (without water). When an aqueous medium was employed, the surfaces of the Fe-Co powders would be oxidised during drying. This restricted the selection to be made from a non-aqueous category. It has been reported that formic acid is a suitable solvent to disperse SiC whiskers among non-aqueous media such as formic acid, formamide, n-butylamine, ethyl ethyl ketone, acetone, isopropyl alcohol, ethanol, toluene, n-hexane [2]. Inglis et al. [4] showed that Fe and Co in the transition series act as catalysts for the decomposition of formic acid into CO_2 and CO. To avoid the risk associated with the catalytic nature of Fe-Co, the two powders were mixed using the commonly used non-aqueous medium (ethanol) under ultrasonic agitation for 1 hour.

6.4 Characterisation of composites

6.4.1 Microstructure of composites with bare whiskers

The optical micrographs (Fig. 6.5) show agglomerates of SiC whiskers in the composites. The number and size of the agglomerates increased with the volume fraction of whiskers. The ultrasonication of SiC whiskers in ethanol was found not to be efficient in dispersing the whiskers in the matrix. In order to disperse the SiC whisker uniformly in the

Fe-Co matrix, it is required to select a dispersion medium better than ethanol and to maintain the volume fraction of the SiC whiskers less than 2%.

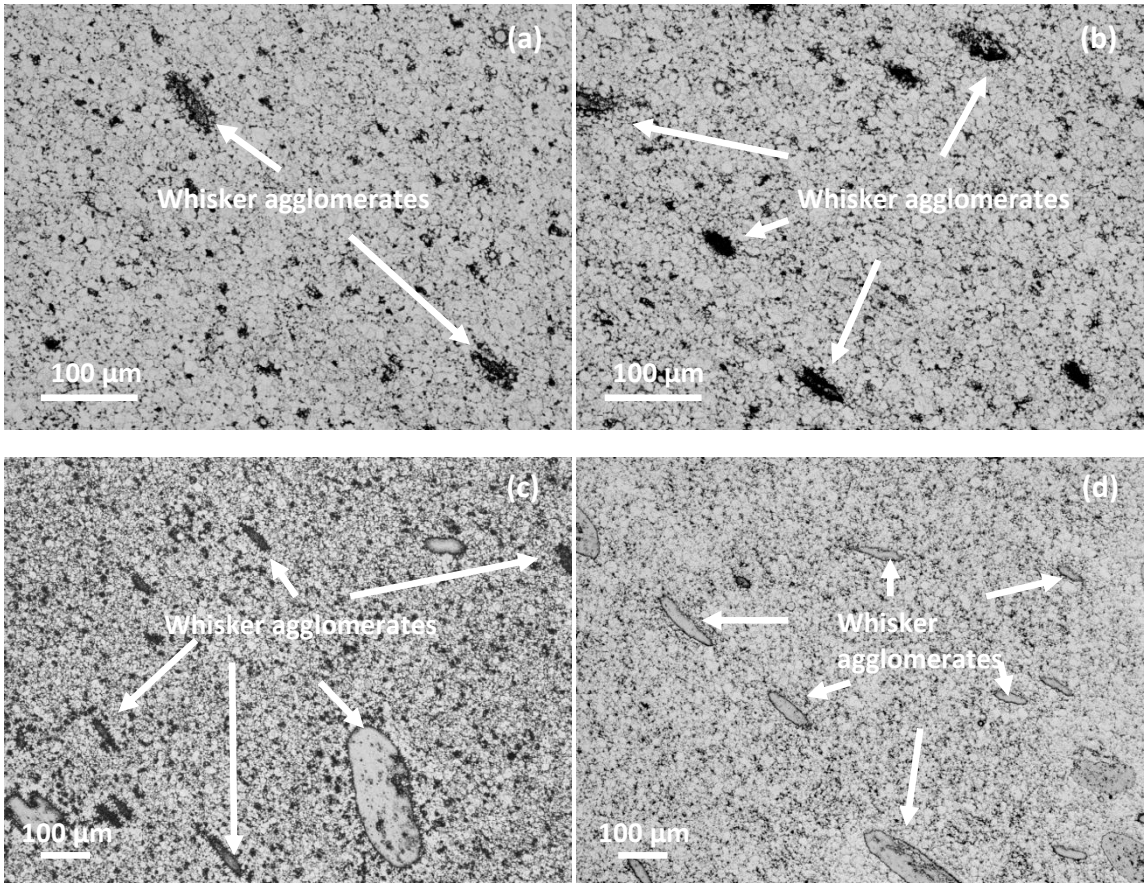

Fig. 6.5 Optical micrographs of Fe-Co composites containing (a) 1 vol% (b) 2 vol% (c) 3 vol% and (d) 5.5 vol% of SiC whiskers

The etched optical micrographs of monolithic and composite materials are shown in Fig. 6.6. The grain size of the matrix in the composites containing 1 and 2 vol% of whiskers (Fig. 6.6(b) and (c)) was similar to monoliths (Fig. 6.6(a)) in some regions. Very fine grains that were observed in monoliths (Fig. 6.6(a)) were completely absent in the composites (Fig. 6.6(b)-(d)). The etch pits (black dots) observed in the composites were formed due to the preferential etching of the whisker/matrix interface. The composites containing 3 vol% of whiskers (Fig. 6.6(d)) showed larger grains than the materials with a lower percentage of whiskers and without whiskers. The non-conductive whiskers in composites, by altering the SPS current pathways and by promoting voltage concentrations away from whiskers might have caused the grain growth of the magnetic and conductive matrix. The grain growth was predominant in materials with more than 2 vol% of uncoated whiskers.

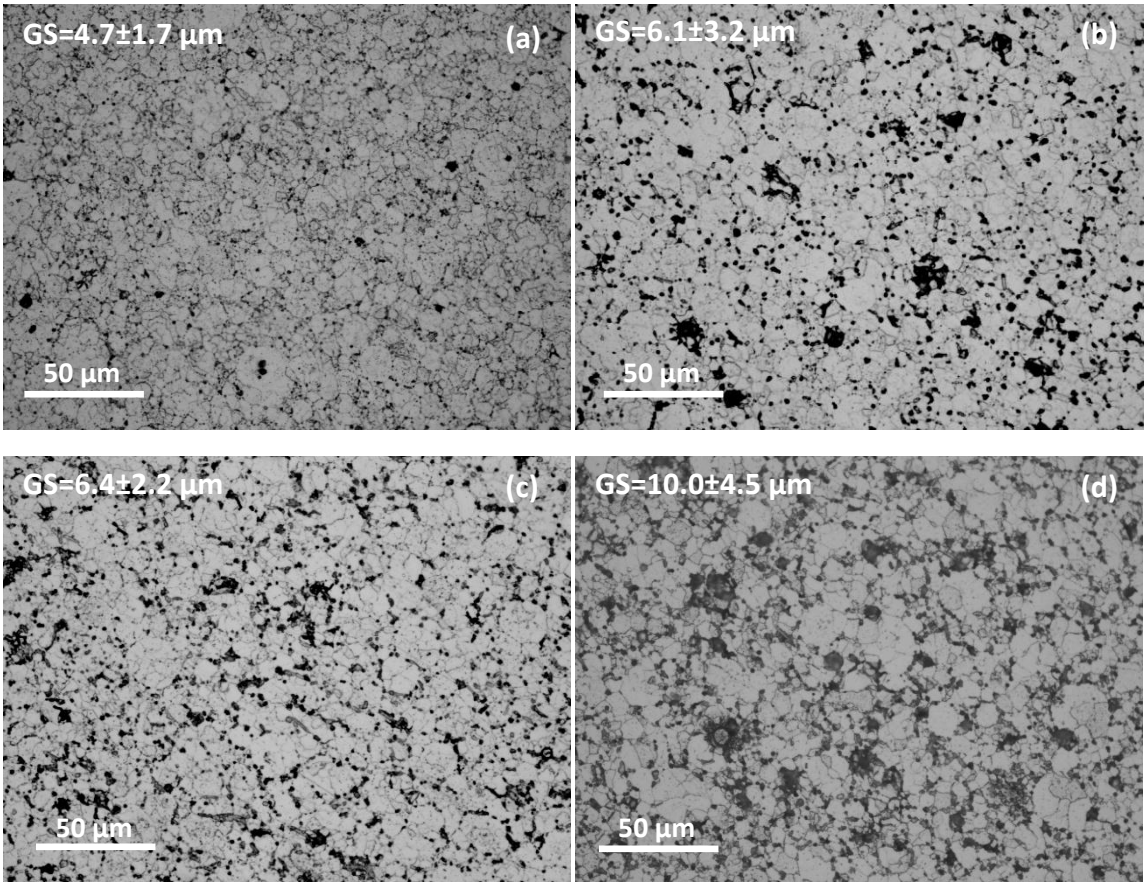

Fig. 6.6 Optical micrographs of Fe-Co (a) monolith and composites containing (b) 1 vol% (c) 2 vol% and (d) 3 vol% of SiC whiskers; GS in the images represents grain size.

6.4.2 Microstructure of composites with coated whiskers

The optical and SEM micrographs of composites containing 2 vol% of copper, Ni-P and cobalt coated SiC whiskers are shown in Figs. 6.7 - 6.11. It was not possible to directly measure the coating thicknesses because of the non-uniform diameters of the as-received whiskers. The average thickness of coating was evaluated by measuring the increase in the weight of the whiskers after electroless plating. Hereafter, the one with a larger volume fraction of the coating material is designated as thick coating and the one with a relatively smaller amount is designated as thin coating as shown in the Table 3.2.

6.4.2.1 Composites with Ni-P coated whiskers

Fine grained features were formed when the amorphous Ni-P coated whiskers were spark plasma sintered with Fe-Co for shorter duration (5 minutes). The fine grained structures were preferentially etched and resulted in a microstructure as shown in Fig 6.7. The micrographs also displayed the high angle grain boundaries of the coarsened matrix as shown by white arrows in SEM images. This confirmed that the matrix grains were coarsened in the regions away from the non-conductive whiskers due to current concentration.

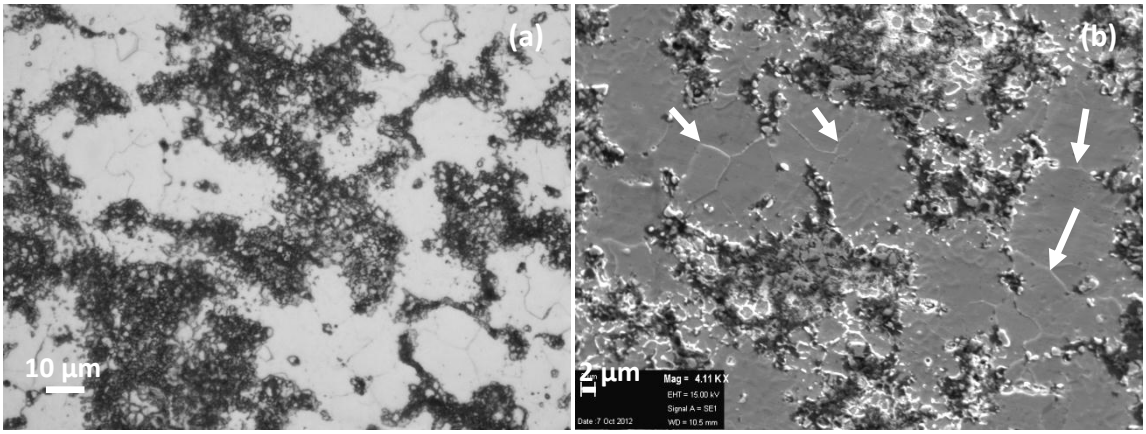

Fig. 6.7(a) Optical and (b) SEM micrographs of Fe-Co composites containing 2 vol% of Ni-P coated (thick) SiC whiskers

6.4.2.2 Composites with cobalt coated whiskers

The etch-pits (black dots observed in the optical micrographs) were formed due to the preferential etching of matrix- whisker interface. The uniform distribution of etch-pits confirmed the homogenous distribution of cobalt coated whiskers in Fe-Co matrix (Fig. 6.8). The EDX elemental point analysis (Fig. 6.9) confirmed the formation of etch-pits near the whiskers. It was also evident that the whiskers were present at the grain boundaries of the matrix.

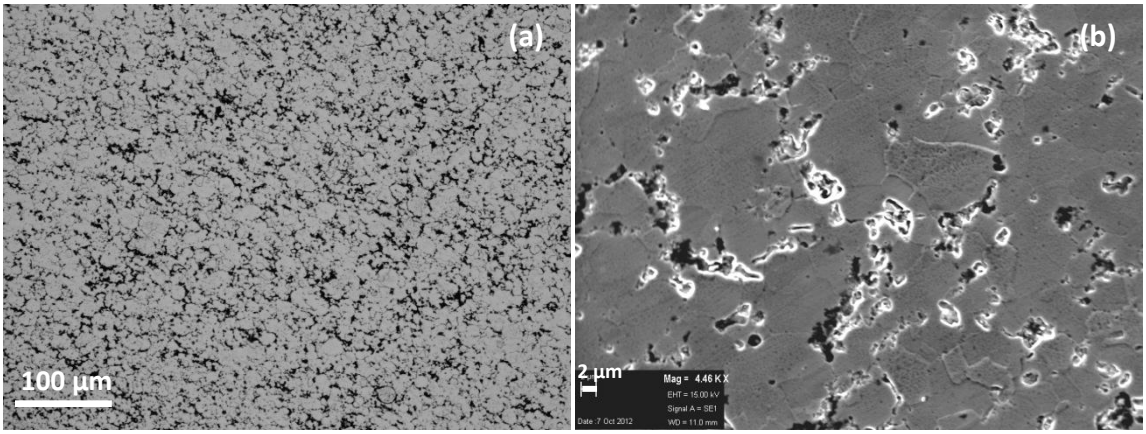

Fig 6.8(a) Optical and (b) SEM micrographs of Fe-Co composites containing 2 vol% of Co coated (thick) SiC whiskers

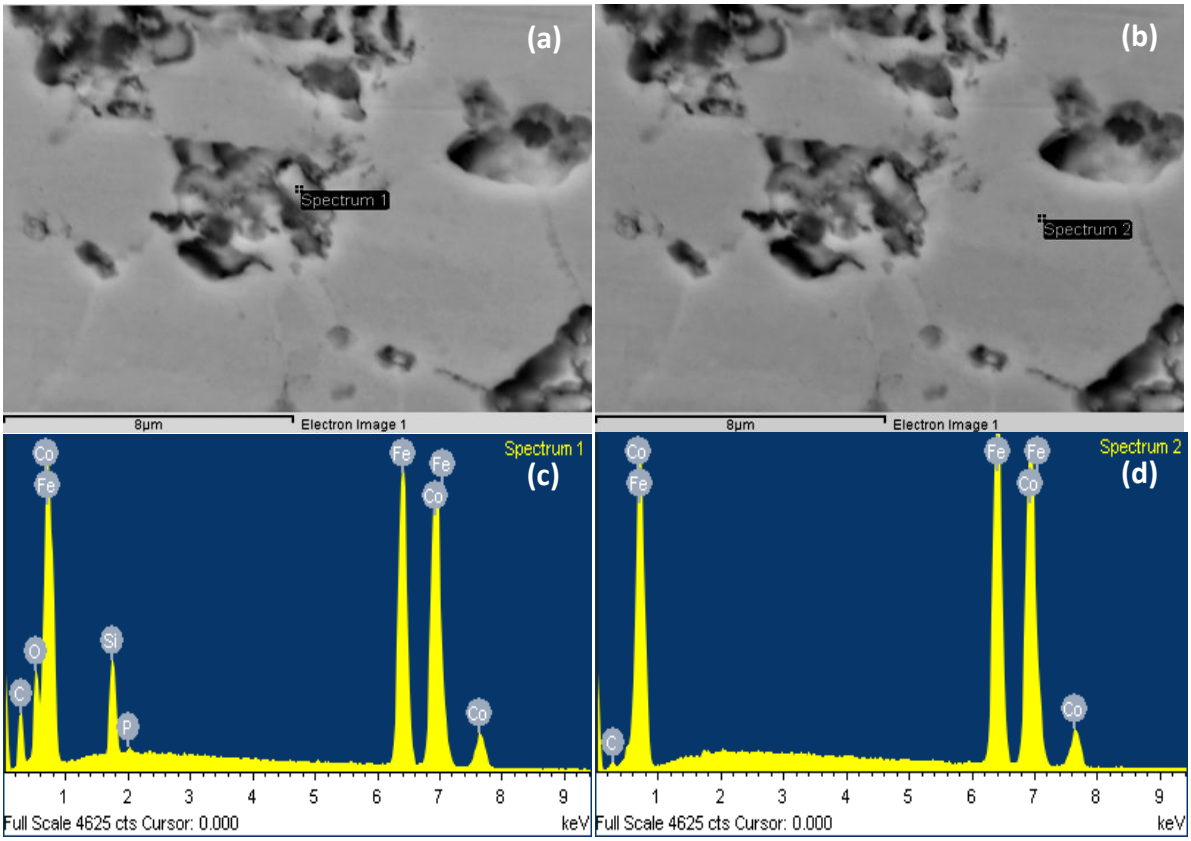

Fig. 6.9 SEM image of an etched composite with cobalt coated whiskers showing the EDX point analysis (a) on a cobalt coated whisker and (b) in the matrix; (c) and (d) the respective EDX spectrum obtained

6.4.2.3 Composites with copper coated whiskers

Unlike in composites with Ni-P and Co coated whiskers, the Cu coated whiskers were difficult to disperse uniformly in the matrix. Whisker clusters were observed in the micrographs similar to materials with uncoated whiskers (Fig 6.10).

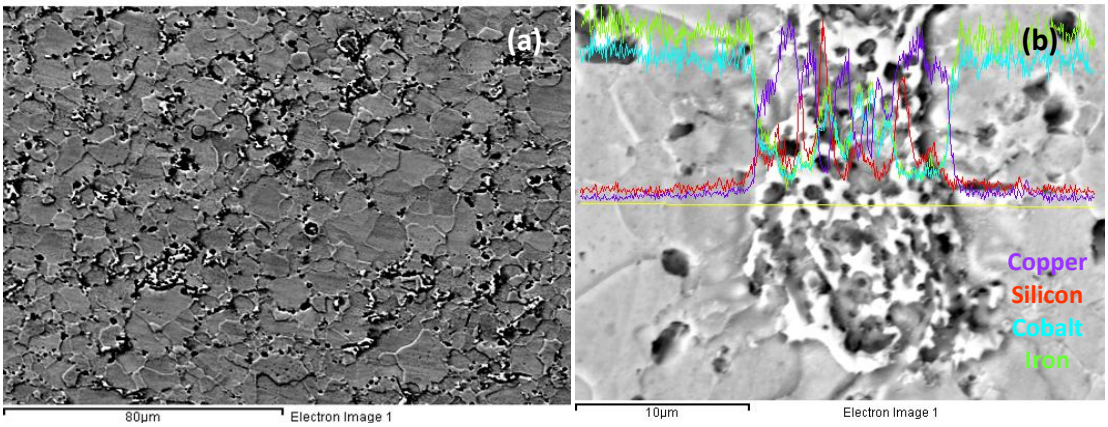

Fig. 6.10 (a), (b) SEM images of 2 vol% of copper coated (thick) whisker showing inhomogeneous distribution of whiskers; (b) a magnified image with EDX line profile near a copper coated whisker cluster

The agglomerates were more predominant in materials with more volume fraction of whiskers and in those with thin copper coating (Fig. 6.11).

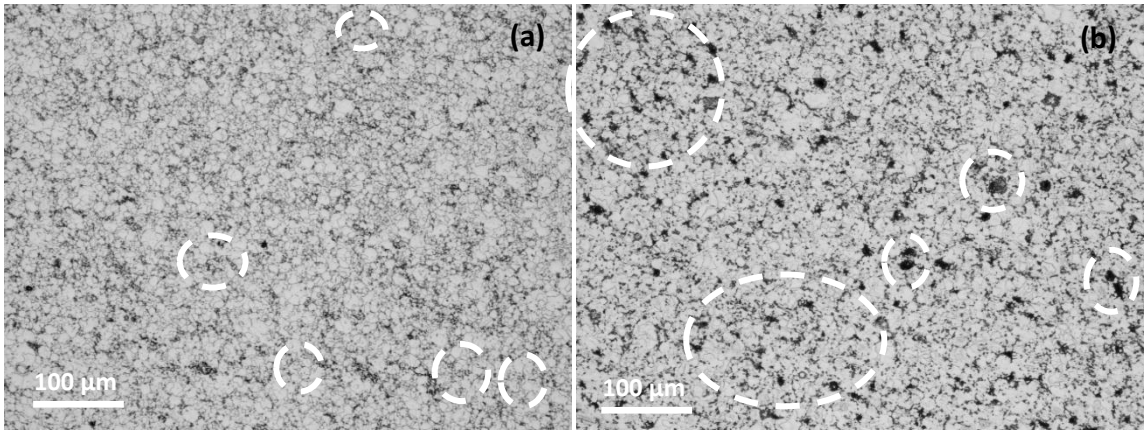

Fig. 6.11(a) Optical micrographs of Fe-Co composites containing 2 vol% (thick) and 3 vol% of copper coated SiC whiskers showing whisker clusters as marked by circles and ovals

6.4.3 Crystallographic phases and long range ordering

The XRD histograms of monoliths and composites containing 2 vol% of uncoated and thick layers of copper, Ni-P and cobalt plated whiskers are compared in Fig. 6.12. The materials containing copper coated and Ni-P coated whiskers formed $Cu_{0.8}Fe_{0.2}$ and Fe_3Ni_2 phases, respectively, during sintering.

The effect of whisker addition on the long range ordering of Fe-Co was studied by comparing the intensities of the superlattice reflection in XRD spectra of monolithic materials and composites. As those characteristic lines were not observed in the fast scan histograms, very slow XRD experiments were performed in the angular ranges where the super lattice reflections are expected to appear. Therefore, the slow scan experiments (0.02 $^o2\theta$/min) were conducted at 2θ angular ranges of 34-39 and 87-92, where (100) and (210) superlattice lines, respectively were supposed to materialise for Fe-50 Co alloys (Fig. 6.12) [5]. There were no notable changes in the intensity values of the (100) super lattice lines of the composites in comparison to the monoliths (Fig. 6.13(a)). In materials with copper coated whiskers, the (220) reflection of $Cu_{0.8}Fe_{0.2}$ fell exactly at the same position of (210) superlattice line and resulted in a relatively high intense peak as shown in the higher angle slow scan spectrum (Fig. 6.13(b)). In composites with Ni-P coated whiskers, the (210) superlattice line and (220) Fe_3Ni_2 line overlapped and produced a broad peak at 89.5. The broad peak corresponding to (220) reflection of $Cu_{0.8}Fe_{0.2}$ and Fe_3Ni_2 phase at an angle 2θ of ~88.7^o and ~89.5^o, respectively, confirmed the nanocrystalline nature of the phases. From the intensity of the

superlattice lines, it is evident that there was no significant change in ordering fractions due to the incorporation of SiC whiskers.

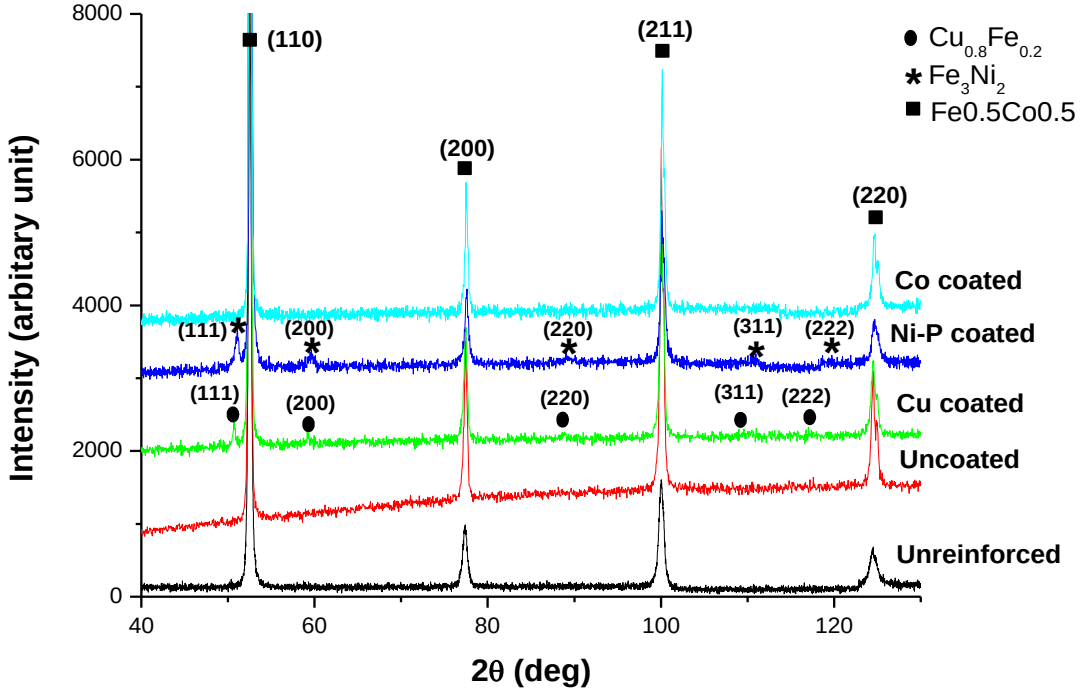

Fig. 6.12 XRD histograms of monoliths and composites with 2 vol% of whiskers

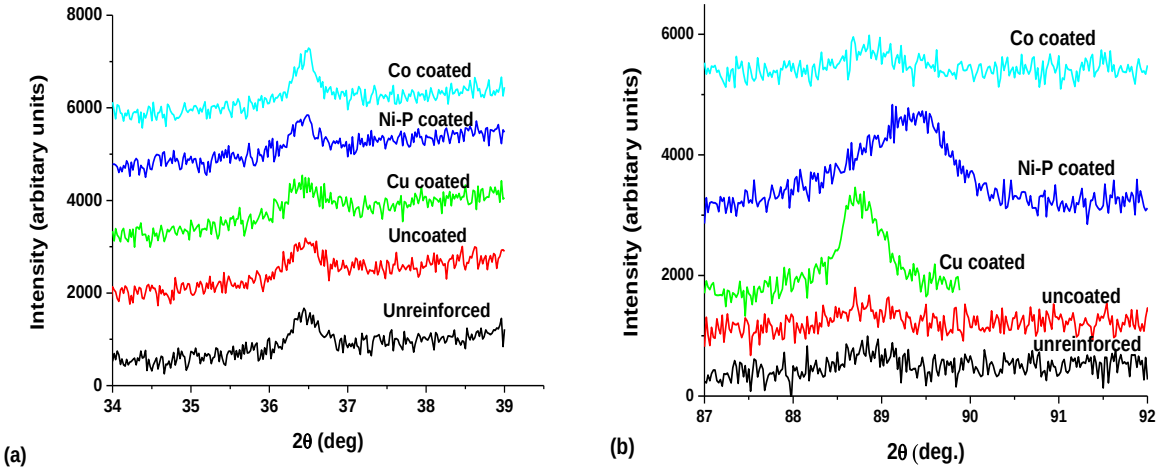

Fig. 6.13 Slow scan X- ray diffraction patterns showing (a) (100) and (b) (210) superlattice reflections of the matrix alloy in monoliths and composites

6.5 Magnetic property measurements

The magnetic induction at 20 kA/m and the coercivities of the monolithic material and composites are outlined in Table 6.1.

6.5.1 Saturation induction

The uncoated and coated SiC whiskers added in Fe-Co alloys caused a decrease in their induction values due to the dilution effect. In case of uncoated whiskers, the drop in the induction values was increased with an increase in the volume fraction of non-magnetic SiC. In composites with coated SiC whiskers, the additional dilution caused by the coatings caused a further fall in the induction values. The drop was observed even in materials with magnetic coatings (Ni-P and Co) and it increased with increase in the coating thickness. Although copper is non-magnetic among the coatings studied, the maximum reduction in the magnetic induction was noticed in materials with a similar amount of Ni-P coated whiskers. This might be due to either one or both of the following reasons: (a) the intermetallic compounds formed in composites with thick copper coated whiskers ($Cu_{0.8}Fe_{0.2}$) were exhibiting higher saturation magnetisation than those observed in the materials with Ni-P plated whiskers, (b) lower saturation magnetisation of Ni (484 emu/cm^3) than Fe (1714 emu/cm^3) and cobalt (1422 emu/cm^3) [6].

6.5.2 Coercivity

6.5.2.1 Composites with uncoated whiskers

The coercivity of the composites decreased with an increase in the volume fraction of reinforcements; however, the values were strongly dependent on the distribution and volume fraction of SiC whiskers in the matrix. This was attributed to the increase in the grain size due to the restrictions in the current pathways caused by the non-conductive whiskers during sintering. Therefore, there were current concentrations and hence, the regions adjacent to them were overheated locally. As the probability for the whiskers to deviate the current flow is higher for the composites with more volume fraction of reinforcements, composites with 5.5 and 3 vol% of uncoated whiskers showed lower coercivity that those with 1 and 2 vol% of whiskers. The coercivity of composites with 5.5 vol% of whiskers is higher than that with 3 vol% whiskers because of the inhomogeneous distribution of fillers as evidenced in the optical micrographs (Fig. 6.5(c),(d))

6.5.2.2 Composites with copper coated whiskers

In materials with copper coated whiskers, the magnetic hardness increased with the thickness of the coating. This was due to the formation of $Cu_{0.8}Fe_{0.2}$ precipitates in composites with more volume fraction of copper. The amount of the intermetallic precipitates formed was strongly dictated by the volume fraction of the coating. Materials with thin copper coatings showed nearly the same or lower coercivity values than the materials with the same volume fraction of uncoated reinforcements. It has to be noted that the addition of 2 and 3 vol% of copper coated (thin) whiskers did not change the coercivity. This may be due to the negation of the detrimental effect due to the copper inclusions by the beneficial grain growth.

6.5.2.3 Composites with Ni-P coated whiskers

In composites with Ni-P coated whiskers, nanocrystalline Fe_3Ni_2 precipitates formed from the amorphous Ni-P coating (as confirmed by the XRD pattern) increased the coercivity values. The coercivity increments were proportional to the volume fraction of coating material as shown in Fig.6.14.

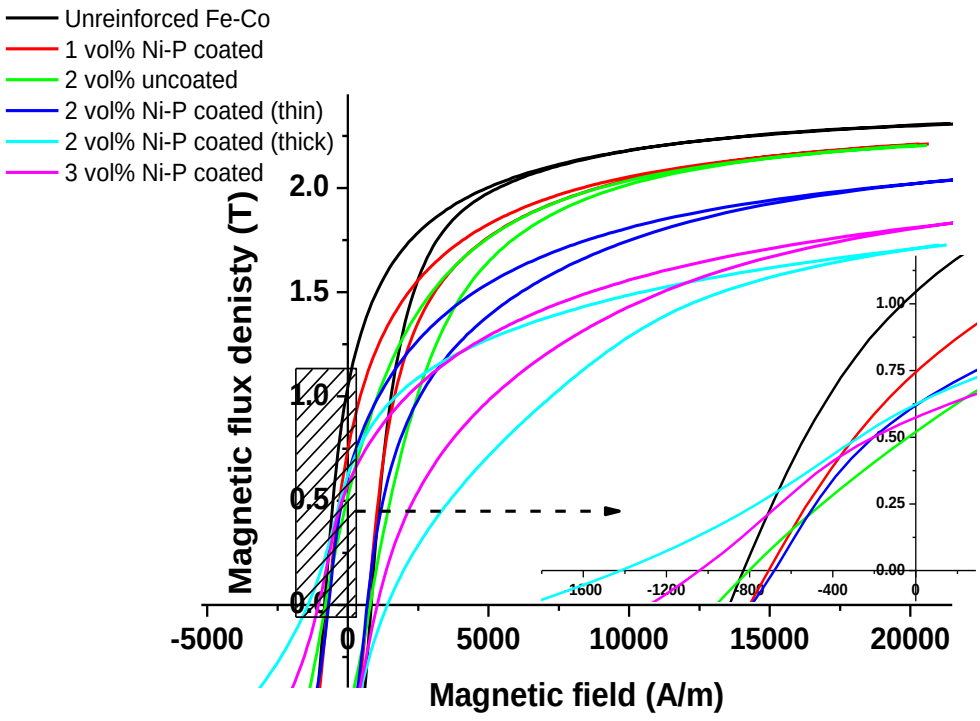

Fig. 6.14 Upper half of the hysteresis curve of unreinforced Fe-Co alloy and its composites containing bare and Ni-P coated SiC whiskers; the shaded part of the curve is enlarged and showed in the inset figure.

The magnetic hysteresis loop forms of these composites were dependent on the volume fraction of Ni-P. The composites with a higher volume percentage of Ni-P showed the wasp-waisted form of loop, a characteristic type observed in some Perminvar (Fe-Co-Ni) alloys [7].

6.5.2.3 Composites with cobalt coated whiskers

The composites with cobalt coated whiskers exhibited the lowest coercivity values among the composites with similar amount of reinforcements. This might be due to the uniform distribution of whiskers in the matrix, which promoted the grain growth during sintering.

6.6 Mechanical properties of monolithic and composite materials

The mechanical hardness and flexural strength of the monolithic Fe-Co and its composites are summarised in Table 6.1. In the following sections, the mechanical properties of the composites and monolithic materials are compared and examined through inspection of their coercivity values, fractographic features and flexural test curves.

6.6.1 Correlation of bending strength with coercivity

The mechanical responses of the materials with and without whiskers are compared (Fig. 6.15) and are correlated with the structure sensitive coercivity values (Fig. 6.16) in the following section.

The materials that exhibited higher bending strength than the monolithic material possessed higher coercivity values. The beneficial mechanical strengthening agents such as nanocrystalline intermetallic precipitates were found to be detrimental for soft magnetic properties. The composites containing more than 2 vol % of SiC whiskers, in the presence and absence of cobalt coating, showed a drastic reduction in the flexural strength and coercivity because of grain growth. In composites with Ni-P coated SiC whiskers, an increase in the flexural strength and coercivity was noticed when the volume fraction of Ni-P was higher than a threshold value. In the case of copper coating, irrespective of the coating thickness, no significant improvement in flexural strength was observed due to clustering of whiskers. However, the coercivity was increased with the increase in the coating thickness due to formation of more volume fraction of intermetallic copper precipitates. In comparison to the short fibre composites, excluding those with large volume fraction of Ni-P and copper

coating, the monoliths exhibited higher flexural strength due to the retention of fine grain morphology by spark plasma sintering.

Table 6.1 *Summary of magnetic and mechanical properties of monolithic and SiC whisker composite materials*

Sample details	Induction at 20 kA/m (T)	Coercivity (A/m)	Hardness (VHN)	Bending strength (MPa)	
				Mean	Std. deviation
Fe-Co	2.30	830	314±4	1148	35
1 vol% composites with					
Uncoated SiC	2.23	792	316 ± 1	1062	21
Cu coated SiC	2.21	860	318±3	1230	23
Ni-P coated SiC	2.21	708	320±3	994	48
Co coated SiC	2.21	682	314±2	1031	27
2 vol% composites with					
Uncoated SiC	2.20	800	326±2	1131	23
Cu coated SiC (thin)	2.18	759	313±4	1050	26
Cu coated SiC (thick)	2.05	940	329±5	1101	74
Ni-P coated SiC (thin)	2.02	682	311±2	1020	36
Ni-P coated SiC (thick)	1.70	1423	397±8	1598	33
Co coated SiC	2.11	747	321±4	1048	31
3 vol% composites with					
Uncoated SiC	2.13	756	313±2	636	46
Cu coated SiC	2.12	760	323±3	1040	36
Ni- coated SiC	1.81	1042	344±4	1316	48
Co coated SiC	2.10	624	286±2	761	21
5.5 vol% composite with Uncoated SiC	2.04	771	318±5	788	38

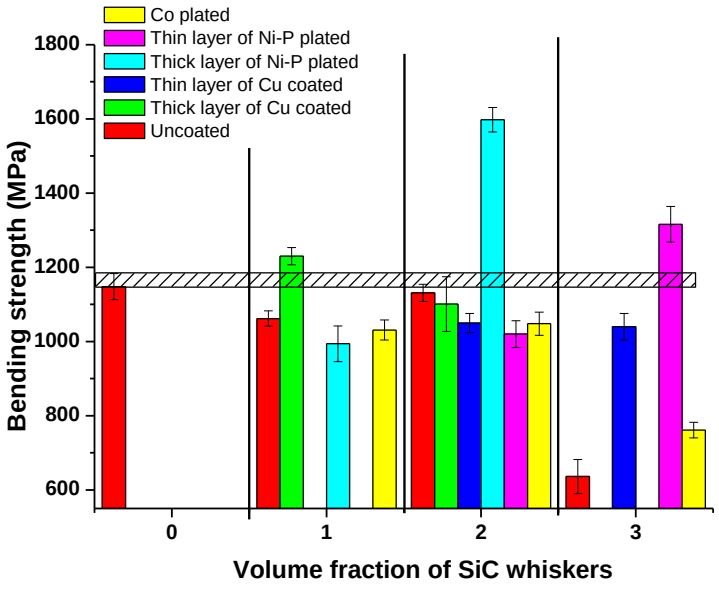

Fig. 6.15 Comparison of the bending strength of monolithic Fe-Co and its composites containing different volume fractions of coated SiC whiskers

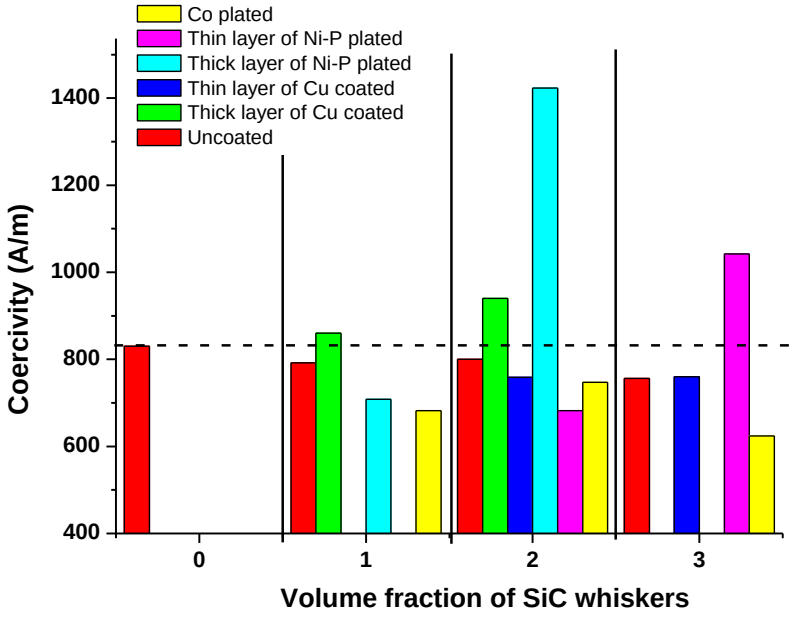

Fig. 6.16 Comparison of the coercivity of monolithic Fe-Co and its composites containing different volume fractions of coated SiC whiskers

6.6.2 Fractographic analysis of composites

It has already been shown that there was no change in the ordering fractions due to the introduction of SiC whiskers. Therefore, the increase or decrease in the mechanical properties in the presence of whiskers were associated with the strengthening and toughening mechanisms such as whisker pullout, crack deflection and whisker breakage, formation of new intermetallic compounds in case of coated whisker reinforced composites and changes in the microstructure of the matrix.

The fractographic images of some of the composites (Fig. 6.17 - 6.21) displayed the impressions of the fibres, which were their original locations (shown by arrows) and the pulled-out fibres (marked by triangle and stars)

6.6.2.1 Composites with bare and cobalt coated whiskers

The fractographic images of composites containing as-received SiC whiskers are shown in Fig. 6.17.

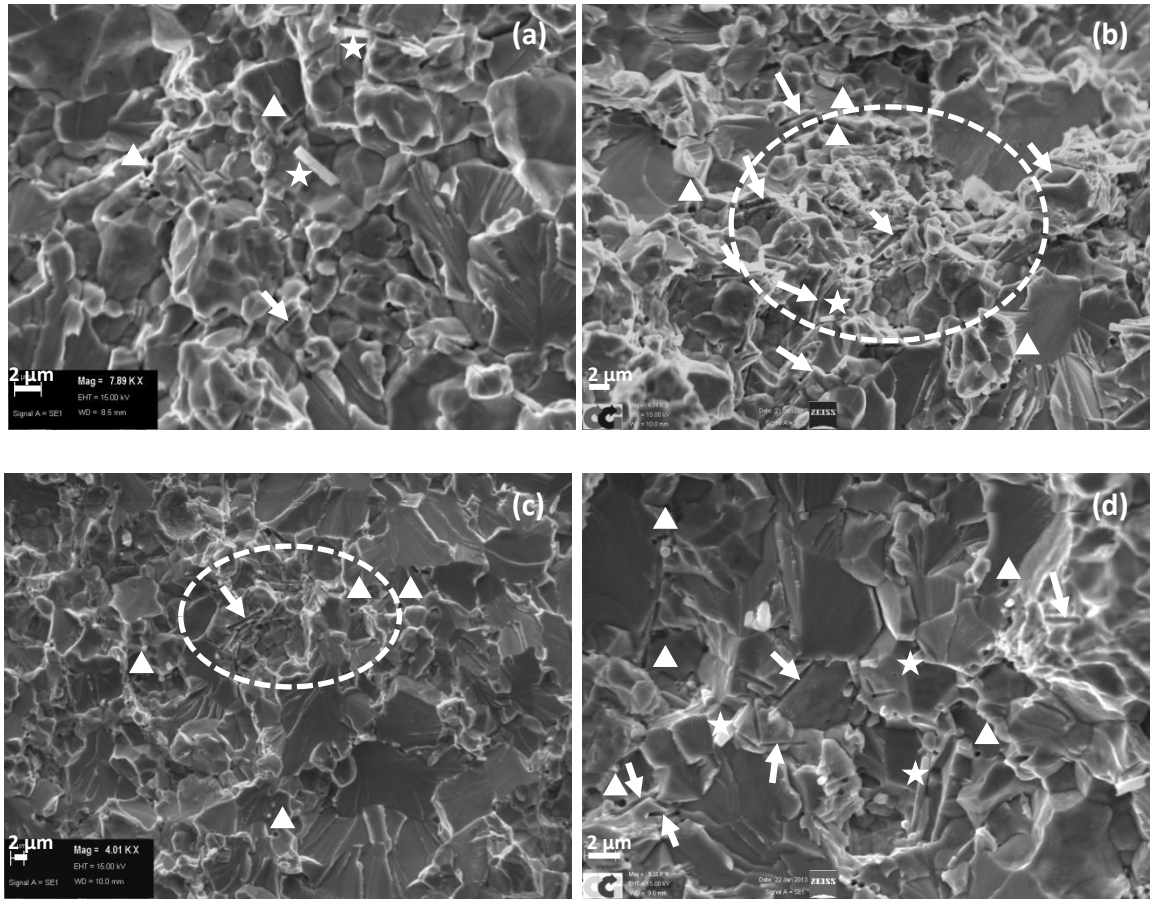

Fig. 6.17 Fracture surface of Fe-Co composites with: (a) 1; (b) 2; (c) 3; (d) 5.5 vol% of whiskers. The images show clusters, impressions of whiskers, pulled out whiskers and presence of whiskers along grain boundaries as marked by circles, arrows, stars and triangles, respectively.

The materials with larger grains exhibited large fan or feather shaped features on large and flat cleavage facets. Such large cleavage facets with minimized small grain structures were observed in composites with more than 2 vol% of uncoated SiC whiskers (Fig. 6.17(c) and (d)) and 3 vol% of cobalt coated SiC whiskers (Fig. 6.18). The excessive grain growth, as confirmed by the fractographic appearances in the aforementioned materials, was responsible for the lower bending strength and magnetic hardness values. The presence of whiskers at the grain boundaries suggested that the whiskers impede the grain boundary migration during the growth process. Thus, the whiskers played a duel and contradictory roles on the grain growth behaviour of Fe-Co alloys. The absence of any impressions of whiskers and presence of pores inside the grains in the materials with 3 vol% of cobalt coated whiskers (Fig. 6.18(b)) implied that the fibers were dissolved in the matrix and the grain growth of the matrix alloy was abnormal. The dissolved SiC increased the Si content of the matrix. Griest et al., observed that the addition of Si in Fe-Co alloys produced a significant drop in their Curie temperature

[8]. It has previously been documented that the spark plasma sintering of Fe-Co alloys near the Curie temperature would cause abnormal grain growth [9].

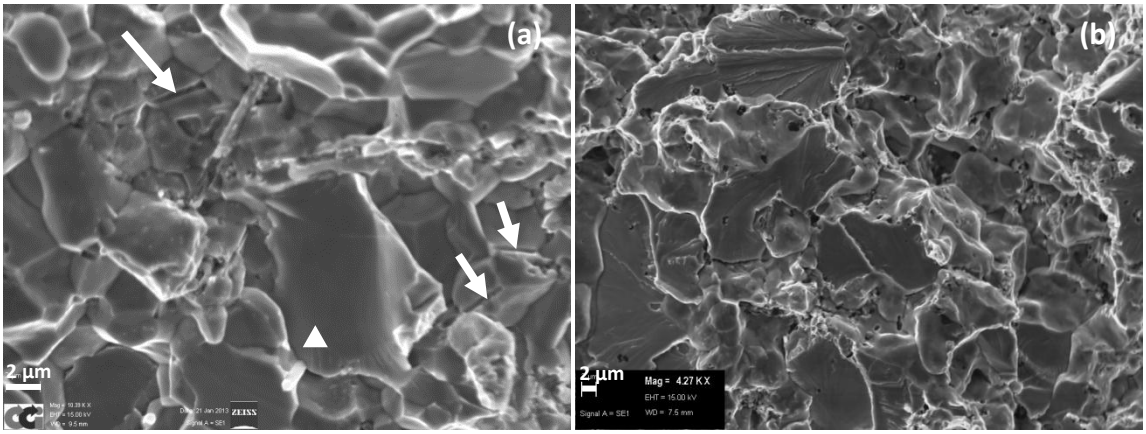

Fig. 6.18 Fracture surface of Fe-Co composites with: (a) 1; (b) 3 vol% of Co coated whiskers. The images show impressions of whiskers as marked by arrows and pulled out fibers as marked by triangles.

6.6.2.2 Composites with Ni-P coated whiskers

Similar to cobalt coated whiskers, an increase in volume fraction of fillers from 2 to 3, changed the brittle fracture mode from intergranular to transgranular. The fine holes in Fig. 6.19(a) represent the original location of the fibers that were pulled out during bending test. The fine features, which increased with the increase in the volume fraction of the coating, were the intermetallic Fe_3Ni_2 precipitates formed during sintering as shown in Fig. 6.12. The coarsened Fe-Co matrix and fine grained precipitates near the whiskers (Fig. 6.19(b)) corroborated that the overheating was predominant in the regions away from the whiskers and it was localised. These fine nanocrystalline precipitates produced the increase in the flexural strength, coercivity and Vickers hardness of the composites.

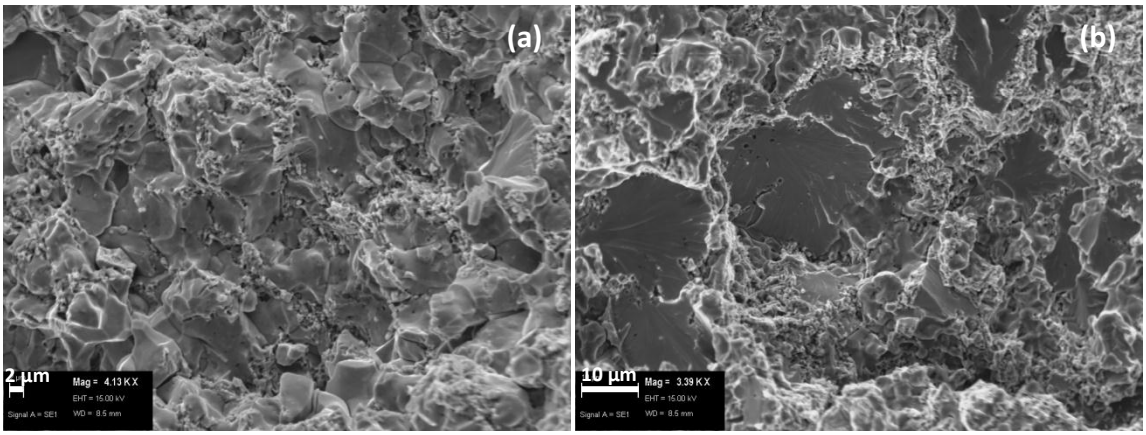

Fig. 6.19 Fracture surface of Fe-Co composites containing: (a) 2; (b) 3 vol% of Ni-P coated SiC whiskers

6.6.2.3 Composites with copper coated whiskers

The fractographic images of composites containing copper coated SiC whiskers are shown in Fig. 6.20 and 6.21. The inability to disperse the copper coated whiskers uniformly in the matrix by ultrasonication in ethanol resulted in the clusters as marked by the ovals and circles in fractographic images Fig. 6.20(b) and 6.21(b). Therefore, the mean bending strength was not improved on increasing the volume fraction of thick layer of copper coated whiskers from 1 to 2; however, there was an increase in the mechanical hardness values because of the increase in the volume fraction of precipitates and whiskers. The whiskers at the grain boundaries (as marked by triangles in Figs. 6.20 and 6.21) confirmed the fact that they pinned the grain boundaries during sintering as observed in composites with bare whiskers.

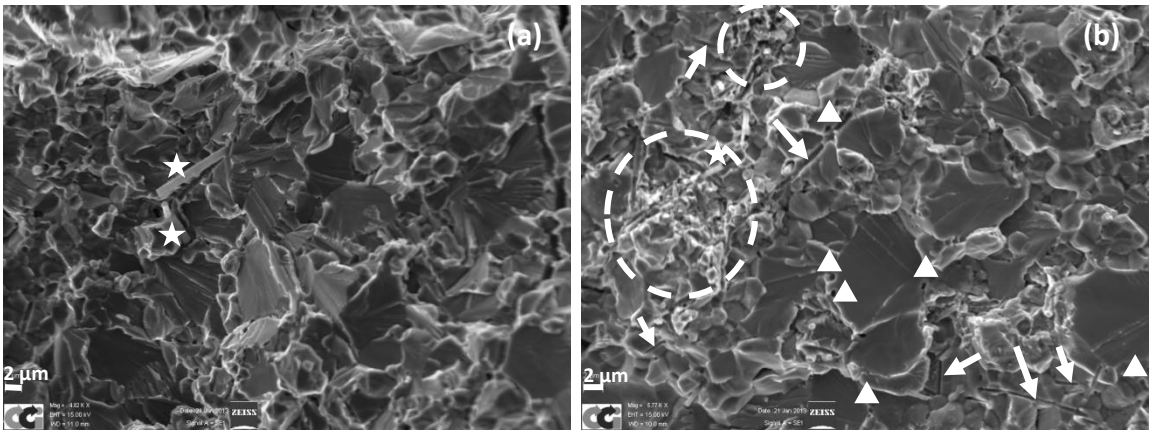

Fig. 6.20 Fracture surface of Fe-Co composites containing: (a) 1; (b) 2 vol% of Cu coated (thick) SiC whiskers showing clusters, impressions of whiskers, pulled out whiskers and presence of whiskers along grain boundaries as marked by circles, arrows, stars and triangles, respectively.

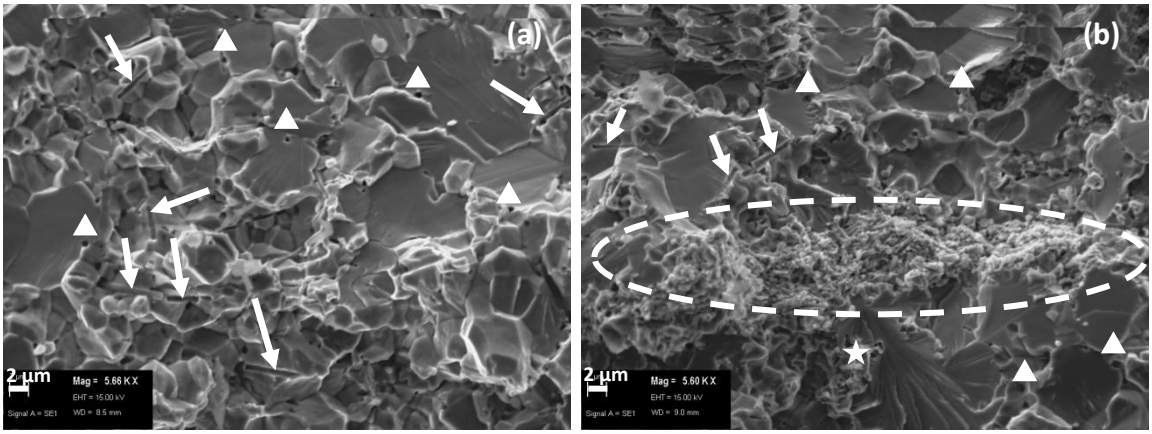

Fig 6.21 Fracture surface of Fe-Co composites containing: (a) 2; (b) 3 vol% of Cu coated (thin) SiC whiskers showing clusters, impressions of whiskers, pulled out whiskers and presence of whiskers along grain boundaries as marked by circles, arrows, stars and triangles, respectively.

6.6.3 Flexural ductility

The flexural responses of strip samples, whose bending strength was close to the mean value in the set of five samples, of a few selected monoliths and composites are compared in Fig. 6.22. The bare and Co coated SiC whiskers were not found to be useful to improve the ductility of the brittle magnetic alloy. The Cu and Ni-P coatings over the whiskers, by forming new intermetallic compounds, helped to improve the ductility, besides improving the mechanical strength. The incremental values were strongly related with the volume fraction and type of the coating material. An increase in the volume fraction of amorphous Ni-P coating produced an increase in the ductility and strength values; however an increase in the copper volume fraction caused a reduction in the ductility values. This might be due to the finer precipitate morphology of Fe_3Ni_2 than $Cu_{0.8}Fe_{0.2}$ and/or the difficulty associated with the dispersion of copper coated whiskers in composites with higher volume fraction of reinforcements.

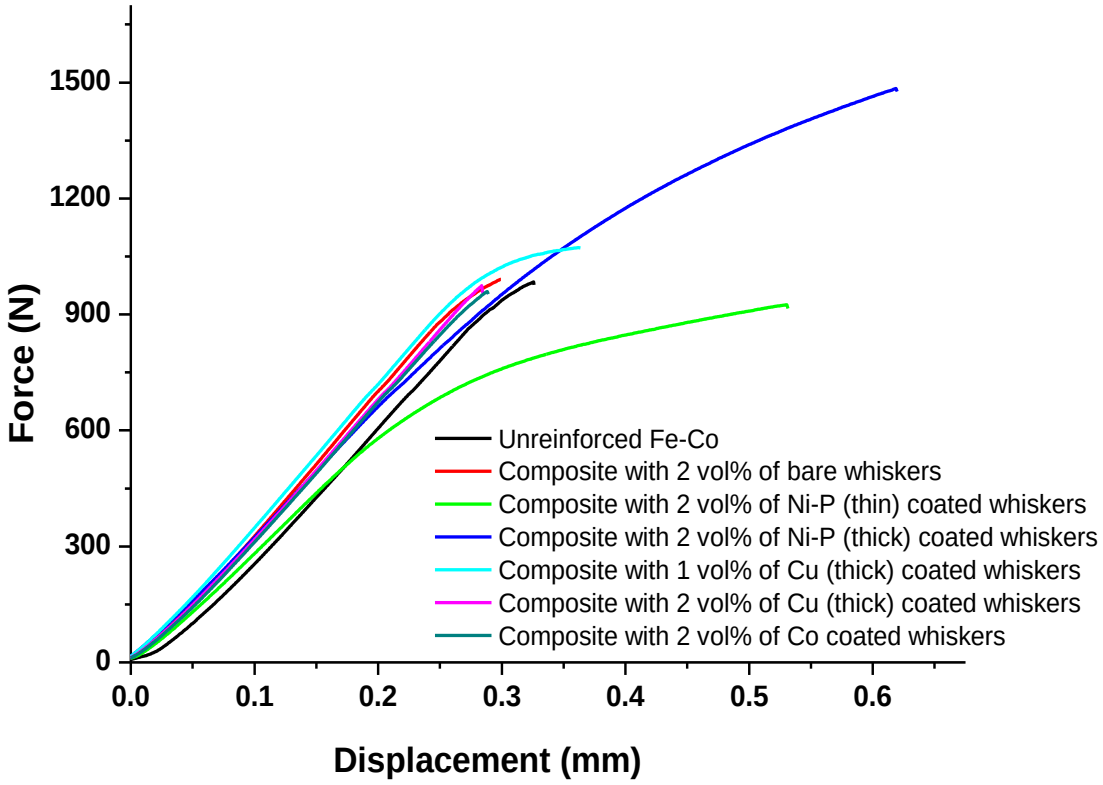

Fig. 6.22 Flexural response of Fe-Co monolith and composites containing bare and copper and Ni-P coated SiC whiskers

References

1. J.Y Song, J. Yu, Residual stress measurements in electroless plated Ni–P films, *Thin Solid Films* **415**,167–172(2002).
2. T.P. O'Sullivan and S.E. Taylor, Dispersion of Silicon Carbide Whiskers and Powders in Aqueous and Non-aqueous Media, *J. Mater. Chem.* **1(3)**, 393-399 (1991).
3. T. Ishii and H.K. Bowen in Ceramic Transactions, Ceramic Powders Science **1I,** edited by G.L. Messing, E.R. Fuller, and H. Hausner (American Ceramic Society, Inc., Westerville, Ohio, 1987) pp. 452-59.
4. H.S. lnglis and D. Taylor, Decomposition of Formic Acid on Titanium, Vanadium, Chromium, Manganese, Iron, Cobalt, Nickel, and Copper, *J. Chem. Soc. A***,** 2985-2987(1969)
5. J.M. Loureiro, A.C. Batista, V.A. Khomchenko, B.F.O. Costa, G. Le Caaer, Order-disorder phenomena from X-ray diffraction in FeCo alloys annealed and ground at high energy, *Powder Diffr.* **26 [3]**, 267-272 (2011).
6. B.D Cullity and C.D Graham, Introduction to magnetic materials, New Jersey, IEEE press and A John Wiley & sons, Inc., publisher, 2 nd edition (2009), pp. 115-116
7. R.M. Bozorth, Ferromagnetism, New York, IEEE press, 2 nd edition (1978) pp. 169-177
8. Griest AJ, Libsch JF, Conard GP (1955) Effect of ternary additions of silicon and aluminium on the ordering reaction in iron-cobalt. Acta Metall. 3:509–510.
9. M.K Mani, G Viola, M.J Reece, J.P Hall, S.L Evans, Structural and magnetic characterization of spark plasma sintered Fe-50Co alloys, *Mater. Res. Symp. Proc.* **1516**, 201-207 (2012)

Chapter 7
Results and discussion: Carbon nanotube reinforced composites

7.1 Introduction

The morphology, purity, structural integrity and phase characteristics of the as-obtained CNTs, as analysed using a Raman microscope, TEM and XRD, are presented and discussed at the start of this chapter. The differences in the sintering behaviours of the as-received and ball milled Fe-Co powders with and without CNTs are explained using the SPS machine data. The crystallographic structural and microstructural characteristics of the sintered composites containing different amounts of bare CNTs are described with the help of XRD observations and optical micrographs. The DC magnetic properties and mechanical properties such as hardness and bending strength of the CNT composites are compared and the optimum volume fraction of CNTs for property enhancement is shown. The structural integrity of the CNTs was checked on the fractured surfaces of all the composites using high resolution SEM and Raman microscopy.

In the second half of the chapter, the results of the electroless Ni-P coated CNTs, as characterterised using XRD, TEM, EDX, Raman microscope, DSC and TGA are described. The influence of the CNT coating on the final magnetic properties and mechanical performance of the composites are explained by correlating them with the XRD, SEM, EDX and optical microscopy observations.

7.2 Characterisation of as-received CNTs

7.2.1 Raman spectroscopy

Fig. 7.1 shows the Raman spectra of the MWCNTs in the as-prepared and plasma treated conditions. Three characteristic bands were observed in both the spectra, namely D band, G band and G′ band at around 1320-1350, 1550-1600 and 2670-2720 cm^{-1}, respectively [1]. A fourth characteristic band namely radial breathing mode (RBM), which is usually observed in single walled CNTs at about 100-400 cm^{-1}, was absent in the spectra because of the larger wall thickness of the MWCNTs [2]. The disorder induced phonon mode (D band) is a double resonance Raman mode and is highly sensitive to non-planar atomic distortions, MWCNT curvature, carbon impurities and structural order. The G band, which corresponds to one of the E_{2g} modes, was produced due to the tangential shear vibration of sp^2 bonded carbon neighbours on the graphite sheet. The bands formed in the spectral range of 1100 to

1800 cm^{-1} are called first order Raman spectra, whereas those observed between 2500-3100 cm^{-1} are termed second order spectra. The G′ band represents the overtone of the first order mode at 1350 cm^{-1} and is also known as the second order harmonic of the D band. In addition to the aforementioned characteristic bands, a shoulder (named D′ band) was observed on the right side of the G band in all the spectra. Similar to the D band, D′ is a double resonance Raman characteristic and is produced due to disorder, defects or ion intercalations between the graphite walls [3]. The broad band at around 2945 cm^{-1} was thought to be present because of the strong nature of the Raman modes at 1350 and 1620 cm^{-1} [4].

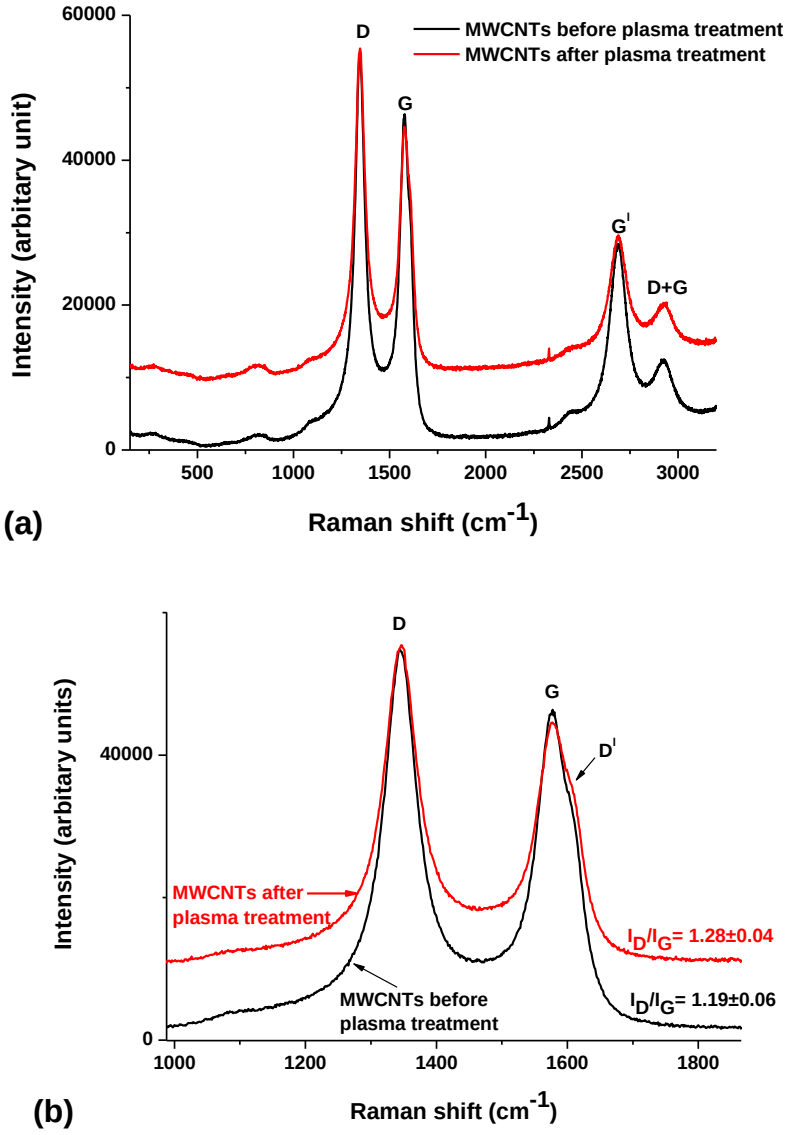

Fig. 7.1 (a) Raman spectra of MWCNTs in the as-prepared and plasma treated condition; (b) Magnified image showing the shoulder peak (D′) right to the G band and integrated intensity ratio values of D and G bands

The integrated intensity ratio ($R=I_D/I_G$) between the D and G bands is widely used to explain the structural integrity of the carbonaceous nanomaterials in the composites containing them [5]. An increase in the defect concentration would raise the intensity of the D band, which in turn would increase the R values. The plasma treatment, which was done to introduce O_2 functional group on CNT surfaces, had increased the disorder density in the nanotubes walls as confirmed by the increase in the integrated intensity ratio (Fig. 7.1(b)).

7.2.2 Transmission electron microscopy

As depicted in the TEM images of the as-received CNTs (Fig. 7.2), the outer tube diameter and number of concentric graphite layers in the walls were not constant. They varied between 5-30 nm and 4-20, respectively. The inner tube diameter followed the same trend as that of the outer diameter.

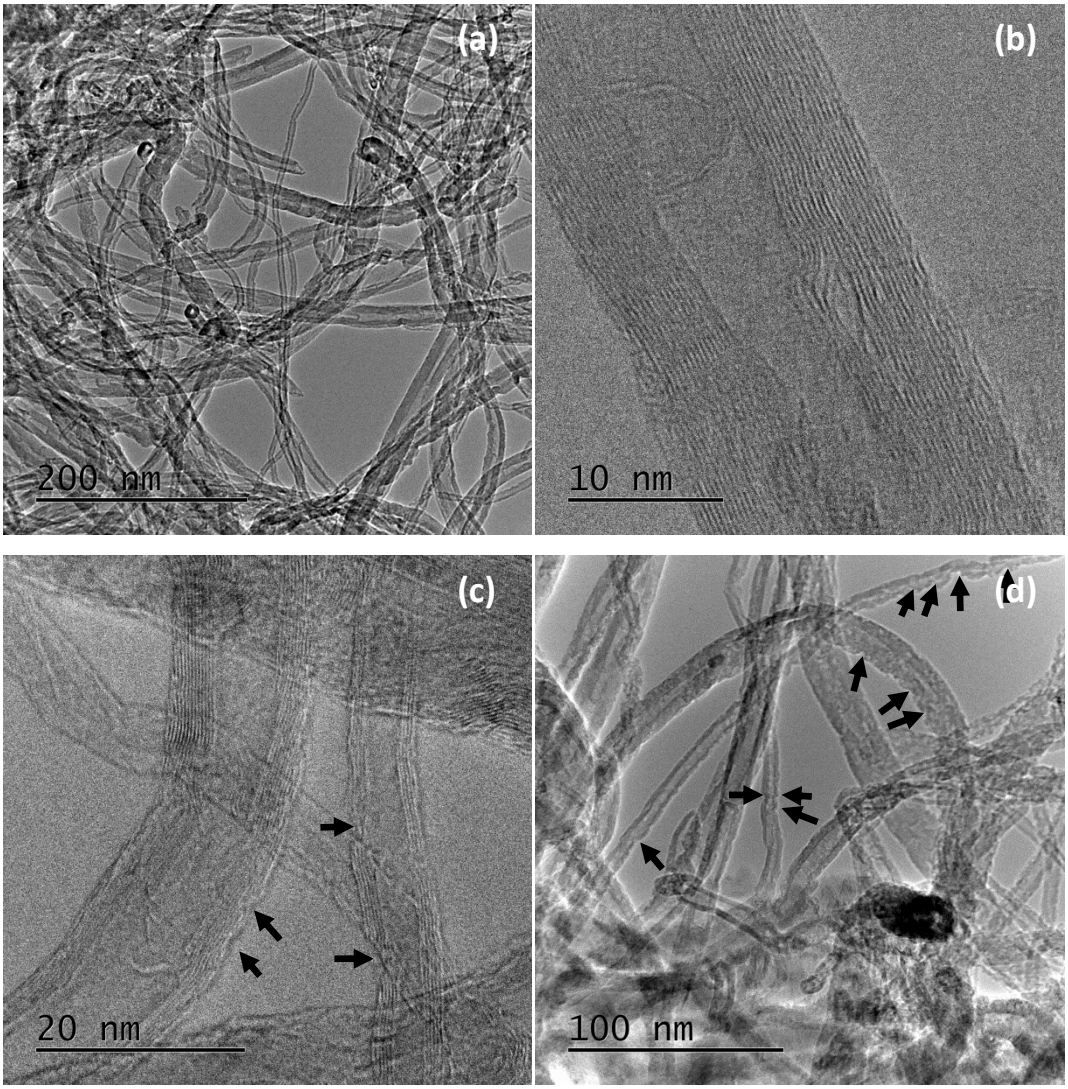

Fig. 7.2 Transmission electron micrographs of as-received CNT in the O_2 functionalised state; (a), (c) and (d) are CNT clusters and (b) one MWCNT; the arrows in (c) and (d) denote the defects on the CNT walls.

The plasma treatment, which was done to introduce the functional group (= O) on the CNT surfaces, damaged the walls of some of the CNTs extensively over the others as shown by arrows in Fig. 7.2(c) and (d).

7.3 Uncoated CNT composites

7.3.1 Influence of ball milling and CNT addition on spark plasma sintering

To understand the effect of ball milling on sintering behaviour, the displacement of the piston in the SPS unit was monitored for the powder and CNT composite powder mixture that were taken with and without ball milling. A positive piston speed represents densification, whereas a negative one denotes expansion. The average piston speed and temperature of the as-received and ball milled Fe-Co powders as a function of sintering time is shown in Fig. 7.3. During heating, the mechanical pressure was gradually increased from 7 MPa to 80 MPa in 4.5 minutes. Most of the densification occurred when the powders were heated under mechanical pressure to the sintering temperature (in the time zone demarcated by the dotted lines). The sintering of the as-received Fe-Co powders occurred over a wide range of temperature due to: (a) non-uniformity in the starting particle size; and (b) the slow and steady increase in the mechanical force while heating. Dwelling at 900^{o}C produced a relatively smaller amount of compaction. The samples expanded when the mechanical pressure was removed during cooling. Ball milling for one hour in atmospheric conditions caused a significant change in the sintering behaviour of Fe-Co powder. Crystallographic imperfections introduced due to milling such as dislocations, oxides, grain boundaries and oxide/particle interfaces caused most of the densification to occur in the initial stages of sintering (as shown by the sudden drop in the piston speed at about 750^{o}C). Similar effects of ball milling on sintering were also noticed during the compaction of powder mixtures containing bare CNTs and Fe-Co (Fig. 7.4). This behaviour suggested that complete densification can be realised at temperatures lower than 900^{o}C, if the sample is ball milled with or without CNTs.

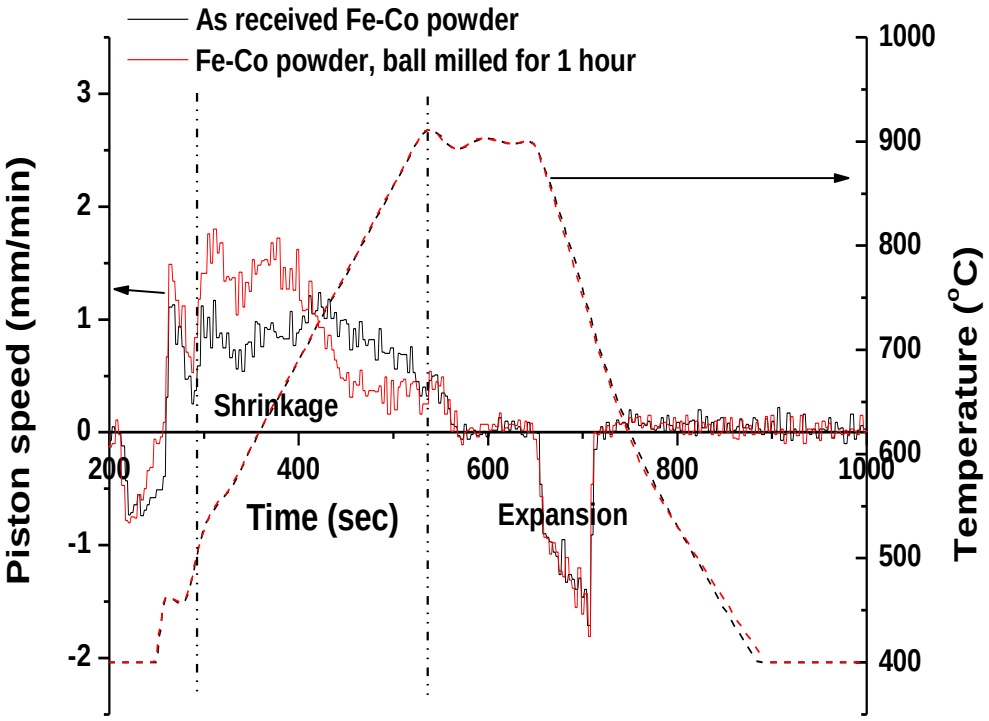

Fig. 7.3 Average piston speed and temperature profiles, as measured for the shown starting materials in the SPS system.

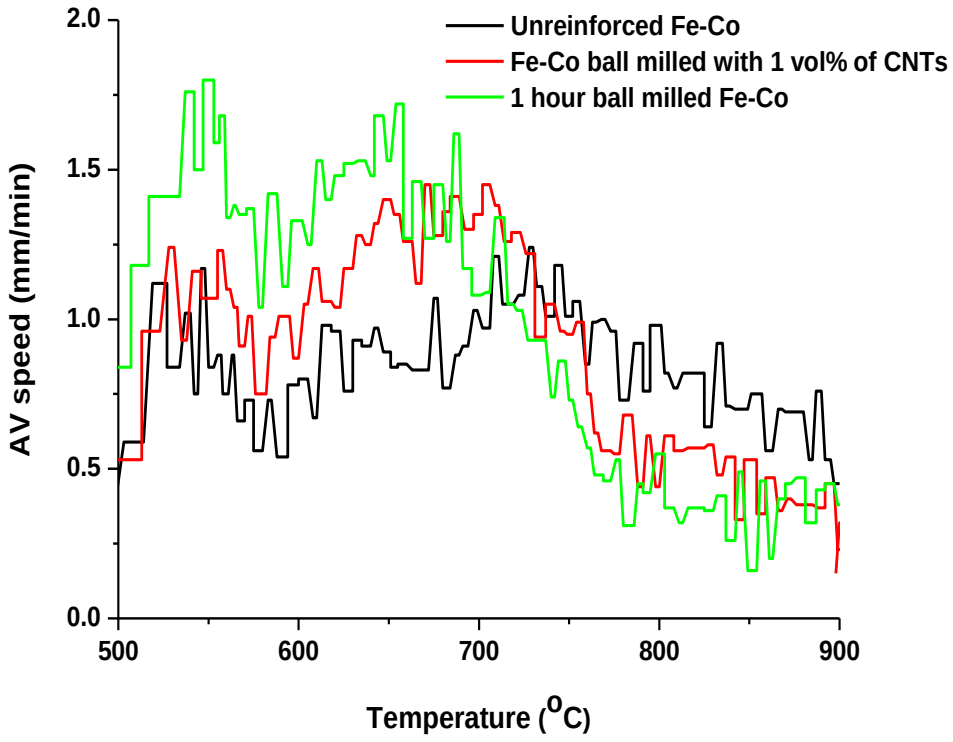

Fig. 7.4 Plots of average (AV) piston speed against temperature, as measured for the shown materials in the SPS unit.

7.3.2 Characterisation of composites

7.3.2.1 Crystallographic structural characterisation

Ball milling of Fe-Co in atmospheric conditions promoted the formation of cubic spinel structured, ferrimagnetic maghemite (γ Fe_2O_3) phase (Fig. 7.5). Maghemite is one of the several forms of iron oxide (including wustite, magnetite, maghemite, haematite) and exhibits low coercivity like magnetite [6]. Maghemite exhibits a saturation magnetisation of 73-74 emu/g and coercivity of 250-350 Oe [7]. The shifting of fundamental Fe-Co lines to lower angles for the compacts prepared after 1 and 5 hours of ball milling than for those sintered with the as-received powder suggested that there was lattice expansion in the material, which might have been introduced by the oxide phase.

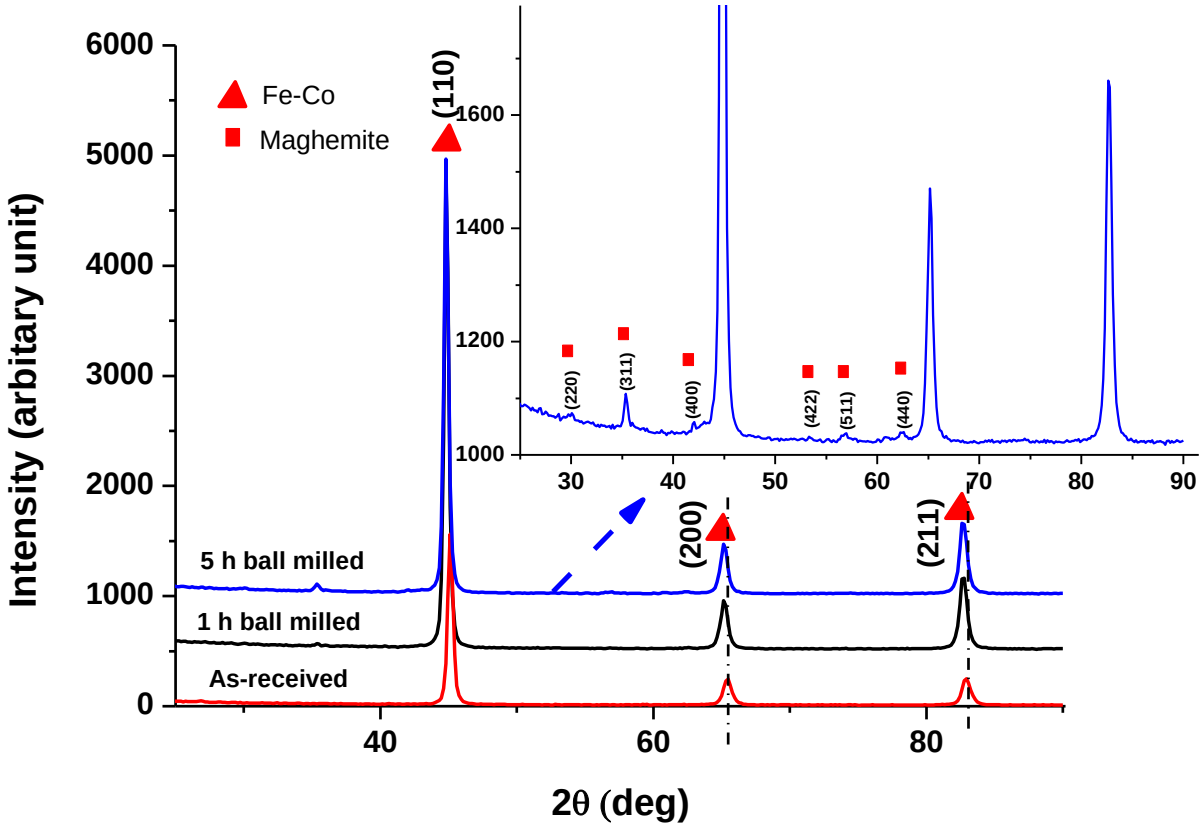

Fig. 7.5 XRD histogram of sintered Fe-Co compact prepared using the powders after the displayed treatments; the inset shows the magnified XRD pattern of the compact prepared using 5 h ball milled powders.

Fig. 7.6 shows the results of very slow scan X-ray diffractometry experiments that were performed using K_α radiation from a Co target on the composites to obtain the superlattice reflections. The degree of ordering of composites containing different amount of CNTs was compared using the intensity of (100) and (210) superlattice lines. Ball milling caused a reduction in the long range ordering fraction as evidenced from the reduction in the

intensity of both the superlattice lines. Addition of about 1 vol% of CNTs did not make any significant improvement in the ordering fraction. However, the introduction of about 5 vol% of CNTs produced an increase in the volume fraction of the ordered alloy as confirmed by the increase in the intensity and the shift in the position of the superlattice lines. The superlattice lines were shifted to lower angles due to the increase in the lattice parameter caused by ordering [8]. The full width half maximum (FWHM) of (100) reflection and the anti-phase domain sizes calculated using the Scherrer formula [8] are displayed in Fig. 7.6. Ball milling produced an increase in the FWHM; however, the effect of CNTs on FWHM varied with the volume fraction. Addition of lower volume fraction of CNTs (~1 vol%) produced an increase in FWHM, whereas higher volume fraction of CNTs (~5 vol%) caused a reduction in FWHM. This suggested that the anti-phase domain sizes could be controlled by the changing the volume fraction of CNTs. With the addition of CNTs, the fundamental peaks were also shifted to lower angles (Fig. 7.7). This assured the lattice expansion in the compacts, which might have been caused due to the increase in the long range ordering and to the formation of the maghemite phase, as confirmed in samples sintered after ball milling (Fig. 7.5).

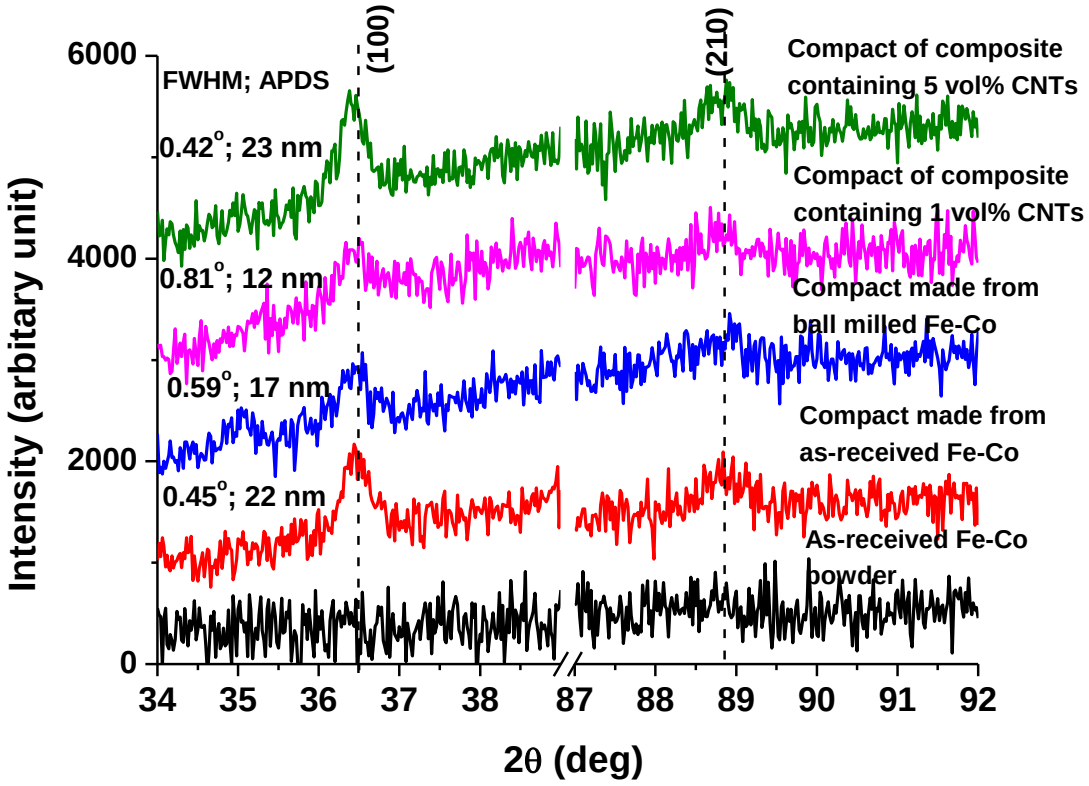

Fig. 7.6 Slow scan XRD pattern showing (100) and (210) superlattice reflections of the as-received powder and the compacts prepared using the mentioned starting materials; the full width half maximum (FWHM) of (100) peaks and the anti-phase domain sizes (APDS) are also displayed (Co K_α radiation was used)

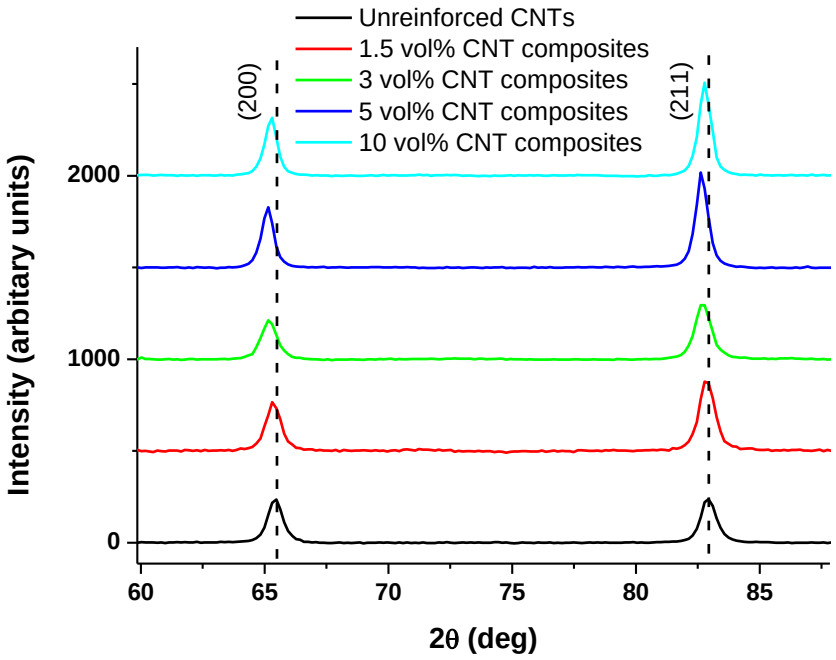

Fig. 7.7 XRD patterns of the shown monolithic and composite materials (Cu K_α radiation was used)

7.3.2.2 Raman spectroscopic studies of composites

Raman spectra of the composites containing different volume fraction of CNTs that were sintered following the two different mixing procedures are shown in Fig. 7.8.

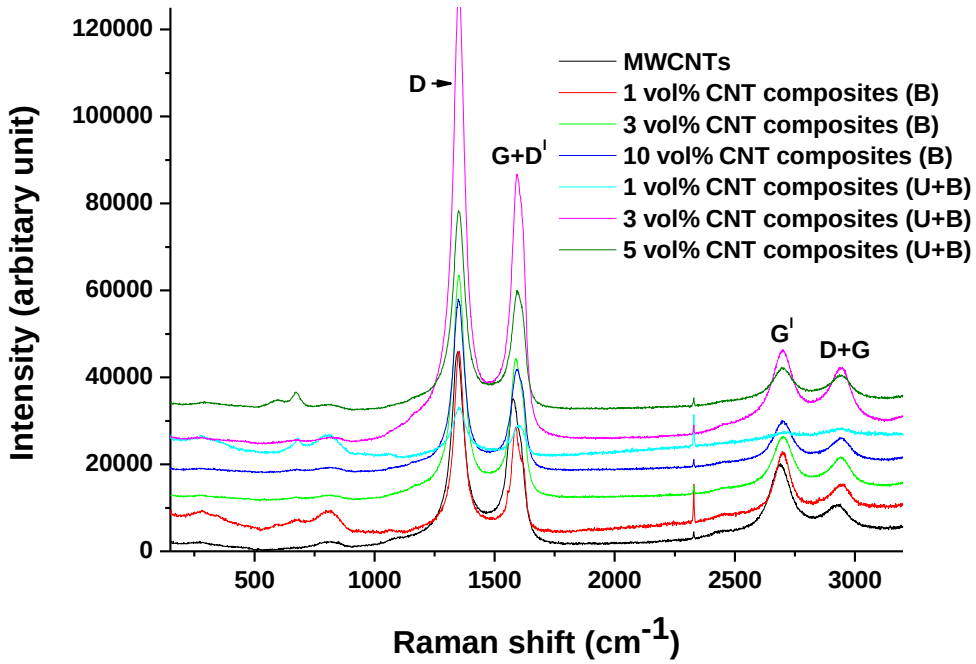

Fig. 7.8 Raman spectra of the Fe-Co- CNT composites and as received MWCNTs;

The shift in the position of the D and G bands to higher frequencies in all the composites compared to the as-received CNTs (Fig. 7.9(a)) implied that the CNTs were strained by the matrix alloy [9, 10]. The peak shift produced due to the straining of CNT walls was also observed in the second Raman reflections (Fig. 7.9(b)).

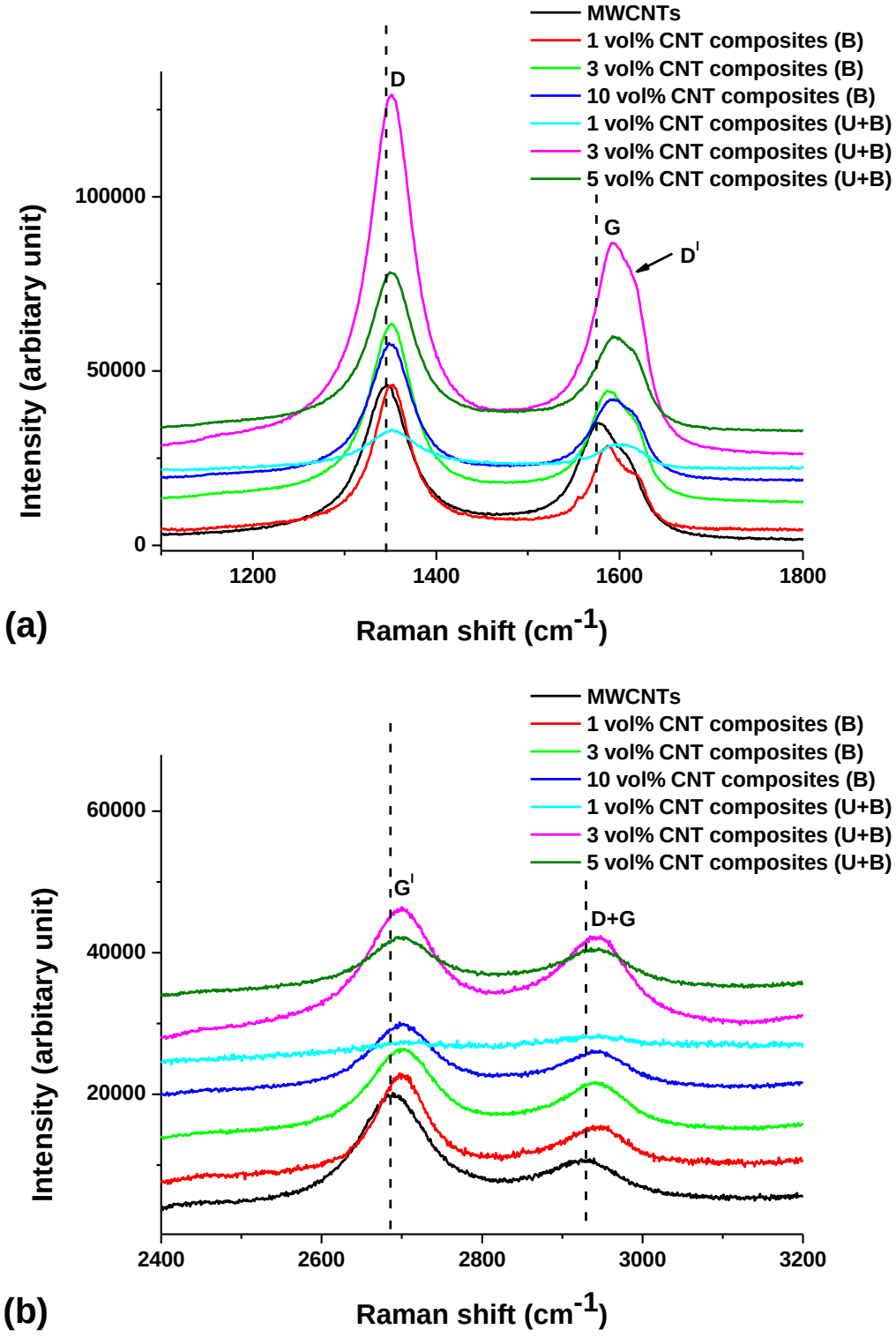

Fig. 7.9 (a) First-order Raman spectra showing D, G and D' bands; (b) Second order Raman spectra displaying G' and (D+G) bands

The presence of G peaks in the composites suggested that the graphite structures were preserved even after mechanical milling and spark plasma sintering. An increase in the R value (I_D/I_G) implied a raise in the amount of the disordered carbon atoms and/or a reduction in the mean crystallite size [11]. The R values of all the composites fabricated are presented in Fig. 7.10. A raise in the R values of all the composites compared to the as-received CNTs indicated that the amount of disorder was increased; however, the increase was higher in composites with lower volume fraction of CNTs than those with higher percentages. This might be because of the increased probability for the CNTs that could be impacted by the grinding media during the high energy ball milling. The defect density on the walls was marginally higher if ultrasonication was preceded by ball milling during powder processing as confirmed by the increased mean R values.

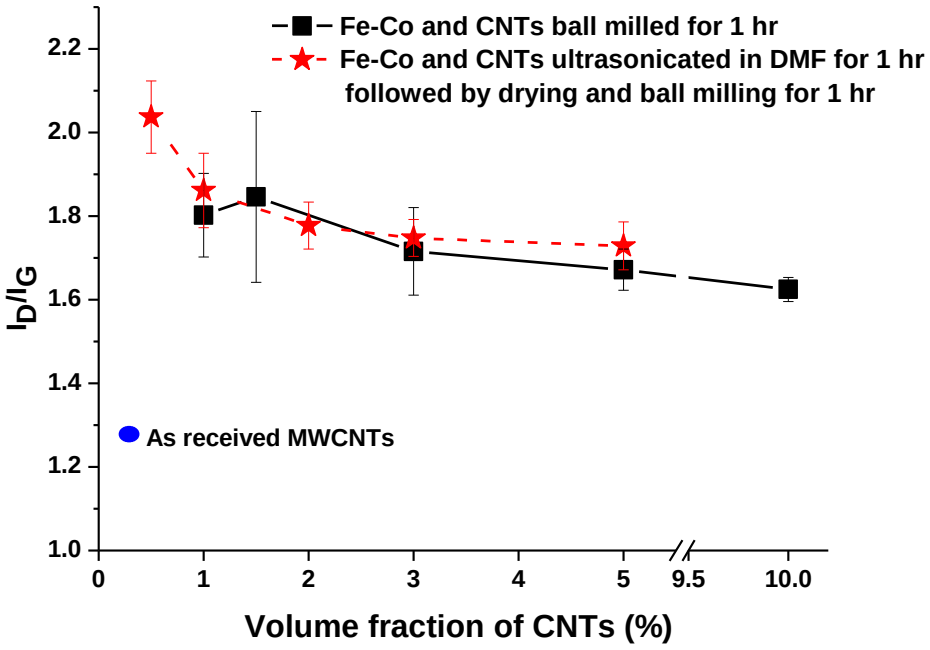

Fig. 7.10 Integrated intensity ratio (I_D/I_G) of the composites prepared after two different mixing procedures

7.3.2.3Microstructural characterisation

In addition to the change in the sintering behaviour as discussed in section 7.3.1, ball milling produced distinct differences in the optical microstructures (Fig. 7.11). The superparamagnetic maghemite particulates formed during atmospheric ball milling were lined up under the influence of SPS current because of their inherent nature to align in the presence of a magnetic field [12]. The grain boundaries in ball milled materials were not distinct like the one prepared using as-received powders because of the surface oxides formed during

milling. The grain morphology of Fe-Co appeared to be more elongated with the increase in the volume fraction of the maghemite particulates in 5 hour ball milled materials [Fig. 7.11(c)]. The long axis of the elongated grains was perpendicular to the direction of force application. The mechanism behind the formation of elongated grains is still under consideration.

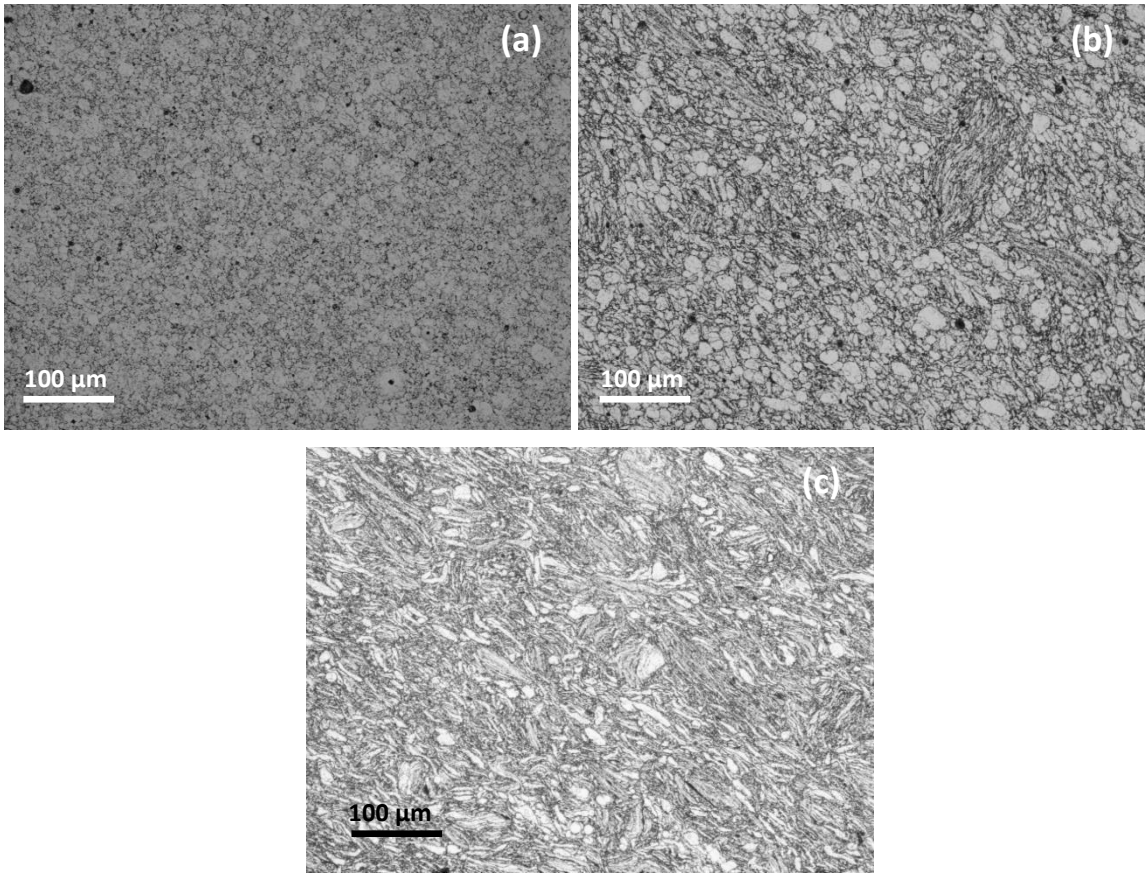

Fig. 7.11 Optical micrographs of compacts prepared using: (a) as-received; (b) one hour ball milled; (c) 5 hours ball milled Fe-Co powders.

Unlike monolithic materials (Fig. 7.12(a)) and similar to ball milled materials, the CNT composites exhibited elongated grain morphologies without clear grain boundaries due to the presence of the oxide phase (Fig. 7.12(b-e)). In composites with more than 2 vol% of CNTs, the CNTs present on the boundaries between the particles were preferentially etched by the etchant (Nital) and revealed the distinct lengthened grain morphologies of the matrix grains. No distinct microstructural difference was observed in the CNT composites that were prepared by B (Fig. 7.12(b) and (c)) and U+B (Fig. 7.12(d) and (e)) method. The grains tended to become equiaxed if the powder was maintained relatively loose under minimum pressure for 3 minutes under pulsed current (Fig. 7.12(f)). This could be due to the removal of surface oxides by the presumed plasma formed at the voids between the particles [13].

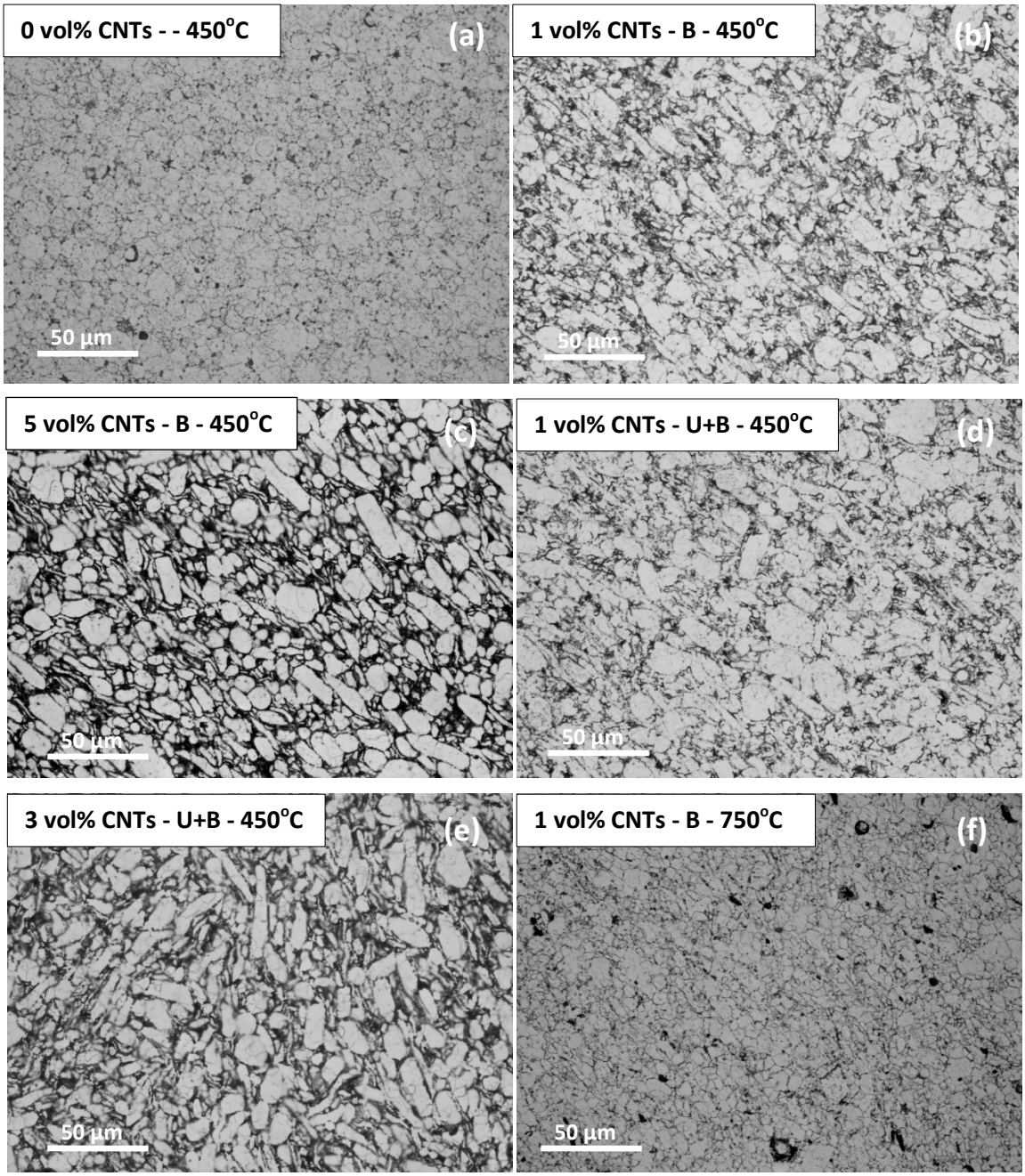

Fig. 7.12 Optical micrographs of the compacts with shown vol % of CNTs – powder blending method - temperature at which the mechanical pressure was applied

7.3.2.4 Effects of ball milling on magnetic and mechanical properties

The magnetic and mechanical properties of compacts sintered under different conditions are summarised in Table 7.1.

Table 7.1 *Summary of the magnetic and mechanical properties of the compacts prepared using as-received and ball milled Fe-Co alloy powders*

Sample details	Induction at 20 kA/m (T)	Coercivity (A/m)	Hardness (VHN)	Bending strength (MPa)	
				Mean	Std. dev.
Fe-Co	2.30	862	316±2	1126	35
Fe-Co ball milled for 1 hour	2.25	697	360±3	902	118
Fe-Co ball milled for 5 hours	2.06	1365	408±5	1104	64
Fe-Co ball milled for 1 hour (Pr. was applied when T was 750^{o}C); heating rate between 450-750^{o}C was 20^{o}C/min	2.28	636	363±5	1014	70
Fe-Co ball milled for 1 hour (Pr. was applied when T was 750^{o}C); heating rate between 450-750^{o}C was 10^{o}C/min	2.30	636	360±2	1099	129

A reduction in the coercivity was noticed in the materials that were ball milled under atmospheric conditions and the fall was increased with the reduction in the heating rates between 450-750^{o}C in the presence of minimum pressure. The reduction in the coercivity can be related to the improvement in the sinterability by the maghemite phase because of their lower sintering temperature [14] or to the formation of nanocrystalline ordered structures with reduced dimensions [15], as confirmed by the XRD result (Fig. 7.6). A plausible explanation for the second possibility was given by Hertzer [16]. He explained that the magneto-crystalline anisotropy of the material, which increases the coercivity, would be proportionately reduced when the diameter of the grain is lowered below the ferromagnetic exchange length (< 100 nm). A significant rise in the coercivity with the duration of ball milling suggested that only a lower volume fraction of maghemeite was helpful in coercivity reduction in comparison to the compact prepared from as-received material. Due to the introduction of the oxide phase, the saturation induction was reduced in the ball milled samples. The fall in the magnetic induction values increased with the increase in the volume fraction of the oxide phase due to the increase in the ferromagnetic dilution. The further fall in the coercivity and rise in saturation induction in the materials heated at slower heating rates between 450-750^{o}C under minimum pressure (7 MPa) might be due to the cleaning by

presumed plasma activation or the increase in the volume fraction of nanocrystalline long range ordered structures [17].

The mechanically hard maghemite phase increased the Vickers hardness of the composite. The volume of the oxide in the composite was increased with the milling time and hence, a further increase in the hardness was observed in the 5 hour ball milled sample. When the ball milled Fe-Co compacts were subjected to bending, the nanocrystalline maghemite might have acted as crack nucleation sites or might have promoted cracking from the existing defects and hence, a reduction in the bending strength values were observed. As a result, the standard deviation of the bending strength values was very high for the ball milled samples.

7.3.2.5 Magnetic properties of CNT composites

The magnetic induction at 20 kA/m and coercivities of the composites prepared after mixing the CNTs and Fe-Co powders by U+B method and B method are presented in Table 7.2 and compared in Fig.7.13.

Table 7.2 *Summary of the magnetic and mechanical properties of the monolithic and CNT composite materials*

Sample details	**Induction at 20 kA/m (T)**	**Coercivity (A/m)**	**Hardness (VHN)**	**Bending strength (MPa)**	
				Mean	**Std. dev.**
Monolithic FeCo	2.30	862	316±2	1126	35
Fe-Co composites prepared after B method of mixing					
1 vol% CNTs	2.33	505	330±4	1199	103
1 vol% CNTs (Pr. applied at 750^{o}C)	2.30	378	317±4	1142	15
1.5 vol% CNTs	2.29	488	310±3	1056	78
2 vol% CNTs	2.30	541	315±3	943	116
3 vol% CNTs	2.23	541	307±5	808	32
5 vol% CNTs	2.12	601	283±2	502	35
10 vol% CNTs	1.83	683	233±5	378	29
Fe-Co composites prepared after U+B method of mixing					
0.5 vol% CNTs	2.33	520	313±3	1174	30
1 vol% CNTs	2.37	515	340±4	1194	83
2 vol% CNTs	2.26	503	311±3	1040	17
3 vol% CNTs	2.24	556	296±8	883	25
5 vol% CNTs	2.12	595	278±5	709	32

The addition of CNTs, lower than 2 vol%, improved the density of the compact (Fig. 7.14) and produced an increase in the magnetic induction. It has been observed that CNT addition up to 10 vol% produced a coercivity reduction; however, the maximum drop was noticed in composites with 1-2 vol% of CNTs. The factors that promoted the decrease in coercivity include: (a) density improvement; and (b) the formation of nanocrystalline ordered domain structures with reduced dimensions. The CNTs introduced higher than 2 vol% were clustered into small pockets between the particles (Fig. 7.12 (c) and (e)) and hindered the sintering process. As a result, the saturation induction of the material was decreased with the increase in the volume fraction of CNTs. The increase in the coercivity with the addition of CNTs higher than 1.5 vol % could be attributed to the increase in: (a) the fraction of the ordered alloy as shown in Fig. 7.6 [16]; (b) porosity levels; and (c) the size of the ordered domains.

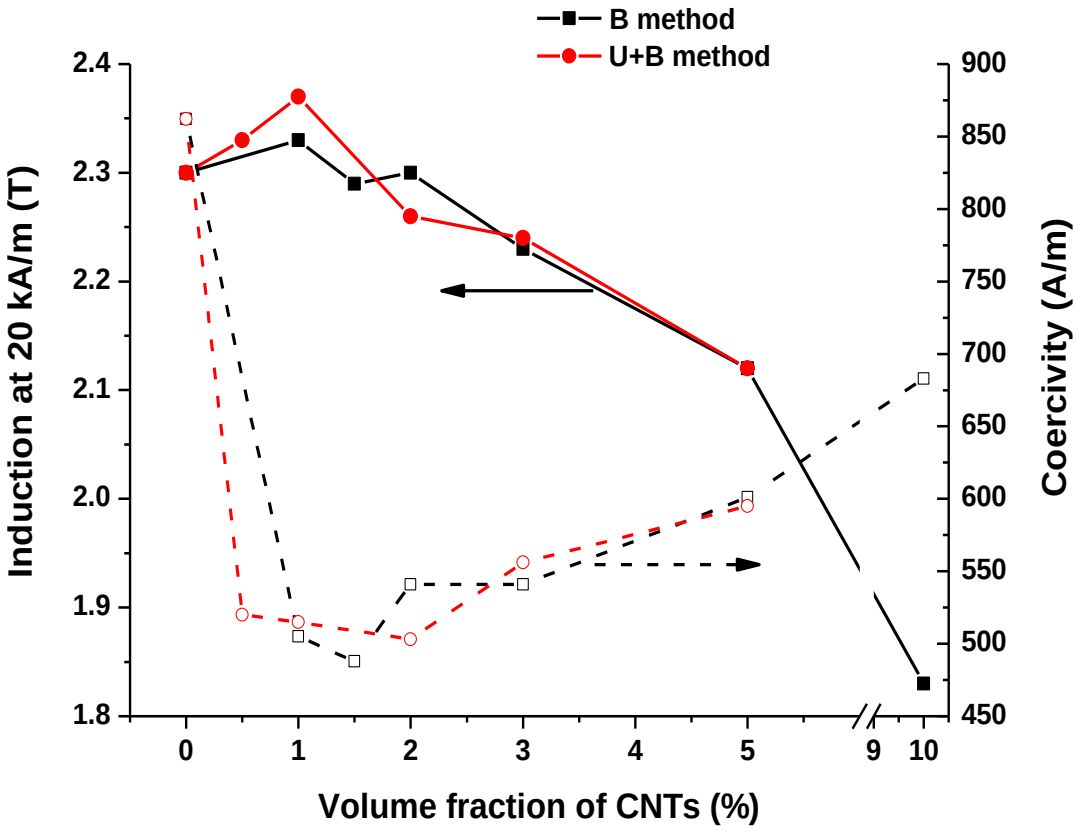

Fig. 7.13 Effect of volume fraction of CNTs on saturation induction (shown by continuous lines and filled symbols) and coercivity (shown by dotted lines and open symbols) of (Fe-Co)-CNT composites prepared by spark plasma sintering following two different dispersion routes

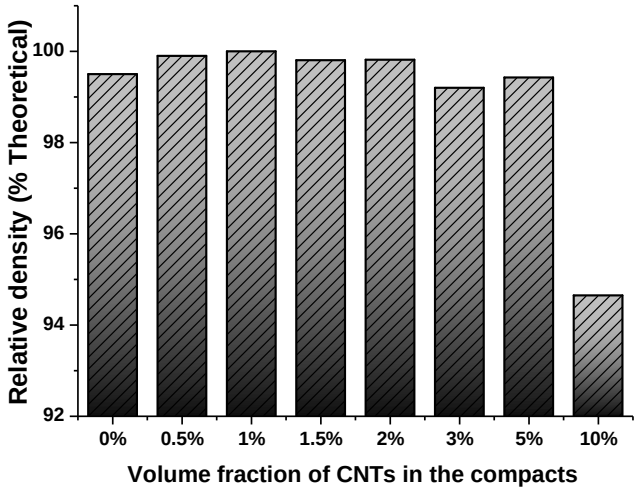

Fig.7.14 Relative density of the SPS sintered compacts containing different volume fraction of CNTs

The coercivity reduction exhibited by the lower vol % CNT composites can be further enhanced by applying the mechanical pressure (in addition to the low pressure 7 MPa applied for electrical contact) during sintering from 750^{o}C, instead of from 450 ^{o}C. The coercivity reduction was due to the removal of oxide that was introduced during ball milling. This was realised by the disintegration of CNTs, as confirmed by the absence of characteristic CNT bands in the Raman spectra for the material prepared by the former route (Fig. 7.15). The Raman peak at 666 cm^{-1} was more intense than the adjacent one at 810 cm^{-1} in the compact prepared from ball milled powder and composites containing lower volume fraction of CNTs (i.e) in materials with larger volume fraction of oxide phase. However, the materials with lower oxide content displayed a lower intense peak at 666 cm^{-1} with respect to the near right wing peak (Fig. 7.15). This can be employed as a reference to understand the oxide level in the composites studied. The broken down carbon could have: (a) reduced the maghemite phase, as corroborated by the reduction in the intensity of sharp maghemite peak at 666 cm^{-1} in relation to the adjacent broad peak; and (b) dissolved into the Fe-Co matrix. The 1 vol% CNT composite prepared by applying the pressure at 750^{o}C showed 56 % coercivity reduction compared to the monolithic material, whereas the one prepared by applying the pressure at 450^{o}C exhibited only 41% reduction in relation to the monolithic alloy.

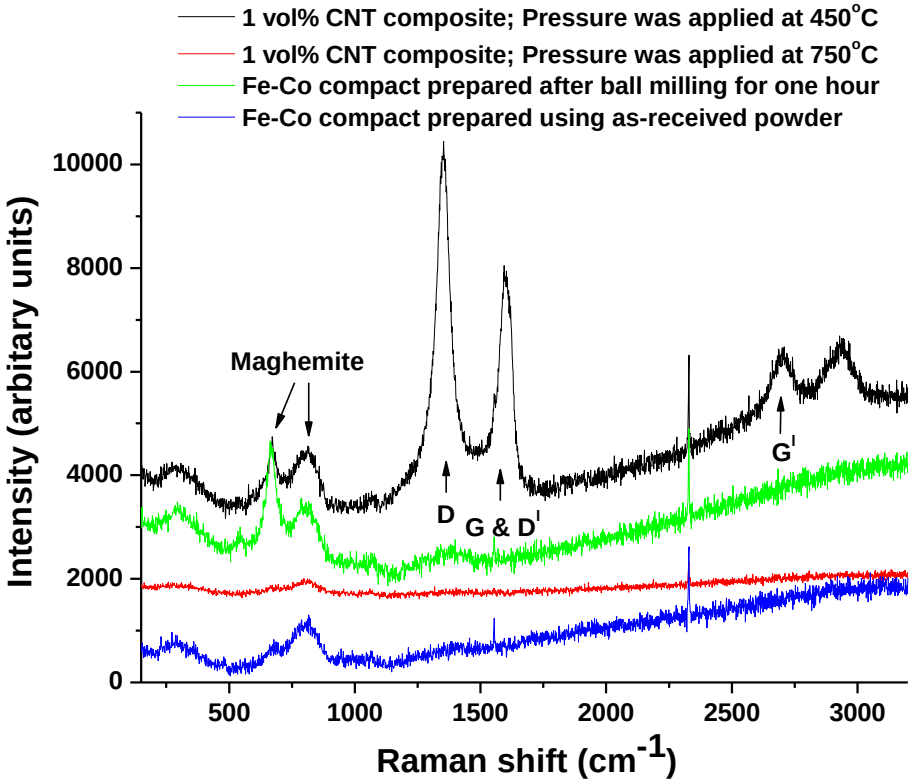

Fig. 7.15 Raman spectra of the shown materials that were prepared by starting the pressure application at two different temperatures

7.3.2.6 Mechanical properties of CNT composites

Addition of smaller volume fraction of CNTs (up to 1 vol%) was found to improve the mean bending strength and mechanical hardness (Fig. 7.16). This may be due to the improvements in density of compacts and/or short fibre strengthening that were realised because of the addition of CNTs. Because of the presence of the oxide impurities in the composites, the standard deviation of the bending strength was large. The standard deviation of the bending strength values could be reduced by blending the powders in an inert atmosphere, as observed in the 1 vol% CNT composite with reduced oxide level that was prepared by applying the pressure at 750°C.

The U+B method was found be more successful than the B method in dispersing the nanofillers in the matrix. Therefore, the composite materials prepared following the U+B method displayed higher bending strength with reduced standard deviation, in particular to the composites with higher vol% of CNTs.

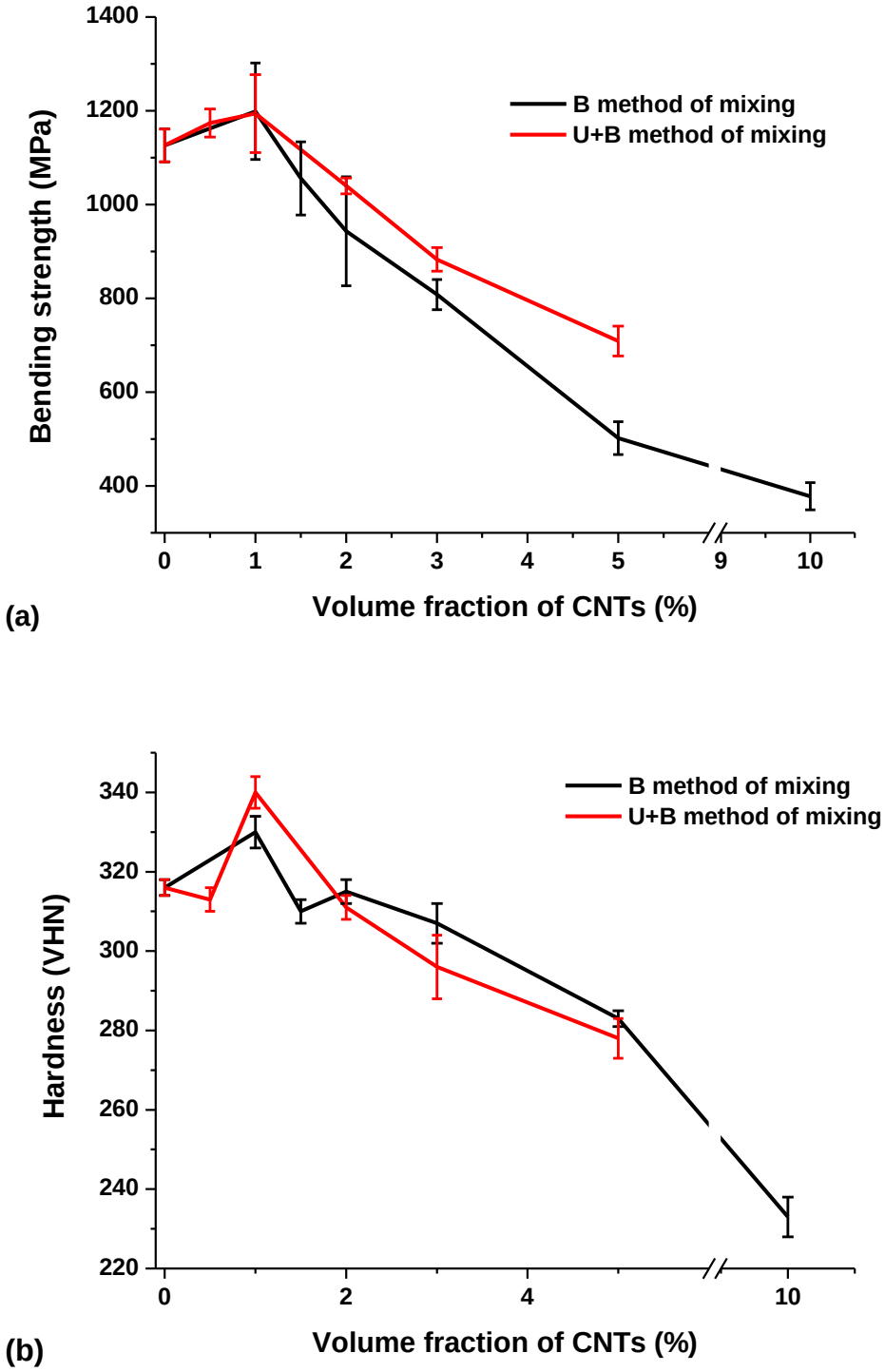

Fig. 7.16 Effect of volume fraction of CNTs on: (a) bending strength; (b) hardness of (Fe-Co)-CNT composites prepared by spark plasma sintering following two different dispersion routes (ball milling for 1 hour or ultrasonication in DMF followed by ball milling)

7.3.2.7 Fractographic studies

The fractographic images of the composites with different volume fraction of CNTs that were prepared by applying the pressure at 450 and 750^{o}C are compared in Fig. 7.17.

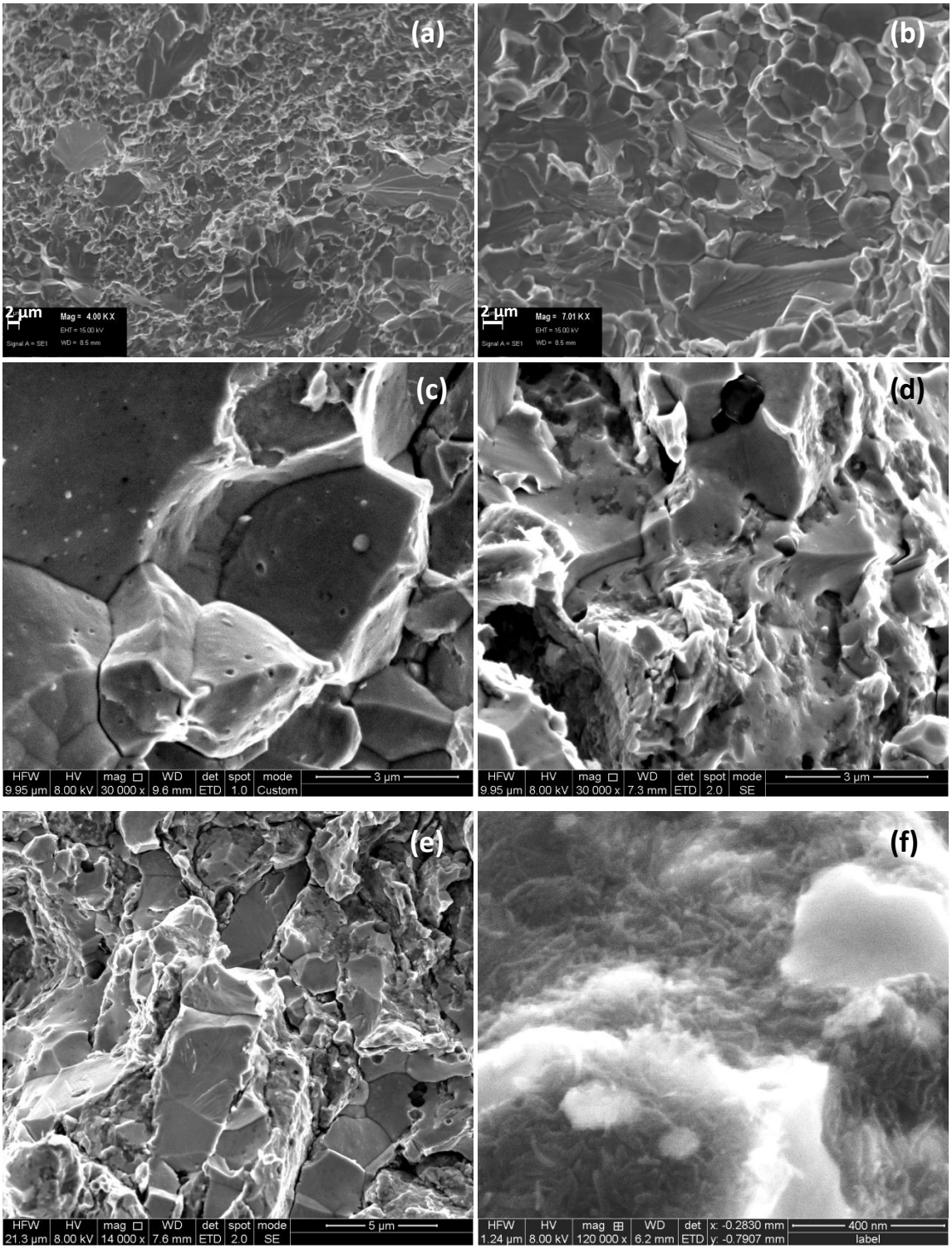

Fig. 7.17 Fractographic images of (a) monolithic Fe-Co and composites containing (b) and (c) 1 vol% of CNTs; (d) 2 vol% of CNTs; (e) 5 vol% of CNTs; (f) 10 vol% of CNTs; the powder samples in all cases were ball milled for one hour; for (a) and (b) the mechanical force was applied at 750^o C during sintering, whereas for other cases, the force was applied at 450^o C

Similar to monolithic materials, the absence of tubular feature and dents due to fibre pulled out in the CNT composites prepared by applying the pressure at 750^{o}C suggested that

the CNTs were completely consumed during fabrication (Fig. 7.17 (b)). The dimples on the fractured facets of the composites prepared by the applying the pressure at 450^{o}C suggested that the CNTs were pulled before fracture and hence, the strength was increased (Fig. 7.17 (c)). The volume fraction of fine dimples and protrusions increased with the increase in the concentration of CNTs. These fine features represent the CNTs and the regions of their pull-out (Fig. 7.17 (c)-(e)). The structural integrity of the CNTs was retained after processing. The CNTs were present along the grain boundaries as shown in composites with larger volume fraction of CNTs (Fig. 7.17(f)).

7.4 Characterisation of coated CNTs

The XRD patterns of as-received and Ni-P plated CNTs are compared in Fig. 7.18. The presence of a broad peak at a 2θ value of ~ 26^{o} and asymmetric (saw-toothed) and overlapped peaks at ~ 43^{o} in the XRD patterns of uncoated CNTs was in good agreement with the patterns obtained for multi-walled carbon nanotubes (MWCNTs) [18, 19]. The diffraction peaks at the 2θ position of ~ 26^{o} and ~ 43^{o} corresponded with that of (002) and (101) and (100) planes of MWCNTs, respectively as marked in Fig. 7.18. The CNTs were devoid of any catalytic impurities as confirmed by the absence of additional diffraction lines in the pattern.

The occurrence of a peak in the XRD pattern of the Ni-P coated CNTs at about 16.6 ^{o}2θ suggested the presence of graphene oxide (GO) in the coated material. Unlike a sharp XRD peak reported for graphene oxide at about 10 ^{o}2θ in [20, 21], the GO peak of the coated material was broad and shifted to higher angles due to the free standing nature of the films and partial restacking of graphene layers at some locations [22]. The presence of two broad peaks at ~ 52 and 75 ^{o}2θ and a relatively sharp peak at ~ 45 ^{o}2θ implied the existence of very fine (in nanometre range) Ni crystallites in the amorphous Ni-P matrix. The XRD result also confirmed the existence of NiO in the coated material.

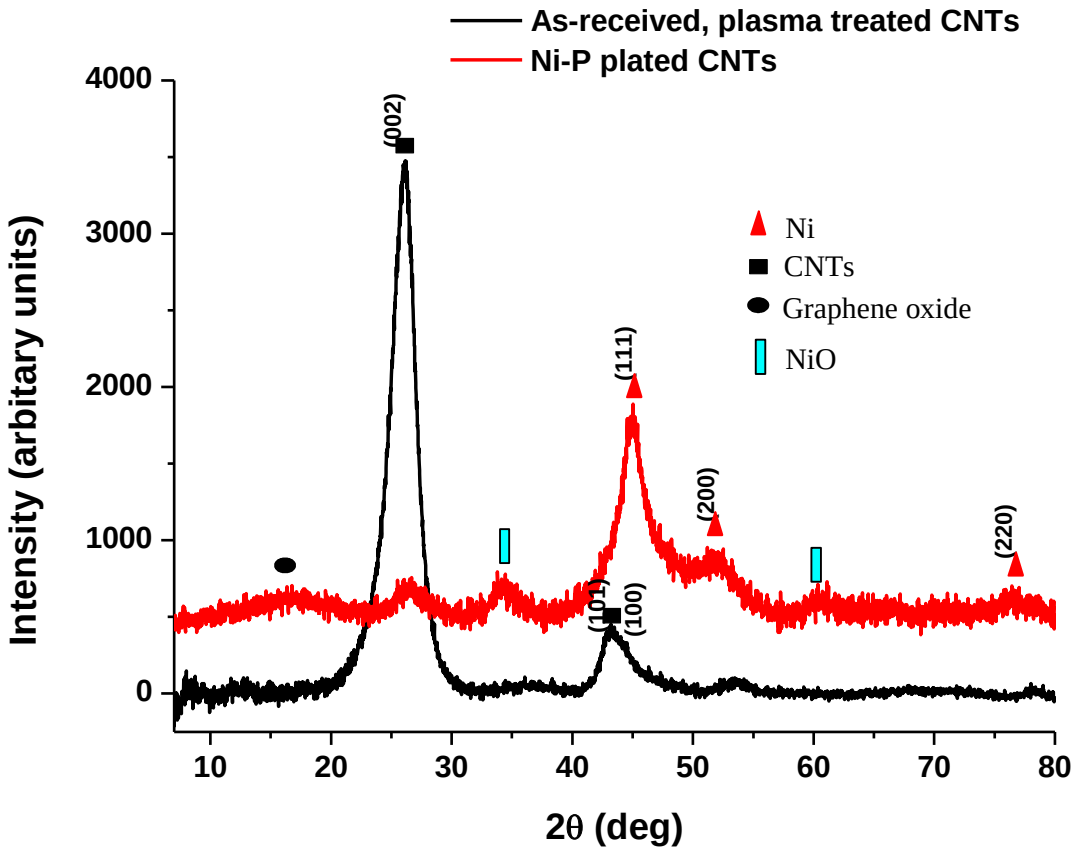

Fig. 7.18 XRD histograms of as-received and Ni-P coated CNTs

As shown in the TEM images (Fig. 7.19), the electroless Ni-P coating over the CNTs was not uniform, with some nanotubes coated with thick layers (about 200 nm), some decorated with thin layers and some remaining uncoated. It was evident that Ni-P coating on the CNTs promoted the nucleation and growth of graphene oxide sheets on their surface during drying in the presence of ethanol. A comprehensive TEM analysis revealed that only thin Ni-P coating favoured the growth of graphene oxide sheets and some of the sheets were folded and wrinkled. The graphene oxide coating was not observed on thick Ni-P layers over the CNTs.

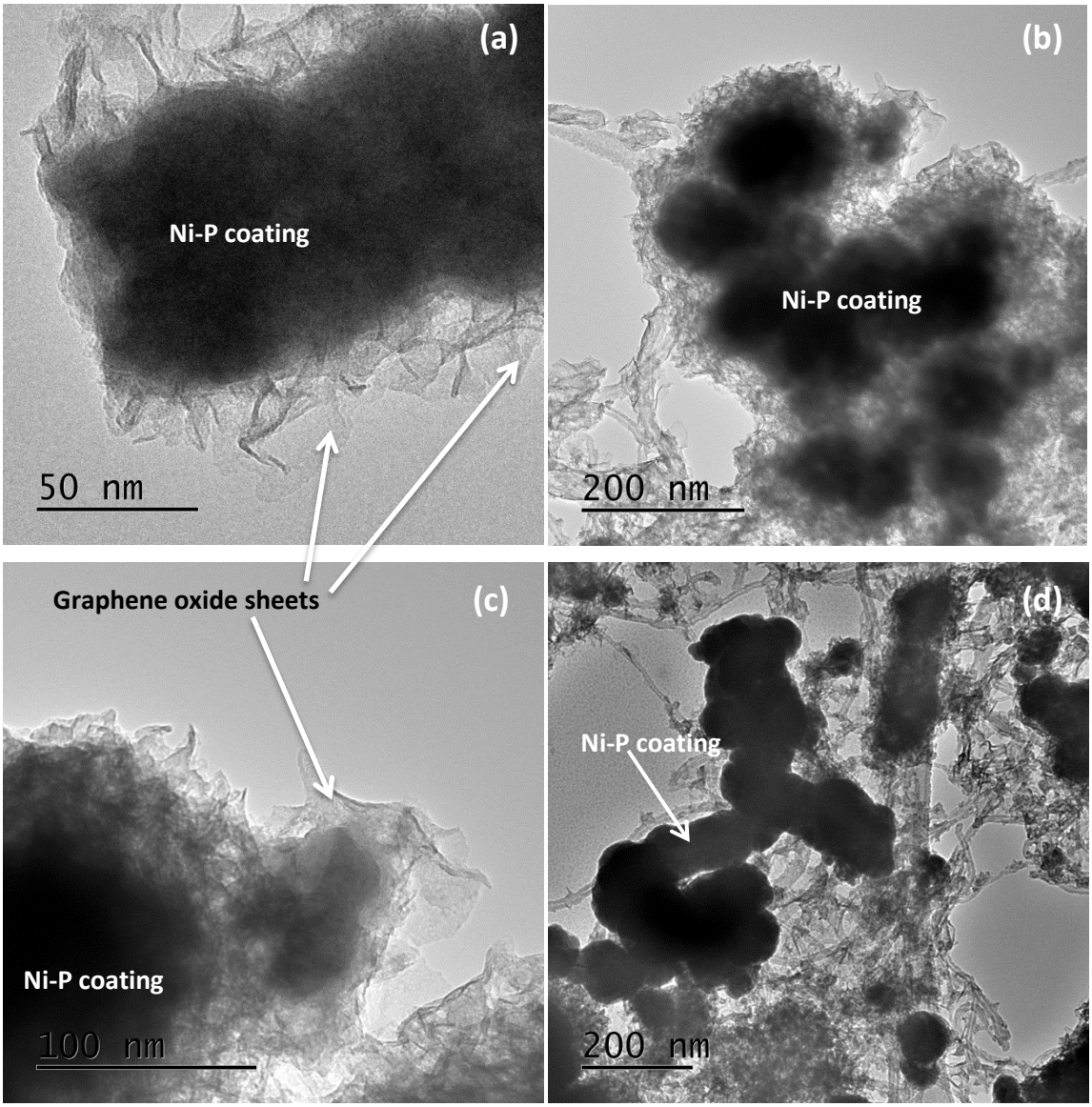

Fig. 7.19 TEM images of Ni-P coated CNTs obtained after drying in atmospheric condition in the presence of alcohol

The dark field TEM image and the EDX area maps of the hybrid nanocomposite with a thick Ni-P coated CNT are shown in Fig. 7.20. The elemental maps confirmed the presence of Ni, P and O in the coating. The elemental distribution of oxygen and carbon in area map was nearly equal because of the presence of oxygen functional group on the surfaces of graphene and CNTs.

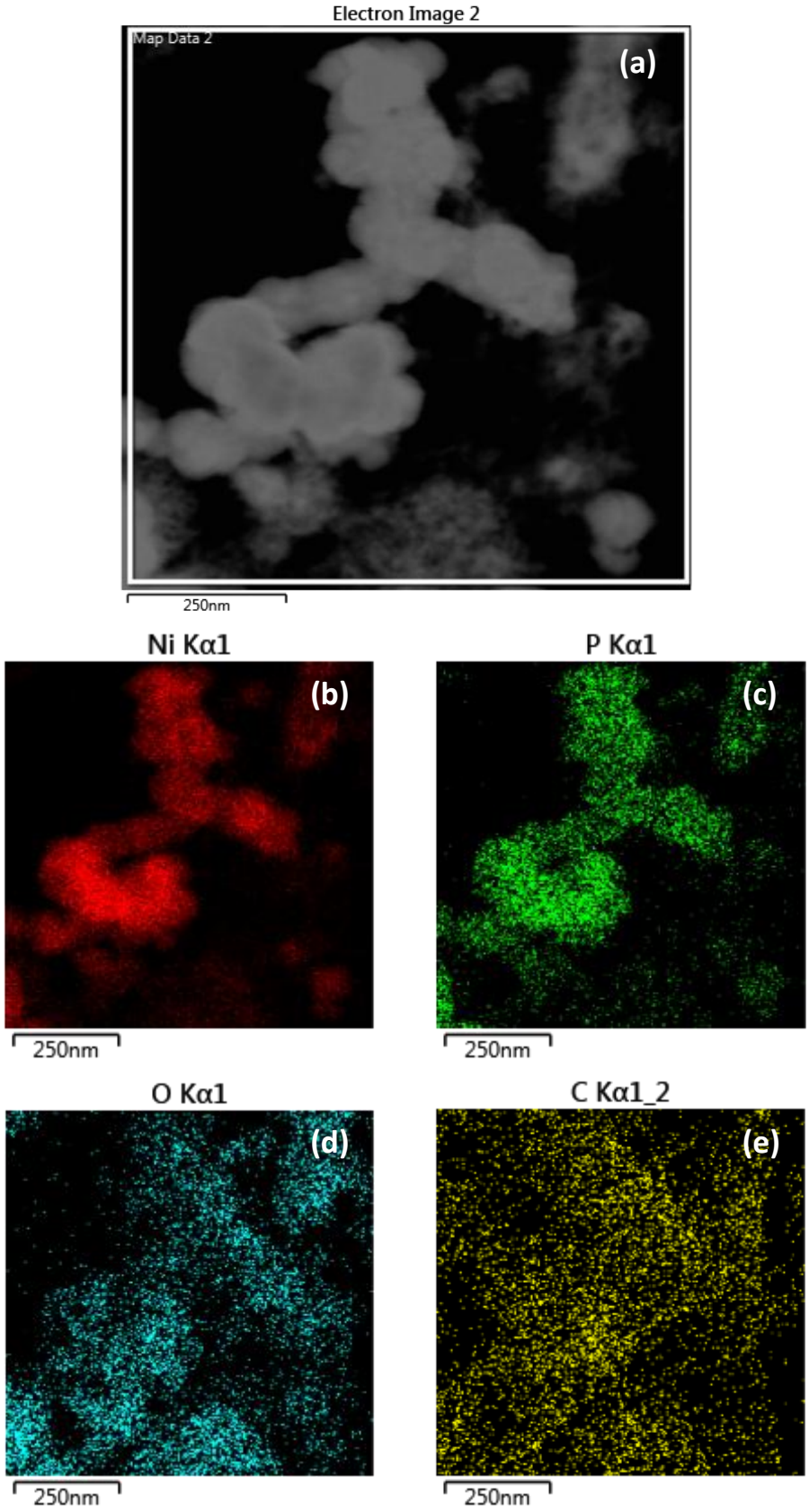

Fig. 7.20 (a) Dark field TEM image and EDX elemental maps of: (b) Ni; (c) P; (d) O; and (e) C in the Ni-P plated CNTs

Two different types of Raman spectra were obtained when the coated CNTs were excited by the laser beam as shown in Fig. 7.21. They are referred as (a), (b) spectrum in Fig. 7.21. The Raman spectrum of the as-received CNTs is also shown in Fig. 7.21 for comparison. The presence of four characteristic bands (1P and 2P) between 400 and 1250 cm^{-1} in the (a) spectrum confirmed the presence of NiO [23]. The absence of a broad two-magnon (2M) scattering at 1490 cm^{-1} corroborated that the NiO crystallite were nanocrystalline in size [23]. The characteristic bands of the carbon nanomaterials namely D, G, D' and D+G were present in the (a) spectra confirming the presence of graphitic structure. A reduced intensity ratio ($R=I_D/I_G$) of (a) spectrum (1.05±0.16) in comparison to that of the as-received CNTs (1.28±0.04) confirmed the presence of graphene oxide in the coated CNTs. The pronounced 1P band in the (a) spectrum suggested that defect density was higher on the NiO surface than the NiO coating that produced (b) spectrum. The defects on the thin NiO coating might have acted as the nucleation sites for the graphene oxide sheets as confirmed by the co-existance of NiO and graphitic bands in the Raman spectrum marked as (a) and the TEM images. The (b) spectrum could have been originated from the thick NiO coating on the CNTs with reduced defects.

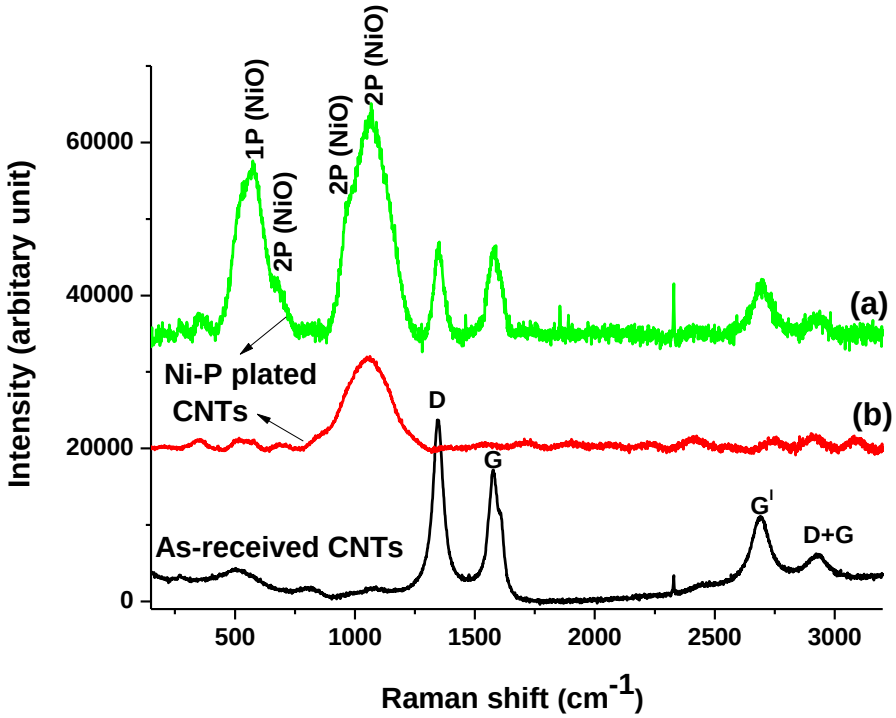

Fig. 7.21 Raman spectra of the as-received and Ni-P plated CNTs

The results of the thermal stability studies conducted on Ni-P plated CNTs is presented in Fig. 7.22. The temperature for the complete crystallisation of Ni-P into Ni and Ni_3P was 351°C [24]. The broad peak (spanning for ~200°C between 100 and 300°C)

observed in the thermogram might be related to the short-range atomic movements and primary crystallization of Ni [25]. The weight loss of the coated sample below 300°C was about 50 % of the total loss. This was attributed to the decomposition of labile oxygen functionalities on the basal planes of GO [21]. The hybrid nanocomposite underwent decomposition when the temperature was increased above 600°C. This was substantiated by the endothermic peak at 698°C in DSC profile and loss in the weight of the sample (about 7 %). The results confirmed that the graphene coating was thermally stable up to 630°C.

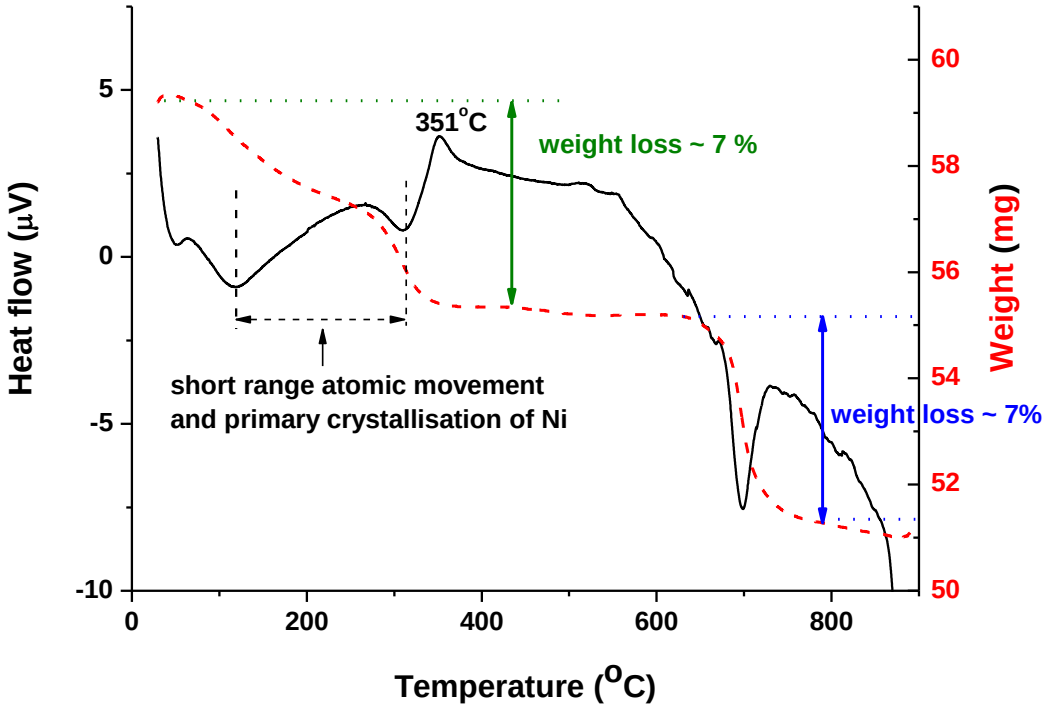

Fig. 7.22 DSC/TGA plots of the Ni-P plated CNTs

7.5 Characterisation of coated CNT composites

7.5.1 Crystallographic structural characterisation

The XRD patterns of the composites containing 1.5 and 3 vol% of bare and duplex plated (graphene oxide and Ni-P) CNTs are compared in Fig. 7.23. The addition of either hybrid nanocomposite or bare CNTs produced a shift in the positions of the fundamental peaks to lower angles. The peak shift was more pronounced in composites with bare CNTs, in particular those with higher volume fraction of CNTs, than those with coated CNTs. As the increase in the lattice parameter of Fe-Co was due to one or both of the following reasons: increase in long range ordering and the presence of maghemite phase as discussed in section 7.3.2.1, it was difficult to distinguish the effect of the coating on ordering using the fundamental XRD peaks.

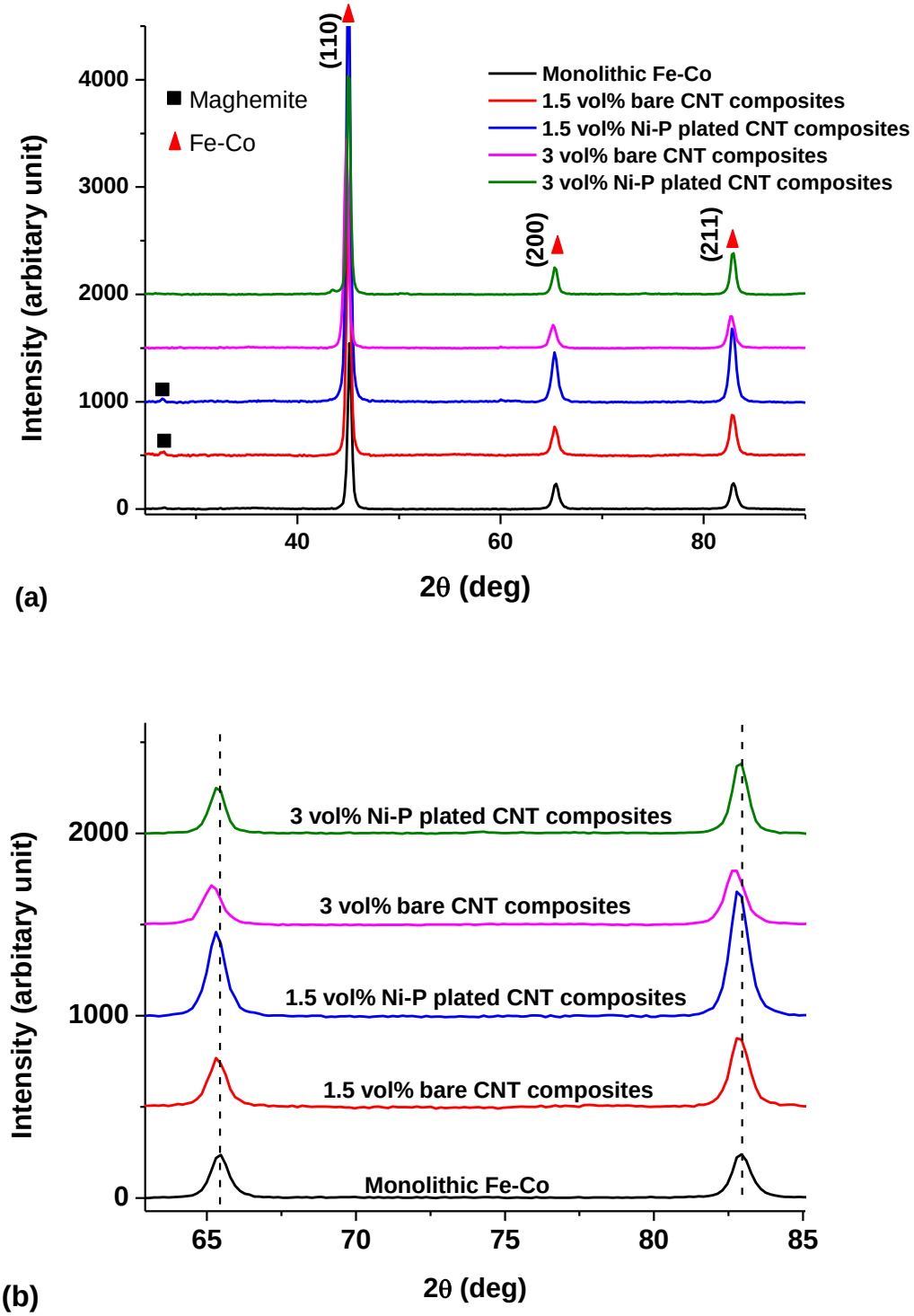

Fig. 7.23 (a) XRD patterns of Fe-Co composites containing bare and coated CNTs; (b) Magnified image showing shift in the positions of (200) and (211) peaks.

7.5.2 Raman spectroscopy

The first and second order Raman spectra of the composites containing 1.5 and 3 vol% of bare and Ni-P CNTs are compared in Fig. 7.24. The stresses imposed by the intermetallic matrix on the CNT walls produced a shift in all the characteristic bands to

higher frequencies. The amount of stress introduced on the CNT surfaces was not changed even in the presence of Ni-P coating. The marginal reduction in the mean values of the integrated intensity ratios (I_D/I_G) for the composites containing coated CNTs in relation to those with bare ones (Fig. 7.25) was due to one or both of the following possibilities: (a) The graphene oxide coating over Ni plating could be severely damaged during processing; (b) the Ni-P coating on the CNTs led to reduce the defects, which could be introduced on the CNT walls during powder processing and consolidation. A plausible reason for the first possibility was the employment of sintering temperature higher than the decomposition temperature of graphene coating as predicted by TGA (Fig. 7.22).

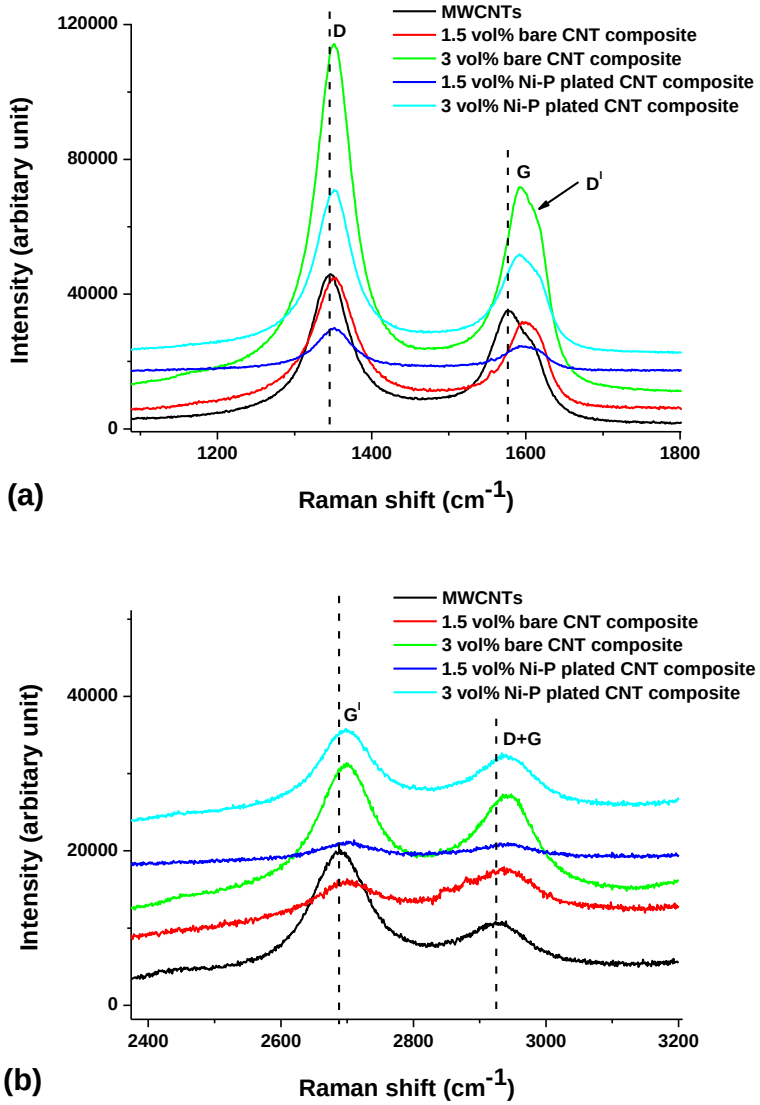

Fig. 7.24 (a) First and (b) second order Raman spectra of Fe-Co composites containing bare and Ni-P plated CNTs

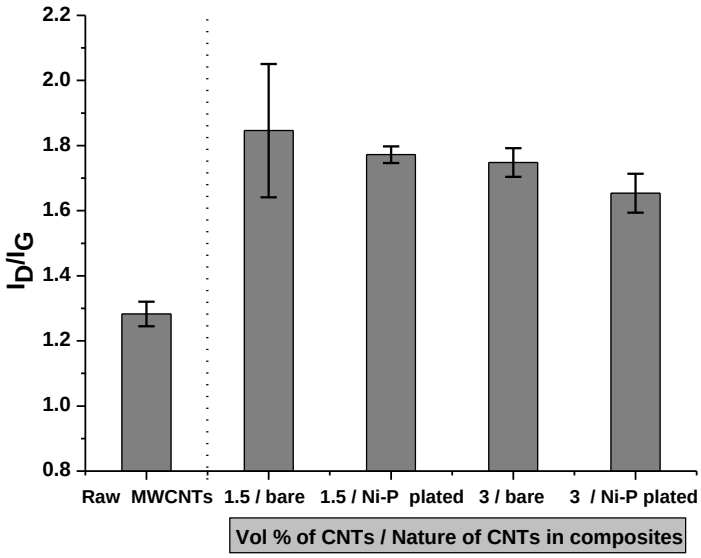

Fig. 7.25 Integrated intensity ratios (I_D/I_G) of Fe-Co composites containing bare and Ni-P plated CNTs

7.5.3 Microstructural characterisation

The duplex coated CNTs, which were agglomerated after drying, showed excellent dispersion in water and poor dispersion in ethanol. Despite this, ethanol was chosen as the colloidal processing medium because of the intolerance of Fe-Co to water. Even after 7 hours of ultrasonication in ethanol, the coated CNTs were not dispersed well in the medium. The microstructure displayed clusters as shown by arrows in Fig. 7.26(a). It was required to ball mill the mixture to disperse the coated CNTs uniformly. The CNT lumps were absent in the ball milled material (Fig. 7.26(b)).

When the polished composite surfaces were etched with Nital, the regions rich in Ni-P coated CNTs were preferentially etched as shown by the area maps formed by Ni X-ray signals (Fig. 7.27) and the EDX point analysis (Fig. 7.28). Ball milling helped to realise uniform distribution of CNTs and it was evident that they were distributed along the grain boundaries of the matrix alloy (Fig. 7.28(a)).The Ni-P coating reacted with Fe-Co during processing and formed a ferromagnetic, intermetallic FCC phase named Taenite (γ(Fe, Ni)) (Fig. 7.29), as confirmed by the XRD result [26].

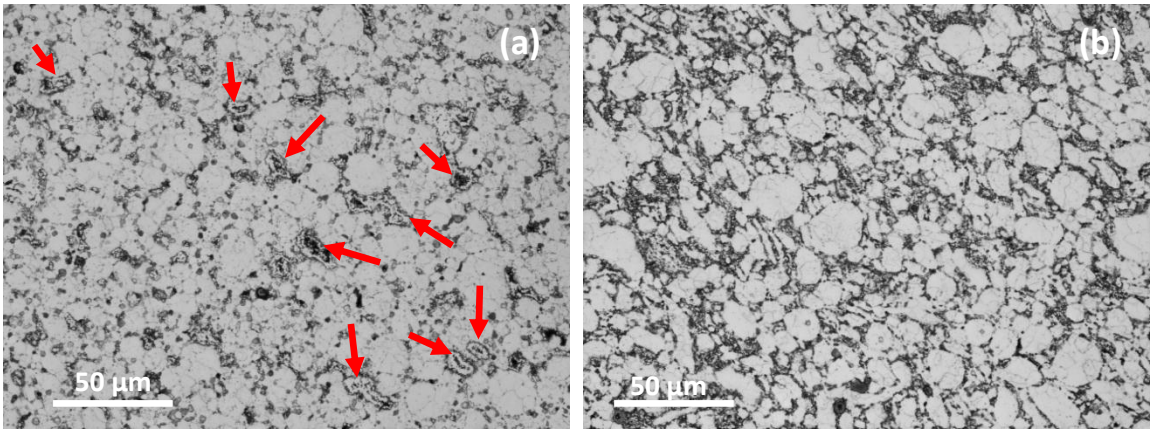

Fig. 7.26 Optical micrographs of composites containing 3 vol% of CNTs coated with Ni-P; coated CNTs and Fe-Co powder were mixed by (a) ultrasonication and (b) ultrasonication followed by ball milling; the arrows showed the presence of agglomerates.

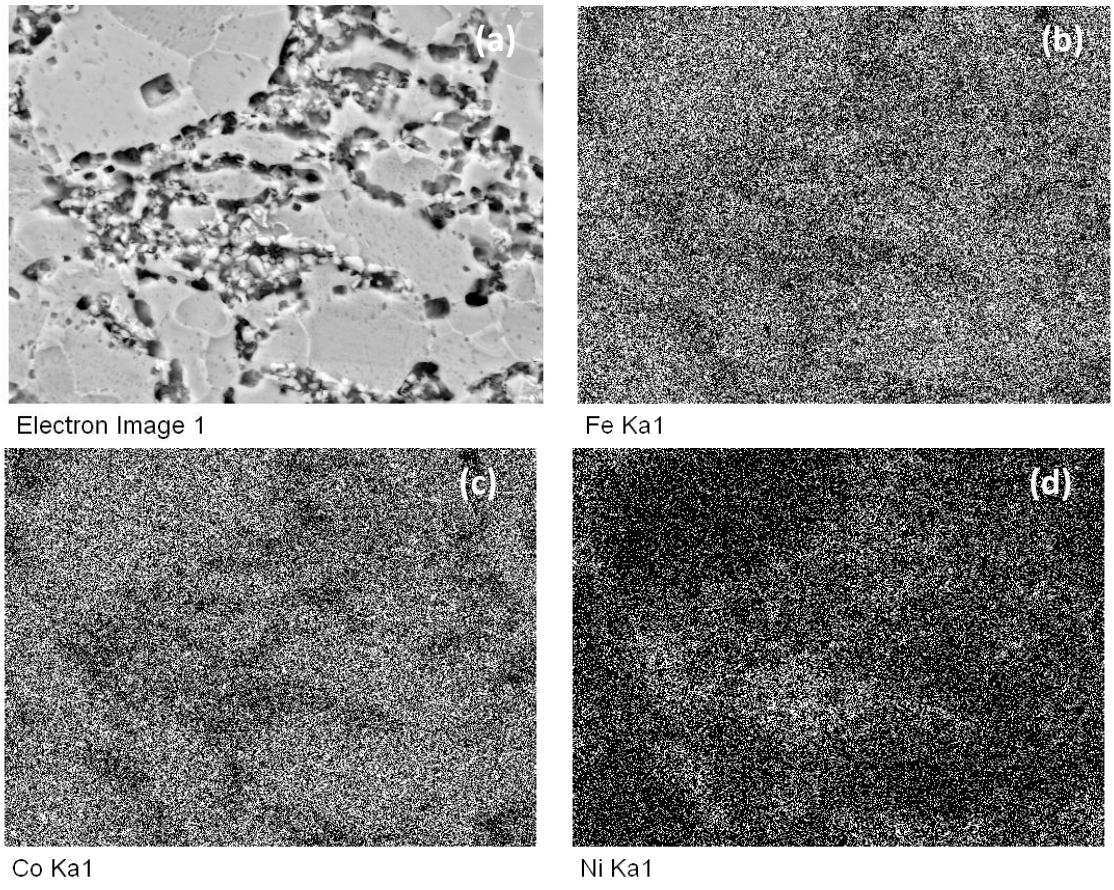

Fig. 7.27 SEM –EDX analysis of a composite containing 3 vol% of CNTs coated with Ni-P: (a) SEM image (b) EDX elemental mapping results showing the distribution of (b) Fe (c) Co and (d) Ni.

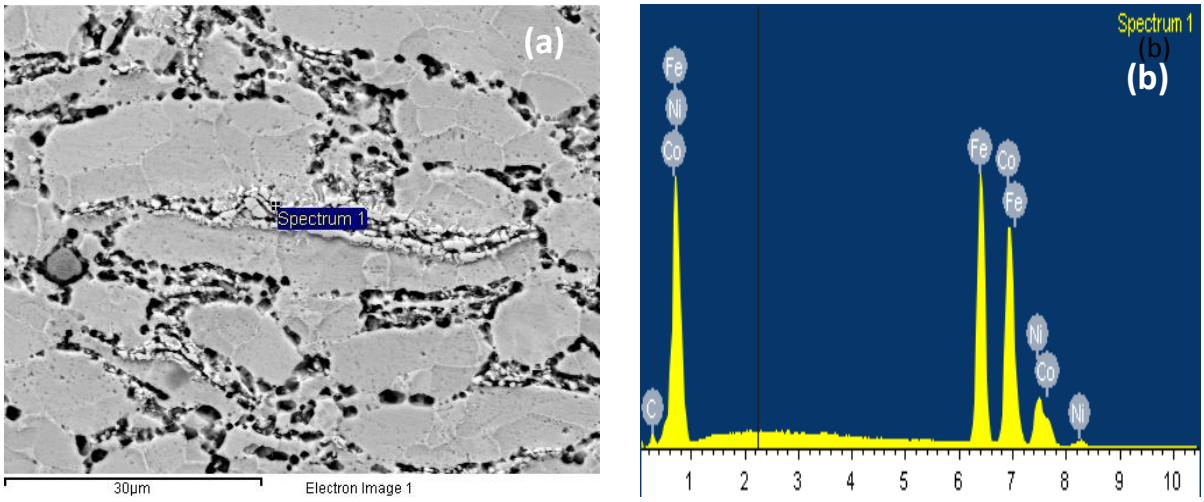

Fig. 7.28 SEM –EDX analysis of a composite containing 3 vol% of CNTs coated with Ni-P: (a) SEM image showing the point of EDX analysis; (b) EDX spectrum obtained

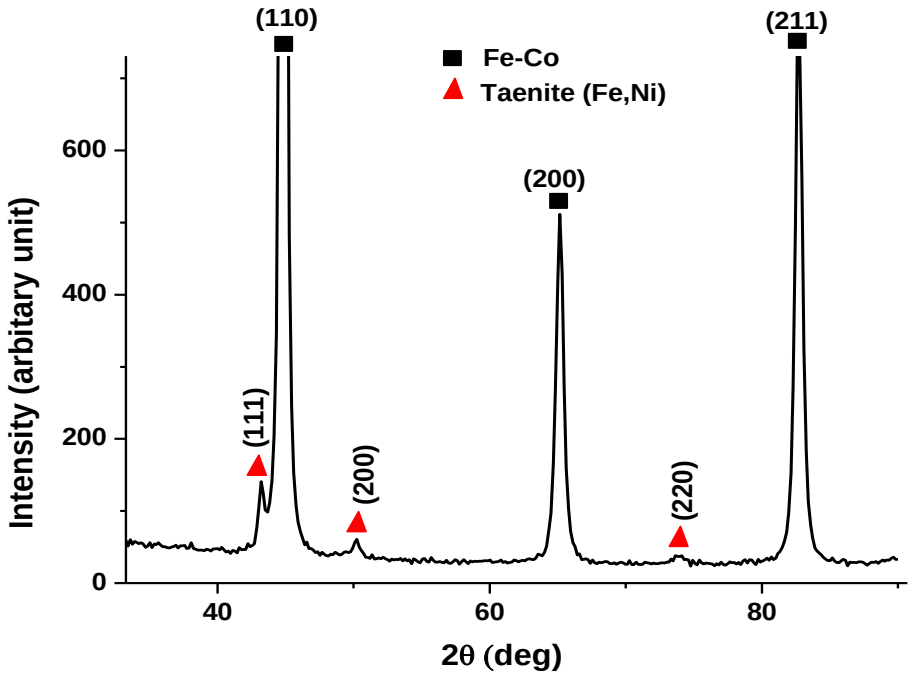

Fig. 7.29 XRD spectra of Fe-Co composites containing 3 vol% of Ni-P coated CNTs.

7.5.4 Magnetic and mechanical properties

The magnetic and mechanical properties of composites with bare and coated CNTs are compared with the monolithic material in Table 7.3.

The distribution efficiency of the mixing methods was found to determine the saturation induction and coercivities of the composites with coated CNTs. The materials prepared after ultrasonication alone displayed magnetic properties close to that of unreinforced material due to inefficient dispersion. Ball milled materials showed reduced saturation induction and coercivity because of the dispersion improvement. The coercivity

reduction can be explained by the increase in the sinterability, as observed in composites with bare CNTs. The coercivity drop of the composite in comparison to the monolithic material was reduced in the presence of coating due to the inclusion of P into the ferromagnetic system and the formation of taenite phase. The fall in saturation induction on the introduction of coated CNTs was due to the dilution caused by the less magnetic coating atoms. With the increase in the volume fraction of the coating the magnetic induction was reduced further due to the additional dilution caused by the coating species,

Table 7.3 *Summary of magnetic and mechanical properties of composites containing bare and coated CNTs*

Sample details	Induction at 20 kA/m (T)	Coercivity (A/m)	Hardness (VHN)	Bending strength (MPa)	
				Mean	Std. dev.
Fe-Co	2.30	862	316±2	1126	35
Fe-Co composites (CNTs and Fe-Co mixed by ultrasonication) containing					
1.5 vol% of Ni-P coated CNTs	2.21	814	315±3	954	134
3 vol% of Ni-P coated CNTs	2.08	836	311±3	1033	45
Fe-Co composites (CNTs and Fe-Co mixed by ultrasonication followed by ball milling) containing					
1.5 vol% of CNTs	2.30	540	310±3	1056	78
3 vol% of CNTs	2.24	556	296±8	883	25
1.5 vol% of Ni-P coated CNTs	2.12	608	320±1	1231	40
3 vol% of Ni-P coated CNTs	2.00	739	325±4	1102	50

An increase in the volume fraction of bare CNTs caused a reduction in the hardness values because of the increased CNT clustering and the resulting drop in the sintering efficiency. With the addition of coated CNTs, a rise in the mean hardness was observed due to the formation of new compounds with the coating atoms. The hardness improvement in the coated CNT composite was marginal and can be attributed to the presence of intermetallic taenite phase.

The addition of bare CNTs in Fe-Co caused a reduction in the mean bending strength values. This was due to the formation of oxide inclusions during ball milling, which might have acted as crack nucleation sites. The coating on the CNTs aided to increase the flexural strength values by promoting uniform dispersion of CNTs and by forming new compounds depending on the preparation route and coating type. When the volume fraction of either the coated or uncoated CNTs was increased from 1.5 to 3%, there was a reduction in the flexural

strength due to the increase in the probability for agglomeration of CNTs. Because of the inefficient dispersion, the composites with Ni-P coated CNTs, which were mixed by ultrasonication alone showed the lowest mean bending strength and highest standard deviation of the bending strength values than those that were sintered after ball milling.

The bending response of the monolithic and composite sample, whose bending strength value was close to the mean value in each set of five samples, are compared in Fig. 7.30. It is evident that ball milling helped to improve the ductility in the Ni-P plated CNT composite by promoting uniform dispersion of fillers in the matrix. The fracture surfaces were examined using high resolution SEM to understand the toughening mechanisms (Fig. 7.31).

The fracture surface displayed agglomerates when the powder mixture with the coated CNTs was sintered after ultrasonication alone (Fig. 7.31(b)). However, ball milling aided in realising uniform dispersion of coated CNTs as shown in Fig (7.31(d) and 7.31(e)). The improvement in toughness noticed in the coated CNT composites can be explained by the pulling out of fibres as shown by the micro dimples and protrusions on the fractured facets, unlike in composites with similar volume fraction of bare CNTs (Fig. 7.31(c)). The absence of flap like features in the fractured surface of the composites with coated CNTs confirmed the decomposition of graphene oxide during processing.

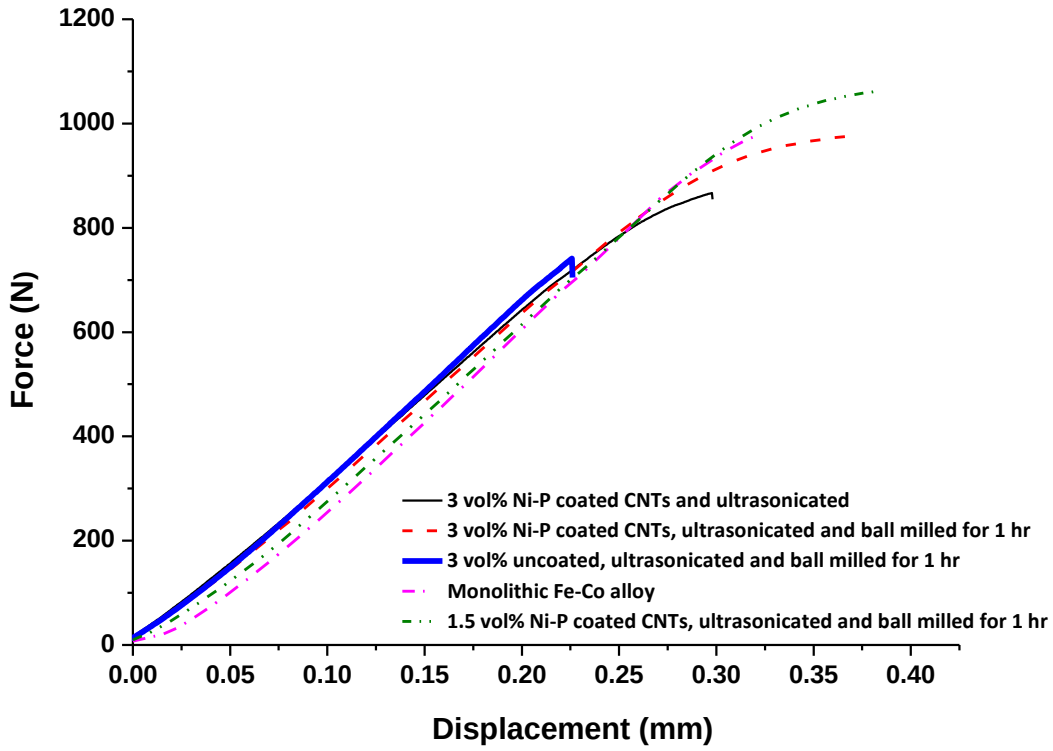

Fig. 7.30 Flexural response of Fe-Co monolith and composites containing bare and Ni-P coated CNTs and mixed by two different methods.

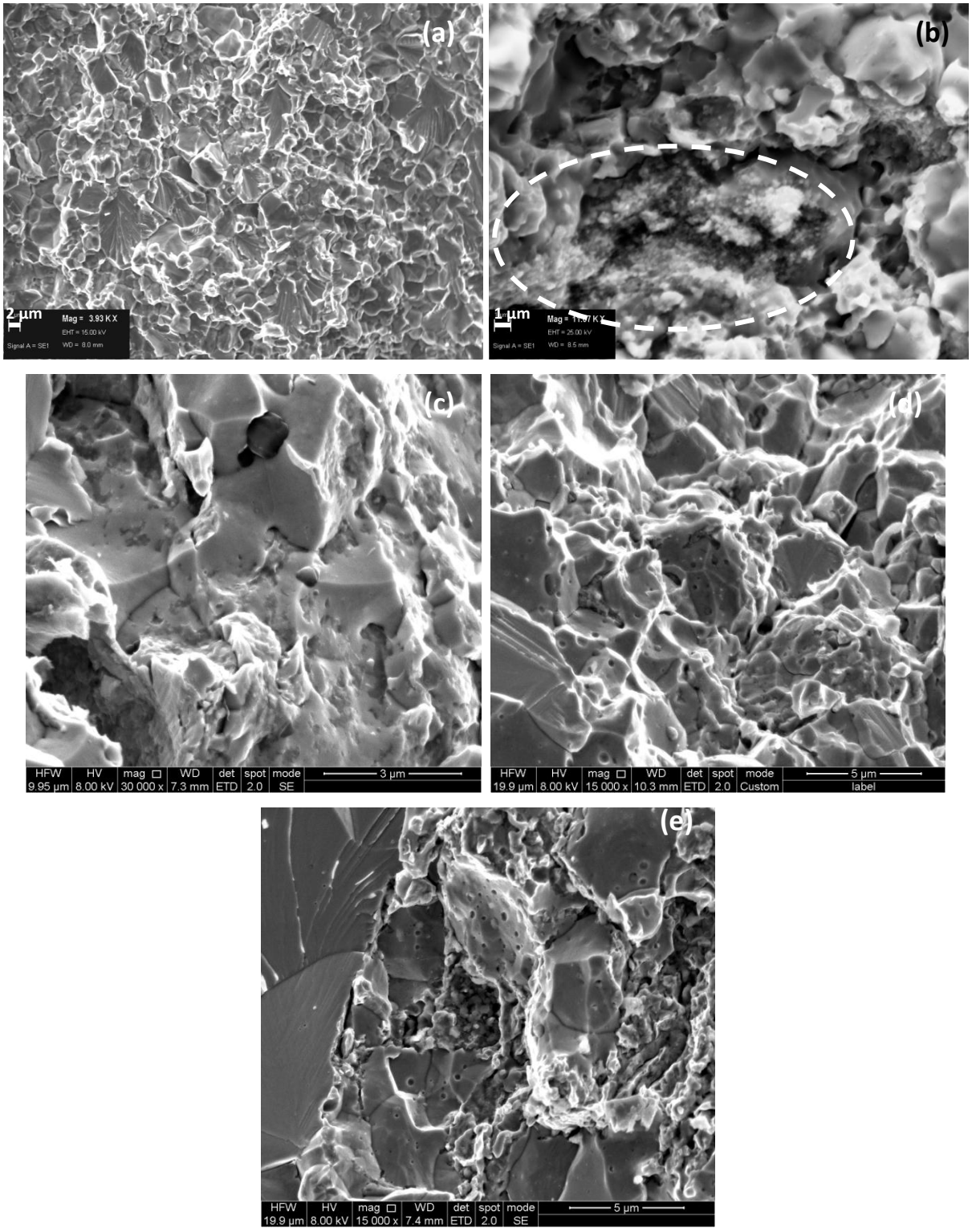

Fig. 7.31 Fractographic images of: (a) monolithic Fe-Co; composites containing (b) 3 vol% of coated CNTs; (c) 3 vol% of bare CNTs; (d) 1.5 vol% of coated CNTs; (e) 3 vol% of coated CNTs; the CNTs and Fe-Co powders were mixed by: (b) ultrasonication alone and (c)-(e) ball milling following ultrasonication; the oval in (b) marks the coated CNT agglomerates

References

1. T. Belin, F. Epron, Characterization methods of carbon nanotubes: a review, *Mater. Sci. Engg., B* **119**, 105–118(2005).
2. M.S. Dresselhaus, G. Dresselhaus, A. Jorio, A.G. Souza Filho, R. Saito, Raman spectroscopy on isolated single wall carbon nanotubes, *Carbon* **40**, 2043-2061(2002)
3. S. Osswald, M. Havel and Y. Gogotsi, Monitoring oxidation of multiwalled carbon nanotubes by Raman spectroscopy, *J. Raman Spectrosc.* **38**, 728–736 (2007)
4. H. Hiura, T.W. Ebbesen, K. Tanigaki, Raman studies of carbon nanotubes, *Chem. Phys. Lett.* **202[6]**, 509-512 (1993)
5. F. Inam, H. Yan, M.J. Reece and T. Peijs, Structural and chemical stability of multiwall carbon nanotubes in sintered ceramic nanocomposite, *Advances in Applied Ceramics* 109, 240-245 (2010)
6. S. Jain, A.O. Adeyeye, S.Y. Chan and C.B. Boothroyd, Interface properties of iron oxide films J. Phys. D: Appl. Phys. **37**, 2720–25 (2004)
7. G. Bate, Particulate recording materials, Proceedings of the IEEE 74, 1513–1525 (1986)
8. D. W Clegg and R. A Buckley, The disorder-order transformation in iron-cobalt-based alloys, *Metal Science Journal* **7**, 48-54(1973)
9. D. Jiang, K. Thomson, J. D. Kuntz, J. W. Agerb and A. K. Mukherjee, Effect of sintering temperature on a single-wall carbon nanotube-toughened alumina-based nanocomposite, *Scripta Mater.* **56**, 959–962 (2007)
10. S. Rul, F. Lefevre-Schlick, E. Capria, Ch. Laurent, A. Peigney, Percolation of single-walled carbon nanotubes in ceramic matrix nanocomposites, *Acta Mater.* **52**, 1061–1067 (2004).
11. F. Tuinstra, J.L Koenig, Raman Spectrum of Graphite, *J. Chem. Phys.* **53,** 1126-1130 (1970)
12. M. A. Correa-Duarte, M. Grzelczak, V. Salgueiriño-Maceira, M. Giersig, L.M. Liz-Marzán, M. Farle, K. Sierazdki and R. Diaz, Alignment of carbon nanotubes under low magnetic fields through attachment of magnetic nanoparticles, *J. Phys. Chem. Lett.* **109**, 19060-19063 (2005)
13. J.R. Groza, M. Garcia and J.A. Schneider, Surface effects in field-assisted sintering, J. Mater. Res. **16[1]**, 286-92 (2001)
14. P. Saravanan, J-H Hsu, D. Sivaprahasam, S.V Kamat, Structural and magnetic properties of γ-Fe_2O_3 nanostructured compacts processed by spark plasma sintering, *J. Magn. Magn. Mater.* **346**, 175-177 (2013)
15. B.D. Cullity and C.D. Graham, Introduction to magnetic materials, New Jersey, IEEE press and A John Wiley & sons, Inc., publisher, 2nd edition (2009), pp. 360-364
16. G. Herzer, Soft Magnetic Nanocrystalline Materials, *Scripta Metallurgica et Materialia* **33**, 1741-56 (1995)
17. R. S. Sundar and S. C. Deevi, Soft magnetic FeCo alloys: alloy development, processing, and properties, *Inter. Mater. Rev.* **50**, 157-192 (2005)
18. T. Belin and F. Epron, Characterisation methods of carbon nanotubes: a review, *Mater. Sci. Engg., B* 119[2], 105-118 (2005).

19. W.K. Hsu, S. Firth, P. Redlich, M. Terrones, H Terrones, Y.Q. Zhu, N Grobert, A Schilder, R.J.H. Clark, H.W. Kroto and D.R.M. Walton, Boron-doping effects in carbon nanotubes, *J. Mater. Chem.* **10**, 1425-1429 (2000)
20. Y. Qian, A. Vu, W. Smyrl, A. Stein, Facile Preparation and Electrochemical Properties of V_2O_5-Graphene Composite Films as Free-Standing Cathodes for Rechargeable Lithium Batteries, *J. Electrochem. Soc.* **159(8)**, A1135-A1140 (2012)
21. S. S. J. Aravind, V. Eswaraiah and S. Ramaprabhu, Facile synthesis of one dimensional graphene wrapped carbon nanotubecomposites by chemical vapour deposition, *J . Mater. Chem* **21**, 15179-15182 (2011)
22. Y. Zhang, S. Wang, L. Li, K Zhang, J Qiu, M. Davis, L. J. Hope-Weeks, Tuning electrical conductivity and surface area of chemically-exfoliated graphene through nanocrystal functionalization, *Mater. Chem. Phys.* **135**, 1057-1063 (2012)
23. N. Mironova-Ulmane, A. Kuzmin, I. Steins, J. Grabis, I. Sildos and M. Pärs, Raman scattering in nanosized nickel oxide NiO, *J. Phys.: Conf. Ser.* 93, 012039 (2007)
24. F. Wang, S. Arai and M. Endo, The preparation of multi-walled carbon nanotubes with a Ni–P coating by an electroless deposition process, *Carbon* **43**, 1716–1721 (2005).
25. K.G Keong, W Sha, S Malinov, Crystallization and phase transformation behavior of electroless nickel–phosphorus deposits with low and medium phosphorus contents under continuous heating, *J Mater. Sci.* **37**, 4445–50 (2002)
26. S.W. Du, R.V. Ramanujan, Characterisation of $Fe_{40}Ni_{38}B_{18}Mo_4$ nanomagnetic alloy, *Mater. Sci. Engg., A* **375–377**, 1040–1043(2004)

Chapter 8

Results and discussion: Phase transitions in ferromagnetic materials and their effects on spark plasma sintering

8.1 Introduction

As a supplement to the research on the improvement of mechanical properties of Fe-50Co by composite strengthening, work was also carried out to explore the possibilities of exploiting the anomalous behaviour of the SPS current near the ferromagnetic Curie transition to calibrate the pyrometers in SPS. The chapter discusses the details of the trials performed and their outcomes. The temperatures and the enthalpy change of all the phase transformations in two ferromagnetic materials, Fe and Fe-50Co, were predicted using a high precision differential scanning calorimeter (DSC). A comprehensive experiment was performed by heating and cooling the ferromagnetic powders and the sintered compacts at different rates in the SPS furnace under minimum and maximum mechanical pressures to obtain a detectable and repeatable difference in the SPS current in the vicinity of Curie temperature, which was already predicted using a DSC.

This chapter also delineates the theory behind the unusual behaviour of SPS current in the vicinity of Curie transformation and the importance of compact density to get a noticeable signal at the magnetic transition temperature.

The magnetic properties of the Fe-50Co compacts prepared above and below Curie temperature by applying a minimum mechanical pressure of 7 MPa are discussed in the final section of the chapter.

8.2 Differential scanning calorimetry

The DSC experiments were carried out on Fe and Fe-Co using a Mettler-Toledo TGA/DSC1 apparatus in DSC mode using the following conditions:

Sample mass:	~50 mg
Heating/cooling rate:	5 °C min^{-1}
Temperature range:	ambient to 1100 °C; cool to below 250 °C
Crucible:	70 µl Ceramic crucible
Atmosphere:	Nitrogen (50 cm^3 min^{-1})

The instrument was calibrated for temperature and enthalpy using high purity samples of Indium and Aluminium and for mass using internal weights.

The results from the DSC experiments are presented in Figs. 8.1 and 8.2 with the heating curve shown in RED and the cooling curve given in BLUE.

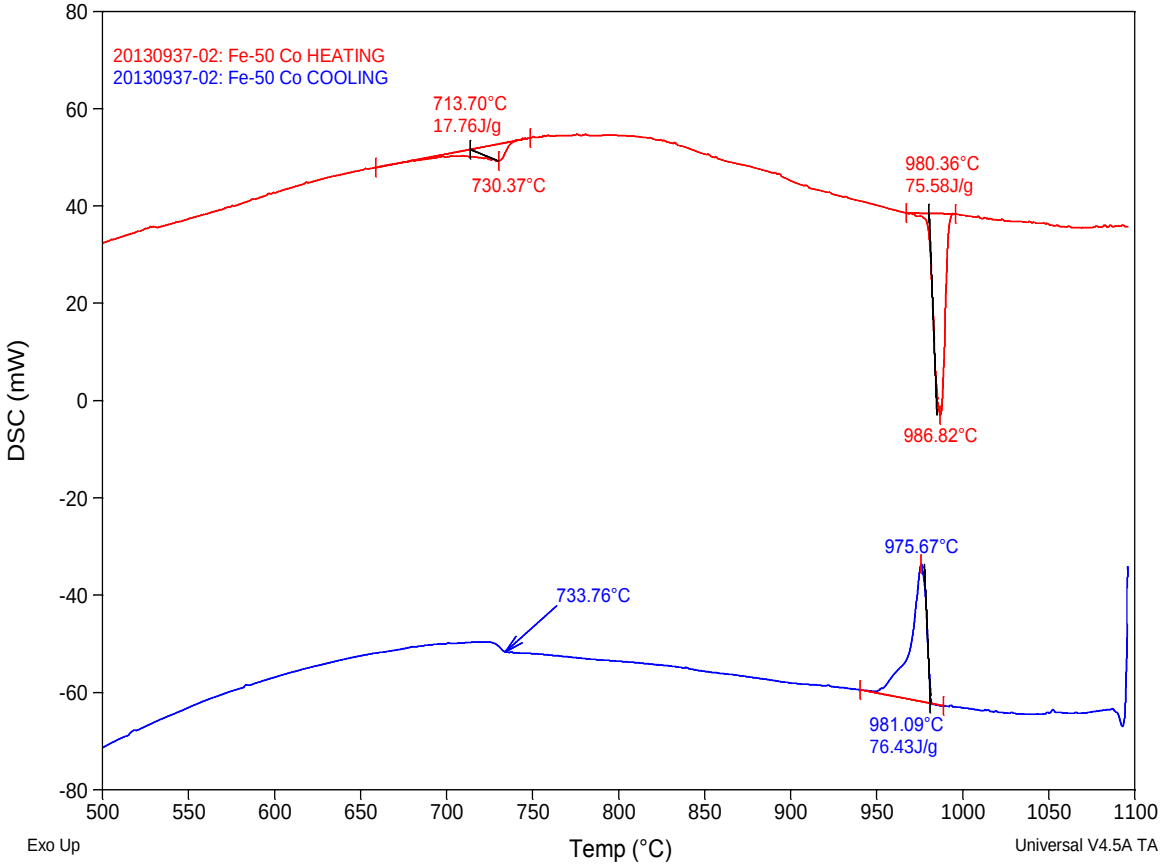

Fig. 8.1 DSC thermogram of Fe-50Co alloy powder

Fig. 8.1 shows the result for the Fe – 50Co sample. On heating, the sample showed no thermal events until around 700 °C, where a small broad endothermic transition was present with an extrapolated onset temperature at 714 °C and a peak temperature at 730 °C. This transition, which showed an enthalpy change of 17.76 Jg^{-1}, can be associated with order-disorder phase transition. The next thermal event was seen in the region of 980 °C when a sharp endothermic transition was produced. This endothermic reaction had an extrapolated onset temperature at 980 °C and a peak temperature at 987 °C and can be concluded to correspond with α to γ phase transition. An enthalpy change of 75.58 Jg^{-1} was determined for the event. On cooling, the reverse exothermic γ to α transformation was observed to start with an extrapolated onset temperature at 981 °C and peak at 976 °C. An enthalpy of 76.43 Jg^{-1} was determined. The only other event was a step change in the DSC curve at 734 °C. This appears to be the reverse of the order-disorder event observed at around 730 °C on heating.

Both the transformations exhibited hysteresis and the hysteresis width obtained for order-disorder and α-γ transformations were 3 and 11°C, respectively.

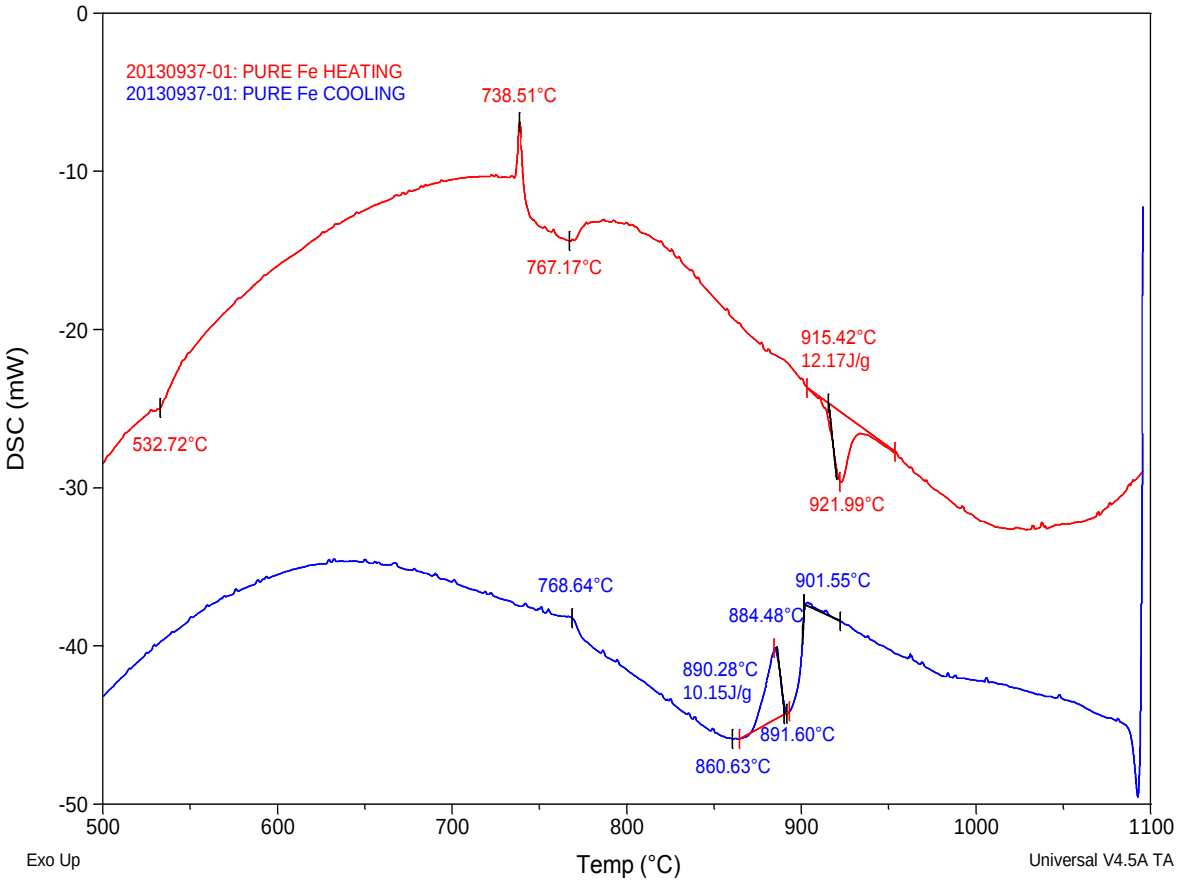

Fig. 8.2 DSC thermogram of pure Fe powder

The result for the pure Fe sample is shown in Fig. 8.2. On heating, the sample showed no thermal events until 533 °C, where a small endothermic transition occurred. Between 735 °C and 790 °C, a sharp exothermic reaction was observed with a peak temperature at 739 °C that leads into a broad endothermic event with a peak at 767 °C. The exothermic peak at 739 °C and the endothermic peak at 767°C can be related to recrystallisation of Fe powders and Curie transformation, respectively. In the region around 920 °C, an endothermic reaction was noticed, which was due to α to γ phase change in the sample. This peak had an extrapolated onset temperature at 915 °C and a peak temperature at 922 °C. An enthalpy of 12.17 Jg^{-1} was determined for this event. The cooling curve for this sample showed nothing until 902 °C at which point the DSC curve exhibits a broad endothermic transition with what appears to be a superimposed exothermic event, which was assumed to be the reverse of the peak seen on heating. The exothermic event appeared to start at 892 °C with an extrapolated onset temperature at 890 °C and peak at 885 °C. A reverse enthalpy of 10.15 Jg^{-1} was

measured. A small exothermic peak, which can be explained by the reversible Curie transition, was observed with a peak temperature at 769 °C. A strong thermal hysteresis was observed for α to γ phase transformation with a width of 35^{o}C.

8.3 Effects of SPS heating rates and mechanical pressure on Curie T anomaly

The Fe-50 Co powder was heated at 200, 100, 50 and 5^{o}C/min under minimum mechanical pressure and the temperature and current, as measured in the SPS system, are plotted as a function of time in Fig. 8.3, 8.4 and 8.5. All the samples were cooled either controllably by varying the current or naturally by convective heat transfer with the cooling water flowed through the steel ram in the SPS furnace. When the mechanical pressure was maintained minimum, the SPS current appeared noisy throughout the controlled sintering experiments. Even in the current profile, a peak was noticed at a temperature where the magnetic transition was expected to take place, when the heating rate was as high as 50^{o}C/min or above. The SPS current was increased/ reduced at higher rates in the fast heating and cooling experiments and hence, the surge in the current was so high as to be easily identified. On decreasing the heating rate, the Curie temperature, as marked by the peak of the current surge, was reduced. With the reduction in the heating rate (as low as 5^{o}C/min), the current profile appeared noisier during both the sintering cycles on packed powder and on the sintered compact obtained after the first cycle. It was difficult to differentiate the variations associated with the Curie temperature anomaly in the noisy current profile. The more fluctuating nature of the current at lower rates might be related with poor electrical contact and lower density of the compact due to the lower mechanical pressure (7 MPa).

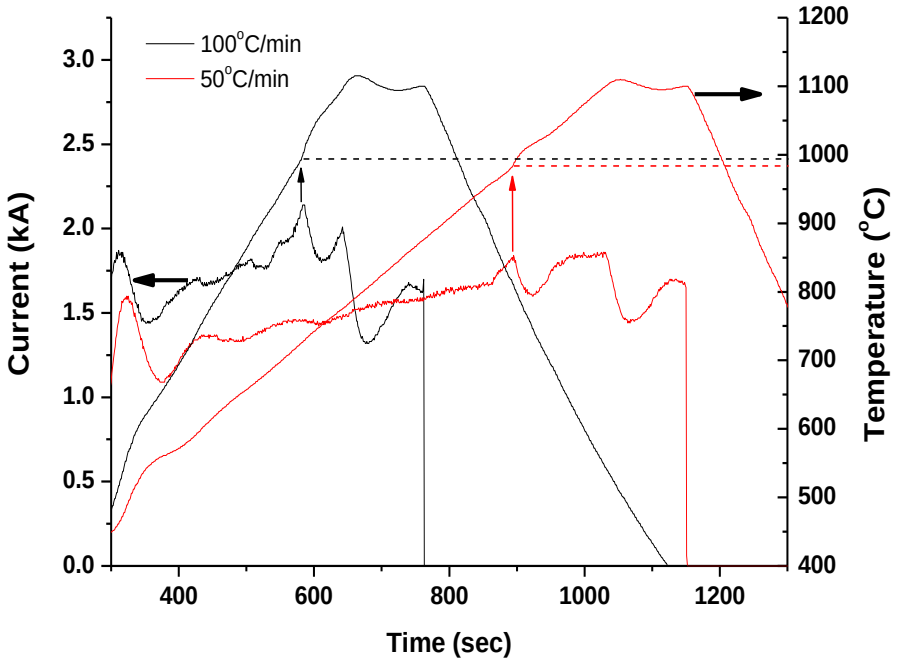

Fig. 8.3 SPS current and temperature profiles of Fe-50 Co powder heated at shown rates and cooled by the convective heat transfer with the cooling water; the sintering pressure and soaking time were maintained constant at 7 MPa and 2 minutes, respectively.

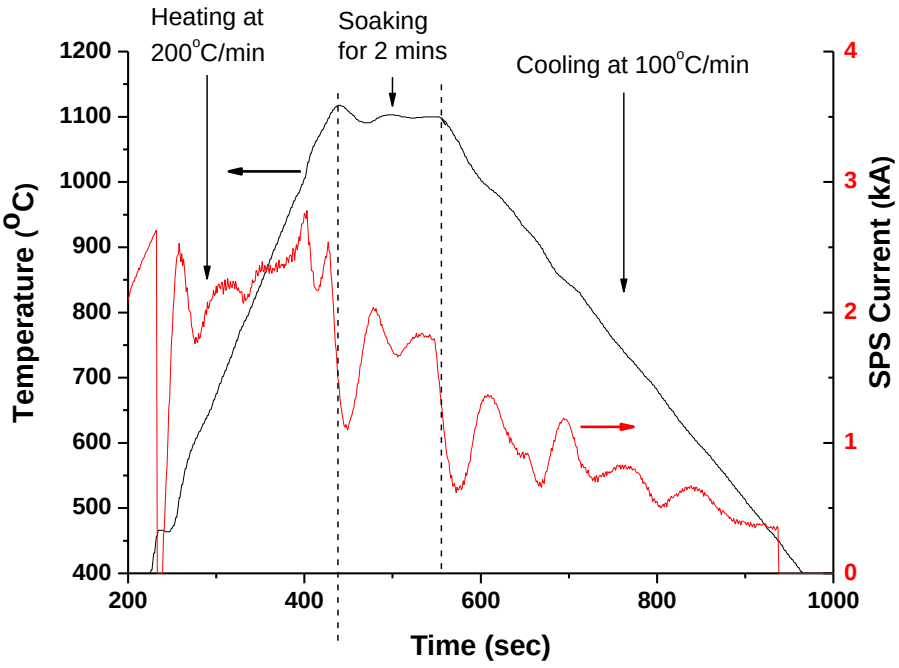

Fig. 8.4 SPS current and temperature profiles of Fe-50 Co powder heated and cooled at 200 and 100°C/min, respectively; the sintering pressure and soaking time were maintained constant at 7 MPa and 2 minutes, respectively.

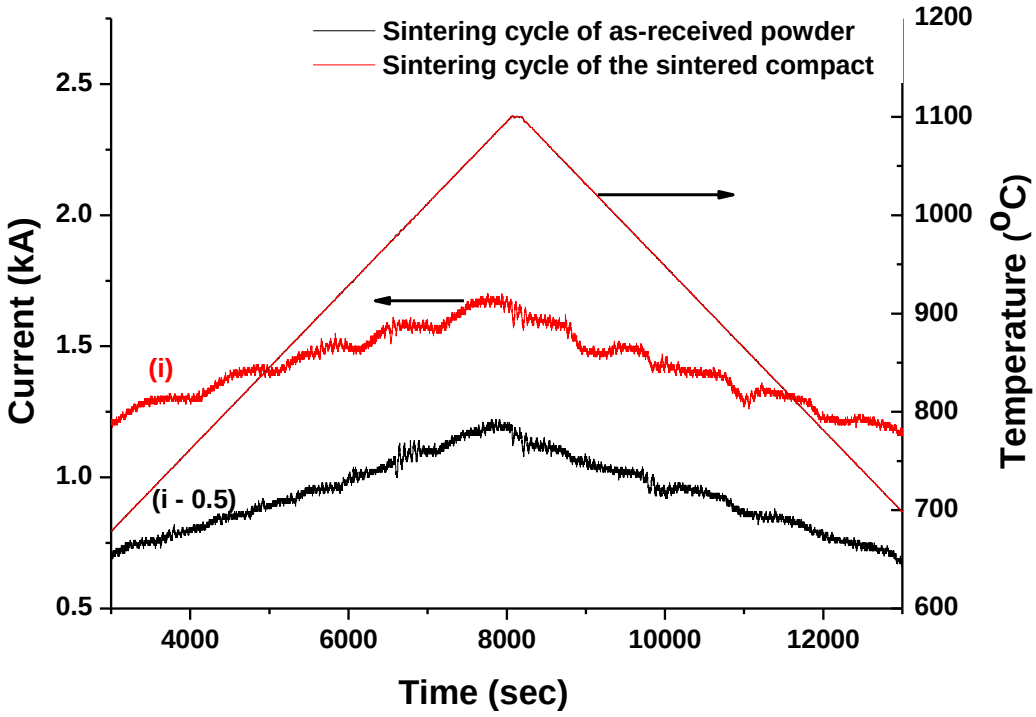

Fig. 8.5 SPS current and temperature profiles of Fe-50 Co powder and sintered compact heated and cooled at 5°C/min; the sintering pressure and soaking time were maintained constant at 7 MPa and 2 minutes, respectively. As shown, a constant (0.5) was subtracted from the SPS current values to stack the current profiles.

Grasso et al. [1] showed that with the increase in the mechanical pressure, the temperature difference across the punch/die/sample will be decreased. In order to improve the electrical contact, to increase the density of the compact and to increase the temperature uniformity, the mechanical pressure was slowly increased during heating such that 80 MPa pressure was attained at the maximum temperature. The current and the temperature values recorded during the sintering cycles of Fe-Co powder and sintered compacts are shown in Fig. 8.6. The SPS current during the start of the temperature measurement (around 500°C) and the start of soaking were not smooth due to the variation in the heating rate at those points. Unlike for the samples heated under minimum pressure, the current profiles for those heated under high pressure appeared relatively smooth. The Curie transition was clearly marked by fluctuations in the SPS current. On repeating the run for the sintered compact, a new rise and fall current pattern emerged at lower temperature. With the increase in the number of runs the amplitude of newly formed oscillations was increased, whereas that of the one observed at higher temperature was reduced. Similar behaviour was observed in the current profile recorded during controlled cooling. The nucleation of new fluctuations at a constant low temperature suggested that a new crystallographic phase was formed in the

system, whose Curie temperature was lower than that of the former phase. It had already shown a drop in the Curie temperature by about 30 K in L10 type ordered Fe-Pt alloys upon complete ordering [2]. With the increase in the number of runs, the volume fraction of the ordered alloy was increased and hence the Curie temperature was lowered in Fe-50 Co alloy. The temperatures corresponding to the first rise and fall in the SPS current fluctuations are noted as the Curie temperature for heating and cooling, respectively. Both the ordered and disordered phases exhibited thermal hysteresis of Curie transition. For 10^{o}C/min sintering experiments, the hysteresis width for the disordered alloys (ΔT~16^{o}C) was smaller than that of the ordered alloy (ΔT~ 51^{o}C).

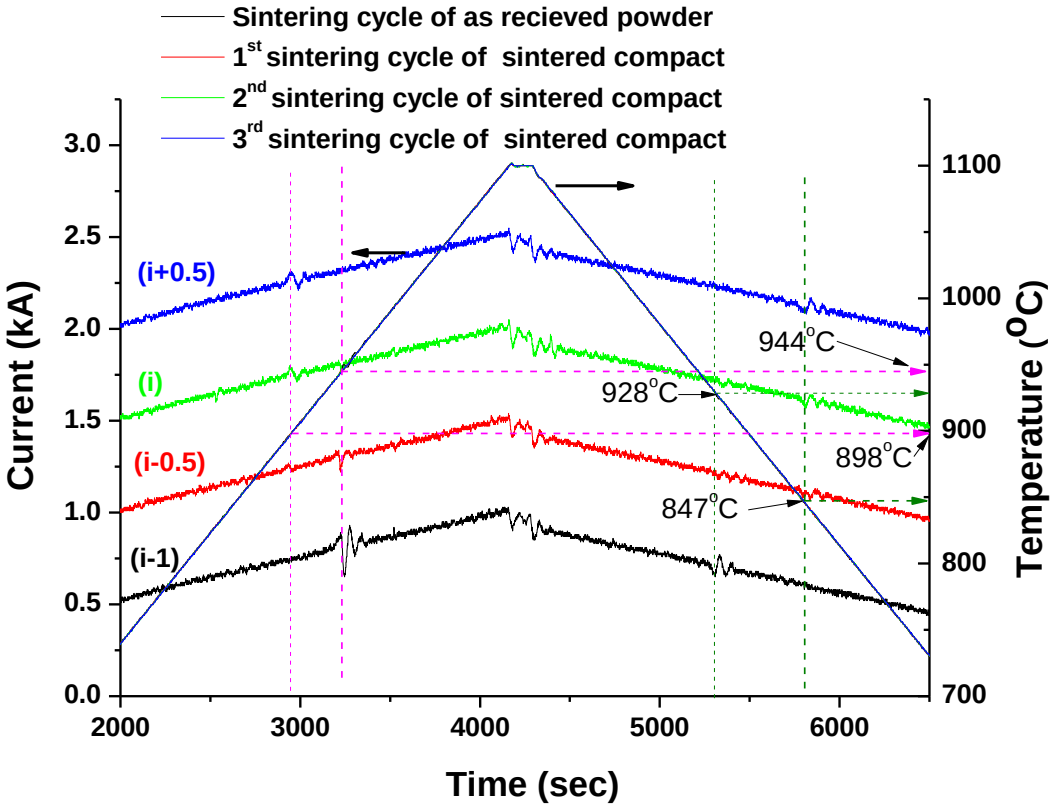

Fig. 8.6 SPS current and temperature profiles of Fe-50 Co powder and sintered compacts heated and cooled at 10^{o}C/min; the soaking time was maintained as 2 min and the pressure was increased such that it was 80 MPa at 1100^{o}C. As shown, constants were subtracted from the SPS current values to stack the current profiles.

The current and temperature recorded during the sintering of pure Fe powder and sintered Fe compact are plotted in Fig. 8.7.

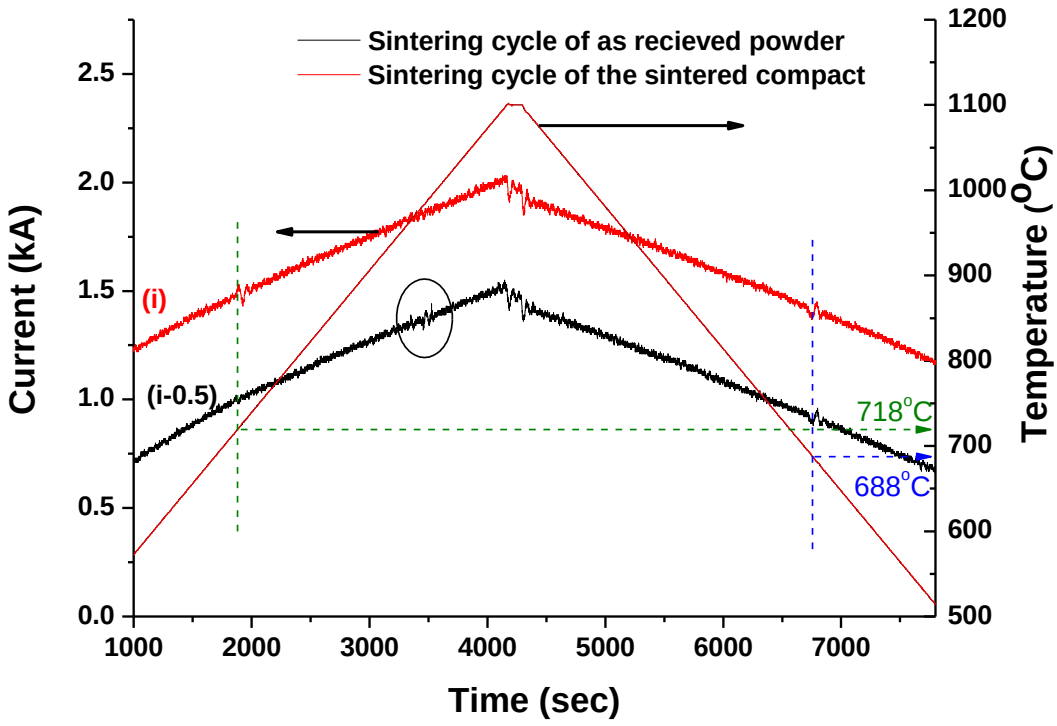

Fig. 8.7 SPS current and temperature profiles of pure Fe powder and sintered compacts heated and cooled at 10°C/min; the soaking time was maintained as 2 min and the pressure was increased such that it was 80 MPa at 1100°C. As shown, a constant (0.5) was subtracted from the SPS current values to stack the current profiles.

As observed in Fe-Co alloys, the fluctuations in the current near the Curie temperature were evident only when the resistivity of the compact was reduced. Because of the lower density of the compact, the fluctuations were not evident during the first heating run. However, density improvements achieved by heating the samples to 1100°C made the oscillations noticeable in the subsequent cooling and heating runs. Due to the absence of any new phase formation, the amplitude of the fluctuations and the temperature at which they were observed remained constant. During the first heating run for Fe powders, the current also fluctuated at about 950°C (as highlighted by an oval). Those variations might be associated with $\alpha - \gamma$ phase transition in iron and were not strong enough to be visible in the following cooling and heating runs. A magnetic transformation thermal hysteresis with a width of 30°C was noted for pure Fe powder. The emergence of fluctuations in the SPS current profile at a significantly lower temperature than that predicted using DSC suggested that the temperature measured by the pyrometer was lower than the actual temperature of the

sample. This confirmed the earlier experimental and finite element modelling results of Zavaliangosa et al. [3].

8.4 Theory behind the SPS current anomaly near Curie temperature

When a ferromagnetic material is heated, part of the supplied energy is expended in increasing the amplitude of thermal vibration of the atoms (lattice specific heat) and the rest in increasing the kinetic energy of the valence electrons (electronic specific heat). If the material is magnetic, additional specific heat to produce magnetic spin disorders will be added, which is termed magnetic specific heat. The number of spins disordered per degree rise in temperature is very large just below Curie temperature, whereas the magnetisation falls precipitously and becomes zero at the Curie temperature. In the presence of a magnetic field, the change to the paramagnetic state is not sharp because of the retention of spin clusters, which are the short range structures formed immediately after Curie temperatures [4]. In addition to saturation magnetisation, physical properties such as resistivity, specific heat, thermal expansivity and elastic constants also change at the Curie temperature [5]. Sales et al. [6] showed that when an ac current is passed through a ferromagnetic wire of higher permeability, the permeability and resistivity values increased with temperature and passeed through a maximum and fell to a lower value in the vicinity of Curie temperature. They also showed that the resistivity change was increased with the increase in the frequency of the ac current and the permeability of the ferromagnetic wire.

In Fe, the magnetic transition at the Curie point involved no crystal structure change. The insignificant enthalpy change associated with the Curie transition of iron was difficult to estimate from the DSC profile. In Fe-50Co, the ferromagnetism was lost because of $\alpha - \gamma$ phase transition. The DSC result showed a larger endothermic enthalpy change of 75.58 J/g during the transition. In the presence of a magnetic field, the enthalpy change associated with α/γ or γ/α transformation in Fe-Co alloys and the transformation temperature were reduced and increased, respectively, because of the large magnetisation difference between α and γ phases [7]. In the presence of ac or dc magnetic field, the Curie transition of ferromagnetic material such as Fe and Ni, which occurs without any change in crystal structure, remained constant [8]. Also, the presence of pressure has no significant effect on the Curie temperature of bcc Fe. It has been both experimentally and theoretically showed that Fe exhibits only about 0.3 K change in temperature for every 100 MPa change in pressure [9-10]. In Fe-50 Co, the bcc ferromagnetic phase changes to an hcp non-ferrmomagnetic structure under a

mechanical pressure higher than 30 GPa [11]. Hence, the mechanical pressure of 80 MPa applied for improving the electrical and thermal contact during SPS processing is believed to have no significant effects on the magnetic and structural phase transitions. The enthalpy change cannot explain the anomalous behaviour of the current because in Fe, the enthalpy change at the Curie point was smaller than that associated with α-γ transition and no abnormalities were observed in the current profile due to the α-γ transition. The fluctuations might be associated with the abrupt change in either resistivity or permeability, or both, of the material in the vicinity of Curie point as reported in [6]. The pulsed dc SPS current which was on for 15 ms and off for 5 ms can be compared with ac current. With the increase in the density of the samples under mechanical pressure, their permeability and conductivity was increased and hence, the fluctuations were more significant in the dense compact.

8.5 Effect of sintering above and below Curie T on magnetic properties

The hysteresis responses of the Fe-50Co compacts sintered under a minimum mechanical pressure (7 MPa) above and below Curie temperature are compared in Fig. 8.8.

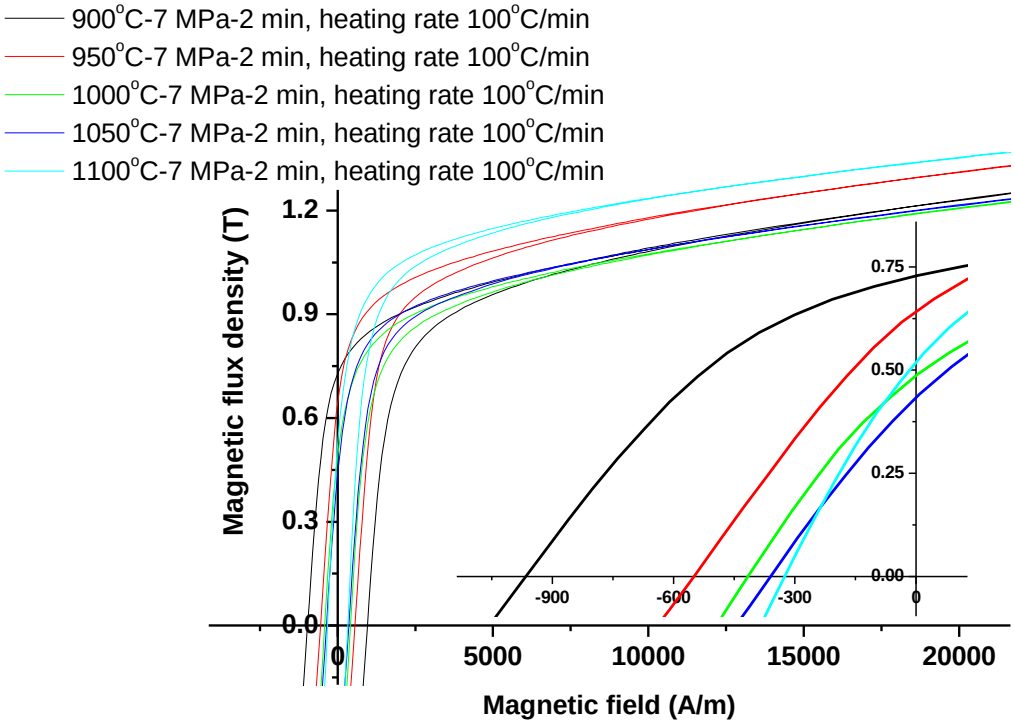

Fig. 8.8 Upper half of the hysteresis curves of the compacts spark plasma sintered at the shown conditions

The density of all the five compacts, as measured using Archemedes method, varied between 6.2 and 6.5 g/cm^3. It was evident that sintering of Fe-Co alloy in the vicinity of and above Curie temperature produced a reduction in the coercivity. The coercivity reduction can be explained either by improvement in density or coarsening of microstructure or both. The only factor that dictates the saturation induction of the monolithic material was the compact density. Due to inefficient densification, spark plasma sintering of Fe-Co alloy in the vicinity of Curie temperature (1000 and 1050^{o}C) yielded compacts with lower saturation induction and remanence. The powders sintered at 1100^o C showed maximum saturation induction and minimum coercivity because of the improvement in density and microstructure coarsening.

References

1. S. Grasso, Y. Sakka, G Maizza, Pressure effects on temperature distribution during spark plasma sintering with graphite sample, *Mater. Trans.* 50[8], 2111-2114 (2009)
2. L. Wang, Z. Fan, A. G. Roy, and D. E. Laughlin, Effects of atomic ordering on the Curie temperature of FePd L10 type alloys, *J. Appl. Phys.* **95**, 7483-7485 (2004)
3. A. Zavaliangosa, J. Zhanga, M. Krammerb, J. R. Groza, Temperature evolution during field activated sintering, *Mater. Sci. Engg.* A **379**, 218–228(2004)
4. B.D Cullity and C.D Graham, Introduction to magnetic materials, New Jersey, IEEE press and A John Wiley & sons, Inc., publisher, 2 nd edition (2009), pp. 117-129
5. R.M. Bozorth, Ferromagnetism, New York, IEEE press, 2 nd edition (1978) pp. 713-728
6. B. C. Sales, M. B. Maple, Low-frequency electrical resistance of iron, cobalt, and nickel in the vicinity of their Curie temperatures, *Appl. Phys. A* **31[2]**, 115-117 (1983)
7. W. Maruno, Y. Morizono and S. Tsurekawa, Differential scanning calorimetry of the α/γ transformation in Fe-Co alloys under a magnetic field, *Mater. Trans.* **54[9]**, 1823-1828 (2013).
8. M.S. Leu, C.S. Tsai, C.S. Lin and S.T. Lin, The determination of Curie temperature by differential scanning calorimetry under magnetic field, *IEEE Trans. Magn.* **27[6]**, 5414-5416 (1991)
9. F. Körmann, A. Dick, T. Hickel, J. Neugebauer, Pressure dependence of the Curie temperature in bcc iron studied by *ab initio* simulations**,** *Phys. Rev. B* **79**, 184406-1-5 (2009)
10. J. M. Leger, C. Loriers-Susse, B. Vodar, Pressure effect on the Curie temperatures of transition metals and alloys, *Phys. Rev. B* **6**,4250 (1972)
11. R. Torchio, S. Pascarelli, O. Mathon, C. Marini, S. Anzellini, P. Centomo, C. Meneghini, S. Mobilio, N.A Morley, M.R.J. Gibbs, Structure and magnetism in compressed iron-cobalt alloys, *High Pressure Research* **31[1]**, 148-152 (2011).

Chapter 9
Conclusions and recommended future work

9.1 Conclusions

This research is a novel attempt to improve the mechanical properties of Fe-50Co alloy by composite strengthening route employing a rapid sintering technology. The influence of the sintering variables and the addition of coated and uncoated SiC particultes, SiC whiskers and carbon nanotubes on the magnetic and mechanical properties of the spark plasma sintered Fe-50Co are investigated and reported in this thesis. The results showed that composite strengthening is a viable option to improve the mechanical properties of the brittle matrix alloy, provided a suitable reinforcement is selected and the material is fabricated under optimum sintering conditions. As the matrix material is iron based, these findings will be of great interest to research community working on iron and or steel based composites. The conclusions drawn out of this research are divided under five sections as follows:

9.1.1 Unreinforced Fe-Co alloys

The effect of SPS variables such as maximum temperature, soaking time, maximum pressure, rate of pressure application, temperature at which the pressure was applied and removed, heating rate and cooling rate on the magnetic and mechanical properties of the monolithic Fe-50Co compacts were investigated and reported.

The soaking time to prepare a nearly full-dense compact can be lowered with the rise in the maximum temperature up to 900^{o}C. An increase in the temperature above 900^{o}C promoted grain growth over sintering.

An increase in the soaking time at temperatures below the order-disorder transition temperature (T_{o-d}) and a reduction in heating and cooling rates produced an increase in the volume fraction of the ordered alloy. With an increase in the soaking time at temperatures above T_{o-d}, the fraction of the disordered alloy was increased; however, the amount of increase for a given holding time was dictated by the difference between T_{o-d} and the soaking temperature. An increase in the ordering fraction produced an increase in saturation induction, coercivity, hardness and mechanical strength of the compact. Therefore, both the final magnetic and mechanical properties of the monolithic materials could be tuned by controlling the fractions of the ordered alloy in the final compact using the SPS parameters.

The mechanical pressure applied during sintering had no significant effect on the density and final properties of the compact sintered at temperatures above $T_{o-d,}$ however, at

lower temperatures it had a pronounced influence on the density and residual stress of the compact and in turn on the properties. When the mechanical pressure was applied above T_{o-d}, the coercivity of the compact was reduced; presumably, due to the formation of very fine ordered domains that exhibit lower coercivity.

Within the range of experiments conducted, the optimum SPS temperature, pressure and time to process Fe-50Co alloy was found to be 900^{o}C, 80 MPa and 2-5 mins, respectively.

Spark plasma sintering of Fe-Co alloys below the Curie temperature (T_c) led to anisotropic of magnetic properties due to the interaction of current and magnetic spins of the material. When the maximum temperature was increased above $T_{c,}$ the magnetic properties remained isotropic.

Annealing of spark plasma sintered materials at temperatures lower than T_{o-d} produced an increase in the ordering fractions. Heat treatment of sintered materials at temperatures between T_{o-d} and T_c promoted grain growth and densification during heating and soaking and ordering during the slow cooling in the furnace. Annealing the compact materials at temperatures higher than T_c promoted excessive grain growth and densification and less ordering because of the coarse grain morphologies that resulted during soaking.

9.1.2 SiC particulate composites

Electroless plating technology was employed to encapsulate non-catalytic ceramic particles with magnetic layers such as Ni-P and Co, non-magnetic Cu layer and duplex coatings with both non-magnetic and magnetic types.

Because of the formation of ferromagnetic and Heusler-like $FeCo_2Si$ compounds at the interface, composites with bare and copper coated particulates exhibited better magnetic induction values, poor flexural characteristics and higher magnetic and mechanical hardness.

Materials with Ni-P plated particles showed intermediate flexural strength and Vickers hardness among the particulate composites studied. They exhibited the lowest coercivity but also the lowest saturation induction.

By forming a coarse grained and porosity free microstructure near the particulates, composites with duplex plated particulates showed the lowest mechanical hardness and intermediate flexural strength and magnetic induction values. The coercivity of the composites remained the same even when the volume fraction of particulates was increased from 5 to 10%.

The composites with cobalt plated particles showed the highest permeability and flexural strength among the sintered materials with fillers because of the better interfacial bonding and the absence of any brittle interfacial compounds. Also the magnetic induction was not changed and the coercivity was reduced compared to the materials with ferromagnetic interfacial compounds.

In summary, electroless Co plating of reinforcement particles has been found to be a viable method to improve interfacial bonding of a selected reinforcement with Fe-Co based materials.

9.1.3 SiC whisker composites

The inclusion of SiC whiskers promoted both the capillary driven processes such as densification and grain growth of the magnetic matrix alloy due to the overheating produced by the restrictions imposed by the non-conducting whiskers for the SPS current flow. The process kinetics was strongly dictated by the distribution and volume fraction of whiskers. Due to grain growth of the matrix, the flexural strength and magnetic hardness were consequently decreased for the composites containing bare whiskers.

Because of the ineffectiveness of the ultrasonication method (in ethanol) to disperse the copper coated whiskers, the mechanical properties of the composite materials containing them were not improved irrespective of the coating thickness. However, an increase in the coating volume fractions increased the coercivity significantly.

The nanocrystalline intermetallic Fe_3Ni_2 precipitates that were formed in the composites containing Ni-P coated whiskers helped to improve their mechanical strength, ductility and mechanical hardness at the cost of soft magnetic characteristics such as coercivity and saturation induction. The mechanical property increments and the magnetic property decrements were dictated by the volume fraction of the coating.

Although cobalt coated whiskers were uniformly dispersed in the matrix, they were not helpful in improving the mechanical properties of the composites when sintered at 900^{o}C because of the grain growth promoted by SPS current-whisker interactions. Also in these materials, no intermetallic compounds were formed at the interface which could help to improve the mechanical properties.

The materials containing more than 2 vol% of relatively uniformly distributed coated and uncoated whiskers showed abnormal grain growth.

The amorphous Ni-P plated whiskers were found to be the most suitable reinforcements for improving the mechanical strength and ductility of brittle Fe-50 Co alloy.

Those materials with nanocrystalline precipitates, which are prepared by a rapid processing route such as SPS, can be employed in electrical machines that operate under DC flux conditions, where the reduction in the magnetic properties is tolerable.

9.1.4 CNT composites

Composites containing up to 10 vol% of CNTs were prepared by spark plasma sintering at 900^{o}C by applying a uniaxial pressure of 80 MPa for 2 minutes after mixing the matrix powder and CNTs by two different routes that involved ball milling.

Atmospheric high energy ball milling of monolithic Fe-Co or composite powder mixture containing CNTs and Fe-Co promoted the formation of maghemite phase in the system.

The addition of CNTs promoted long range ordering in the matrix alloy and the ordering fraction increased with the increase in the CNT content.

The structural integrity of the bare CNTs was maintained in the composites even after high energy ball milling and spark plasma sintering provided the mechanical pressure application was started at 450^{o}C during sintering. Application of pressure at higher temperatures helped to realise oxide removal in the system at the expense of the integrity of the CNTs.

Composites containing less than 1.5 vol% of bare CNTs showed improvements in saturation induction and mean flexural strength and reduction in coercivity due to enhancement of spark plasma sinterability. On increasing the volume fraction beyond 1.5 vol%, CNT clustering was promoted and a fall in the sinterability resulted.

Drying of electroless Ni-P plated CNTs in the presence of ethanol under atmospheric conditions promoted the nucleation and growth of graphene oxide on the surface of thin Ni-P coating.

The duplex coated CNTs (Ni-P and graphene oxide) helped to reduce the structural damage of CNT walls during processing.

In comparison to the monolithic materials, the composites with a lower volume fraction of coated CNTs (1.5 vol%) showed an increase in ductility, flexural strength and hardness and a drop in coercivity provided the short fibres were uniformly distributed in the matrix. Because of the inclusion of Ni and P into Fe-Co, a fall in the saturation induction and a rise in the coercivity were noted in composites with coated CNTs with respect to the composites with bare CNTs.

With the advancement in the CNT production methods and in the powder sintering technologies, the Fe based magnetic CNT composites can be produced economically for the next generation electrical machines.

9.1.5 Phase transitions in ferromagnetic materials and their effects on spark plasma sintering

Heating and cooling of pure Fe and Fe-50Co under pulsed high current produced repeatable and detectable variations in the current profile in the vicinity of the Curie point due to the abrupt change in permeability and resistivity of the material at that point. This behaviour, which was observed in very dense ferromagnetic material and in the presence of high pressure, can be successfully employed to calibrate the SPS system.

Among pure iron and Fe-50 Co alloy, the former was found to be more suitable because there is no crystal structure change during the ferromagnetic transition and the presence of magnetic field or pressure did not produce any significant change in the transition temperature.

9.2 Recommended future work

9.2.1 High temperature mechanical property measurements

It is required to predict the high temperature mechanical properties of Fe-Co composites to successfully employ them in electrical subsystems in the transport industry. For example, some of the electric power systems in more electric aircrafts (MEA) are subjected to higher temperatures of up to 600^{o}C during service and it is required for designed composites to exhibit 600 MPa or greater at 600^{o}C and a creep strength of $5x10^{-10}$ s^{-1} for a period of 5000h at 550^{o}C [1]. In order to warrant the designed composites for critical components such as in MEA, experiments are needed to understand the relationship between the steady state creep rates and rupture time with the variation of stress and temperature, high cycle and high temperature fatigue behaviour.

9.2.2 Processing of SiC whisker composites

In this research, the main problems reported in the composites with bare SiC whiskers were agglomeration of whiskers and grain growth at 900^{o}C in composites with higher than 2 vol% of SiC whiskers. Vigorous sonication using an ultrasonic probe could be tried to disperse the whiskers during colloidal processing. Non-aqueous liquid media other than ethanol could be tested to find a suitable medium to disperse the CNTs in water intolerant Fe-

Co alloys. Sintering experiments could be performed to study the influence of the process parameters such as sintering time and temperature on the grain growth behaviour of these composite materials, in particular using the composites with cobalt plated whiskers.

9.2.3 Ductility measurements in short fibre composites

Using the bend test responses, it has been reported in this work that some composites improved the ductility of the brittle Fe-Co alloys. Standard tensile test experiments are required for those materials to quantify the ductility enhancements compared to the monolithic materials. Those strength and ductility values can be compared with that of the commercial Fe-Co derivatives prepared by the conventional casting and metal forming route.

9.2.4 Resistance measurements and magnetic property measurements under AC conditions

Some of the components in the current interest MEA would be operated under AC conditions (frequencies up to 400 Hz) [1]. The amount of energy loss due to eddy currents, which are generated when a magnetic component is employed under AC conditions, is given by [2]

$$W_e = k_e \frac{B_m^2 f^2 L t}{\rho \pi}$$

where B_m is the maximum flux density swing, f is the frequency, t is the thickness of the sample, r is the resistivity, L is the domain width and k_e is a constant. The eddy current loss can be minimised by reducing the resistivity of the material employed. The changes in the resistivity due to the addition of conductive reinforcements such as CNTs and non-conductive ones such as SiC particles and whiskers are required to be measured. The measurements can be done using a four-point probe method. The eddy current loss of the monolithic and composite materials could be measured using either a ring or a bar sample, cut from the circular sintered samples. In the case of a bar sample, yokes of soft magnetic material are required to provide a closed flux path (or contain the magnetic flux).

9.2.5 Magnetic measurements of coated short fibres

The DC magnetic characteristics of the coated short fibres such as whiskers and carbon nanotubes could be measured using a vibrating sample magnetometer (VSM) in the as-coated and heat treated conditions. The optimised and economical Ni-P and cobalt coated CNTs with improved spatial resolution and good mechanical properties could be employed as a magnetic tip for magnetic force microscopy (MFM) probe to study nanocrystalline magnetic materials and miniaturised magnetic recording media [3].

9.2.6 Domain studies on monolithic and CNT composites

The full width half maximum of the superlattice lines obtained using an X-ray diffractometer with Co target suggested that the antiphase domain sizes in these ordered Fe-Co alloys are in the nanocrystalline ranges. Neutron diffraction studies can be undertaken to quantify the ordering alloy fractions in all the materials. MFM could be employed to study the domain patterns of these nanocrystalline structures in both the monolithic and composite materials for future developments.

9.2.7 Vacuum ball milling of CNTs and Fe-Co

Ball milling of Fe-Co in atmospheric conditions produced maghemite phase, which was found to be affect the mechanical strength and toughness drastically. Ball milling under an inert atmosphere could be tried to study the influence of CNT addition alone on the final properties.

References

1. R. S. Sundar and S. C. Deevi, Soft magnetic FeCo alloys: alloy development, processing, and properties, *Inter*. *Mater. Rev.* **50**, 157-192 (2005)
2. G. Y. Chen and J. H. Wernick: 'Ferro magnetic material', vol. 2, (ed. E. P. Wohlforth), 55–188; 1980, North-Holland Pub. Co.
3. Z. Deng, E. Yenilmez, J. Leu, J. E. Hoffman, E. W. J. Straver, H. Dai, K. A. Moler, Metal-coated carbon nanotube tips for magnetic force microscopy, Appl. Phys. Lett. 85, 6263-6265 (2004).

List of publications based on this research

1. **M K Mani,** G. Viola, M. J Reece, J. P Hall and S. L Evans**, "Structural and magnetic characterization of spark plasma sintered Fe-50Co alloys",** MRS Proceedings, vol. 1516, 2012, pp. 201-207, DOI: 10.1557/opl.2012.1669

2. **M K Mani,** G. Viola, M. J Reece, J. P Hall and S. L Evans**, Influence of coated SiC particulates on the mechanical and magnetic behaviour of Fe-Co alloy composites** (article in the press of Journal of Materials Science), DOI: 10.1007/s10853-013-7954-9

3. **M K Mani,** G. Viola, M. J Reece, J. P Hall and S. L Evans**, Mechanical and magnetic characterisation of SiC whisker reinforced Fe-Co alloy composites**, *Mater. Sci. Engg. A* **592 C**, 19-27 (2014) DOI: http://dx.doi.org/10.1016/j.msea.2013.10.099

4. **M K Mani,** G. Viola, M. J Reece, J. P Hall and S. L Evans**, Fabrication of carbon nanotube reinforced iron based magnetic alloy composites by spark plasma sintering,** *J. Alloys Compd.* **601[15]**, 146-153 (2014) DOI: http://dx.doi.org/10.1016/j.jallcom.2014.02.169

5. **M K Mani,** G. Viola, M. J Reece, J. P Hall and S. L Evans**, Calibration of temperature during spark plasma sintering using ferromagnetic Curie transition** (under review)

6. **M K Mani,** G. Viola, M. J Reece, J. P Hall and S. L Evans**, Improvement of interfacial bonding in carbon nanotube reinforced Fe-50Co composites by Ni-P coating: Effect on magnetic and mechanical properties** (*accepted for publication in Mater. Sci. Engg. B*)

7. **M K Mani,** G. Viola, M. J Reece, J. P Hall and S. L Evans, **Mechanical properties of spark plasma sintered Fe-Co alloys** (under review)